Design and Optimization of Haptic Interfaces for Robot-Assisted Neurosurgery

by

Ali Torabiparizi

A thesis submitted in partial fulfillment of the requirements for the degree of

Doctor of Philosophy

in

Biomedical Engineering

Department of Electrical and Computer Engineering

University of Alberta

Abstract

Haptic interaction is the human's most basic way to understand an environment and effect change in it. Haptic feedback provides humans who operate machines with a sense of touching objects they are not actually touching but are manipulating by the machines. Haptic feedback allows the human operators of machines to handle objects more gently, safely, reliably, and precisely.

Haptic interfaces (HIs) produce the illusion of touch by applying forces to the users' hands. An HI should satisfy the requirements of back-drivability, low apparent inertia, large workspace, and low friction for the best perception of small reflected forces, and large intrinsic stiffness and force feedback capability for the best perception of large reflected forces. Then, the HI can recreate soft and stiff contact experiences for the user with high fidelity.

The currently available HIs are either parallel mechanisms with higher force feedback capability, a higher intrinsic stiffness and a smaller workspace or serial mechanisms with lower force feedback capability, a lower intrinsic stiffness and a larger workspace. Since a high force feedback capability, a high intrinsic stiffness and a large workspace are desirable; this research will secure the best of both worlds by appropriate design and control of redundant haptic interfaces, which have more degrees of freedom than minimally required to perform a task.

This research helps create haptic interaction and teleoperation systems with enhanced fidelity and performance. To achieve this, first, we introduce the intrinsic benefits of redundant haptic interfaces in terms of better kinematic

and dynamic characteristics. Then, a quantifiable measure of the combined HI-slave system manipulability is formulated that can be used in the kinematic design of HIs as well as their controller design. Next, a null-space controller is developed for the redundant haptic interface that employs the proposed manipulability index to enhance the performance of teleoperation tasks by matching the kinematics of the redundant HI to the kinematics of the slave robot. We also propose two task-dependent null-space controllers in which the internal motion of the redundant haptic interface is appropriately controlled to achieve a desired performance, i.e., low back-drive friction in case of free-space motion and soft contact or large force feedback capability in case of stiff contact. The advantages and effectiveness of the proposed approaches are demonstrated through experiments.

Preface

The overarching objective of this research is to enable a user to experience believable and complex interaction with an environment (be it virtual or physical, nearby or remote) via a haptic interface in ways nearly indistinguishable from direct touch. This thesis is part of a multidisciplinary research collaboration, led by Dr. Mahdi Tavakoli (principal investigator) at the Department of Electrical and Computer Engineering, University of Alberta, Dr. Koroush Zareina at the Department of Mechanical & Industrial Engineering, Ryerson University, and Dr. Garnette Sutherland at the Faculty of Medicine, University of Calgary. All of the work presented in this thesis was conducted in the Telerobotic and Biorobotic Systems Lab at the University of Alberta. The research project, of which this thesis is a part, received research ethics approval from the University of Alberta Research Ethics Board, "Measuring user performance in controlling a robot through a user interface", No. Pro00055825.

I was responsible for the experiment design, performing the experiments, data collection and analysis, and the manuscript preparation. Also, the experimental setup was designed by myself. Dr. Mahdi Tavakoli was the supervisory author on this project and was involved throughout the project in concept formation and manuscript composition.

Chapter 1 presents the motivation and objectives of this project and summarized the thesis organization and contributions. Parts of this chapter and Chapter 2 have been published in a book chapter: Angel R. Licona, Fei Liu, David Pinzon, Ali Torabi, Pierre Boulanger, Arnaud Lelevé, Richard Moreau, Minh Tu Pham, Mahdi Tavakoli, "Applications of Haptics in Medicine," In Troy McDaniel and Sethuraman Panchanathan (Eds.), Haptic Interfaces for Accessibility, Health, and Enhanced Quality of Life, Springer, 2020.

Chapter 3 of this thesis has been published as: Ali Torabi, Mohsen Khadem, Kourosh Zareinia, Garnette Sutherland, and Mahdi Tavakoli, "Application of a Redundant Haptic Interface in Enhancing Soft-Tissue Stiffness Discrimination," IEEE Robotics and Automation Letters, vol. 4, no. 2, pp. 1037 - 1044, April 2019.

Chapter 4 of this thesis has been presented as: Ali Torabi, Mohsen Khadem, Kourosh Zareinia, Garnette Sutherland and Mahdi Tavakoli, "Manipulability of Teleoperated Surgical Robots with Application in Design of Master/Slave Manipulators," The International Symposium on Medical Robotics, Atlanta, GA, 2018.

Chapter 5 of this thesis has been published as: Ali Torabi, Mohsen Khadem, Kourosh Zareinia, Garnette Sutherland, and Mahdi Tavakoli, "Using a Redundant user Interface in Teleoperated Surgical Systems for Task Performance Enhancement," Robotica, 2020. In press.

Chapter 6 of this thesis has been published as: Ali Torabi, Kourosh Zareinia, Garnette Sutherland, and Mahdi Tavakoli, "Dynamic Reconfiguration of Redundant Haptic Interfaces for Rendering Soft and Hard Contacts," IEEE Transactions on Haptics, 2020.

Chapter 7 of this thesis has been presented as: Ali Torabi, Kourosh Zareinia, Garnette Sutherland, and Mahdi Tavakoli, "Redundant Haptic Interfaces for Enhanced Force Feedback Capability Despite Joint Torque Limits," IEEE/ ASME International Conference on Advanced Intelligent Mechatronics, Boston, USA, 2020.

Acknowledgements

This Ph.D. thesis would not have been possible without the guidance, support and help of my supervisors, family, and friends. First and foremost, I would like to thank my supervisor, Dr. Mahdi Tavakoli, who believed in my abilities, and supported and encouraged me to push my limits past what I initially thought was possible. I am incredibly thankful and consider myself truly lucky to have worked with a successful, incredibly patient, caring, and outstanding mentor and role model. He has made it possible for me to enjoy access to a world-class lab facility and the most advanced robots. I would like to thank my co-supervisor, Dr. Kourosh Zareinia, for his insightful comments and feedback, and for his expert advice and suggestions. Thank you to Dr. Garnette Sutherland for providing expert opinions and advice on the neurosurgery and the clinical aspects of this thesis. I want to thank my supervising committee member, Dr. Tongwen Chen, and the members of the Ph.D. Exam Committee, Dr. Jee-Hwan Ryu and Dr. Qing Zhao, for their valuable comments and feedback.

Many thanks to the current and past members of the Telerobotic and Biorobotics Lab at the University of Alberta. Thanks to Jay Carriere, Thomas Lehmann, Carlos Rossa, Bita Fallahi, Lingbo Cheng, Renz Ocampo, Jason Fong, Carlos Martinez, Mehrnoosh Afshar, Mojtaba Akbari, Teng Li, Javad Khodaei-Mehr, Amir Zakerimanesh, Abed Soleymani, Mojtaba Sharifi, and Hongjun Xing for the help, advice, discussions, support, and friendship. I would like to extend a special thanks to Dr. Mohsen Khadem for mentoring me when I was a junior member of the lab and helping me get started when I first arrived at the lab. Also, I am thankful to my wonderful friends and colleagues who have made the last four years a fantastic experience and kept

me sane over the years.

Most importantly, I would like to express my sincere gratitude to my dearest and beautiful wife, Elaheh. Without her love, supports, and sacrifices, I would not have finished this thesis. She is the love of my life, whose inputs, understanding and encouragement have been invaluable.

Finally, I would like to thank my parents, parents-in-law, little sister, brothers-in-law, and sister-in-law for their constant love, encouragement, understanding, patience, and support. I am indebted to each of you.

The research presented in this thesis was supported by the Canada Foundation for Innovation (CFI), the Government of Alberta, the Natural Sciences and Engineering Research Council (NSERC) of Canada, the Canadian Institutes of Health Research (CIHR), and the Alberta Economic Development, Trade and Tourism Ministry's grant to Centre for Autonomous Systems in Strengthening Future Communities.

Contents

List of Tables

List of Figures

Acronyms

2AFC	Two-Alternative Forced-Choice
ANOVA	Analysis of Variance
ASCM	Actuator Saturation Compensation Method
ASO	Actuator Saturation Observer
DH	Denavit-Hartenberg
DM	Directional Manipulability
DoF	Degrees of Freedom
FDR	False Discovery Rate
FME	Force Manipulability Ellipsoid
HI	Haptic Interface
JND	Just Noticeable Difference
ME	Manipulability Ellipsoid
NHI	Non-redundant Haptic Interface
PSE	Point of Subjective Equality
RHI	Redundant Haptic Interface
SPD	Symmetric Positive Definite
SVD	Singular Value Decomposition
TMI	Teleoperation Manipulability Index
VME	Velocity Manipulability Ellipsoid
WF	Weber Fraction
WMHI	Wheeled Mobile Haptic Interface
WMM	Wheeled Mobile Manipulator

Chapter 1

Introduction

1.1 Motivations

The first sensory modality that develops in humans is the sense of touch. Haptic perception encompasses tactile perception via skin stimulation and kinesthetic perception via muscle stimulation, which informs a human about an object's material, stiffness, and shape properties [91]. To recreate haptic feedback about an environment that is accessed indirectly rather than touched directly by a user, a Haptic Interface (HI) displays forces received from a virtual or a robotic proxy (slave) probing the environment [1]. Depending on whether the slave is virtual or robotic, a haptic virtual environment or a haptic teleoperation system is formed. Regardless, as the user utilizes the HI to operate the slave that interacts with the environment, haptic feedback about slave-environment interaction displayed by the HI engages the user's sense of touch and should give transparency (i.e., realism and fidelity) to the interaction [109].

Haptic interfaces are used for a variety of applications. Many haptic interfaces are used for training surgeons without risking a patient's health [35], [53], [88]. In the same way that a flight simulator works for pilot training, virtual operating rooms can be used for surgeon training while guaranteeing quantitative feedback so that the student can refine their practice before exercising the skills gained on actual patients [11], [19]. Better task performance has been shown by simulator-trained surgeons than those without such training [2], [10]. Given that patients are not placed in jeopardy in these sim-

ulations, early student training can be accomplished using these devices with better overall results [64]. Haptic devices have been used in surgery [27], [80], [140], rehabilitation [9], [125], scientific data visualization [20], enhancement of nano-manipulation systems [130], and CAD/CAM [98].

Surgical procedures are being transformed by robots entering operating rooms. Robots are enhancing surgical techniques and expanding surgeons' capabilities. Surgical robots present the patient to the surgeon through an HI and replicate the surgeon's forces and motions on the patient. Haptics enhances robot-assisted surgery by providing a surgeon with the sensation of operating on a patient via direct touch even though it is done through an HI and then a surgical robot. Haptics has the potential to increase the surgeon's task performance ability and empower him/her to complete more complex surgical tasks. In a teleoperated robotic surgical system, the patient side surgical manipulators are controlled via an HI, operated by the surgeon. The HI connecting the surgeon to the surgical manipulator and environment is an integral part of any robot-assisted surgical system and should be able to intuitively transfer surgical maneuvers to the surgical robot [62], [140]. The HI should also provide sufficient sensory feedback such as haptic sense to the surgeon to more intuitively control the robotic manipulators. The haptic force feedback can reduce unintentional injuries[139], surgeon's fatigue [97], and assist tissue characterization [154].

There are trade-offs between the desirable characteristics of HIs, such as maximum force feedback capability vs. minimum inertia or maximum stiffness vs. workspace size. Indeed, a large force feedback capability requires large actuators, increasing the HI's inertia. A large workspace requires long links, decreasing the HI's stiffness (and increasing its inertia). Therefore, the design of the HI has to be optimized for a specific surgical application. In this thesis, the focus is on designing and optimizing an HI for robot-assisted neurosurgery.

1.1.1 Desired Characteristics of Haptic Interfaces

High-fidelity haptic feedback, which is critical to the safety and success of any interaction, requires appropriate haptic design and control. To this end, HIs

are required to meet the following criteria.

1. Criteria for high kinematic performance:

    - Large workspace: The workspace of the HI needs to be large enough to match the workspace of the human arm and the slave. Otherwise, the user has to employ "clutching" to repeatedly move the HI to another position and orientation (pose) without moving the slave, slowing down the operation.
    - High manipulability: Manipulability or dexterity of the HI measures its ability to take any arbitrary pose and apply any arbitrary force and torque (wrench) across the workspace [156]. Also of importance is the HI's isotropy, which measures if the HI can move and apply force equally well in all directions (i.e., directional uniformity). Singularities conspire to reduce the HI's manipulability and isotropy.
    - Large stiffness and maximum force feedback: The HI should be able to recreate highly stiff environments by providing large forces against the user's hand despite a limited amount of joint torque. Otherwise, stiff environments would be perceived as soft.

2. Criteria for high dynamic performance:

    - Lightweight, low-friction and back-driveable: The HI should not exert any wrench on the user's hand if the slave is moving in free space. Thus, the HI should have a low apparent impedance (mainly inertia) and low friction, especially if the motions involve high accelerations. The HI's mechanical structure, actuators, and configuration determine the inertia and friction. An impedance (ratio of force output to motion input) has inertia, damping and stiffness components.
    - Fast response (large bandwidth): Bandwidth, which defines the maximum speed or frequency at which the HI can operate, needs

to be high to enable rendering of transitions between free space and stiff contact and of different textures. Lightweight HI design leads to a larger bandwidth.

- Large Z-width: An HI's Z-width is the range of impedances that it can stably display [36]. The larger the Z-width, the richer the haptic information presented to the user. A small Z-width can make it hard to distinguish between different environments because they are presented as similar impedances.

1.1.2 Nature of Medical Intervention Dictates the Haptic Interface Design and Control

It is noticeable that there are many available HIs, each of which has its advantages and disadvantages. This, in part, relates to an unavoidable trade-off to optimize the overall design specifications to match a specific application. In teleoperated surgeries, the HI's workspace, maneuverability, degrees of freedom, and sensory feedback should ideally match the intuitive movements of the surgeon's hand to induce the experience and sensation of conventional surgery. As mentioned in Section 1.1.1, the HI should simultaneously satisfy requirements of back-drivability, low apparent inertia and low friction for the best perception of small reflected forces, and large intrinsic stiffness and force feedback capability for the best perception of large reflected forces. Then, the HI can recreate soft and stiff contact experiences for the user with high fidelity. Also, uniformity of haptic feedback and sufficient sensitivity over the practical workspace is of paramount importance to ensure surgical safety and accuracy. Additionally, a HI needs to have a practical workspace that will allow efficient and smooth navigation of the surgical site.

The design of a new HI or the selection of a commercially available HI is application-driven. The specific surgical application regulates the constraints of HI design or selection. These constraints are listed as following:

- The required number of Degrees of Freedom (DoF) of the HI's end effector: The required number of DoF is the minimum number of DoF

that is required to perform a task in the Cartesian space. Most surgical applications are a 7-DoF operation; 3 DoFs for translational movement, 3 DoFs for orientational movement, and one DoF for grasping motion. However, some surgical applications demand lower DoF for the HI's end effector. For instance, needle insertion is a 5-DoF action; 3 DoFs for translational movement and 2 DoFs for orientational movement.

- The required number of DoF of haptic feedback: Ideally, the number of DoF of the force and torque feedback should be matched with the number of DoF of the end effector of the HI. However, in practice, the number of DoF of haptic feedback is a trade-off between the interface complexity, cost, and the degree of benefit of the feedback. In addition to the application requirements, the force and torque feedback DoFs are dictated from the existing measured force and torque at the end effector of the slave. Furthermore, some DoFs of the haptic feedback can be substituted with the graphical cues. Although some studies showed the benefits of haptic feedback [143], some studies showed that the task accuracy and performance is comparable for both haptic feedback and graphical cues modalities, which means that in cases where the haptic feedback is not available, graphical cues can adequately and cost-effectively substitute for haptic feedback [139].

- The required resolution of position and orientation sensing: The resolution of both position and orientation sensing must satisfy the requirements of the surgical application. For instance, a brain tumour ablation in neurosurgery requires millimeter and sub-radian precision [95]; therefore, the HI should meet this requirement by sensing the position and orientation of the surgeon's hand with sufficient resolution and transferring this information to the slave. The just noticeable difference for wrist, elbow, and shoulder of human is 2°, 2°, and 0.8°, respectively [138].

- The required force and torque feedback capability and resolution: To determine the force and torque feedback capability and resolution, the

requirements of the medical intervention need to be inspected. The HI must provide the range of forces and torques that are presented in the particular medical intervention with a sufficient resolution. For example, a common minimally invasive surgery demands a force range of $\pm$10N with a resolution of 0.2N [143]. For the applications in which solid objects such as bones need to be rendered, the HI must provide enough force feedback to render an immovable object. A virtual object with the stiffness of 2000N/m is stiff enough to represent a solid object [94]. The human's hand ability to distinguish a difference in force is 5 to 15 percent of the reference force [137]. High force and torque output resolution are needed to provide the small changes in the environment distinguishable for the user [138].

- The required workspace size: The workspace of the HI must be large enough to guarantee that the desired task is executable. Also, the workspace should be free of singularities. In the process of workspace selection for the HI, careful attention must be paid to the motion scaling between the interface and the slave. Also, the interface footprint to the workspace ration must be small enough for mobility and ease of integration in the operation theatre.

1.1.3 Using a Redundant User Interface in Teleoperated Surgical Systems

A possible approach to address the above-mentioned design trade-offs is employing kinematic redundancies in the HI design. A kinematically redundant manipulator has more Degrees of Freedom (DoF) than required to implement a task. Redundancy in the joint-space of a manipulator enables possible joint motions that do not change the position and orientation of the end-effector. This inner joint motion is commonly referred to as self-motion. The self-motion of a redundant manipulator can be used to achieve a secondary objective while performing a primary task [128]. The secondary objectives involve, e.g., singularity avoidance, manipulability enhancement, or force feedback capability

maximization of the robot while the primary tasks involve, e.g., position, force, or impedance control of the robot in the Cartesian space. The human arm and fingers have kinematic redundancy [100]. Studies have shown that human users employ kinematic redundancies in their arm along with compliant task space control to perform complex dexterous tasks [121]. Also, in a recent study on the performance of experienced surgeons, it was shown that they exploit their arm's redundancy to stabilize hand movements more than novice surgeons [107].

The overarching objective of this research is to enable a user to experience believable and complex interaction with an environment (be it virtual or physical, nearby or remote) via an HI in ways nearly indistinguishable from direct touch. Here, the advantages offered by re-configurability (via redundancy) of redundant HIs (RHIs) for best meeting the criteria in Section 1.1.1 will be explored. We will relax the above trade-offs by adding redundancy in the HI mechanical design, further optimize the kinematic and dynamic characteristics of RHIs through closed-loop control and reconfigure and adapt RHIs based on information about the task.

1.2 Dissertation Contributions and Overview

The major contributions of this dissertation are summarized as follows:

- **Intrinsic Advantages of Redundant Haptic Interfaces:** The intrinsic advantages of RHIs over non-redundant haptic interfaces (NHIs) in terms of meeting the criteria in Section 1.1.1 is investigated. Such intrinsic advantages relate to the kinematics and dynamics of RHIs and do not depend on any algorithm or computer-based control. It is shown that by adding one or more DOFs to the base of any NHI, the resultant RHI's manipulability index, workspace volume and force feedback accuracy (all kinematic performance measures) will be greater than those of the original NHI. Furthermore, the RHI's apparent inertia and friction (dynamic performance measures) will become smaller than those of the original NHI.

- **Manipulability Performance Measure for Teleoperated Surgical Robots and Haptic Interactions:** A Teleoperation Manipulability Index (TMI) is developed as a novel quantifiable measure of the combined HI-slave system manipulability. The proposed index can be used in the design and control of HI-slave robotic systems to 1) enhance surgeon's control over force/velocity of a surgical robot, 2) minimize the haptic interface's footprint, 3) optimize the surgeons' control effort, and 4) avoid singularities and joint limits of the haptic interface and slave robots.

- **Redundant Haptic Interfaces Redundancy Resolution for Optimizing Kinematic and Dynamic Characteristics:** The redundancy of the RHI is exploited in closed-loop joint-level control to achieve secondary objectives. A secondary objective is achieved by using a null-space controller, which works in parallel to the controller for the primary objective.

  - **Redundant Haptic Interfaces for Enhanced Soft-Tissue Stiffness Discrimination Ability:** We demonstrate that the RHI redundancy can further reduce the reflected joints' friction at its end-effector via appropriately manipulating the extra degrees of freedom of the interface. This will consequently enhance the haptic feedback resolution (sensitivity) for the user. A psychophysical experiment is performed to validate the improved force perception for the user in a virtual soft-tissue palpation task. A set of perceptual experiments is conducted to evaluate how a redundant and non-redundant user interface affects the perception of the virtual stiffness. Experimental results demonstrate that the redundancy in the haptic user interface helps to enhance tissue stiffness discrimination ability of the user by reducing the distortions caused by the kinematics and dynamics of the user interface.

  - **Redundant Haptic Interface for Teleoperated Surgical Robots' Manipulability Enhancement:** A null-space controller is

developed for the redundant haptic interface that employs the previously proposed teleoperation manipulability index to enhance the performance of teleoperation tasks by matching the kinematics of the redundant haptic interface to the kinematics of the slave robot. The null-space controller modulates the redundant degrees of freedom of the haptic interface to reshape its manipulability ellipsoid towards the manipulability ellipsoid of the slave robot. The manipulability ellipsoid is the geometric interpretation of the kinematics of a robot. By reshaping the haptic interface's manipulability, the haptic interface's and slave robot's kinematics is matched. By leveraging the redundancy of RHI, we are able to enhance the RHI-slave system manipulability and more intuitively transfer the slave robot's dexterity to the user. An experimental study is performed to validate the performance of the proposed control strategy. Results demonstrate that by employing the proposed null-space controller, we can enhance the user's control over the force/velocity of a surgical robot and minimize the user's control effort for a teleoperated task.

– **Dynamic Reconfiguration of Redundant Haptic Interfaces for Improving Haptic Interaction Fidelity:** A contact-aware null-space control approach for redundant haptic interfaces is proposed. First, we introduce a task-dependent null-space controller in which the internal motion of the redundant haptic interface is appropriately controlled to achieve a desired performance, i.e., low back-drive friction in case of free-space motion and soft contact or large force feedback capability in case of stiff contact. Next, a transition method is developed to facilitate the adaptation of the null-space controller's varying objectives according to the varying nature of the task. The transition method prevents discontinuities in the null-space control signal. This transition method is informed by a proposed Actuator Saturation Observer (ASO) that monitors

the distance of joint torques from their saturation levels. The overall outcome is an ability to recreate the feelings of soft contacts and hard contacts with higher fidelity compared to what a conventional non-redundant haptic interface can achieve. Experimental results verify the effectiveness of the proposed control strategies. It is shown that the proposed controller can perform well in the soft-contact, hard-contact, and transition phases.

– **Actuator Saturation Compensation of Redundant Haptic Interfaces for Improving Force Feedback Capability** An Actuator Saturation Compensation Method (ASCM) is proposed to enhance the force feedback capability of a redundant haptic interface by leveraging its kinematic redundancy. This method acts in the null-space of the Jacobian matrix of the RHI and distributes the overloaded actuator's torque among the available unsaturated actuators at the joints. This method empowers design engineers to utilize smaller actuators that have lower rotor inertia and friction in the design of new haptic interfaces. This is advantageous because having low apparent inertia and friction is a requisite for truthfully recreating the feeling of moving in free space. By employing ASCM, the required torque for rendering a stiff environment will be optimally distributed among small-capacity actuators that otherwise become saturated. Moreover, manipulability enhancement of the RHI along the direction of the task is proposed as a tertiary objective – the primary objective is force reflection and the secondary objective is actuator saturation compensation. The tertiary objective acts if the primary and secondary objectives are feasible, and the haptic interface still has remaining redundancy. Experimental results with a four DoF planar haptic interface are reported that verify the practicality of the proposed method.

This thesis is is structured as follows: Chapter 2 presents a summary of the literature. In Chapter 3, the intrinsic benefits of redundant haptic inter-

faces in terms of better kinematic and dynamic characteristics, i.e., increased manipulability and reduced apparent inertia are presented. This chapter also includes a null-space controller design that further reduces the reflected joints' friction at the end-effector of the RHI. A set of perceptual experiments is presented in Chapter 3 that shows the redundancy in the haptic user interface helps to enhance tissue stiffness discrimination ability of the user by reducing the distortions caused by the kinematics and dynamics of the user interface. In Chapter 4, the teleoperation manipulability index is introduced as a quantifiable measure of a HI-slave robotic system. In Chapter 5, a null-space controller is introduced that employs the kinematic redundancies of the redundant HI to improve the teleoperation manipulability index during a teleoperation task. In Chapter 6, a novel task-dependent null-space controller is introduced. The null-space controller reconfigures the RHI from the ideal behaviour for the free-space motion to that for the hard contact case. A transition method, which is informed by a proposed actuator saturation observer, is also developed in this chapter to facilitate the adaptation of the null-space controller's varying objectives according to the varying nature of the task. Chapter 7 describes a novel null-space controller that enhances the force feedback capability of the RHI by distributing the overloaded actuator's torque among the available unsaturated actuators. We conclude and discuss future work in Chapter 8.

Chapter 2

Literature Review

2.1 Haptic Interface Design

Robotic teleoperation systems have transformed several surgical interventions, where many steps involved in localization, access, and surgical execution would benefit from distinct robotic capabilities. Teleoperated robotic systems combine the decision-making of human users with the precision of a robot, allowing minimalist intervention in confined spaces with accuracies beyond human capabilities [136]. One of the main capabilities of teleoperated robotic systems is providing haptic feedback to the surgeon. The haptic sense in telerobotics provides realistic interactions between a human user and a remote or virtual environment. To provide haptic feedback to the human user, there is a need for haptic interfaces that relay forces from the teleoperated robots interactions with the real or the virtual environment back to the human operator [63].

In a teleoperated robotic surgical system, the patient side surgical manipulators are controlled via a Haptic Interface (HI), operated by the surgeon. The HI connecting the surgeon to the surgical manipulator and environment is an integral part of any robot-assisted surgical system and should be able to intuitively transfer surgical maneuvers to the surgical robot [62], [140]. To recreate haptic feedback about an environment that is accessed indirectly rather than touched directly by a user, a haptic interface displays forces received from a virtual or a robotic proxy (slave) probing the environment. Depending on whether the slave is virtual or robotic, a haptic virtual environment or a haptic teleoperation system is formed. Regardless, as the user utilizes the HI to

operate the slave that interacts with the environment, haptic feedback about slave-environment interaction displayed by the HI engages the user's sense of touch and should give transparency (i.e., realism and fidelity) to the interaction [91], [109]. The haptic force feedback can reduce unintentional injuries[139], surgeon's fatigue [96], and assist tissue characterization [154].

High-fidelity haptic feedback, which is critical to the safety and success of any interaction, requires appropriate HI design and control [139]. The HI's workspace, maneuverability, degrees of freedom, and sensory feedback should ideally match the intuitive movements of the user's hand to induce the experience and sensation of direct touch [47]. There are several commercially available HIs, each of which has its advantages and disadvantages [61], [94], [134], [135]. This, in part, relates to unavoidable trade-offs in the design specifications for a specific application. HI should simultaneously satisfy requirements of low inertia and back-drivability for ease of movement and excellent control as well as the capability of providing large enough stiffness and forces to cover reflected forces from stiff contacts. Also, the Z-width of the HI, which represents the range of impedances that it can stably display to the user, needs to be large enough to present rich haptic information to the user. A small Z-width can make it hard to distinguish between different environments because they are presented as similar impedances [36]. In addition to the above requirements, an HI needs to have a practical workspace that will allow efficient and smooth navigation of the environment, while having a small enough footprint for mobility and ease of integration in the user's workstation. Due to these reasons, the design and optimization of haptic robots have been widely studied [46], [120].

One way of classification of the haptic interfaces is based on the design of their kinematic chain that can be [76], [93]: open kinematic chain (or serial design), closed kinematic chain (or parallel design, in which, there should be at least two distinct kinematic paths from the base link to the end-effector), or a combination of open and closed kinematic chains, which is called a hybrid design (a mixture of serial and parallel designs). Depending on the application, one of the above-mentioned designs that is more suitable is used in the design

of the haptic interface.

The type of kinematic pairs and actuators used in the design of a haptic device are very important aspects in the type synthesis. Revolute joints and rotary actuators usually impose less friction and have superior back-drivability compared to prismatic joints and linear actuators. Therefore, they are most commonly used in commercially available haptic devices [76]. While being used, the haptic device and the human operator are mechanically coupled. As a result, it is very important to match the characteristics of these two systems such as the size of the workspace and positional bandwidth, the magnitude of the force and force bandwidth, the velocity and acceleration, and accuracy or the resolution of the systems [133]. This will ensure that the designed haptic interface provides a safe and effective interaction experience for the human operator and is not overqualified for the task in hand [108].

Several HIs have been designed by different researchers. One of the most widespread HIs is the PHANToM haptic device (3D Systems Inc., Morrisville, NC, USA) [94]. There are various versions of the PHANToM haptic device which are designed for different applications. 3D Systems Touch is probably the most popular one due to its relatively low price. It has six degrees of freedom (DoFs) in position and orientation sensing with the workspace size of $160 \times 120 \times 70$ mm and can provide maximum force feedback of 3.3N in three translational DoFs. The specifications of the 3D Systems touch are enhanced for its modified version, 3D Systems Touch X. This interface has a bigger workspace, a better position resolution, and a better force feedback capability (7.9 N). 3D Systems Inc. has designed and commercialized PHANToM Premium models to fulfill the requirements of the applications which require a larger workspace, better position resolution, and better range of force feedback rendering than the Touch and Touch X models. There are three main variants for the PHANToM Premium family; PHANToM Premium 1.0, PHANToM Premium 1.5, and PHANToM Premium 3.0. Also, A version of the PHANToM Premium 1.5 and PHANToM Premium 3.0 is available that provides 3 DoFs force feedback and 3 DoFs torque feedback. For instance, the six-DoF version of Premium 3.0 has the workspace size of $838 \times 584 \times 406$ mm and can

provide 22N force feedback and 515mNm torque feedback. The 3D Systems HIs have a large workspace thanks to their serial kinematics design, but they can provide lower force and torque feedback than the HIs with the parallel kinematics design.

A family of haptic hand-controllers with a parallel kinematic design is manufactured by Force Dimension (Nyon, Switzerland) [60], [142]. The force Dimension HIs can be categorized into three groups as Omega, Delta, and Sigma. As the kinematic design of these HIs is parallel, they can provide larger force feedback but with a relatively smaller workspace than the HIs with the serial kinematics design. Among the Force Dimension HIs, the Sigma 7 provides the largest force and torque feedback (20.0N and 400 mNm, respectively) and the best position resolution in all six DoFs. It has the workspace size of $\varnothing 190 \times 130\ mm$. Omega.6 has six DoF position sensing and can provide three DoF force feedback. The economic version of the Omega.3 is Novint Falcon, which is designed and manufactured by Novint Technologies (Albuquerque, New Mexico, USA). The Falcon HI has lower force feedback capability (9N), position resolution, and workspace size ($101 \times 101 \times 101\ mm$) than the Omega 3 HI.

Virtuose HIs family (Haption, Soulgé-sur-Ouette, France) are designed with serial kinematics with 6 DoF of position sensing. The 3D models provide three DoF active translational force feedback, and the 6D models provide three DoF force feedback and three DoF torque feedback. The workspace and force feedback capability is various among the Virtuose HIs. For example, Virtuose 6D provides a maximum force up to 35N with the workspace size of $1080 \times 900 \times 600\ mm$. The Freedom 7 (MPB Technologies Inc., Pointe-Claire, Quebec, Canada) is an HI which is designed specifically for medical simulations [65]. This HI has a serial kinematic design with the workspace size of $170 \times 220 \times 330\ mm$ and is capable of providing high position resolution, low joint friction, and low apparent inertia. However, it can only offer 0.6N force feedback, which is small relative to other HIs.

The HIs based on pantograph kinematics are introduced by Quanser Inc. (Markham, Ontario, Canada). One of the Quanser HIs is High-Definition

Haptic Device (HD^2), which provides 6 DoF haptic feedback with 6 DoF of position sensing [134]. The dual-pantograph kinematics allows the HD^2 to have a relatively large workspace ($800 \times 250 \times 350\ mm$) while generating relatively large force and torque feedback of 19N and 1710 mNm, respectively. The Maglev 200 (Butterfly Haptics, LLC, Pittsburgh, PA, USA) is a 6 DoF magnetic levitation HI [16]. In this device, the mechanical mechanism is replaced with a single moving part levitated by magnetic fields. Therefore, it has zero static friction, zero mechanical backlash, high position resolution, and wide stiffness range. This HI can also provide 3-DoF force feedback with a maximum of 40N along the z-axis and 3-DoF torque feedback with a maximum of 3600 mNm. The main disadvantage of the Maglev 200 is its very small workspace, which is a 24 mm diameter sphere.

So far, the discussed HIs were all back-drivable with either low force and torque feedback capability or small workspace. There is another category of HIs which can provide large force and torque feedback while having a large workspace. These HIs are not back-drivable and are admittance controlled. The Haptic Master (MOOG Inc., New York, USA) is one of the admittance controlled HIs [87], which has 3 DoFs of force feedback and can generate up to 100 N of force feedback with the workspace size of 280 mm $\times$400 mm $\times$1 rad. Another example of admittance controlled HIs is VISHARD10 [145], which has a workspace size $\varnothing 1700 \times 600\ mm$ and can provide 170N force feedback and up to 13000 mNm torque feedback. The drawback of admittance controlled HIs is that small force feedback can be obscured by the mechanical properties (including apparent inertia) and joint frictions of the HI, which degrade the haptic feedback resolution and sensitivity for the user. Therefore, the admittance controlled HIs are generally designed for rehabilitation applications in which the high force feedback capability is more important than the force feedback resolution.

2.2 Redundant Haptic Interfaces

Redundant manipulators have been widely used in industrial applications [33]. Recently, it has been shown that the self-motion capability of a redundant manipulator is very promising in control of physical human-robot interactions as it can be employed to improve the overall performance of the interaction while performing a primary task [49]. Despite the promising features of RHIs, only limited attention has been paid to their design and control. The rest of the literature mostly concerns redundant robot arms for object manipulation or physical human-robot interactions with industrial robots. It should be noted that kinematic redundancy adds complexity to the design of haptic interfaces. A redundant haptic interface has higher number of links, joints, actuators, and sensors than a non-redundant haptic interface which potentially cause the RHI to become more costly. Also, controlling the extra DoFs of the RHI requires complex algorithms that demand high computational power. These are some of the reasons why there are few studies on the design of RHIs. Industrial robots are either mechanically designed for fast motion at the end-effector or large payload capability. On the other hand, the HI's design needs to address these two conflicting requirements at the same time in addition to being back-drivable and having low apparent inertia and low friction. This imposes additional design constraints and makes the design and control of HIs different from industrial robots.

One of the papers on the design of an RHI is [145], but the design does not meet several of the design criteria of HIs as the designed RHI is not back-drivable and has large apparent inertia. Baser *et al.* also designed a 7-DoF RHI with a relatively larger workspace in compare to 6-DoF non-redundant HIs without enlarging the RHI's links length [13], [14]. The da Vinci Surgical System (Intuitive, Inc. CA, USA) has an RHI but no design-related information is available for proprietary reasons [118]. Barrow *et al.* [12], Kim *et al.* [77], and Gosselin *et al.* [59] added one degree of redundancy to the base of HIs to enlarge their workspaces, however, there is no discussion about the redundancy resolution in these papers. Nath *et al.* [105] studied the teleoper-

ation of a redundant manipulator using an RHI of the same number of DOFs. The rest of the literature has focused on redundant slave robots, e.g., for teleoperation. In [158], a controller is developed for a redundant slave robot for manipulability enhancement in a teleoperation system with time-varying delays. In [68], the performance of a teleoperated system with a redundant slave robot is studied. In [89] and [90], task-space teleoperation with a redundant remote robot has been studied in which control theoretic framework was used to guarantee the position and velocity tracking between the local and remote robots in the presence of constant delays.

There is also another category of redundancy for the haptic interfaces that is actuation redundancy [22], [39], [81]. This type of redundancy is only possible for the parallel robot [58]. The main advantage of serial robots over parallel robots is their relatively larger workspace. Also, the forward kinematics problem for serial robots has a closed-form mathematical solution. For the parallel robot, usually, this is not the case and the forward kinematics problem needs to be solved numerically, which is very computationally expensive. Parallel robots have relatively larger force feedback capability than serial robots. Also, actuation redundancy can be incorporated to render an environment with very high stiffness. The drawback of actuation redundancy for parallel robots is that having actuators instead of passive joints makes the apparent inertia and reflected friction at the end-effector of the robot larger, which is not desirable for the free-space movement.

Many redundancy resolution methods for standard redundant manipulators can be extended to RHIs, including the reduced gradient-based method [41], the damped least-squares inverse Jacobian method [103], and the weighted inverse Jacobian method [24]. Furthermore, the self-motion of the WMM can be used to execute sub-tasks, such as joint limit avoidance [69], obstacle avoidance, manipulability maximization, and/or singularity avoidance [15], [157]. The joint velocity, acceleration, or torque of the RHI in the null space of its Jacobian can be regulated in such a way as to not affect the position, velocity, and force/torque of its end-effector. This regulation leads to the so-called self-motion movement [67] since the manipulator's movement in joint

space is not observed at the end-effector. Thus, besides the main task and for various applications, the self-motion can be controlled by designing an appropriate auxiliary function gr to achieve a sub-task control.

2.3 Manipulability as a Performance Measure for Haptic Interfaces

Manipulability of robots was first introduced in [119], [157]. Manipulability describes how a manipulator can freely apply forces and torques or move in arbitrary directions, and quantifies the ability to perform an action quickly and skilfully [7]. Manipulability analysis consists of describing directions in the task or joint space of a robot with the best ratio between some measure of effort in joint space (e.g., joint torque) and a measure of performance in task space (e.g., position accuracy). Yoshikawa introduced the manipulability index [157] as a quality index for a single manipulator, which describes the characteristics of feasible motions in the Cartesian space corresponding to unit joint velocity vectors. He defined a quality measure based on the analysis of the manipulability ellipsoid (ME). ME is a volume/surface in the Cartesian space, which is mapped from the unit sphere in the joint space by a Jacobian transformation [157].

Manipulability analysis has been widely used for the analysis of the motion of multiple cooperating robots. Lee [83] defined a dual-arm ME as the maximum volume ellipsoid determined by the intersection between the two single-arm MEs. This is because the required cooperation between the two arms imposes additional kinematic constraints on the manipulability of individual arms. Chiacchio *et al.* [30] extended the concept of ME to the multi-arm case independent of the number of arms involved in the cooperation by regarding the system of multiple arms as a closed-chain system. Chiacchio *et al.* also introduced the concept of force manipulability for fully actuated robotic chains by a duality argument, considering the principal directions for force and velocity MEs are the same while the lengths of axes are inversely proportional to each other [30]. Bicchi *et al.* [17] extended the kinematic

ME problem to general cooperating arms, with arbitrary number of joints per arm. Melchiorri [99] applied similar tools to address force manipulability in cooperative robots with active and passive joints [18]. The concept of task compatibility, which optimizes the velocity or force requirements in a given direction, was presented by Chiu [34], and Ajoudani *et al.* [5] improved this concept by introducing a weighting matrix to scale the joint torques in view of the joint torque differences.

Researchers have studied the application of the manipulability index in the design and control of surgical robots. Konietschke *et al.* [79] and Li *et al.* [86] used the manipulability index to optimize the design of single robots. Maddahi *et al.* [92] showed the correlation between the manipulability of a haptic interface (HI) and the performance of a teleoperated surgical system emulating a micro-neurosurgical task defined in terms of actuators efforts and distances travelled by the slave end-effector.

Chapter 3

Advantages of Redundant Haptic Interfaces[1]

3.1 Introduction

For most surgical procedures, stiffness transparency is required to offer a realistic feel of the tissue [110]. Stiffness transparency allows surgeons to discriminate between tissues. Distorted haptic feedback can reduce the user's ability to perform tissue discrimination. Especially in neurosurgery, the user's tissue stiffness discrimination ability may be reduced due to small forces that are involved in the interaction with the brain tissue [80], which may be masked by the HI's mechanical properties.

In the design of HIs, there are trade-offs between desirable characteristics such as force feedback reflection capacity, closed-loop stiffness, workspace size, manipulability, and apparent inertia [66]. For example, to provide large force feedback, the HI should have larger actuators. This, however, increases the inertia of the robot and somewhat masks the force feedback. Also increasing the HI's workspace commonly leads to longer links, which decreases the mechanical stiffness and increases the inertia of the HI.

To address the design trade-offs and achieve desirable characteristics for HIs, one can use a kinematically redundant haptic interface (RHI). RHI has

[1] A version of this chapter has been published as Ali Torabi, Mohsen Khadem, Kourosh Zareinia, Garnette Sutherland, and Mahdi Tavakoli, "Application of a Redundant Haptic Interface in Enhancing Soft-Tissue Stiffness Discrimination," IEEE Robotics and Automation Letters, vol. 4, no. 2, pp. 1037 - 1044, April 2019.

more degrees of freedom than what is minimally required to perform a task in the Cartesian space. Kinematic redundancy in the task space of a robot makes it possible to have joint motions that do not affect the position and orientation of the end-effector. These inner joints' motions can be used in control to achieve a secondary objective while performing a primary objective. The secondary objective can involve reducing apparent inertia, singularity avoidance, manipulability enhancement, and/or joint limit avoidance [128].

In this chapter, we investigate the benefits of an RHI as the master robot in a tissue discrimination scenario. We employ an RHI to reduce the apparent inertia of the interface and enhance its manipulability and consequently enhance the force resolution (sensitivity) for the user. We demonstrate that an RHI can provide better and more realistic force feedback to the user than a non-redundant haptic interface (NHI). The rest of this chapter is organized as follows: In Section 3.3, the intrinsic advantages of an RHI over NHI is described. In Section 3.4, a secondary task is introduced that employs the kinematic redundancies of the RHI to further maximize its manipulability in the desired direction. Section 3.5 describes the experimental setup and protocol. Psychophysical experiment results to validate the effectiveness of the proposed secondary task and redundancy of the haptic interface are presented in Section 3.6. Concluding remarks appear in Section 3.7.

3.2 Preliminaries

In order to provide haptic feedback for the user, the kinematics for the HI should be established. The kinematic modelling contains two parts: the first is the forward kinematics, which given the joint positions calculates the HI's end-effector pose (position and orientation) and the second is the inverse kinematics that given the end-effector pose leads to the joint positions. For a redundant HI, the latter is usually an optimization process in which the redundancy of the robot is utilized in different ways to realize different sub-tasks in parallel to the main task [33].

The forward kinematics of the RHI with respect to base frame can be

expressed as

$$x = f(q), \tag{3.1}$$

where $x \in \mathbb{R}^m$ is the pose of the end-effector and $q \in \mathbb{R}^n$ is the joints position of the RHI. $f(q)$ denotes the forward kinematics for the RHI, where it can be obtained using Denavit-Hartenberg (DH) convention.

The end-effector velocity is the differential of (3.1) with respect to time. For a robot, the Jacobian matrix provides a transformation from the joint velocities to the velocity of the end-effector in Cartesian space as

$$\dot{x} = \begin{bmatrix} \dot{t} \\ \omega \end{bmatrix} = \begin{bmatrix} J_t \\ J_r \end{bmatrix} \dot{q} = J\dot{q} \tag{3.2}$$

where $\dot{q}$ is an n-dimensional vector that represents a set of joint velocities, $\dot{x}$ is an m-dimensional velocity vector of the end-effector, and J is the $m \times n$ Jacobian matrix. $\dot{t}$ is a t-dimensional translational velocity vector, and ω is an r-dimensional orientational velocity vector of the end-effector. J_t and J_r are the $t \times n$ translational and $r \times n$ orientational Jacobian matrices, respectively. For the RHI, $n > m$, and for the NHI, $n = m$.

The inverse kinematics of the RHI is built by resorting to an optimization technique that solves the joints position given an end-effector desired pose. The cost function for the RHI can be written as

$$\begin{aligned} &\min_{\dot{q}} \{\frac{1}{2}(\dot{q} - \dot{q}_0)^{\mathrm{T}} Q (\dot{q} - \dot{q}_0)\}, \\ &\text{s.t.} \qquad\quad \dot{x} = J(q)\dot{q}, \end{aligned} \tag{3.3}$$

where $Q \in \mathbb{R}^{n \times n}$ is a symmetric and positive definite weighting matrix, $\dot{q}_0 \in \mathbb{R}^n$ is the desired value for the joint velocity, and $J_(q) \in \mathbb{R}^{m \times n}$ is the robot Jacobian as shown in (3.2). Then, we can obtain the solution to the optimization problem in (3.3) as

$$\dot{q} = J^{\dagger}\dot{x} + (I_{n \times n} - J^{\dagger}J)\dot{q}_0, \tag{3.4}$$

where $J^{\dagger} = Q^{-1}J^{\mathrm{T}}(JQ^{-1}J^{\mathrm{T}})^{-1}$ is the weighted pseudoinverse of J, and $I_{n \times n}$ is an $n \times n$ identity matrix.

3.3 Intrinsic Advantages of Redundant Haptic Interfaces

A haptic interface should satisfy requirements of low apparent inertia and friction for the best perception of reflected forces by the user, a big workspace for ease of movement, and a large enough stiffness and maximum force feedback capability to recreate reflected forces from both soft and stiff contacts. In this section, we show the intrinsic advantages (i.e., enhanced manipulability and lower apparent inertia) of a redundant haptic interface over a non-redundant interface. An RHI has intrinsic advantages over an NHI as long as the RHI has at least one DoF more than the NHI. Intrinsic advantages are related to the kinematics and dynamics of the RHI and do not need any algorithm or computer-based control. In Section 3.4, we demonstrate that by employing an RHI, the intrinsic advantages of an RHI can be more enhanced via a secondary task controller.

3.3.1 Effective Manipulability

For a given robot, a unit hypersphere in the joint space, $\|\dot{q}\|^2 = 1$, can be mapped into an ellipsoid in Cartesian space, using [156]

$$\|\dot{q}\|^2 = \dot{q}^T\dot{q} = \dot{x}^T(J^\dagger)^T(J)^\dagger\dot{x} = \dot{x}^T(JJ^T)^\dagger\dot{x} = \dot{x}^T\mathcal{M}^\dagger\dot{x} \tag{3.5}$$

where $\dagger$ indicates the pseudo-inverse of a matrix and $\mathcal{M}$ is an $m \times m$ matrix and called the Velocity Manipulability Ellipsoid (VME). The VME is a useful tool for visualizing the velocity transmission characteristics of a manipulator at a given configuration. The optimal direction for affecting velocity as well as the optimal direction to control the force is along the major axis of the VME [129]. This means that for an HI, along the major axis of the VME, the user can move the end-effector with minimum movements of the robot's joints (i.e., feeling the least joint frictions). Also, along with the major axis of the VME, the force feedback to the user can be most accurately controlled (i.e., the highest resolution of force feedback).

The effective manipulability for VME along the direction of a unit vector

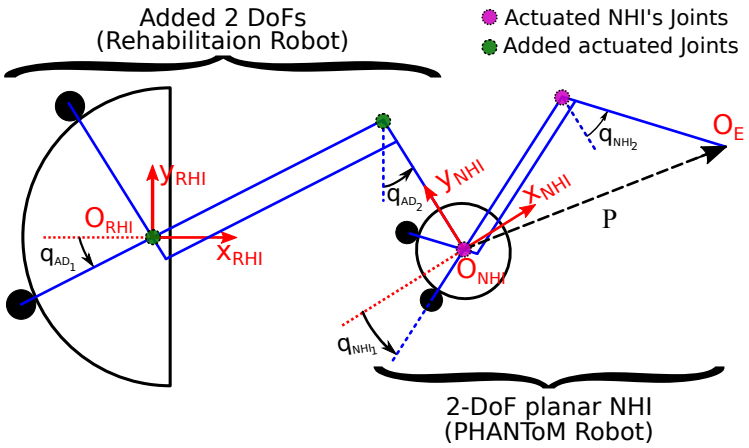

Figure 3.1: Schematics of a 4-DoF planar RHI.

u is calculated as [129]

$$\rho = (u^T \mathcal{M}^\dagger u)^{-1/2}, \tag{3.6}$$

ρ takes its maximum along the major axis of the VME.

Consider an RHI which is made by adding one or more DoFs to the base of an NHI. An example of an RHI is illustrated in Fig. 3.1. Let P represent the vector connecting the origin of the NHI, O_{NHI}, to the origin of the end-effector, O_E, expressed in the reference frame attached to the origin of the RHI, O_{RHI}. Consider $\dot{t}_{NHI}$ and ω_{NHI}, which represents the translational and angular velocities of the origin of the NHI, O_{NHI}, as the result of the motion of the added DoFs, and $\dot{t}_E$ and ω_E, which represents the translational and angular velocities of the end-effector, O_E, as the result of the motion of the NHI. The Jacobian matrix of the RHI can be calculated as

$$\begin{aligned}
\begin{bmatrix} \dot{t} \\ \omega \end{bmatrix} &= \begin{bmatrix} \dot{t}_{NHI} + \dot{t}_E + \omega_{NHI} \times P \\ \omega_{NHI} + \omega_E \end{bmatrix} \\
&= \begin{bmatrix} J_{t_{AD}} - [P]_\times J_{r_{AD}} & J_{t_{NHI}} \\ J_{r_{AD}} & J_{r_{NHI}} \end{bmatrix} \begin{bmatrix} \dot{q}_{AD} \\ \dot{q}_{NHI} \end{bmatrix} \\
&= \left[\begin{bmatrix} I & -[P]_\times \\ 0 & I \end{bmatrix} \begin{bmatrix} J_{t_{AD}} \\ J_{r_{AD}} \end{bmatrix} \quad \begin{bmatrix} J_{t_{NHI}} \\ J_{r_{NHI}} \end{bmatrix} \right] \begin{bmatrix} \dot{q}_{AD} \\ \dot{q}_{NHI} \end{bmatrix} \\
&= \left[\begin{bmatrix} I & -[P]_\times \\ 0 & I \end{bmatrix} J_{AD} \quad J_{NHI} \right] \begin{bmatrix} \dot{q}_{AD} \\ \dot{q}_{NHI} \end{bmatrix} \\
&= \begin{bmatrix} \hat{J}_{AD} & J_{NHI} \end{bmatrix} \begin{bmatrix} \dot{q}_{AD} \\ \dot{q}_{NHI} \end{bmatrix} = J_{RHI} \dot{q}_{RHI}
\end{aligned} \tag{3.7}$$

where $[P]_\times$ is the cross-product operator of the vector P. $\dot{q}_{AD}$ and $\dot{q}_{NHI}$ are the

joint velocity vectors corresponding to the added DoFs and NHI, respectively. J_{AD} and J_{NHI} are the Jacobian matrices of the added DoFs and NHI which are expressed in the frame attached to the origin of the RHI, and J_t and J_r are the translational and orientational parts of the Jacobian matrices. I and 0 are the identity and null matrices, respectively, with appropriate dimensions.

Remark I: By adding one or more DoFs to the base of an NHI to make it redundant, the effective manipulability of the new redundant robot will be greater than that of the NHI.

For the RHI, the effective manipulability (3.6) along a direction u can be written as

$$\begin{aligned}\rho_{RHI} &= (u^T(J_{RHI}J_{RHI}^T)^\dagger u)^{-1/2} \\ &= (u^T(\begin{bmatrix}\hat{J}_{AD} & J_{NHI}\end{bmatrix}\begin{bmatrix}\hat{J}_{AD}^T \\ J_{NHI}^T\end{bmatrix})^\dagger u)^{-1/2} \\ &= (u^T(\hat{J}_{AD}\hat{J}_{AD}^T + J_{NHI}J_{NHI}^T)^\dagger u)^{-1/2}.\end{aligned} \tag{3.8}$$

As the VME belongs to the set of Symmetric Positive Definite (SPD) matrices, it can be shown that

$$u^T(\hat{J}_{AD}\hat{J}_{AD}^T + J_{NHI}J_{NHI}^T)^\dagger u \leq u^T(J_{NHI}J_{NHI}^T)^\dagger u, \tag{3.9}$$

and thus,

$$\rho_{RHI} \geq \rho_{NHI}. \tag{3.10}$$

The inequality (3.10) shows that the effective manipulability for the RHI is greater than that for the NHI in any direction. Therefore, the user would feel less joint friction when he/she moves the end-effector of the RHI.

3.3.2 Effective Apparent Inertia

Remark II: The effective apparent inertia of the RHI, which is made by adding one or more DoFs to the base of an NHI, is smaller than that of the NHI.

The effective apparent inertia describes the relationship between a force (torque) applied on the end-effector of the robot along (about) an arbitrary direction and its resulting translational (rotational) acceleration in that direction, taking into account the effects of the other links and joints of the

robot. In other words, effective apparent inertia represents the mass perceived at the end-effector of the robot in response to the applied force (torque) along (about) an arbitrary direction.

The apparent inertia of an HI (redundant or non-redundant) can be written as $M_x = (JM_q^{-1}J^T)^{-1}$ [74], where M_x is the $m \times m$ end-effector inertia matrix in Cartesian space (apparent inertia), and M_q is the $n \times n$ inertia matrix in the joint space. The inertia matrix of the RHI is shown to be [75]

$$M_{q,_{RHI}} = \begin{bmatrix} M_{q,_{AD}} & \hat{M}_q \\ \hat{M}_q^T & M_{q,_{NHI}} \end{bmatrix} \tag{3.11}$$

where $M_{q,_{AD}}$ is the inertia matrix of the added DoFs, $\hat{M}_q$ is the co-term of the inertia matrix of the added DoFs and NHI, and $M_{q,_{NHI}}$ is the inertia matrix of the NHI. The terms in (3.11) are expressed in the RHI reference frame. The apparent inertia of the RHI is calculated as

$$M_{x,_{RHI}} = (J_{_{RHI}} M_{q,_{RHI}}^{-1} J_{_{RHI}}^T)^{-1} = (M_{x,_{NHI}}^{-1} + \hat{M}_x^{-1})^{-1} \tag{3.12}$$

where $J_{_{RHI}}$ is calculated from (3.7),

$$\hat{M}_x^{-1} = (\hat{J}_{_{AD}} - J_{_{NHI}} M_{q,_{NHI}}^{-1} \hat{M}_q)(M_{q,_{AD}} - \hat{M}_q^T M_{q,_{NHI}}^{-1} \hat{M}_q)^{-1}$$
$$(\hat{J}_{_{AD}} - J_{_{NHI}} M_{q,_{NHI}}^{-1} \hat{M}_q)^T, \text{and} \quad M_{x,_{NHI}}^{-1} = (J_{_{NHI}} M_{q,_{NHI}}^{-1} J_{_{NHI}}^T).$$

The effective apparent inertia in the direction u is calculated as

$$\Lambda = (u^T M_x^{-1} u)^{-1}. \tag{3.13}$$

Therefore, the effective apparent inertia of the RHI can be calculated as

$$\Lambda_{_{RHI}} = (u^T M_{x,_{RHI}}^{-1} u)^{-1} = (u^T M_{x,_{NHI}}^{-1} u + u^T \hat{M}_x^{-1} u)^{-1}. \tag{3.14}$$

As $(u^T \hat{M}_x^{-1} u)$ is always positive [75], thus

$$(u^T M_{x,_{RHI}}^{-1} u)^{-1} \leq (u^T M_{x,_{NHI}}^{-1} u)^{-1}. \tag{3.15}$$

The inequality (3.15) indicates that the effective apparent inertia of the RHI is smaller than that of the NHI along any direction.

To further explain Remark II through an example, let us consider a one-DoF robot that has a point mass M_1, Viscous friction B_1, and a prismatic joint

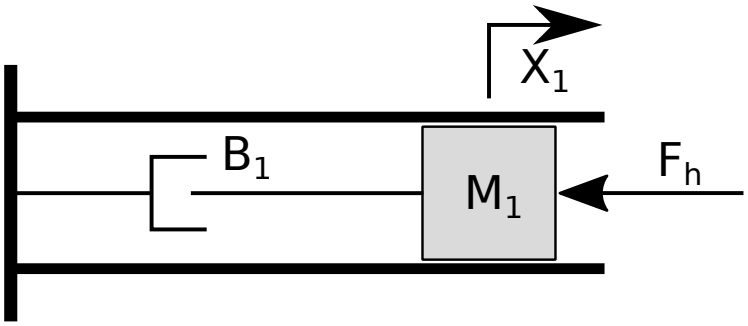

Figure 3.2: Schematics of a one-DoF robot.

as shown in Fig. 3.2. The equation of motion for the one-DoF robot when an external force F_h is applied to the end-effector (i.e., the mass) is

$$F_h = M_1\ddot{X}_1 + B_1\dot{X}_1. \tag{3.16}$$

Using Laplace transform, the equation of motion can be expressed as

$$A_1 = \frac{F_h}{s^2 X_1} = M_1 + \frac{B_1}{s}, \tag{3.17}$$

where A_1 is the apparent inertia of the one-DoF system.

Now, let us add another DoF (as redundancy) to the base of the same one-DoF system. The redundant system is shown in Fig. 3.3. Using the free body diagram of the masses and Newton's second law, the equation of motion for the two-DoF system is

$$\begin{cases} F_h = M_1\ddot{X}_1 + B_1(\dot{X}_1 - \dot{X}_2) \\ 0 = M_2\ddot{X}_2 + B_1(\dot{X}_2 - \dot{X}_1) + B_2\dot{X}_2 \end{cases} \tag{3.18}$$

Using Laplace transform, the equation of motion for the two-DoF system can be written as

$$A_2 = \frac{F_h}{s^2 X_1} = M_1 + \frac{\frac{B_1}{s}(\frac{B_2}{s} + M_2)}{\frac{B_1}{s} + (\frac{B_2}{s} + M_2)}, \tag{3.19}$$

where A_2 is the apparent inertia of the two-DoF system. As $|\frac{(\frac{B_2}{s}+M_2)}{\frac{B_1}{s}+(\frac{B_2}{s}+M_2)}| \leq 1$, thus, the apparent inertia of the redundant two-DoF robot is smaller than that of the non-redundant one-DoF robot.

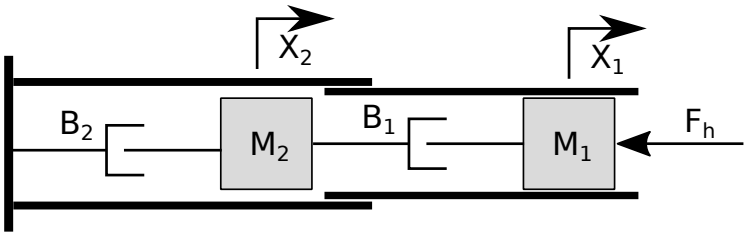

Figure 3.3: Schematics of a two-DoF redundant robot.

3.4 Non-Intrinsic Advantages of Redundant Haptic Interfaces

In Section 3.3, the intrinsic advantages of the RHI over NHI were investigated. In this section, the redundancy of the RHI will be exploited to achieve a secondary objective. In Section 3.5, we experimentally validate the application of the proposed approach in enhancing the soft-tissue discrimination by using an RHI.

For an RHI, the joint torque vector for a desired end-effector force can be calculated as [74]

$$\tau = J^T F + \underbrace{(I - J^T J^{\#^T})(\tau_N - k_D \dot{q})}_{\text{Null space controller}}, \tag{3.20}$$

where τ is the joint torque vector required to create a desired end-effector force F. τ_N is the null-space torque vector corresponding to the secondary objective and is projected in the null space of the Jacobian matrix through the $(I - J^T J^{\#^T})$ matrix. $k_D > 0$ is a suitable damping coefficient. $J^{\#}$ is generalized inverse of the Jacobian matrix defined as $J^{\#} = M_q^{-1} J^T [J M_q^{-1} J^T]^{-1}$. The joint torques given by (3.20) can ensure stability for both the primary and null space controllers [104]. A block diagram of the control system is shown Fig. 3.4.

The torque vector, τ_N, which is desired to fulfill secondary goals needs to optimize a secondary objective using the gradient projection method, i.e.,

$$\tau_N = -\alpha \frac{\partial \nu(q)}{\partial q} \tag{3.21}$$

where α is a scalar step size and $\nu(q)$ is the objective function corresponding to the secondary task. Using τ_N in (3.21), the robot tries to decrease the value of $\nu(q)$ while executing the primary task.

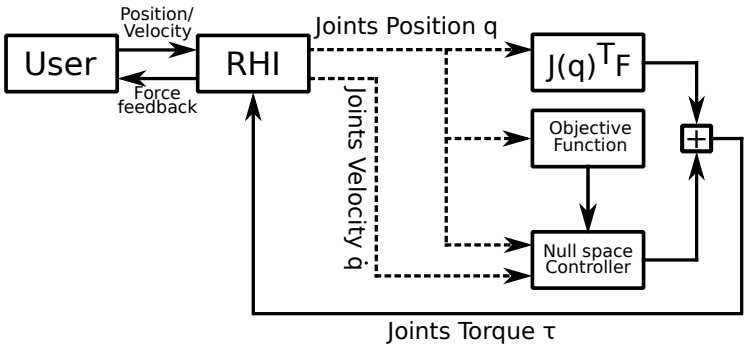

Figure 3.4: Block diagram of the control system.

As discussed in Section 3.1, different secondary objectives can be selected. An ideal HI is such that the user does not sense the dynamics of the HI. This can be achieved by maximizing the manipulability of the HI and minimizing its apparent inertia along the desired direction of motion. We note that by designing a suitable closed-loop controller (e.g., impedance control [124]) for the HI, the apparent inertia can be decreased and the joints' friction can be compensated for. However, such controller needs an exact model of the HI joints friction, inertia matrix and centrifugal torques in addition to a force sensor that are hard to achieve in practical applications. Therefore, having intrinsic low apparent inertia and friction, and high manipulability is desirable for HIs.

We define an objective function for the secondary task to match the VME of the RHI, $\mathcal{M} = (J_{RHI} J_{RHI}^T)$, to a desired VME, $\mathcal{M}_{des}$, by utilizing the inner joints motion of the redundant robot. The objective function is defined as

$$\nu(q) = \texttt{logdet}(\frac{\mathcal{M}_{des} + \mathcal{M}}{2}) - \frac{1}{2}\texttt{logdet}(\mathcal{M}_{des}\mathcal{M}). \tag{3.22}$$

As stated before, $\mathcal{M}$ belongs to the set of SPD matrices. (3.22) is selected as the cost function because it is a Riemannian distance metric on SPD matrices [131] and forms a convex optimization problem that ensures convergence [132]. $\mathcal{M}_{des}$ is designed such that its major axis is aligned to the desired direction of motion and it has small minor axes. By using this $\mathcal{M}_{des}$, the effective manipulability will be maximized along the desired direction. If $u \in R^m$ is the unit vector that indicates the direction of motion, by using Singular Value Decomposition (SVD), it can be decomposed as $u = U\Sigma V^T$, where U is $m \times m$

unitary matrix, Σ is an $m \times 1$ vector in which non zero value is known as the singular value of u, and V is a scalar.

The desired VME can be defined as

$$\mathcal{M}_{des} = U \begin{bmatrix} \Sigma, & \begin{bmatrix} 0_{1\times(m-1)} \\ \beta I_{(m-1)} \end{bmatrix} \end{bmatrix} U^{-1} \tag{3.23}$$

where $I_{(m-1)}$ is an $(m-1) \times (m-1)$ identity matrix, $0_{1\times(m-1)}$ is a vector of zeroes. β is a scalar scaling factor that defines the length of the minor axes of the $\mathcal{M}_{des}$. In theory, an ideal $\mathcal{M}_{des}$ is a line (i.e. $\beta = 0$); however, such a desired VME causes an internal motion that puts the HI into a singular configuration. Therefore, the parameter β needs to be small but non-zero to avoid singularity in any direction.

In the cost function (3.22), the effective manipulability (3.6) is maximized along the desired direction of motion. Also, there is control over the desired VME shape in the cost function (3.22), and thus singularities can be prevented by selecting an appropriate value for β. Furthermore, this cost function forms a convex optimization problem. Therefore, the optimization converges to the global solution of the problem and does not depend on the initial configuration of the robot.

3.5 Experimental Setup and Protocol

Here, the effect of the proposed control strategy on the performance of the user in soft-tissue stiffness discrimination is investigated. Using three robots – two planar 2-DoF NHIs and a planar 4-DoF RHI – a user study is performed. The experiments aim to study user perception of changes in stiffness. Based on the discussions in Section 3.4, it is hypothesized that because the RHI has lower effective apparent inertia and larger effective manipulability, which as a result, has higher force feedback accuracy compared to the NHIs, the RHI can enhance the soft-tissue stiffness discrimination ability of a user.

The 4-DoF planar RHI is developed by serially connecting two robots, a 2-DoF PHANToM 1.5A (3D Systems Inc., Morrisville, NC, USA) and a 2-DOF planar upper-limb rehabilitation robot (Quanser Inc., Markham, ON,

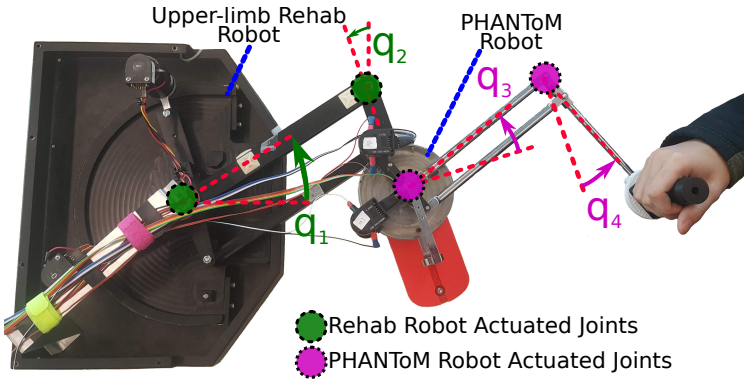

Figure 3.5: Top view of experimental Setup (4-DoF planar RHI). The first NHI (PHANToM) is made by fixing $q_1 = 0$ and $q_2 = 0$. The second NHI (Rehab) is made by fixing $q_3 = 0$ and $q_4 = 0$.

Canada). The base joint of the 3-DoF PHANToM robot has been removed to turn it into a 2-DoF planar robot. Throughout this thesis planar task is defiend as a two DoF positioning task. Therefore, a passive revolute joint is added to the end-effector of the 4-DoF RHI to allow for any arbitrary orientation of the user's hand. For interfacing the robots with the computer, MATLAB/Simulink (MathWorks Inc., Natick, MA, USA) with Quarc real-time control software (Quanser Inc., Markham, ON, Canada) is used.

The experimental setup is shown in Fig. 3.5. One of the NHIs is made by fixing the first two joint angles of the RHI at zero, i.e., upper-limb rehabilitation robot's joints (q_1 and q_2) are set to zero. The second NHI is made by fixing the last two joint angles of the RHI at zero, i.e., PHANToM robot's joints (q_3 and q_4) are set to zero. The first NHI's kinematics and dynamics are equivalent to the PHANToM robot's kinematics and dynamics and will be called PHANToM hereafter, and the second NHI's kinematics and dynamics are comparable to the rehabilitation robot's kinematics and dynamics and will be called Rehab hereafter.

The Jacobian matrix of the RHI, PHANToM, and Rehab are

$$J_{_{RHI}} = \begin{bmatrix} -d_1 sq_1, & d_2 cq_2 - d_3 sq_{23} + d_4 cq_{24}, & -d_3 sq_{23}, & d_4 cq_{24} \\ d_1 cq_1, & d_2 sq_2 + d_3 cq_{23} + d_4 sq_{24}, & d_3 cq_{23}, & d_4 sq_{24} \end{bmatrix},$$

$$J_{_{PHANToM}} = \begin{bmatrix} -d_3 sq_3, & d_4 cq_4 \\ d_3 cq_3, & d_4 sq_4 \end{bmatrix},$$

$$J_{_{Rehab}} = \begin{bmatrix} -d_1 sq_1, & (d_2 + d_4) cq_2 - d_3 sq_2 \\ d_1 cq_1, & (d_2 + d_4) sq_2 + d_3 cq_2 \end{bmatrix},$$

where $q_i,\ i = 1, 2, 3, 4$, is the HIs joint angles, s and c denote $sin(.)$ and $cos(.)$, and $q_{ij} = q_i + q_j$. The links' length of the HIs are given in meters as $d_i = [0.254,\ 0.141,\ 0.21,\ 0.181]$. The inertia matrix in the joint space for the RHI, PHANToM, and Rehab are obtained based on the work of [23] and [45].

Ten subjects aged 22-33 participated in the experiments. The subjects had average experience with HIs, and all of them were right-handed. Each subject was asked to sit in front of an HI and move the end-effector of the HI with their dominant hand in a given direction and receive haptic feedback form a virtual environment without having any visual feedback. Subjects were instructed to keep the end-effector of the HI moving during the experiments. Before starting the experiments, the subjects performed a round of training to become familiar with the experimental setup.

A psychophysical experiment is performed to study the users' perception of changes in stiffness. The Two-Alternative Forced-Choice (2AFC) procedure, which forces the subjects to choose which stimuli in a pair of reference and comparison sample is stiffer, was employed in each trial. Also, the method of constant stimuli [55], in which a reference stimulus and a set of comparison stimulus are presented to the subject in the random order, is used. The virtual environment is modelled by a spring whose stiffness changes by the stimulus value.

The subjects' primary goal was distinguishing between different virtual stiffnesses. In each trial, one of the haptic interfaces (RHI, PHANToM, or Rehab) and pairs of virtual tissue samples (virtual stiffnesses) were presented to the subject. Each pair consists of a reference stimulus value and a comparison stimulus value. The reference value was selected to be in the lower band of the brain tissue stiffness. The Young's modulus of brain tissue is 0.6

to 180kPa [122]. By using Hooke's law, Young's modulus is converted to the spring stiffness. Therefore, the stiffness values for a cube of the tissue sample with a length of 8 cm is in the range of 50 to 14,500 N/m. Here, the reference stimulus value was selected to be 50 N/m, which is the lowest in the range for the brain tissue. The minimum stiffness for the brain tissue has been selected as the reference stimuli because it corresponds to very small forces that can be obscured by the mechanical impedance (including apparent inertia) and joint frictions of the HI [109]. Larger stiffnesses that correspond to forces overshadowing such dynamical effects are indeed easier for the human user to feel. Thus, the most challenging case for the human user (feeling and discriminating small stiffnesses) has been chosen to investigate the effectiveness of RHIs in terms of enhancing stiffness discrimination capabilities for human users compared to NHIs.

A total of nine comparison values were selected so that four comparison values were smaller than the reference, four were larger than the reference, and one was equal to the reference. The comparison values selected are $\pm 5\%$, $\pm 15\%$, $\pm 25\%$, and $\pm 35\%$ of the reference stimulus value. In each trial, a pair of reference virtual stiffness and a virtual tissue sample from the comparison set was presented to the user. The user was asked to probe the first virtual tissue sample from the pair in the given direction. After the virtual tissue sample was probed, it was replaced by the other virtual tissue sample from the pair upon the subject's verbal signal concerning his/her readiness.

For each HI, the nine pairs of reference and comparison virtual stiffnesses were presented ten times in random orders to the subjects. Therefore, a total of 90 stiffness comparisons with each HI (270 comparisons in total) were made by the subjects. There was no time limit for probing the virtual stiffnesses in each trial. However, a physical obstacle is placed at 8 cm away from the starting point of the experiments to limit the range of the end-effector movement. If the range of motion was not limited, as the virtual tissues follow the Hooke's law, the users could move the end-effector of the HI farther and discriminate the tissues by feeling the extra forces. Also, to ensure that the participants move their hand in a specific direction, a virtual fixture (software-generated

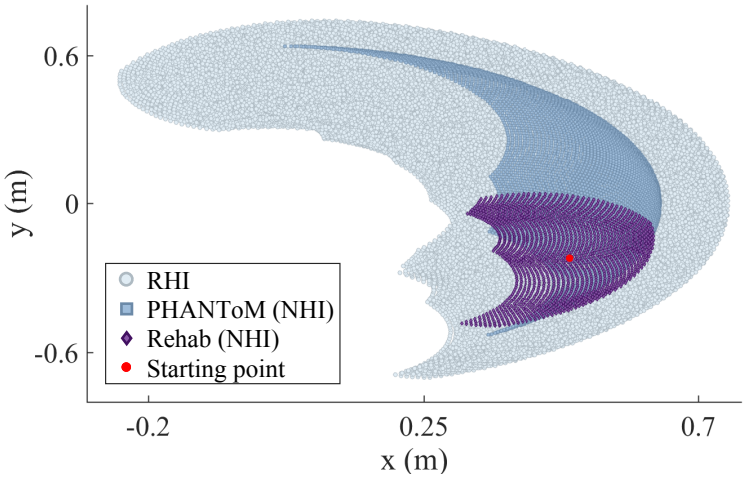

Figure 3.6: The workspace of the redundant robot, the workspace of the PHANToM, the workspace of the Rehab, and the starting point for the experiments.

force fields) is imposed on the end-effector of the HIs to limit the movement of the end-effector along the specific direction. The subjects were asked to always choose the stiffer tissue sample in a pair even if such a choice appeared challenging. To reduce the effects of fatigues in the experiments, the subjects had ten minutes optional rest time after every 45 comparisons. Also, after every 135 comparisons, the subjects had to have at least one hour rest.

The study was performed with the end-effector always starting from a point in the middle of the PHANToM workspace, $(0.49,\ -0.22)$, which is then moved in the right-hand direction (i.e., $u = [0,\ 1]^T$) towards the tissue. Fig. 3.6 depicts the workspace of the RHI, PHANToM and Rehab, and the location of the starting point in the workspaces. The base frame of the RHI and Rehab is located at $(0,\ 0)$ m and the base frame of PHANToM is located at $(0.254,\ -0.141)$ m.

As proven in Remark I in Section 3.3, the effective manipulability of the RHI is greater than or equal to that of the PHANToM at every point of its workspace. Also, as proven in Remark II in Section 3.3, the effective apparent inertia of the RHI is upper bounded by that of the PHANToM at every point of its workspace. This means that the apparent inertia of the RHI is smaller than the PHANToM's apparent inertia, despite the fact that the RHI

Table 3.1: Theoretical values for effective apparent inertia Λ and effective manipulability ρ at two points

	Point	RHI	PHANToM	Rehab
Λ (Kg)	(0.49, -0.22)	0.0576	0.0628	0.4379
	(0.49, -0.14)	0.0590	0.0606	0.4414
ρ (m/s)	(0.49, -0.22)	0.371	0.188	0.296
	(0.49, -0.14)	0.387	0.167	0.315

has two more links and actuators (resulting to the bigger workspace shown in Fig. 3.6). Therefore, it can be expected that the RHI provides higher fidelity force feedback for the user compared to the PHANToM because the RHI's mechanical properties mask the force feedback less than those of the PHANToM. To further investigate this, the effective manipulability and apparent inertia along $u = [0,\ 1]^T$ for the RHI, PHANToM, and Rehab are calculated at two points using (3.6) and (3.13), respectively. The perceptual experiments are performed for a line segment with these two points as its extremes. Results are listed in Table 3.1. Data reported for the RHI in Table 3.1 corresponds to the optimized configuration of the RHI with the objective function given in (3.22). Parameter β in (3.23) is selected equal to 0.01 in the simulation studies and the experiments. The optimized configuration for the RHI at point $(0.49,\ -.22)\ m$ is $[0.125,\ 0.022,\ 0.298,\ 0.175]$ rad, and the optimized configuration at point $(0.49,\ -0.14)\ m$ is $[0.298, 0.077, 0.413, 0.208]$ rad.

Table 3.1 indicates that at sample points in the shared workspace of the RHI, PHANToM, and Rehab, the effective apparent inertia Λ in a specific direction for the RHI is smaller than that of the PHANToM and Rehab, although the effective manipulability ρ for the RHI is larger than that of the PHANToM and Rehab. Having a smaller apparent inertia for the RHI leads to the smaller sensation of its linkages, and having a larger effective manipulability for the RHI leads to the smaller sensation of its joints' frictions, both of which are desirable features.

Experiments are performed to validate the effective apparent inertia of HIs reported in Table 3.1 along $u = [0,\ 1]^T$. For this purpose, a 6-DoF force sensor (50M31A3-I25, JR3 Inc., Woodland, CA, USA) is attached to the end-effector

Table 3.2: Experimental values for effective apparent inertia Λ in the right direction at two points

	Point	RHI	PHANToM	Rehab
Λ (Kg)	(0.49, -0.22)	0.0691	0.0734	0.5399
	(0.49, -0.14)	0.0718	0.0728	0.5683

of the HI. Next, the end-effector of each HI is modelled to have the dynamics

$$\Lambda \ddot{X} + F_r = F_{ext}, \tag{3.24}$$

where Λ is the scalar mass or effective apparent inertia in the direction of motion, X is the scalar position of the end-effector, F_{ext} is the scalar external force, and F_r is the scalar friction force. The friction term is modelled as the viscous friction $F_r = B\dot{X}$. Experiments are performed to identify Λ and F_r in (3.24). For each HI, ten trials are conducted. In each trial, a constant external force is applied to the end-effector of the HI along the direction of u starting at 1 cm before the points given in Table 3.1 in the workspace. The starting point is not chosen at the given points to eliminate the effects of Coulomb friction in the experiments. The acceleration and velocity of the end-effector of each HI as well as the external forces are measured. In the experiments, the HIs' joint angles are measured and by using forward kinematics of the HIs, the position of the end-effector is calculated. The velocity and acceleration of the end-effector are obtained by taking the first and the second derivative of the position of the end-effector using a second order filter, respectively. The external forces are exerted in the range of $0.5 - 1.5\ N$. The measured signals are passed through a 5th-order lowpass filter, and then the parameters are identified by fitting experimental data to (3.24) using linear least-squares method. The experimental results for the effective apparent inertia are listed in Table 3.2. These experimental results are in agreement with the theoretical results in Table 3.1. There is a small difference between the theoretical and experimental values which could be the result of measurement noises and model uncertainties, but the trend of apparent inertia value changes between the three HIs is consistent.

In addition to the theoretical values reported in Table 3.1, a simulation

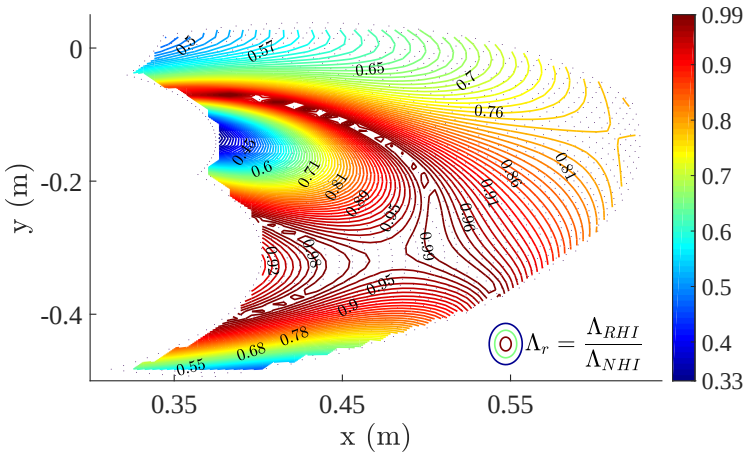

Figure 3.7: Effective apparent inertia ratio of the RHI and PHANToM.

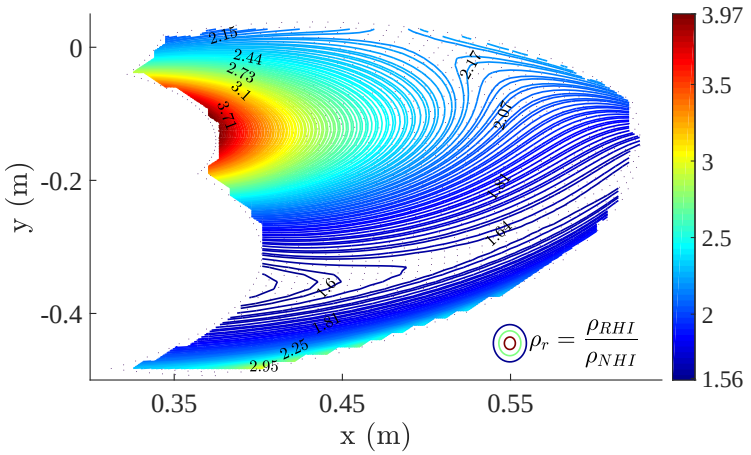

Figure 3.8: Effective manipulability ratio of the RHI and PHANToM.

study is performed to verify Remark I and Remark II in Section 3.3 in all points of the common workspace of the RHI and the PHANToM (NHI). Thus, (3.10) is re-written as $\rho_r = \frac{\rho_{RHI}}{\rho_{NHI}} \geq 1$, and (3.15) is re-written as $\Lambda_r = \frac{\Lambda_{RHI}}{\Lambda_{NHI}} \leq 1$, where ρ_r and Λ_r are effective manipulability ratio and effective apparent inertia ratio, respectively. Theoretical values for the ρ_r and Λ_r along $u = [0,\ 1]^T$ are calculated at every point of the common workspace of the RHI and the PHANToM. Results are depicted in Fig. 3.8 and Fig. 3.7 which corroborate Remark I and Remark II statements, respectively.

3.6 Results and Discussion

In order to quantify the users' perception of changes in stiffness in the experiments, we employed the Just Noticeable Difference (JND), Point of Subjective Equality (PSE), and corresponding Weber Fraction (WF) measures. The JND is the minimum amount by which stiffness value must be altered to make a noticeable change in the user's perception. The PSE is the stiffness stimuli that appears to subjects the same as reference stiffness stimuli. The Weber fraction is calculated as

$$WF = \frac{JND}{PSE}. \tag{3.25}$$

Weber's Law states that the JND is a constant proportion of the original stimulus value.

The positive fraction is defined as the percentage of times each subject stated that the comparison stimuli value was stiffer than the reference stimuli value. A Psychometric function was fitted to each subjects' positive fraction data using the Psignifit Toolbox version 2.5.6 for MATLAB. The Psychometric function describes the relationship between the users' ability to perform tissue discrimination and the physical aspect of the stimulus (i.e., stiffness) [149]. PSE, the upper threshold (UT) (where 75% of the responses report stiffer stimuli), and the lower threshold (LT) (where 25% of the responses report stiffer stimuli) are extracted from the fitted curve for each subject. A sample of representative results of the positive fraction for each HI for subject #3 as well as the ideal result are shown in Fig. 3.9. The JND is defined as the half of the interval between UT and LT, which can be written as

$$JND = \frac{UT - LT}{2}. \tag{3.26}$$

The box graphs in Fig. 3.10(a) and Fig. 3.10(b) depict the mean and median values of the WF and JND for the three HIs, respectively. The experiments results are summarized in Table 3.3. When compared to the previous stiffness discrimination studies using NHIs, the WFs for all three HIs are in a typical range (the stiffness WFs reported ranging from 0.08 to 0.30 [54], [73], [141]). The mean value for the WF and JND for the tissue stiffness discrimination

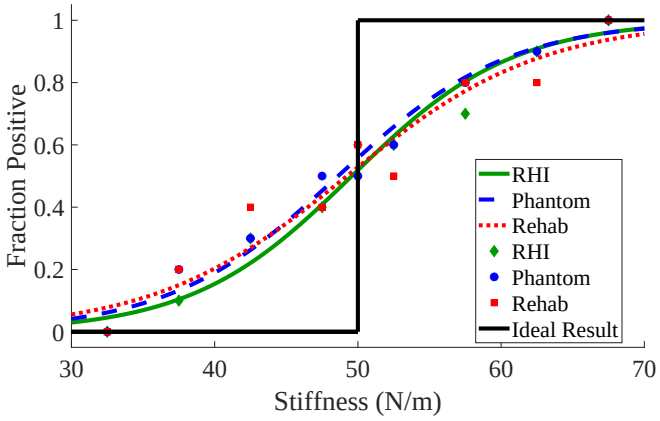

Figure 3.9: Representative results of the positive fraction for subject #3 and the ideal result.

Table 3.3: Mean and Std values for the experiment measures for each HI

	RHI	PHANToM	Rehab
WF (%)	0.111 (std=0.019)	0.118 (std=0.021)	0.145 (std=0.021)
JND (N/m)	5.571 (std=0.916)	5.953 (std=1.068)	7.205 (std=1.024)
PSE (N/m)	50.035 (std=0.578)	50.238 (std=1.695)	49.654 (std=1.267)

with RHI are smaller than that with PHANToM and Rehab. This shows the effectiveness of the proposed redundant interface. To further inspect this, a one-way ANOVA test was applied to the WF data ($F(2, 27) = 7.36, P = 0.0032$), which indicates the statistically significant difference between three HIs. For more accurate analysis, the paired-sample t-test on the WF data is used between different pairs of HIs. The P-values are adjusted with the Holm–Bonferroni method. The t-test between RHI and PHANToM shows no statistically significant difference ($P = 0.2958$). However, the t-tests between RHI and Rehab ($P = 0.00002$) and between PHANToM and Rehab ($P = 0.0075$) indicate that the mean of WFs is significantly lower for RHI and PHANToM in comparison to that for Rehab.

One reason for the same performance achieved with the RHI and the PHANToM is that the PHANToM has itself small friction and apparent inertia [94], and the difference between the performance of the RHI and the

PHANToM lies below the sensitivity threshold of the human hand for stiffness sensing. However, as can be seen in Fig 3.6, the added kinematics redundancy to the base of the PHANToM solves the comparatively small workspace problem of the PHANToM. Having a small workspace requires the user to use the clutching mechanism to move the end-effector of the HI to another position or orientation in the workspace (e.g., in the middle of the workspace) [159]; clutching is required in a master-slave system where the slave's workspace is significantly bigger than the master's. This will slow down the user to perform a task. As for the Rehab, it was observed that its relatively large apparent inertia and friction make it hard for the human subjects to perceive the difference between two soft tissues that have close stiffness value. Also, Fig. 3.7 shows that the effective manipulability ratio in other points of the workspace is relatively smaller than the effective manipulability ratio at the point used in the perceptual experiments. Therefore, if the experiments were performed at other points of the workspace, we would expect to get better tissue stiffness discrimination performance from the RHI as compared to the PHANToM.

3.7 Concluding Remarks

In this chapter, first, the intrinsic advantages of redundant haptic interfaces over non-redundant haptic interfaces was shown. Next, it is shown that by leveraging the redundancy of the RHI, it is possible to further optimize its kinematic and dynamic characteristics through a closed-loop null-space control. Finally, we compared users' performance for a soft-tissue stiffness discrimination task using redundant and non-redundant haptic interfaces. Our goal was to study how a redundant haptic interface (RHI) can be used to decrease the apparent inertia and increase the manipulability of the human interface, and consequently improve the resolution of force feedback for the user. We conducted a set of perceptual experiments to evaluate how different HIs affect the perception of virtual stiffnesses for human users. Experimental results demonstrate that the RHI leads to better sensitivity in discriminating between stiffness of two tissue samples.

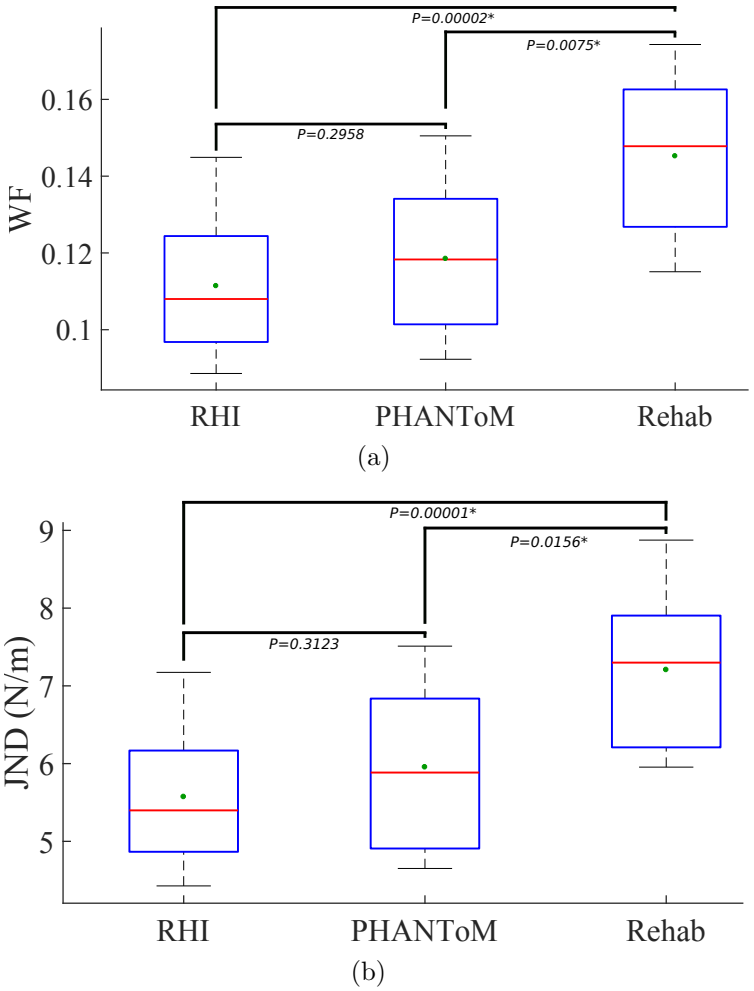

Figure 3.10: (a) WF, and (b) JND . The median and mean values are shown with red line and green circle, respectively.

Chapter 4

Manipulability Performance Measure for Haptic Teleoperated systems and Haptic Interactions[1]

4.1 Introduction

Intrinsic and non-intrinsic advantages of RHIs are discussed in Chapter 3. However, application of dexterous redundant haptic interfaces in teleoperation is limited as there is no quantifiable measure of dexterity for the teleoperated robotic system. In telerobotic surgical applications, the HI's workspace, maneuverability, degrees of freedom, and sensory feedback should ideally match the intuitive movements of the surgeon's hand and mimic the experience and sensation of conventional surgery.

Haptic interfaces currently used in the clinic present several drawbacks such as the mismatch between slave and haptic interface workspaces and the inability to intuitively transfer the slave robot's dexterity and joint limits to the user. The first step in improving the kinematic dissimilarity and workspace mismatch in a teleoperated robotic systems is to define and estimate a measure that quantifies the teleoperation system's manipulability. In this chapter,

[1]A version of this chapter has been presented as Ali Torabi, Mohsen Khadem, Kourosh Zareinia, Garnette Sutherland and Mahdi Tavakoli, "Manipulability of Teleoperated Surgical Robots with Application in Design of Master/Slave Manipulators," The International Symposium on Medical Robotics, Atlanta, GA, 2018.

we propose the Teleoperation Manipulability Index (TMI) as a quantifiable measure of kinematic similarity between the HI and slave robot. Such a quantifiable measure of dexterity can be used for analysis and comparison of designs of HI-slave robotic systems. Also, this allows for considering dexterity in motion planning and control of complex surgical tasks such as suturing or navigation in the presence of anatomical obstacles.

Most studies of the manipulability of teleoperated systems only consider the manipulability of one robot (HI or slave). By using the manipulability index of one robot as the design criterion, the solution to the design space search would result in a robot with very large links, such that joints angle deviate as little as possible from the isotropic pose while still reaching the target in the workspace. However, long links reduce the flexural stiffness of the manipulator and increase inertia and the robot's footprint. The robots used in the operation room work in a limited workspace and must have a small footprint with maximum rigidity and stability.

The aim of this chapter is to develop a manipulability index for quantifying the dexterity of surgical HI-slave systems. We also demonstrate the application of manipulability in the design of HI-slave robotic systems. We demonstrate that by modifying a commercially available HI using the proposed manipulability index, we are able to enhance the surgeon's control over force/velocity of the surgical robot, minimizes the HI's footprint, optimizes the surgeons' control effort, and avoid singularities of the HI and slave robots. Moreover, the index will be used in Chapter 5 to develop an optimal controller for a teleoperation system benefiting from a redundant haptic interface. The controller uses the redundancies of the HI to optimize the proposed manipulability index and kinematically match the slave and master robots.

The rest of this chapter is organized as follows: In Section 4.2, an overview of manipulability index for a single robot is presented. In Section 4.3, manipulability of teleoperated systems is discussed. Application of the TMI in the design of HI-slave robotic systems and simulation results to validate the performance of such designs are presented in Section 4.4. Concluding remarks appear in Section 4.5.

4.2 Manipulability for a Single Robot

For a robotic manipulator, the Jacobian matrix provides a transformation from the velocity of the end-effector in Cartesian space to the actuated joint velocities as the

$$\dot{x} = J\dot{q} \tag{4.1}$$

where $\dot{q}$ is an n-dimensional vector that represents a set of actuated joint rates, $\dot{x}$ is an m-dimensional output velocity vector of the end-effector, and J is the $m \times n$ Jacobian matrix. The Jacobian J defines the mapping from R^n to R^m. The unit sphere in R^n can be mapped into an ellipsoid in R^m through J as shown bellow:

$$\|\dot{q}\|^2 = \dot{q}^T\dot{q} = \dot{x}^T(J^\dagger)^T(J^\dagger)\dot{x} = \dot{x}^T(JJ^T)^{-1}\dot{x} \tag{4.2}$$

here the superscript "†" indicates the pseudo-inverse of a matrix, $J^\dagger = J^T(JJ^T)^{-1}$. The ellipsoid in R^m, JJ^T is called the manipulability ellipsoid (ME), and describes the versility of moving in the task space. The ME is a surface/volume that helps to visualize the feasible directions of velocity at the end-effector of a robot. This ellipsoid can be spanned using the singular values of the Jacobian matrix, which can be calculated using the singular value decomposition (SVD) [57]. As J is $m \times n$, there exist orthogonal matrices $U \in R^{m\times m}$ and $V \in R^{n\times n}$ such that

$$J = U\Sigma V^T \tag{4.3}$$

where $U = [u_1 \cdots u_m]$ is an $m \times m$ unitary matrix, Σ is an $m \times n$ rectangular diagonal matrix in which the diagonal entries $(\sigma_i, i = 1 \cdots m)$ are known as the singular values of J with $\sigma_1 \geq \sigma_2 \geq \cdots \geq \sigma_m$, and $V = [v_1^T \cdots v_n^T]$ is an $n \times n$ unitary matrix.

The velocity ME is a useful tool for visualizing the velocity transmission characteristics of a manipulator at a given posture. The velocity transmission shows the transformation of velocity from joint space to the Cartesian space in any direction. The directions of the principal axes of the ellipsoid are the optimal directions for effecting velocity and are determined by the eigenvectors of the matrix JJ^T . The magnitudes of the axes are equal to the square roots of

the eigenvalues of JJ^T. The velocity transmission along an arbitrary direction u, in the Cartesian space can be calculated as [129]

$$\sigma = \left(u^T (JJ^T)^\dagger u\right)^{-\frac{1}{2}}. \tag{4.4}$$

Inspired by definition of force manipulability ellipsoid [156], the reflected friction ellipsoid at the end-effector of the robot can be obtained as

$$\|F_q\|^2 = F_q^T F_q = F_x (JJ^T) F_x \leq 1, \tag{4.5}$$

where F_q is the $n \times 1$ vector of the joint friction torques and F_x is the $m \times 1$ vector of friction forces/torques reflected at the end-effector. Similar to the velocity transmission concept, a reflected friction factor is defined which shows the reflection of the joint friction at the end-effector of the robot. Now, the reflected friction factor along an arbitrary direction u is calculated as

$$\lambda = \left(u^T (JJ^T) u\right)^{-\frac{1}{2}}. \tag{4.6}$$

By comparing (4.4) and (4.6), it can be seen that the velocity transmission σ is the reciprocal of the reflected friction factor λ along the same direction. This means that along the direction where the velocity transmission is maximized, the joints friction force reflected at the end-effector is minimized. As the result, when the user moves the end-effector of the haptic interface along the maximised velocity transmission direction, he/she will feel the least amount of joint friction. The velocity transmission and reflected friction factor along u for a 2-DoF planar robot in a sample configuration are shown in Fig. 4.1.

Now, the manipulability index can be defined based on the ME. Proportional to the volume of the ME spanned by singular values of J, the manipulability index can be defined as [157]

$$\mu = \sqrt{det(JJ^T)} = \sigma_1 \sigma_2 \cdots \sigma_m. \tag{4.7}$$

μ is the manipulability index at one point in the robot's workspace. To define a global manipulability index, one can use

$$GM = \frac{\int_W \mu dW}{\int_W dW} \tag{4.8}$$

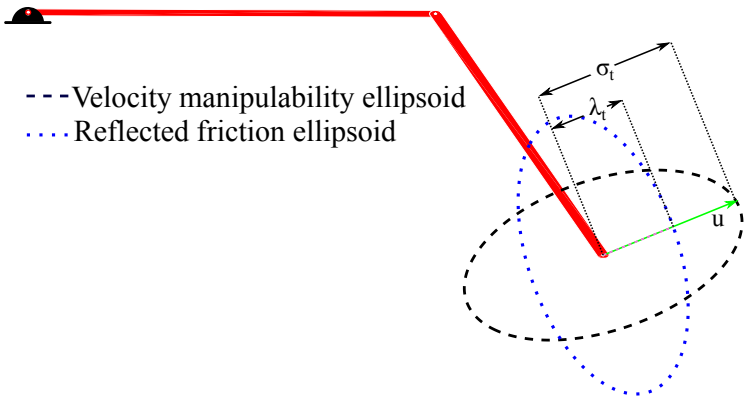

Figure 4.1: The velocity transmission σ and reflected friction factor λ for a 2-DoF planar robot along direction u.

where W is the workspace of the robot.

In addition to the manipulability index, the isotropy of the robotic arm is also important [119]. It is a measure of how well the mechanism can move in all directions, i.e., directional uniformity. Assuming that the surgical motion demands are uniform with respect to the robot in the surgical site, a good isotropy score would indicate that the load on the motors of each joint would be similar. The isotropy index has been introduced as the inverse of the condition number of the Jacobian, i.e., the relation of the smallest to the largest singular value

$$\frac{1}{\kappa} = \frac{1}{\|J\|\|J^{-1}\|} = \frac{\sigma_m}{\sigma_1}. \tag{4.9}$$

Using (4.9) the global isotropy index or commonly called global conditioning index GC can be defined as

$$GC = \frac{\int_W (\frac{1}{\kappa}) dW}{\int_W dW} \tag{4.10}$$

4.3 Manipulability of Teleoperated Surgical Systems

In this section, we modify the manipulability index to extend the definition of manipulability to teleoperated HI-slave surgical systems. In teleoperation, we want the user to feel as if he/she is directly interacting with the slave's environment. This requires matching of the positions and forces on both the

slave and the HI side. It is assumed that the HI and the slave robot follow each other position perfectly. Thus, it can be assumed that the end-effector of the HI and the end-effector of the slave are physically attached together, similar to two cooperative robots manipulating a mass-less point object with tight grasps. This prompts the observation that the teleoperation manipulability is the volume of the intersection between the MEs for the individual arms, where the intersection of the two MEs is subject to the constraints imposed by the teleoperation system.

4.3.1 Teleoperation Manipulability Ellipsoid

Let us assume that the teleoperation task is defined in the slave robot workspace, and the ME of the HI is transformed into the task frame, i.e., slave robot frame. Using (4.2), the MEs for the HI and the slave robot can be found as

$$\dot{x}^T (H J_M J_M^T H^T)^{-1} \dot{x} = 1 \tag{4.11a}$$

$$\dot{x}^T (J_S J_S^T)^{-1} \dot{x} = 1 \tag{4.11b}$$

where J_M is the Jacobian of the HI, J_S is the Jacobian of the slave robot, and H is the transformation matrix that transforms the Jacobian of the HI to the task frame. Following the approach first presented in [83], the combined ME of two arms is the largest ellipsoid that can be fitted into the intersection of the ME of the HI defined in (4.11a) and the ME of the slave robot given in (4.11b). To find the largest ME in the intersection of the two given MEs in (4.11a) and (4.11b), we first assume that the principal axes of the intersecting ellipsoid coincide with the principal axes of the HI's ME. Knowing the intersection points of HI and slave MEs, we find the intersecting ME. Next, it is assumed that the principal axes of the intersecting ellipsoid coincide with those of the slave robot's ME and the intersecting ME is calculated again. Finally, the ME that has the largest volume between the two calculated MEs is selected as the TME. This strategy is discussed in the following.

An ellipsoid can be specified by a set of principal axes $\sigma_i u_i$ where $u_i, i = 1, \ldots, m$ denote the orthonormal vectors specifying the orientation of the principal axes, and $\sigma_i, i = 1, \ldots, m$ represent the length of the corresponding prin-

cipal axes. The principal axes of the intersecting ellipsoid $\sigma_i^I u_i^I$ can be obtained assuming they coincide with the principal axes of the HI's ME as

$$ {}_1\sigma_i^I \, {}_1u_i{}^I = \begin{cases} \eta_i^1 u_i{}^M, & \text{if } \eta_i^1 < \sigma_i^M \\ \sigma_i^M u_i{}^M, & \text{if } \eta_i^1 \geq \sigma_i^M \end{cases} \tag{4.12} $$

where $\sigma_i^M u_i^M, i = 1, \ldots, m$ are the set of principal axes of the HI's ME, and $\eta_i^1 u_i{}^M, i = 1, \ldots, m$ represents the intersecting points between the principal axes of HI's ME in (4.11a) and the boundary of slave robot ME in (4.11b). $\eta_i^1, i = 1, \ldots, m$ can be obtained using equation (4.11b). Considering $\eta_i^1 u_i{}^1$ lies on the slave robot ellipsoid, we have

$$ (\eta_i^1 u_i{}^M)^T (J_S J_S^T)^{-1} (\eta_i^1 u_i{}^M) = 1 \tag{4.13} $$

and thus

$$ \eta_i^1 = [(u_i{}^M)^T (J_S J_S^T)^{-1} u_i{}^M]^{-1/2} \tag{4.14} $$

Now, we assume that the principal axes of the intersecting ellipsoid coincide with those of the slave robot ME. This results in a different representation for the intersecting ellipsoid:

$$ {}_2\sigma_i^I \, {}_2u_i{}^I = \begin{cases} \eta_i^2 u_i{}^S, & \text{if } \eta_i^2 < \sigma_i^S \\ \sigma_i^S u_i{}^S, & \text{if } \eta_i^2 \geq \sigma_i^S \end{cases} \tag{4.15} $$

here, $\eta_i^2 u_i{}^S$ represents the intersecting point between the principal axes of slave robot ME and the boundary of HI ME. Following the same method used in the derivation of η_i^1, η_i^2 can be obtained by

$$ \eta_i^2 = [(u_i{}^S)^T (H J_M J_M^T H^T)^{-1} u_i{}^S]^{-1/2}. \tag{4.16} $$

4.3.2 Teleoperation Manipulability Index

The TMI (λ) is the largest ME between ellipsoids defined in (4.12) and (4.15).

$$ \lambda = max\{\prod_{i=1}^{m} {}_1\sigma_i^I, \prod_{i=1}^{m} {}_2\sigma_i^I\} \tag{4.17} $$

Now we can define the global teleoperation manipulability index (GM_T) to determine the overall conditioning of the manipulability index of the teleoperation system across the slave workspace W rather than at each point therein:

$$GM_T = \frac{\int_W \lambda dW}{\int_W dW}. \tag{4.18}$$

Larger values of GM_T correspond to better manipulability of the teleoperation system.

We note that beside the singular values and manipulability index, joint limits have a major impact on the end-effector's dexterity in the workspace. In order to consider the effects of mechanical constraints of the manipulator, we deployed the joint-limit constrained Jacobian J^q [150]. The constrained Jacobian J^q is formed by penalizing the columns of Jacobian individually using

$$J_i^q = P_i^q J_i \tag{4.19}$$

where J_i is the i^{th} column of the robot Jacobian. P_i^q is the joint-wise penalization function given by

$$P_i^q = \frac{1 - exp(\frac{-4k_q(q_i - q_{i,min})(q_{i,max} - q_i)}{(q_{i,max} - q_{i,min})^2})}{1 - exp(-k_q)} \tag{4.20}$$

where the coefficient "4" and the denominator "$1 - exp(-k_q)$" in equation (4.20) are needed to normalize the penalization term such that P_i^q spans the interval $[0, 1]$. At the joint-limits, P_i^q becomes zero. In the neutral position,$\frac{q_{i,max}+q_{i,min}}{2}$, P_i^q becomes one. The scaling coefficient k_q specifies the functional shape in between these points. Using this penalty function, the individual columns of J are penalized when the ith joint value q_i approaches the limits $q_{i,min}$ or $q_{i,max}$.

Penalization of the Jacobian for calculating the manipulability index was first addressed by Tsai *et al.* [30]. However, unlike the global penalization approach used in [144], the individual columns of J are penalized. Now, by substituting the constrained Jacobian J^q in (4.7), (4.9), (4.14), and (4.16) for J, we can calculate the manipulability and isotropy indices for a single robot and the TMI considering the robot mechanical constraints.

Considering conservation of energy and neglecting the potential terms, a measure of HI's and slave robots' joints kinetic energy, $\|\dot{q}\|^2$, can be directly related to the human users effort while manipulating the robot, and the effort

needed to move the slave's joints. Assuming the HI is manipulated to move the slave robot's end-effector in its task space at a velocity $\dot{x}$, $\|\dot{q}\|^2$ can be calculated as follows

$$\|\dot{q}\|^2 = \dot{q}^T\dot{q} = \dot{x}^T(J_T^\dagger)^T(J_T^\dagger)\dot{x} = \dot{x}^T(J_T J_T^T)^{-1}\dot{x} \tag{4.21}$$

where

$$(J_T J_T^T) = U_T \Lambda_T U_T^{-1} \tag{4.22}$$

in which $U_T = [u_1^I, \cdots, u_m^I]$ and $\Lambda_T = diag(\sigma_1^I, \cdots, \sigma_m^I)$ are set of principal axes of the teleoperation system's ME.

In the next section, we will use GM_T as a design criterion to modify the HI of a teleoperated system. Simulations are performed to demonstrate the benefits of using the TMI such as reducing the surgeon's control effort while manipulating the slave robot's end-effector.

4.4 Teleoperation Manipulability as a Design Criterion

A slave robot will not perform according to its full potential if paired with an HI with lower dexterity and manipulability. There are several commercial HIs designed and developed to operate in conjunction with slave robots, offering advantages in terms of generality and ease of use. However, their lack of kinematic similarity to a given slave robot presents several disadvantages such as reduced overall manipulability and dexterity, as discussed below.

The control of a HI-slave system can be based on force control, position control or a combination of both. To improve the control accuracy for teleoperated robotic systems in all these cases, one must improve the manipulability of the system. There are two ways to do this.

Most studies consider only the global manipulability index, GM_M, and global conditioning index, GC_M, of the HI[79], [86], [92], [150]. Following this approach, the optimal design for the HI can be obtained by

$$\underset{D}{\text{maximize}}\{C_1 := K_1 GC_M + K_2 GM_M\} \tag{4.23}$$

where D is the set of parameters to be optimized, and K_1 and K_2 are appropriate scaling factors. By using (4.23), the kinematics of the HI is optimized by maximizing the HI manipulability and isotropy. In this optimization, the kinematic performance of the teleoperated system is enhanced by enlarging the HI's links length which faces practical limitations. In fact, such a solution would result in an HI with large links, small flexural stiffness, and a big footprint. The robots used in the operating room work in a limited workspace and must have a small footprint with maximum rigidity and stability.

Instead of the above, we propose an approach that considers the global condition index GC_M of the HI and the global manipulability index GM_T of the teleoperated system as design criteria. This way, in addition to maximizing GC_M for the HI, which enhances the surgeon's control over force/velocities, kinematic compatibility between the HI and slave robot is also considered. The goal is to design an HI for a given slave robot with maximum possible manipulability while maintaining a small footprint. By considering the kinematics of the slave robot, the optimal design for the HI can be obtained by

$$\underset{D}{\text{maximize}}\{C_2 := K_1 GC_M + K_2 GM_T\}. \tag{4.24}$$

By using (4.24), the kinematics of the HI is optimized for the best kinematic similarity to the slave robot.

As a case study, the PHANToM 1.5A robot (3D Systems Inc., Morrisville, NC, USA), which provides position measurement and force feedback at its end-effector in three translational DOFs is used as the HI, and a 2-DOF planar upper-limb rehabilitation robot and haptic device (Quanser Inc., Markham, ON, Canada) is used as the slave robot. The schematic diagram of rehabilitation robot and PHANToM robot are shown in Fig. 4.2. We propose to use C_2 as a quantitative measure for optimal selection of the PHANToM robot's placement and other kinematic parameters.

The Jacobians of the rehabilitation and the PHANToM robots in their base

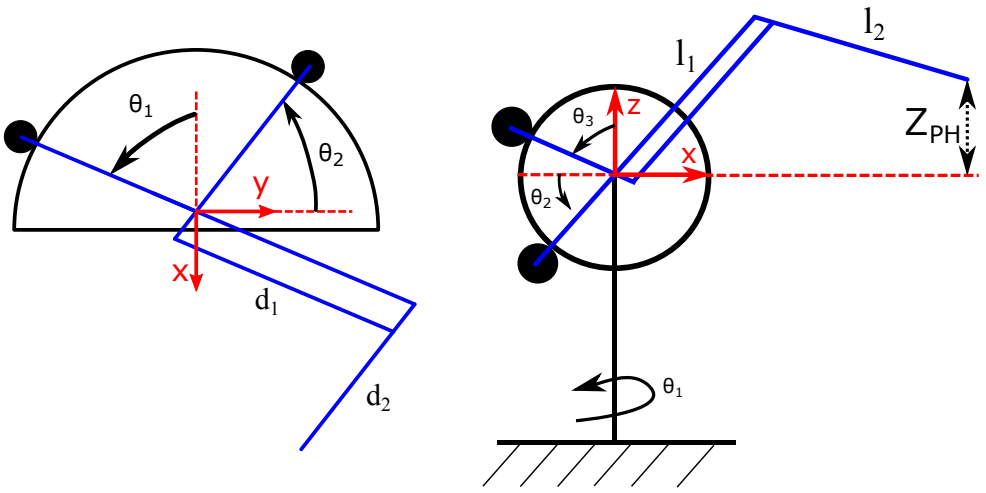

Figure 4.2: (a) Top view of Rehabilitation Robot. (b) Side view of PHANToM 1.5A.

frames are

$$J_{RE} = \begin{bmatrix} -d_1 s_1, & d_2 c_2 \\ d_1 c_1, & d_2 s_2 \end{bmatrix} \tag{4.25a}$$

$$J_{PH} = \begin{bmatrix} -s_1(l_1 c_2 + l_2 s_3), & -l_1 c_1 s_2, & l_2 c_1 c_3 \\ c_1(l_1 c_2 + l_2 s_3), & -l_1 s_1 s_2, & l_2 c_3 s_1 \\ 0, & l_1 c_2, & l_2 s_3 \end{bmatrix} \tag{4.25b}$$

where $s_i = sin(\theta_i)$, $c_i = cos(\theta_i)$, $i = 1, 2, 3$.

The Jacobian of the HI needs to be transformed to the slave coordinate frame. The transformed Jacobian of the HI is

$$J_M^{2D} = \begin{bmatrix} c_z & -s_z & 0 \\ s_z & c_z & 0 \end{bmatrix} J_{PH} \tag{4.26}$$

where $s_z = sin(\theta_z)$, $c_z = cos(\theta_z)$, and θ_z is the orientation of the HI with respect to the center of the workspace of the slave robot. θ_z is shown in Fig. 4.3.

For the HI, there are three parameters to be optimized, i.e. the last link's length (l_2), the orientation of the HI (θ_z), and the level, Z_{PH}, of the plane in which the HI works as a 2D robot. This means $D = \{l_2, \theta_z, Z_{ph}\}$.

In our simulations, first, the HI's parameters are optimized without considering the slave robot kinematic. The cost function for this optimization is

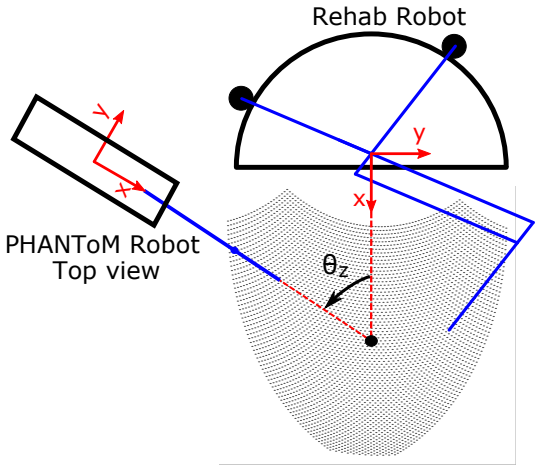

Figure 4.3: Orientation of the PHANToM robot with respect to the rehabilitation robot, θ_z

C_1 given in (4.23). The constraints for the optimization are

$$0.165 < l_2 < 0.365, -\frac{\pi}{2} < \theta_z < \frac{\pi}{2}. \tag{4.27}$$

Next, the cost function is selected such that the kinematics of the slave robot is also considered. For this optimization, the cost function is C_2 given in (4.24). The same constraints given in (4.27) are used. In the first round of simulations, it is assumed that the HI orientation, θ_z, is the only optimization variable. The teleoperation system manipulability can be optimized by rotation of the HI around the center of the slave workspace. For this case, $l_2 = 0.165m$ and $Z_{PH} = 0.0539m$ are constants. θ_z equals to 89° and θ_z equals to 2° are obtained from maximizing the C_1 and C_2 cost functions, respectively. The optimization result shows that if the orientation of the HI changes from 89° to 2°, the GM_T varies from 0.0378 to 0.0437 while GM_M for the phantom robot changes from 0.0433 to 0.0428. The MEs at six points of the workspace for the HI, slave robot, and the teleoperated system are depicted in Fig. 4.4.

In the second round of optimization, l_2, θ_z, and Z_{PH} are all considered as optimization variables. The optimized variables are summarized in Table 4.1. As it can be seen, the optimization for C_1 cost function results in a bigger link length l_2. It can also be noticed that the global manipulability index GM_M and the global conditioning index GC_M of the HI are higher for C_1 optimization.

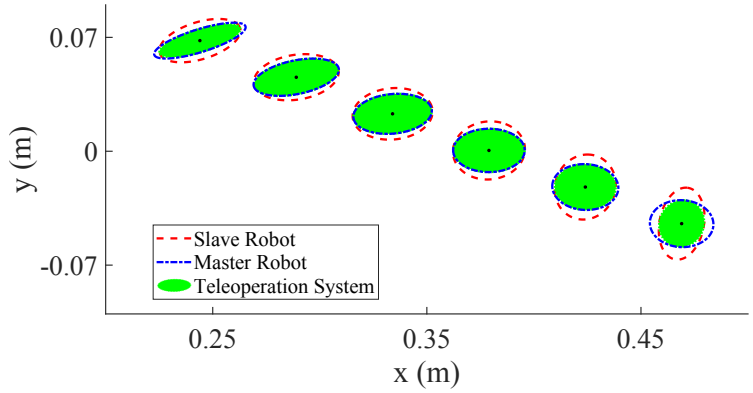

(a)

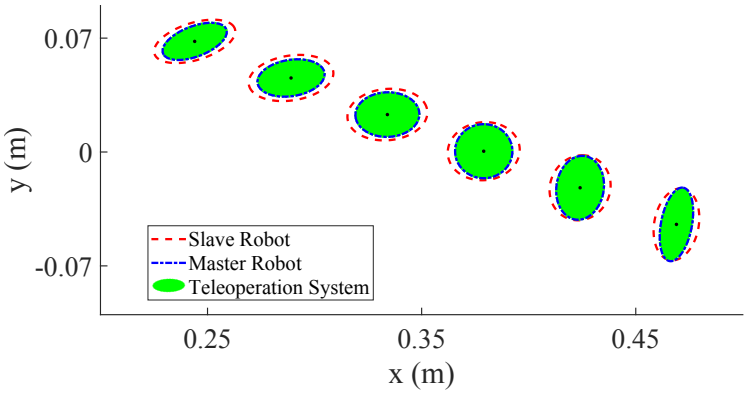

(b)

Figure 4.4: (a) $\theta_z = 89°$, as a result of maximizing the C_1 cost function. (b) $\theta_z = 2°$, as a result of maximizing the C_2 cost function. $D = \{\theta_z\}$

Table 4.1: Optimization results, $D = \{l_2, \theta_z, Z_{ph}\}$

	C_1 as the cost function	C_2 as the cost function
l_2 (m)	0.365	0.269
Z_{PH} (m)	-0.2162	-0.065
θ_z (deg)	-63.5	0
GM_T	0.0549	0.0590
GC_M	0.7785	0.7315
GM_M	0.1023	0.0728

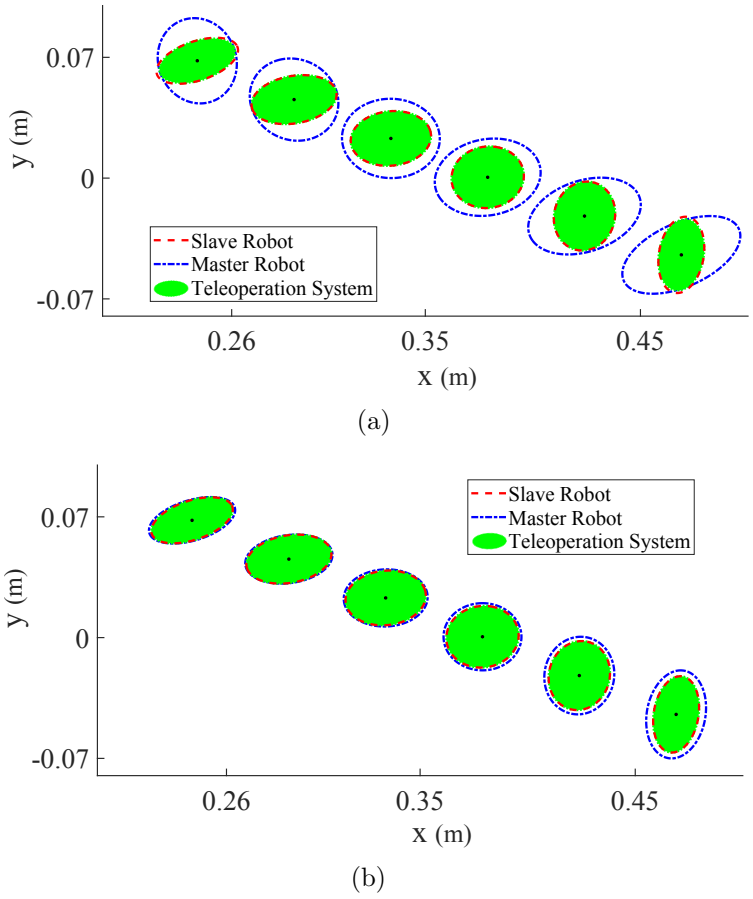

Figure 4.5: (a) Results of C_1 optimization. (b) Results of C_2 optimization. $D = \{l_2, \theta_z, Z_{ph}\}$

However, the global manipulability index of the teleoperated system, GM_T, decreases for the C_1 optimization.

Fig. 4.5 shows the MEs at six points of the workspace for the HI, slave robot, and the teleoperated system. The ME of the HI for C_2 optimization is smaller than that from C_1 optimization. However, the principal axes of the ME of the HI are aligned with principal axes of the ME of the slave robot, which results in an overall large ME for the teleoperation system. The calculated TMI from optimization using C_1 and C_2 is depicted in Fig. 4.6

From the ellipsoid obtained in the simulations, one can calculate a measure of HI's and slave robot's joints kinetic energy, defined as $\|\dot{q}\|^2$ by using (4.21). Fig. 4.7 shows the teleoperation system's joint energy for various simulation scenarios discussed above in a task of moving an object from point A (0.424

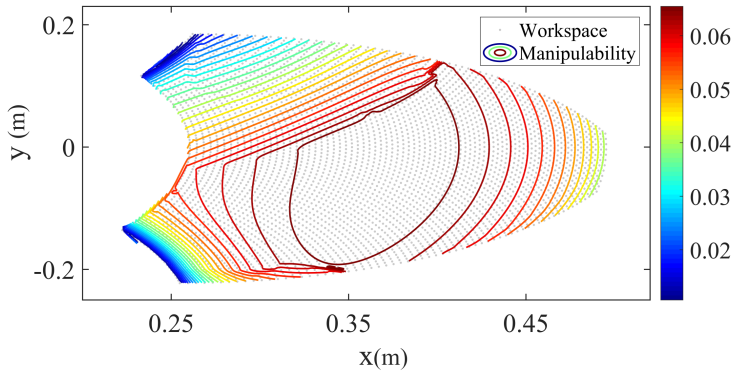

(a)

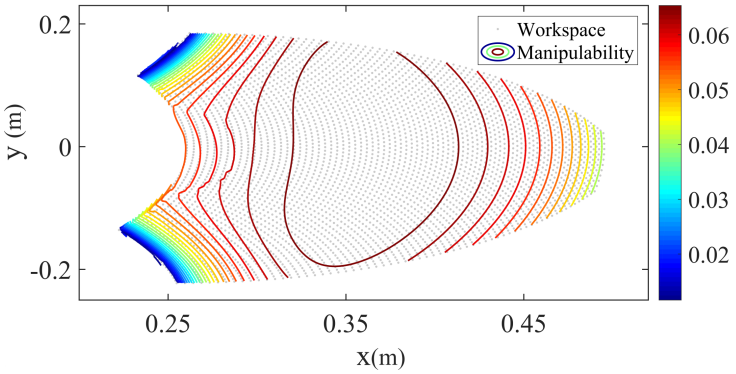

(b)

Figure 4.6: (a) The TMI as a result of maximizing the C_1 cost function. (b) The TMI as a result of maximizing the C_2 cost function. $D = \{l_2, \theta_z, Z_{ph}\}$

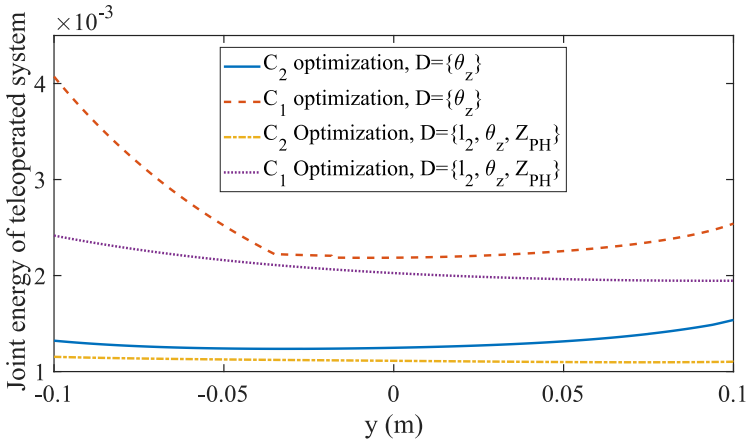

Figure 4.7: A comparison of user's effort for different optimization approaches.

m,-0.1 m) to point B (0.424 m, 0.1 m) at a constant speed of $\dot{y} = 0.01m/s$ in the slave robot frame. It can be seen in Fig. 4.7 that the teleoperation system's joint energy and consequently, the user's input energy for performing a task in the slave robot's task space for cases where C_2 is optimized is much smaller.

4.5 Concluding Remarks

In this chapter, the teleoperation manipulability index (TMI) for a surgical HI-slave robotic system is defined. We demonstrate the application of the TMI in the design of HI-slave robotic systems. It is shown that by modifying the design of a commercially available HI using the proposed manipulability criterion, we are able to enhance the surgeon's control over force/velocity of the surgical robot, minimizing the master robot's footprint via minimizing its link length, and optimizing the surgeons control effort via minimizing the required input energy for moving the slave's end-effector.

Chapter 5

Redundant Haptic Interface for Improving Manipulability Performance Measure[1]

5.1 Introduction

The enhanced dexterity and manipulability offered by HI-slave teleoperated surgical systems have significantly improved the performance and safety of minimally invasive surgeries. However, effective manipulation of surgical robots is sometimes limited due to the mismatch between the slave robot and HI kinematics and workspace. In this section, we develop a null-space controller for the redundant haptic interface that employs the proposed manipulability index to enhance the performance of teleoperation tasks by matching the kinematics of the redundant HI to the kinematics of the slave robot.

As stated in Chapter 4, one of the well-established tools for motion and dexterity analysis of robot manipulators is the Manipulability Ellipsoid (ME) [156]. This geometric measure indicates the ability to perform motion and exert force along the different task directions in a given joint configuration [52]. Manipulability of robots was first introduced in [156] to describe how a manipulator can move in arbitrary directions, and to quantify the ability to perform an action quickly and skilfully [7]. Manipulability analysis consists

[1]A version of this chapter has been published as Ali Torabi, Mohsen Khadem, Kourosh Zareinia, Garnette Sutherland, and Mahdi Tavakoli, "Using a Redundant user Interface in Teleoperated Surgical Systems for Task Performance Enhancement," Robotica, 2020. In press

of describing the motion of the robot in the task as a function of a measure of the robot's effort in joint space (e.g., joint torque). Yoshikawa defined a quality measure based on the analysis of the ME. ME is a volume/surface in the Cartesian velocity space, which is mapped from the unit sphere in the joint velocity space by a Jacobian transformation [156].

The null-space controller modulates the redundant degrees of freedom of the redundant HI to reshape its manipulability ellipsoid towards the manipulability ellipsoid of the slave robot. The manipulability ellipsoid is the geometric interpretation of the kinematics of a robot. By reshaping the redundant HI's manipulability, we match the redundant HI and slave robot kinematics. We demonstrate that by using a redundant HI, we are able to enhance the HI-slave system manipulability and more intuitively transfer the slave robot's dexterity to the user. Simulation and experimental studies are performed to validate the performance of the proposed control strategy. Results demonstrate that by employing the proposed manipulability index, we can enhance the user's control over the force/velocity of a surgical robot and minimize the user's control effort for a teleoperated task.

This chapter is organized as follows: In Section 5.3, an optimal controller is introduced that employs the kinematic redundancies of the haptic interface to optimize the teleoperation manipulability during a teleoperation task. Experimental and simulation results to validate the performance of the proposed controller and teleoperation manipulability measure are presented in Section 5.4.1 and Section 5.4.2, respectively. Concluding remarks appear in Section 5.5.

5.2 Preliminaries

The dynamic model of an HI in the joint space can be defined by

$$M_q(q)\ddot{q} + C_q(q,\dot{q})\dot{q} + G_q(q) + F_q = \tau_m + J^T(q)F_h, \tag{5.1}$$

where $M_q(q)$ is the $n \times n$ inertia matrix, $C_q(q,\dot{q})$ is the $n \times n$ matrix of Coriolis and centrifugal terms, $G_q(q)$ is the $n \times 1$ vector of gravitational torques, F_q is

the $n \times 1$ vector of the friction torques, $J = [J_t^T, J_r^T]^T$ is $m \times n$ robot Jacobian, τ_m is the $n \times 1$ control torque, and F_h is the $m \times 1$ torque/force applied by the user's hand on the end effector of the HI.

The end effector dynamics of the HI in the task space can be written as [74]

$$M_x\ddot{x} + C_x\dot{x} + G_x + F_x = F_m + F_h \tag{5.2}$$

where $M_x = (JM_q^{-1}J^T)^{-1}$ is the $m \times m$ end effector inertia matrix or apparent inertia,
$C_x = M_x(JM_q^{-1}C_q - \dot{J})J^{\#}$ is the $m \times m$ matrix of the end effector's centrifugal and Coriolis terms, $G_x = J^{\#^T}G_q$ is the vector of gravitational forces/torques and $F_x = J^{\#^T}F_q$ the vector of friction forces/torques reflected at the end effector, and $F_m = J^{\#^T}\tau_m$ is the task space control force/torque which corresponds to the joint space control torque. $J^{\#}$ is generalized inverse of the Jacobian matrix defined as

$$J^{\#} = M_q^{-1}J^T[JM_q^{-1}J^T]^{-1}. \tag{5.3}$$

5.3 Null-Space Control of Redundant Haptic Interface

Kinematic redundancy of the manipulators can offer greater flexibility to the end user to execute complicated surgical tasks. In this section, we propose an approach to improve the teleoperation manipulability introduced in Section 4.3 using the redundant HI kinematic redundancy. In teleoperated systems, the HI and the slave robot usually have different kinematics. Therefore, they have different singularity points in their shared workspace. As a result, the user can move the HI even if the slave robot is in the singular configuration. Here, the kinematics of the redundant HI is matched to that of the slave robot so that the singularities will occur for both robots at the same point in the workspace. This is advantageous as a unified singularity avoidance/resolution scheme will suffice for both robots.

In our approach, it is assumed that we are implementing a general redundant haptic interface to teleoperatively control slave robots that are designed

for a specific task. Thus, the slave robot is kinematically compatible with the desired task. We also note that the slave robot can be redundant as well, and can have its null-space controller. In this work, we have considered unilateral teleoperation in which an impedance controller and a position controller are designed for the redundant HI and the slave robot, respectively. Here we demonstrate that the teleoperation performance will be improved in the unilateral case, and we intend to study the bilateral case in our future work.

The proposed redundant HI is considered as an impedance-type device. Therefore, an impedance controller needs to be designed for this device. The task space dynamics of the HI can be modified to an impedance model with null stiffness by choosing F_m in (5.2) as follows

$$F_m = -M_x(M_x^d)^{-1}B^d\dot{x} + M_x(M_x^d)^{-1}(F_h) - F_h + C_x\dot{x}_x + G_x + F_x. \tag{5.4}$$

Thus, the reference impedance model of the HI becomes

$$M_x^d\ddot{x} + B^d\dot{x} = F_h \tag{5.5}$$

where M_x^d and B^d are the desired apparent inertia and damping matrices which are positive definite.

Now, we modify the control law for a redundant HI robot by selecting the desired robot's inertia equal to its apparent inertia, $M_x^d = M_x$. The reason for this is that: 1) We eliminate the need for calculating the precise model of the HI, M_x, and the user force, F_h, which is commonly noisy, time-delayed, and inaccurate. 2) The HIs are designed back-drivable with low apparent inertia. 3) The robot loses its passivity and becomes unstable if one makes the apparent inertia lower than a certain physical threshold [37]. Thus, by selecting $M_x^d = M_x$, the new control law becomes

$$F_m = -B^d\dot{x} + C_x\dot{x} + G_x + F_x, \tag{5.6}$$

with the corresponding joint torque control law

$$\tau_m = J^T F_m. \tag{5.7}$$

In practice, the real values for the parameters in (5.6) cannot be modeled exactly. Therefore, the impedance model of the HI (5.5) can be rewritten as

$$M_x^d \ddot{x} + B^d \dot{x} + \mathcal{F} = F_h \tag{5.8}$$

where $\mathcal{F}$ is the force vector reflecting the effects of uncertainties in the dynamic parameters. For instance, the stiction term, which is part of F_x in (5.2) and hard to model, can be integrated into this term. The presence of $\mathcal{F}$ limits the achievable transparency of the system.

In the case of the redundant HI, equation (5.2) describes only the end effector dynamics and does not include the null-space dynamics of a redundant HI corresponding to self-motion of the robot. The control actions used for achieving the self-motion (i.e., secondary objective) are bound to act in the null-space of the Jacobian matrix. Thus, the primary and secondary objectives are decoupled, and the primary controller precludes the effect of secondary objective control actions. To separate the null space and the task space controller we use the following control law [74]

$$\tau_d = \underbrace{\tau_m}_{\text{Impedance controller}} + \underbrace{(I - J^T(J^{\#})^T)(\tau_N - k_D\dot{q})}_{\text{Null space controller}}, \tag{5.9}$$

where τ_d is the $n \times 1$ desired joint torque vector, τ_m is the $n \times 1$ is torque vector calculated from (5.7), τ_N is the $n \times 1$ null-space torque vector corresponding to the secondary objective. τ_N is projected in the null space of the Jacobian through the matrix $I - J^T(J^{\#})^T$. It is an arbitrary joint torque vector acting in the Jacobians null-space, which does not produce any force/motion in task space and produces only joint self-motion of the robot. $-k_D\dot{q}$, with $k_D > 0$, is a suitable damping torque. The control law (5.9) ensures stability both for the primary and secondary tasks [104].

Now, we introduce τ_N, which accounts for secondary goals as

$$\tau_N = -\alpha \frac{\partial \nu(q)}{\partial q} \tag{5.10}$$

where α is a scalar step size and $\nu(q)$ is the secondary objective. With this choice of τ_N, the robot tries to decrease the value of $\nu(q)$. We note that

the gradient projection method is used in (5.9), which is a local optimization technique and deals with the instantaneous kinematics of motion. Global optimization techniques that minimize some performance index across a whole trajectory perform better than local optimization solutions. However, they are impractical for online feedback control, due to the heavy computational requirements and unexpected human motions.

Cost function $\nu(q)$ can be defined as the Jensen-Bregman Metric [28] for the distance between the ME of the slave robot and the ME of the HI. The manipulability ellipsoid, $\mathcal{M} = JJ^T$, belongs to the set of symmetric positive definite (SPD) matrices that describe the interior of the convex cone. The Jensen-Bregman Metric is selected as it forms a convex optimization problem that ensures convergence and also it is computationally efficient [28], [132]. The proposed cost function is defined as

$$\nu = \texttt{logdet}(\frac{{}^s\mathcal{M}_i + {}^m\mathcal{M}_i}{2}) - \frac{1}{2}\texttt{logdet}({}^s\mathcal{M}_i{}^m\mathcal{M}_i) \tag{5.11}$$

where ${}^s\mathcal{M}$ and ${}^m\mathcal{M}$ is the ME of the slave robot and HI, respectively. ν is an index that quantifies the kinematic similarity between the HI and slave robot MEs in task space. When ν is zero, the HI and slave robot have similar MEs. Thus, the intersection of the HI's and the slave robot's ME is maximized.

The proposed controller maximizes the teleoperation system's manipulability by minimizing cost function ν. By minimizing the cost function, we can enhance the user's control over the force/velocity of the slave robot of the surgical system and optimize the user's control effort. Also by using the index penalized Jacobian, we will prevent the HI from approaching limits of the joints in addition to enhancing the teleoperation manipulability.

5.4 Case study

For a case study, simulations and experiments are performed on a HI-slave robotic system comprised of a planar four degree of freedom (DoF) HI and two DoF planar slave robot. The 4 DoF HI is made of two serially connected robots, a two DoF PHANToM 1.5A robot (3D Systems Inc., Morrisville, NC, USA))

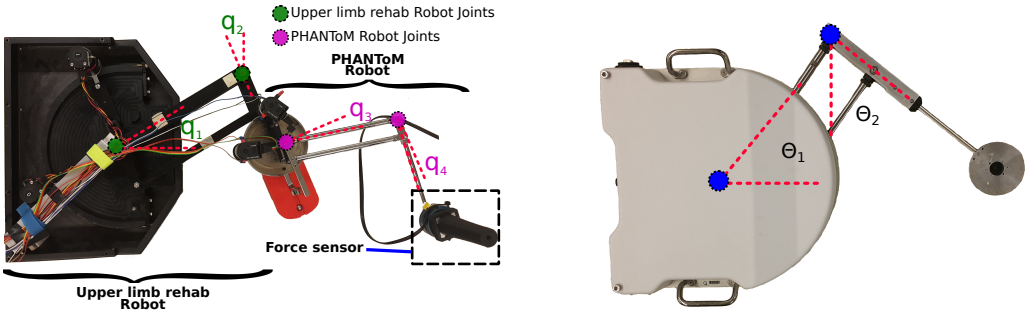

(a) (b)

Figure 5.1: (a) Top view of the haptic interface. (b) Top view of the Slave robot.

connected to a two DOF planar upper-limb rehabilitation robot 1.0 (Quanser Inc., Markham, ON, Canada). The base joint of the 3-DoF PHANToM robot has been removed to turn it into a 2-DoF planar robot. The slave robot is the upper-limb rehabilitation robot 2.0 (Quanser Inc., Markham, ON, Canada), which has relatively larger links and range of motion than the rehabilitation robot 1.0. The HI and slave robot used in the simulations and experiments are shown in Fig. 5.1.

The Jacobians of the haptic interface and the slave robots in their base frames are

$$J_m = \begin{bmatrix} -d_1 s q_1, & d_2 c q_2 - d_3 s q_{23} + d_4 c q_{24}, & -d_3 s q_{23}, & d_4 c q_{24} \\ d_1 c q_1, & d_2 s q_2 + d_3 c q_{23} + d_4 s q_{24}, & d_3 c q_{23}, & d_4 s q_{24} \end{bmatrix} \tag{5.12a}$$

$$J_s = \begin{bmatrix} -l_1 s\theta_1, & l_2 c\theta_2 \\ l_1 c\theta_1, & l_2 s\theta_2 \end{bmatrix} \tag{5.12b}$$

where q_i $(i = 1, 2, 3, 4)$ is the HI joints angle, θ_i $(i = 1, 2)$ is the slave robot joints angle, s and c are shorthand notations for $sin(.)$ and $cos(.)$, $q_{ij} = q_i + q_j$, and J_m and J_s are the Jacobian matrix of the HI and slave robot, respectively. The links' length of the HI and the slave robot are given in meters as $d_i = [0.254,\ 0.1405,\ 0.21,\ 0.181]$ and $l_n = [0.34,\ 0.375]$, respectively. The HI joints' limits are defined as

$$Q_i^{min} = [-55,\ 0,\ -55,\ -20] \quad \text{degrees},$$
$$Q_i^{max} = [90,\ 145,\ 115,\ 80] \quad \text{degrees}.$$

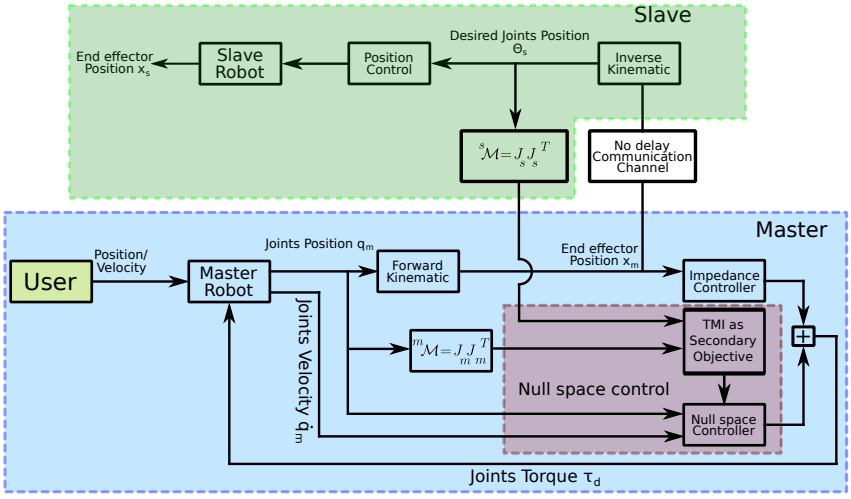

Figure 5.2: Block diagram of the unilateral teleoperation system.

Also, the following constraints are imposed due to structure of the robot

$$35^\circ \leq q_1 - q_2 + 90^\circ \leq 145^\circ$$

$$35^\circ \leq q_3 - q_4 + 90^\circ \leq 145^\circ.$$

The dynamics of the HI is obtained based on the works of [23] and [45]. As we are considering the unilateral teleoperation in this research and a position-based controller is used for the slave robot, the dynamics of the slave robot is neglected. A block diagram of the unilateral teleoperation system with a kinematically redundant HI is shown in Fig. 5.2.

It should be noted that the robots are planar and only perform translational tasks in Cartesian space. Therefore, the manipulability ellipsoid and the cost function for the null-space controller are simplified to the translational part. Here, we considered a non-redundant two DoF robot as the slave robot. However, the slave robot can also be redundant and has its own secondary objective.

5.4.1 Simulation Studies

In the first simulation study, the end-effector of the HI and slave robot are fixed at a certain point in the XY plane. Then, the null-space controller is used to minimize ν (i.e., maximize the teleoperation manipulability). The results of simulations are shown in Fig. 5.3. The configuration of the HI and

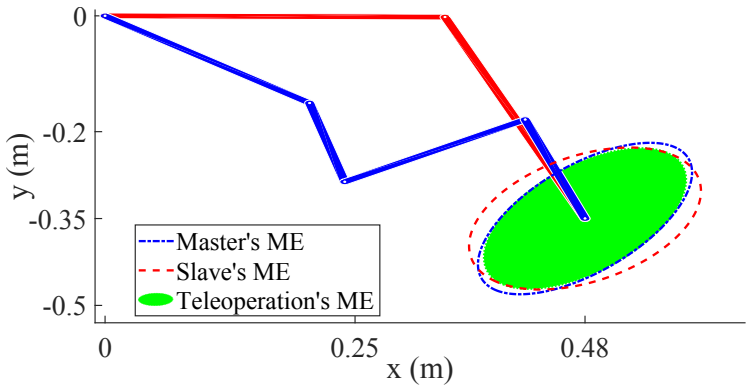

(a)

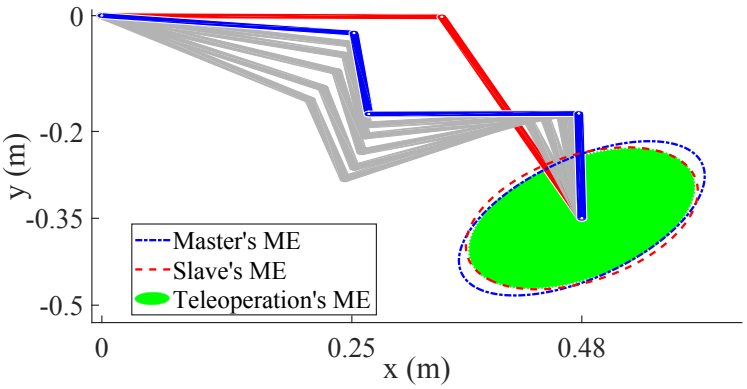

(b)

Figure 5.3: Comparison between the manipulability ellipsoids of the slave, HI, and teleoperated system. (a) Initial configuration of the HI. (b) Evolution of the HI configuration and the final configuration with manipulability optimization. The HI and slave robot are shown in solid blue and red, respectively. The evolution of the HI configuration in time is shown in grey.

slave robot, the corresponding velocity MEs, and the intersection of the slave robot and HI MEs (i.e., the teleoperation manipulability ellipsoid) with and without the null space controller are shown.

In the simulation, the HI's and slave robot's end-effector position are initially at $(X, Y) = [0.48m,\ -0.35m]$. The initial configuration of the HI is selected as

$$q_i = [-0.63,\ 0.25,\ 0.28,\ 0.09]^T rad.$$

The values of desired damping parameter is $B^d = \text{diag}\{0.3,\ 0.3\}\text{Ns/m}$. B^d is chosen sufficiently small such that the free space force ($F_h \rightarrow 0$) and the

stability are achieved. Also, the uncertainty term in (5.8) is modeled as

$$\mathcal{F} = J^{\#^T} F_q^{un} = J^{\#^T} \Gamma \dot{q} \tag{5.13}$$

where F_q^{un} is the uncertainty term in the joint space and Γ is approximated equal to diag$\{0.01,\ 0.01,\ 0.01,\ 0.01\}$.

As shown in Fig. 5.3, by using the null space controller, the configuration of the HI changes to maximize the teleoperation ME, while the end-effector of the HI and slave robot are fixed. The area of the teleoperation ME is increased by 18.1% via the null space controller.

In the next simulation study, it is considered that the slave robot follows the HI's end-effector position, and the HI follows a given trajectory in the slave's workspace. Control input defined in (5.9) is used to maximize the teleoperation manipulability while following the given trajectory in the slave robot's workspace with a constant speed of $2cm/s$. To achieve this, an internal PD controller is designed to change the external force, F_h, such that the end-effector of the robot follows the trajectory with the given constant speed.

To show the advantages of the proposed control strategy, the results are compared to unilateral teleoperation control with 1) a two DoF HI which is made by fixing the last two DoFs of the redundant HI, and will be called Rehab robot hereafter, and 2) a null space controller that only optimizes the kinematics manipulability of the HI. The second controller can be achieved by selecting the null space controller input as $\tau_N = \alpha \dfrac{\partial \mu(q)}{\partial q}$, where μ is the classic manipulability index of a single robot defined as [156]

$$\mu(q) = \sqrt{\det(J_m J_m^T)} \tag{5.14}$$

A "W-shaped" curve that follows various points in the slave robot's task space is selected as the robot's trajectory (see Fig. 5.4). The reference trajectory is selected to, 1) cover most of the slave robot's workspace, 2) be in the two DoF HI's workspace, and 3) be aligned with the major axis of the slave robot's ME. As shown in Fig. 5.4, although the RHI and the two DoF HI have links of the same length, the RHI has a bigger workspace compared to the two DoF HI. This is one of the advantages of the RHI over the traditional NHI.

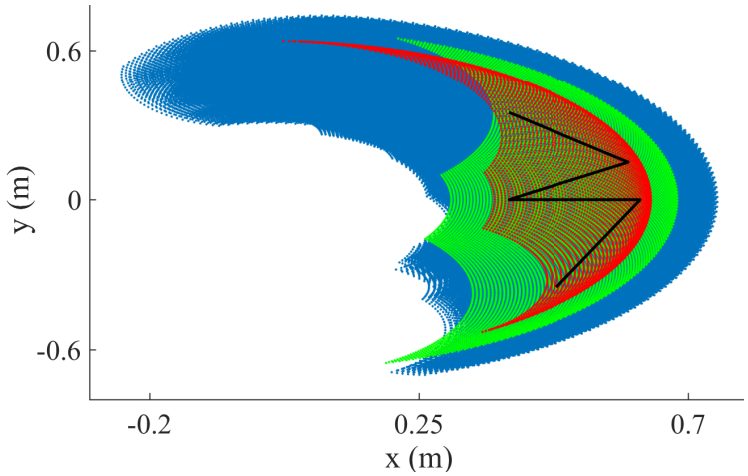

Figure 5.4: Redundant haptic interface's workspace (blue dots), two DoF HI's workspace (red dots), slave robot's workspace (green dots), and reference trajectory (solid black line) are shown.

Fig. 5.5 shows a comparison of simulation results for three scenarios: 1) The RHI with the proposed teleoperation manipulability optimizer. 2) The RHI with its manipulability optimizer. 3) The Rehab robot. It can be seen that the ME of the HI is maximized in the case of the RHI with its manipulability optimizer (see Fig. 5.5(b)). However, the teleoperation ME is smaller than the teleoperation ME as the kinematics of the slave robot is not considered. The mean area of the teleoperation manipulability is 0.1034 when the HI's manipulability is optimized, which is 15.3% less than the mean area of the teleoperation manipulability when our proposed approach is employed.

Fig. 5.5(a) shows a comparison between the haptic interface ME, the slave robot ME, and the teleoperation ME over the given trajectory for the case of a redundant robot with the proposed teleoperation manipulability optimizer. It can be seen that the proposed redundancy resolution is effective, and the ME of the HI matches the ME of the slave robot, and the teleoperation manipulability is improved. The ME of the Rehab robot is compared with the ME of the rehabilitation robot 2.0 in Fig. 5.5(c). This figure shows the difference in the kinematics of the Rehab robot and the slave robot.

Another way to show the effectiveness of the proposed approach is to compare the user effort in the three control scenarios. Considering the conservation

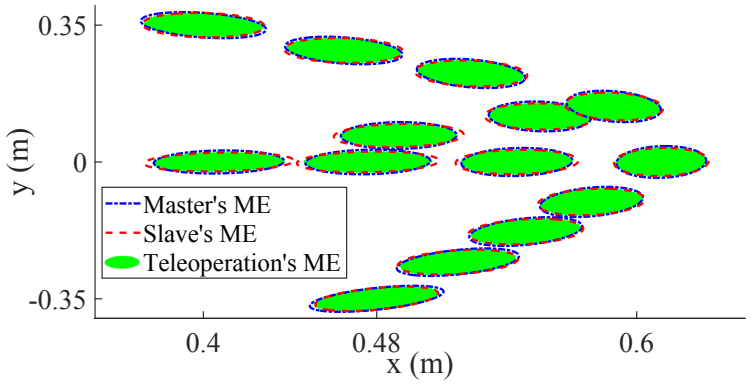

(a)

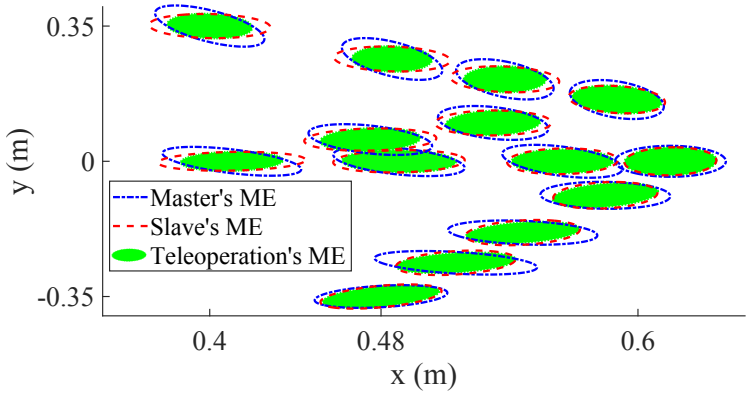

(b)

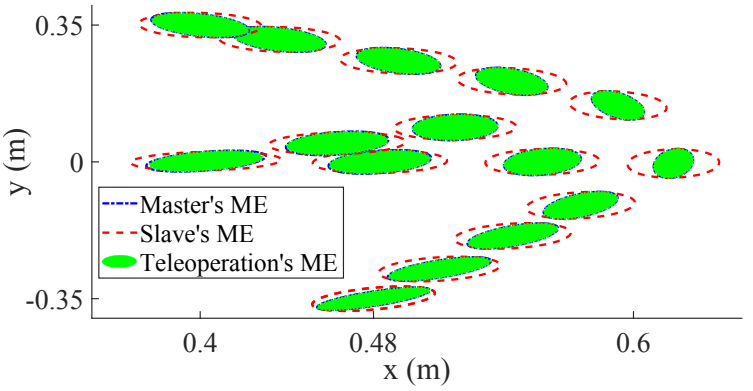

(c)

Figure 5.5: Simulation results for trajectory tracking (a) with RHI with the teleoperation manipulability optimization, (b) with RHI with the HI's manipulability optimization, and (c) with non-redundant two DoF HI. The manipulability ellipsoids of the slave, HI, and teleoperated system during trajectory tracking are shown.

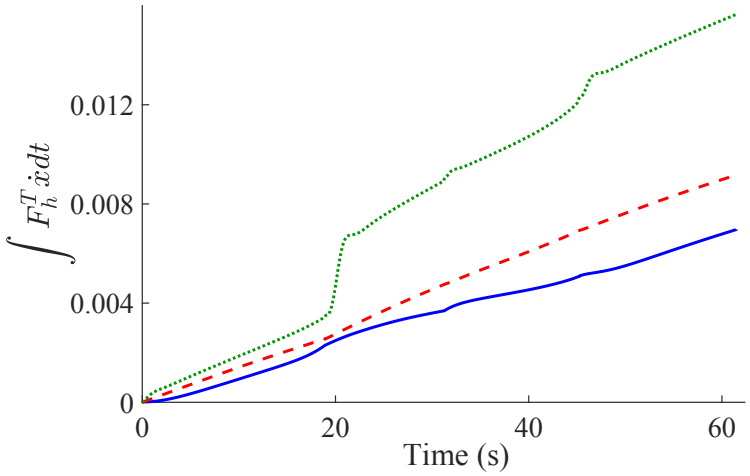

Figure 5.6: A comparison between the user's effort for controlling the position of the slave robot with the proposed teleoperation manipulability optimization for redundant HI (Solid blue line), HI manipulability optimization for RHI (Dashed red line), and two DoF NHI (Doted green line).

of energy, the work done by the user is measured as

$$W = \int_0^T F_h^T \dot{x} dt, \tag{5.15}$$

where $\dot{x}$ is the velocity of the HI end-effector, which is equal to the velocity of the user's hand, and F_h is the forces applied by the user.

Now we use (5.15) to estimate the human user effort over time during the trajectory tracking scenario. The same value for the B^d is chosen for all simulation studies. Results are shown in Fig. 5.6. As it can be seen in this figure, the energy used to move the slave robot to follow the W-shaped trajectory for our proposed null-space controller is less than the two other approaches. This difference grows with time, which will have a significant impact on the performance of the user in a relatively long teleoperation task. This is important especially in the long surgeries in which the surgeon makes better decisions when he/she is less tired [114].

5.4.2 Experiments

In this section, experiments are performed to evaluate the performance of the proposed controller. The setup is shown in Fig. 5.1 is used to perform the experiments. For interfacing the robots with the computer, MATLAB/Simulink

(MathWorks Inc., Natick, MA, USA) with Quarc real-time control software (Quanser Inc., Markham, ON, Canada) is used. In the experiments, eight users (6 males and 2 females), all right-handed, were asked to move the HI so that the slave robot end-effector would follow the same reference trajectory from the simulation studies. Also, they were asked to take the path following accuracy as the primary objective and the task's completion time as the secondary objective. The reference trajectory and the position of the slave robot end-effector were shown to the user in real-time. Before starting the experiments, the subjects were asked to perform a training run to become familiar with the experimental setup. The users had some exposure to the haptic devices and teleoperation systems.

Three different scenarios were implemented in the experiments: 1) unilateral teleoperation with the RHI and proposed teleoperation manipulability as the null-space controller, 2) unilateral teleoperation with the RHI and the manipulability of the HI as the null-space controller, and 3) unilateral teleoperation with non-redundant two DoF HI. In this chapter, in order to isolate the positive impact of the HI's redundancy on users during trials, the experiments are performed with a unilateral teleoperated system. In a bilateral teleoperation experiment, the absence of full transparency would have made it difficult to isolate the impact of the redundancy of the HI because there are so many other factors at play.

In the above scenarios, the same position controller (i.e., a PD controller) is used for the slave robot. The following Cartesian-space control law used for the HI in the experiments:

$$F_m = -B^d \dot{x} + C_x \dot{x} \tag{5.16}$$

In each trial, one of the HIs were presented to the user. Thus each user performed three trials. The trials were presented in a randomized order to the users to minimize the effect of learning in the study. The same desired damping parameter, B^d, as the simulation studies is used in the experiments (i.e., $B^d = \text{diag}\{0.3,\ 0.3\}$Ns/m). Also, the friction forces, F_x, is not compensated for the experiments.

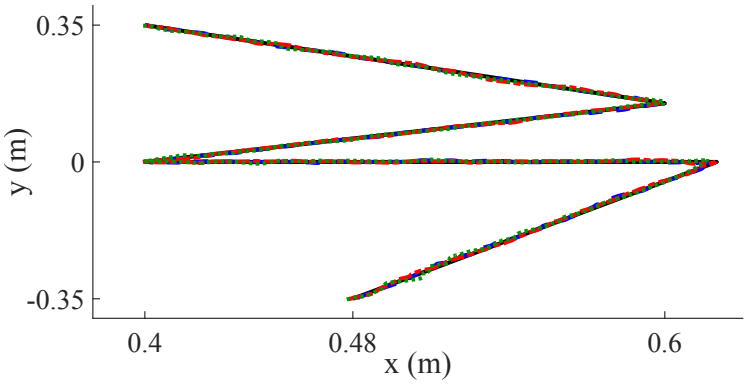

Figure 5.7: Reference (Solid black line), Scenario 1 (Blue Dashed line), Scenario 2 (Red Dashed-dot line), and Scenario 3 (green dot line) paths of user #3 for trajectory following task.

To compare the performance of the user in the three scenarios, the trajectory tracking error, the user's effort, and the execution time of the trajectory are considered as the performance metrics. The sample representative results of the end-effector movement for the three experimental scenarios of the user #3 as well as the reference trajectory are shown in Fig. 5.7.

The trajectory tracking error is defined as the norm of the distance between the desired trajectory and the user's actual trajectory ($error = \|L_d - L_t\|$). In order to compare the user's effort during the trajectory following task, (5.15) is used to measure the work done by the user. The forces are measured via a 6 DoF force/torque sensor (50M31A3-I25, JR3 Inc., Woodland, CA, USA) placed on the HI's user interface (see Fig. 5.1).

The experiment results are summarized in Table 5.1. The mean values for the trajectory error, the execution time, and the user's effort are smaller in scenario one than in the other two scenarios. This demonstrates the enhanced control of the user over the slave robot's trajectory and improved accuracy of the proposed null space controller compared to previously used methods.

The test results for the three performance metrics are shown as bar graphs in Fig 5.8. Fig 5.8(a) shows the results of all trials for the users' effort in the three scenarios. A one-way Analysis of Variance (ANOVA) test was used to investigate further, which confirms a significant difference between the scenarios ($F(2,21) = 32.63$, $p = 3.61E-7$). Also, the paired-sample t-test indicates

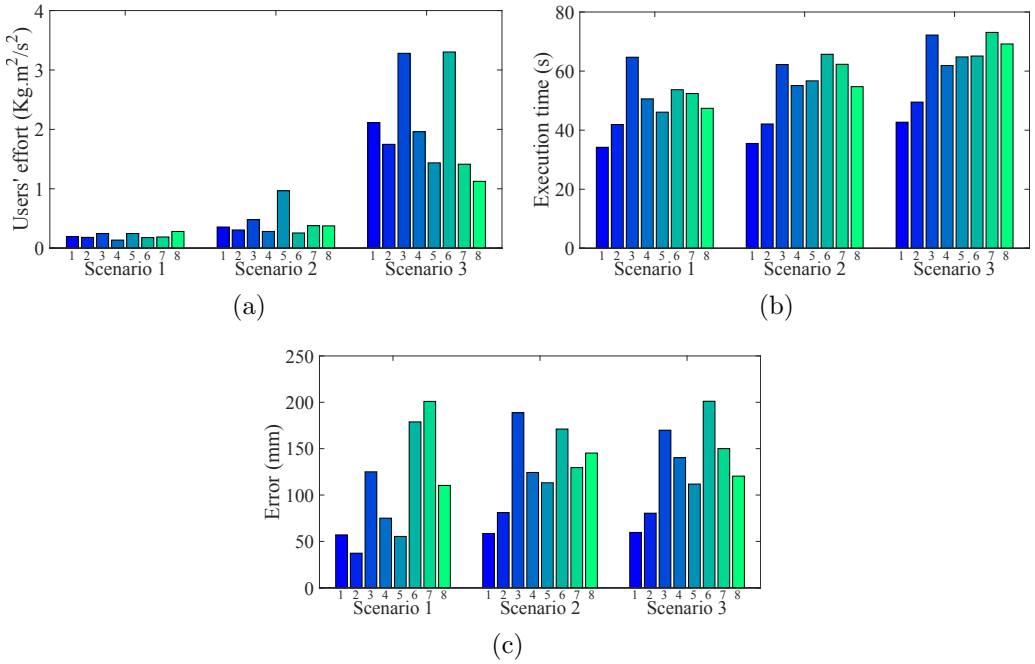

Figure 5.8: Bar plot results for (a) Users' effort, (b) Execution time, and (c) Trajectory tracking error.

Table 5.1: Mean and Std Values for the Performance Metrics in each Scenarios

	Scenario 1	Scenario 2	Scenario 3
User's effort ($Kg.m^2/s^2$)	0.207 (std=0.047)	0.425 (std=0.229)	2.048 (std=0.830)
Task completion time (s)	48.8 (std=8.9)	54.3 (std=10.4)	62.3 (std=10.8)
Trajectory error (mm)	105.0 (std=60.2)	126.5 (std=43.3)	129.2 (std=46.3)

Table 5.2: Hypotheses and adjusted p-values of t-test for the execution time

Hypothesis	p-value	Significant
Scenario 1 < Scenario 2	0.0245	True
Scenario 1 < Scenario 3	0.00039	True
Scenario 2 < Scenario 3	0.0012	True

that the users' effort in each scenario was statistically different from every other scenario ($p \leq 0.05$). The P-values are adjusted with the False Discovery Rate (FDR) method.

Fig. 5.8(b) shows the experimental results for the execution time for the three different scenarios. As stated in Table 5.1, the users completed the task with the lowest time in scenario one. The statistical significance of the results is confirmed by using the one-way ANOVA test ($F(2, 21) = 3.57$, $p = 0.046$). In order to further investigate this, a paired-sample t-test was used between different pairs of scenarios. The results of the t-test are shown in Table 5.2.

Fig. 5.8(c) shows the trajectory following error for all users in three scenarios. This graph does not show any clear trend for the trajectory following error. Also, a one-way ANOVA test for the three scenarios ($F(2, 21) = 0.55$, $p = 0.583$) shows that there is no statistically significant difference between the trajectory following errors. This is as the result of the fact that the users have been told to perform the path taking into account the accuracy as a primary objective. Thus, the error is similar for the three scenarios, but the task completion time and users' effort is significantly smaller for scenario one.

It should be noted that changing the damping parameter B^d in software has a considerable impact on the user's effort in a given task [115]. For this reason, in our experiments, the same damping was used for the three different HIs (Scenario 1, Scenario 2, and Scenario 3). The difference between the users' efforts in each scenario was because of the difference in the robots' kinematics (redundancy vs. non-redundancy) and configuration (due to different cost functions for the redundant case), which affected the friction reflected to the users' hand. The overall finding was that when the kinematics of the RHI matches to that of the slave robot, the user had to apply the least effort to perform the task.

As stated before, it is considered that the slave robot is properly designed for the given task (e.g., a particular trajectory-following task). This assumption means that the major axis of the manipulability ellipsoid of the slave robot is aligned with the desired trajectory direction. The optimal direction for affecting velocity as well as the optimal direction to control the force is along the major axis of the manipulability ellipsoid (ME). This means that for a robot, along the major axis of the ME, the user can move the end-effector with minimum movements of the robot's joints (i.e., feeling the least amount of joint frictions). By matching the ME of the HI to that of the slave robot, the major axis of the ME of the HI will be aligned to the desired task as well. This consequently minimizes the reflected joints friction at the end-effector of the HI, which was not compensated for in the experiments.

The proposed approach can be used in practice to minimize the effects of friction, which is of practical importance as the robot joint friction is hard to model and identify. For instance, once a desired task-dependent damping for the HI is determined and programmed in software, we can ensure that the effects of robot joint friction are minimal such that the total damping that the user experiences is close to the desired robot damping.

5.5 Concluding Remarks

In this chapter, the application of the proposed teleoperation manipulability index in designing an optimal controller, which can enhance the manipulability of the system, was demonstrated. We evaluated the enhanced performance of the proposed approach via a comparison with two other existing control strategies. It was shown that by implementing our controller in a robotic HI-slave system that benefits from a redundant haptic interface, we are able to improve the overall manipulability of the system, which can improve the user's control over slave robot's end-effector force/velocities and reduce the user's control effort.

Chapter 6

Dynamic Reconfiguration of Redundant Haptic Interfaces for Improving Haptic Interaction Fidelity[1]

6.1 Introduction

As stated in Chapter 3, a serial Redundant Haptic Interface (RHI) can be considered as the addition of one or more extra DoFs to the base of a Non-redundant Haptic Interface (NHI) (see Fig. 6.1). Compared to this NHI, the RHI has several intrinsic advantages. For instance, the RHI has smaller apparent inertia in any arbitrary direction than that of the NHI in the same direction. As shown in [117], when an HI cannot provide enough static force feedback to render an environment with high stiffness, the stiff contact feeling can be reproduced by using acceleration feedback. Having small apparent inertia for the HI helps to provide a broad range of stiffnesses [38], making the use of RHIs advantageous. Another intrinsic advantage of the RHI over the NHI is its larger effective manipulability. This means that the user requires to move the joints of the RHI less than the joints of the NHI for the same Cartesian space movement, exciting less joint friction. Therefore, the RHI can display forces to the user with higher fidelity than the NHI.

[1] A version of this chapter has been published as Ali Torabi, Kourosh Zareinia, Garnette Sutherland, and Mahdi Tavakoli, "Dynamic Reconfiguration of Redundant Haptic Interfaces for Rendering Soft and Hard Contacts," IEEE Transactions on Haptics, 2020.

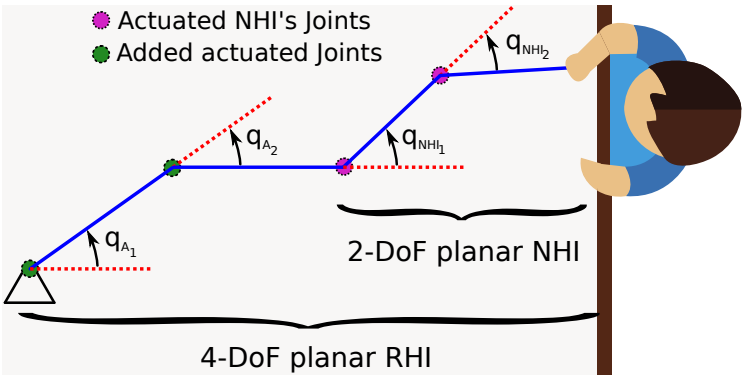

Figure 6.1: Schematics of a planar RHI.

In this chapter, two contradictory secondary objectives are introduced for soft contacts and hard contacts. In free-space movement and soft-tissue manipulation, the RHI should have low friction and low apparent inertia so that the kinematics and dynamics of the RHI do not interfere with the user-environment interaction. In the hard-contact case, however, the RHI should have large force feedback capability and stiffness so that it can recreate the feeling of contact with solid objects. For instance, for neurosurgery applications, the RHI should satisfy the requirements of low back-drive friction and inertia so that its mechanical properties do not conceal the small interaction forces involved in the soft-tissue manipulation. Also, the RHI requires to provide large force feedback such that hard contacts with bones can be rendered for the user with a high degree of fidelity [80]. As another example, in physical rehabilitation environments for people with disabilities such as stroke, an impaired user performs repetitive free-space tasks (e.g., reaching movements). Sometimes, a human therapist or a computer algorithm needs to apply large forces to the user's hand to either assist the user in performing a task or resist the user's movements to build their muscle strength, or provide body weight support. In the free-space movement case, the back-drive friction of the RHI must be minimized in order to not fatigue the physically weak patient or impede their motion. In the assistive and resistive therapy case, the RHI needs to reflect large forces to the user similar to what is needed during hard contacts [9], [126].

As the requirements of the task varies with respect to time (switching from

soft contact to hard contact), one or more of the RHI actuators may saturate. Therefore, in this chapter, an actuator saturation controller is proposed based on an actuator saturation observer. The actuator saturation observer continuously monitors the distance between the actuators torque vector and the maximum admissible torques vector in the n-dimensional space where n is the number of DoFs of the RHI. Informed by this, the actuator saturation controller ensures that, where possible, a minimum distance between the above two vectors is maintained. This is achieved by changing the secondary objective continuously from the ideal behaviour for the free-space motion to that for the hard contact case. This keeps the control effort continuous and avoids disruptions to the performance that would result in the absence of a continuous change between the two secondary objectives. This research is the basis for a framework that can be used to design a haptic robot with a large workspace, relatively small apparent inertia, superior manipulability, and large enough force feedback.

This chapter makes it possible for a user to exercise better (i.e., more efficient/precise and with higher fidelity) control and navigation of virtual or physical tools being manipulated from haptic interfaces by seamlessly integrating automatic control and task-dependent performance-related cost function optimization. For specific applications in surgery, this is part of a bigger tendency to only delegate the computationally-expensive aspects of robot-assisted intervention to the machine and keep the human operator (i.e., the clinician) in the loop and in charge of completing the main purpose of the intervention [155].

This chapter is organized in sections as follows. Section 6.2 gives preliminaries while a null-space task-dependent controller is developed in Section 6.3. In Section 6.4, experimental results are reported to verify the practicality of the proposed control strategy. Concluding remarks appear in Section 6.5.

6.2 Preliminaries

Consider a redundant haptic interface with its end effector in an m-dimensional Cartesian space, X, and with an n-dimensional vector of joint variables, q. The joints' velocity are transformed to the end effector's velocity through the Jacobian matrix, $J \in \mathbb{R}^{m \times n}$, as

$$\dot{x} = J\dot{q}. \tag{6.1}$$

For an RHI, joint-level control law can be calculated by leveraging the kinematic redundancy of the RHI through the null-space control as [74]

$$\tau = \tau_m + \tau_N, \tag{6.2}$$

where τ_N is the null-space controller defined as

$$\tau_N = (I - J^T J^{\#^T})\tau_S. \tag{6.3}$$

τ_S is an $n \times 1$ torque vector corresponding to the secondary task in the joint space and does not create any end effector force/torque, I is the $n \times n$ identity matrix, and $J^{\#}$ is the generalized inverse of the Jacobian matrix defined as [75]

$$J^{\#} = M_q^{-1} J^T [J M_q^{-1} J^T]^{-1}, \tag{6.4}$$

in which $M_q \in \mathbb{R}^{n \times n}$ is the joint-space inertia matrix. In equation (6.2), τ_m is the corresponding $n \times 1$ joint control law to a given $m \times 1$ Cartesian space primary task control law, F_m, related by

$$\tau_m = J^T F_m. \tag{6.5}$$

6.3 Joint Space Secondary Objective

A secondary objective can be achieved by using a null-space controller, which works in parallel with the controller for the primary task. The null-space controller projects a suitable vector in the null-space of the RHI's Jacobian matrix. In the gradient projection approach [128], which is utilized here, this vector is selected as the gradient of a desired cost function $\nu(q)$. Conflicts

between the primary-task controller and secondary objectives are handled in an assigned order of priority, i.e., a lower-priority objective is satisfied only in the null space of a higher-priority objective. The null-space control law, τ_S, which realizes a secondary objective is calculated as

$$\tau_S = -\beta \frac{\partial \nu(q)}{\partial q} - K_d \dot{q}, \tag{6.6}$$

where β is a suitable scalar step size and K_d is a damping scalar. With this choice of τ_N, the robot tries to decrease the value of the cost function, $\nu(q)$, while executing a primary time-varying task.

6.3.1 Cost Function Selection

The secondary objective selection is application-driven, i.e., the specific application regulates the requirements of the secondary objective. Manipulability ellipsoid (ME) of a robot, which was first introduced by Yoshikawa [156], indicates the ability to perform motion and exert force along with the different task directions in a given joint configuration. Thus, a secondary objective based on the manipulability ellipsoid can be utilized to resolve the configuration of the RHI for a desired task performance. For this, a desired ME can be defined based on the requirements and direction of the task, and then the configuration of the RHI is altered such that its ME matches the desired one. The Cartesian space Force Manipulability Ellipsoid (FME) for an RHI is defined as $\mathcal{M} = (JJ^T)^{-1}$ because it maps a hyper-sphere in the joint space to an ellipsoid in the Cartesian space:

$$\|\tau\|^2 = \tau^T \tau = \Gamma^T (JJ^T) \Gamma = \Gamma^T \mathcal{M}^{-1} \Gamma \leq 1. \tag{6.7}$$

Here, τ is the joint torque vector, and Γ is an m-dimensional output force/torque vector. It is essential to note that the FME is the inverse of the velocity ME (VME), JJ^T. This means that the direction along which the RHI has the largest force/torque feedback capability is perpendicular to the direction along which the user can move the end-effector of the RHI with minimum joints movement to evoke minimum joint friction and thus distortion to the user's perception.

To be more clear, let us define the reflected joint friction ellipsoid at the end-effector as

$$\|F_q\|^2 = F_q^T F_q = F_x(JJ^T)F_x \leq 1 \tag{6.8}$$

where F_q is the vector of the joint friction torques and F_x is the vector of friction forces/torques reflected at the end-effector. By comparing (6.7) and (6.8), it can be seen that along the direction that the robot has the maximum force capability, the reflected joint friction at the end-effector is also maximum.

In (6.7), the RHI's actuators torque limits are not explicitly taken into account. During interactions between a user and an RHI, it is likely to require large torques in response to an unexpected situation; e.g., contacting with a solid object. Therefore, a more accurate FME can be calculated by scaling the joints torque with $W = \text{diag}(\frac{1}{\mathcal{T}_i})$, where $\mathcal{T}_i$ is the torque limit for the ith joint, i.e., $|\tau_i| \leq \mathcal{T}_i$ [31]. Now, the modified FME is calculated as

$$\hat{\mathcal{M}} = (JWWJ^T)^{-1}. \tag{6.9}$$

The user operates the RHI in two cases, namely, free-space motion and in contact with the environment. For both cases, the user should not feel any distorted perception as the result of the RHI's joints friction. This defines the requirement of low back-drive friction for the RHI. Also, when there is a contact with the environment, the RHI should be able to provide adequate force feedback and stiffness such that the user feels the true large stiffness of an environment. This means that the joints' actuator of the RHI should not be saturated while rendering a stiff environment for the user. Therefore, two situations can be defined for the RHI; the first situation is when the RHI's actuators are far away from saturation, whereas the second situation is when the RHI's actuators are near their saturation levels. For each of these situations, a desired FME needs to be defined to meet the requirements of the task.

In Chapter 3, it is shown that by aligning the minor axis of the FME (major axis of VME) of an RHI along the desired direction of motion, the interference of joints friction of the RHI with the user's perception of the environment stiffness is minimized. In another work, the major axis of the

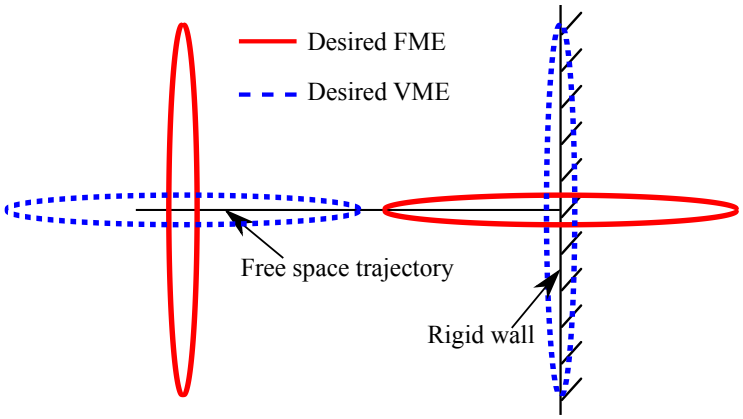

Figure 6.2: Desired FME and VME for a planar task. The principal axes of the FME coincide with that of the VME with the inverse dimension of length.

FME of a redundant robot is aligned with the desired direction to maximize the force output capability of the robot by avoiding joints actuator saturation [5]. Therefore, for the first situation in which the RHI's actuators are far from their saturation levels (i.e., free-space movement and soft-tissue contact), we propose to design the desired FME such that its minor axis is aligned with the direction of the movement or contact to minimize the effect of joints friction. For the second situation (hard contacts), the major axis of the proposed desired FME is aligned with the direction of the contact to maximize the force feedback capability of the RHI. To illustrate this, let us consider a planar task in which the user moves the end effector of the RHI along a straight path in free-space and hits a rigid virtual wall at the end of the path. Assume that rendering the rigid virtual wall would put the RHI's actuators near their saturation levels. The desired FMEs are depicted in Fig. 6.2. Although in theory an ideal desired FME is a line, such an FME will take the RHI to a singular configuration, which is undesirable. Therefore, the minor axis of the FME should be designed small but not zero.

Here, we employ a geometry-aware cost function for the secondary objective to match the FME of the RHI to the desired FME. The cost function, ν, is defined as

$$\nu = \text{logdet}(\frac{\hat{\mathcal{M}} + \mathcal{M}^{des}}{2}) - \frac{1}{2}\text{logdet}(\hat{\mathcal{M}}\mathcal{M}^{des}) \tag{6.10}$$

in which $\mathcal{M}^{des}$ is the desired FME. The force manipulability ellipsoid is a sym-

metric positive definite matrix. Introduced by Cherian *et al.* [29], (6.10) forms a distance function for symmetric positive definite matrices that is convex [132]. It has been shown that this function and its derivative are computationally less expensive than classical Riemannian distance functions. Also, Rozo *et al.* [116] have employed this distance function for matching the velocity manipulability of a redundant robot to a desired one. They have also shown that the convergence rate of this distance function is much faster than the maximization of the major-axis alignment method used in [5]. Thus, (6.10) has been employed in this work to match the FME of the RHI to the desired one based on the requirements of a given task.

Using the symmetric positive definiteness property of the desired manipulability ellipsoid, it can be calculated as $\mathcal{M}^{des} = \mathcal{J}\mathcal{J}^T$, where $\mathcal{J}$ is an $m \times n$ matrix. Matrix $\mathcal{J}$ can be decomposed using singular value decomposition as $\mathcal{J} = U\Sigma\Omega^T$, where U is an unitary $m \times m$ matrix, Σ is a diagonal $m \times n$ matrix and Ω is an unitary $n \times n$ matrix. Thus, the desired FME can be written as

$$\mathcal{M}^{des} = U\Sigma\Omega^T\Omega\Sigma^T U^T = U\Sigma\Sigma^T U^T = U\Lambda U^T. \tag{6.11}$$

Here, U can be regarded as the rotation matrix, which indicates the direction of the principal axes of the FME, and the diagonal elements of the Λ matrix determine the length of the principal axes. More details on the selection of U and Λ matrices are given below.

First, let us consider a situation in which the RHI's actuators are far away from saturation levels. As stated before, to reduce the reflected joints friction at the end-effector of the RHI and consequently minimize the distortion caused by RHI on the user's perception of the environment, the minor axis of the FME needs to be aligned along the direction of motion. If $u_F \in \mathbb{R}^m$ is the unit vector corresponding to the direction of motion, the desired FME for this situation is defined as

$$\mathcal{M}^{des}_{Free} = U_F \underbrace{\left[\begin{bmatrix} \zeta \\ 0_{(m-1)\times 1} \end{bmatrix}_{m\times 1}, \quad \begin{bmatrix} 0_{1\times(m-1)} \\ \mathcal{K} I_{(m-1)} \end{bmatrix}_{m\times(m-1)}\right]}_{\Lambda_{Free}} U_F^T \tag{6.12}$$

where U_F is calculated from singular value decomposition (SVD) of u_F as $u_F = U_F\Sigma_F V_F^T$. Parameters ζ and $\mathcal{K}$ are the constant scalar scaling factors

that determine the length of the minor axis and the major axes of the desired FME, respectively. It appears that $\mathcal{K}$ should be equal to infinity and ζ should be equal to zero for best results. However, with these values, the RHI would be put into a singular configuration, which is undesirables. Therefore, $\mathcal{K}$ and ζ are proposed as $\mu\lambda_{max}\{\hat{\mathcal{M}}_0\}$ and $\frac{1}{\mu}\lambda_{min}\{\hat{\mathcal{M}}_0\}$, respectively. Here, $\lambda_{max}\{\hat{\mathcal{M}}_0\}$ is the maximum eigenvalue and $\lambda_{min}\{\hat{\mathcal{M}}_0\}$ is the minimum eigenvalue of the FME of the RHI at the non-singular home configuration. The home configuration is created by a particular set of joint positions of the RHI where the robot goes to when it is powered on. Therefore, ζ and $\mathcal{K}$ are unique and constant for each RHI. Also, μ is an appropriately selected scaling factor to shape the desired FME. It should be noted that ζ and $\mathcal{K}$ parameters are constant, and these two parameters are set prior to the experiments to shape the desired FME. In our experience, this selection of $\mathcal{K}$ and ζ assures that the null space controller puts the configuration of the RHI far away from the singularity while achieving the desired performance.

Now, consider the situation in which the RHI's actuators are near their saturation levels and the environment force, F_e, is presented to the user through the RHI. For this situation, the desired FME is calculated as

$$\mathcal{M}^{des}_{Stiff} = U_e \underbrace{\left[\begin{bmatrix}\mathcal{K}\\ 0_{(m-1)\times 1}\end{bmatrix}_{m\times 1}, \quad \begin{bmatrix}0_{1\times(m-1)}\\ \zeta I_{(m-1)}\end{bmatrix}_{m\times(m-1)}\right]}_{\Lambda_{Stiff}} U_e^T. \tag{6.13}$$

This ellipsoid is spanned using the SVD of the environment force vector as $F_e = U_e\Sigma_e V_e^T$. By using (6.13), the major axis of $\mathcal{M}^{des}_{Stiff}$ is aligned with direction of the environment force.

Example

To elaborate the concept, consider a 3 DoF planar RHI with the links length $L_i = [0.25,\ 0.25,\ 0.25]$ m, $i = 1, 2, 3$. The link masses are equal to 0.5 Kg for all links and assumed to be located at the center of mass of each link, i.e., the middle point of each link. The joint torques bounds are given as $|\mathcal{T}_i| \leq 0.5$ N.m, and thus the FME scaling matrix is calculated as $W = \text{diag}\{2,\ \ 2,\ \ 2\}$. At the initial configuration of $q_i = [\frac{\pi}{6},\ -\frac{\pi}{3},\ -\frac{3\pi}{4}]$ rad, the RHI is supposed to provide

force feedback to the user when he/she holds the end-effector of the RHI fixed in the task space. The desired force is $F_e = [3.5\sin(t\pi/2),\ 0]^T$ N, where t is time. Thus, the joint space control law corresponding to this desired force is $\tau_m = J^T F_e$. For this example, the FME of the 3-DoF RHI is matched with the desired FMEs using the cost function (6.10). Fig. 6.3 shows the torques of the RHI joints and the output force feedback of the RHI at three different configurations: the initial configuration, the optimized configuration matching the FME of the RHI to $\mathcal{M}^{des}_{Free} = \text{diag}\{.2 \times 2.6,\ 5 \times 5.8\}$, and the optimized configuration matching the RHI's FME to $\mathcal{M}^{des}_{Stiff} = \text{diag}\{5 \times 5.8,\ .2 \times 2.6\}$, (assuming $\mu = 5$).

To preserve the force feedback direction for the above simulation studies, a scaling factor α is implemented to scale the desired force feedback as soon as one of the RHI's actuators is saturated. By matching the RHI's FME with $\mathcal{M}^{des}_{Free}$, the force feedback capability of the RHI is decreased in return for better manipulability in the desired direction for the free-space movement and soft-tissue manipulation. On the other hand, when the FME of the RHI is matched with $\mathcal{M}^{des}_{Stiff}$, the force feedback capability of the RHI is enhanced and the desired force feedback is rendered without any saturation for the joint's actuators. Fig. 6.4 illustrates the initial configuration of the RHI, the optimized configurations of the RHI for the free motion and soft contact (matching its FME to $\mathcal{M}^{des}_{Free}$) and its optimized configuration for the hard contacts (matching its FME to$\mathcal{M}^{des}_{Stiff}$), and the FMEs.

6.3.2 Actuator Saturation Controller

As can be seen in Fig. 6.2, the desired FME remains constant in the free-space motion and soft-tissue manipulation, and the minor axis of the FME is aligned with the trajectory, but for the case of stiff contact the desired FME is transformed in such a way that the major axis of the FME is aligned with the contact direction. Therefore, a smooth transition between the desired FMEs is required; otherwise, fast reconfiguration of the internal motion of RHI would happen which may cause RHI's internal motion instability, RHI self-collision, and/ or RHI collision with the user.

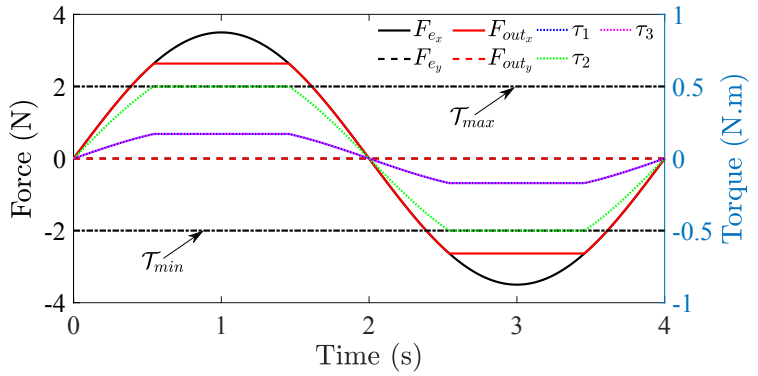

(a)

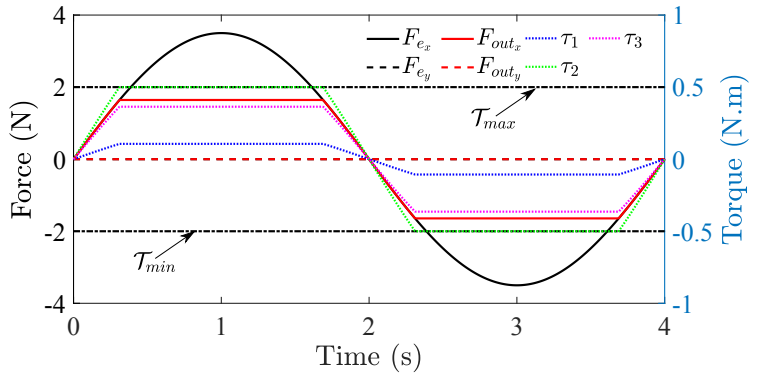

(b)

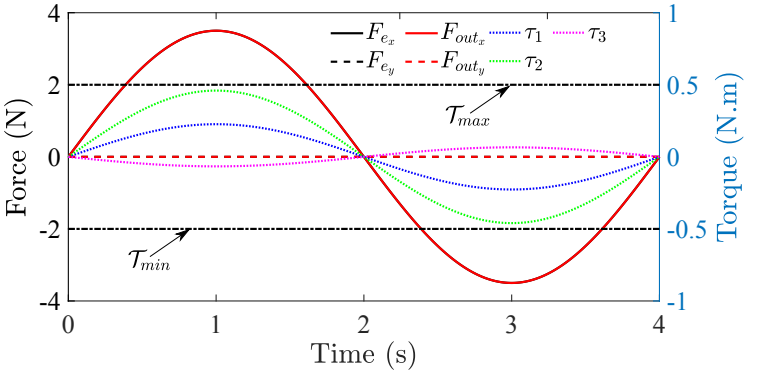

(c)

Figure 6.3: Joint torques and output force feedback of a 3-DoF RHI at (a) initial configuration, (b) optimized configuration by matching its FME to $\mathcal{M}^{des}_{Free}$, and (c) optimized configuration by matching its FME to $\mathcal{M}^{des}_{Stiff}$.

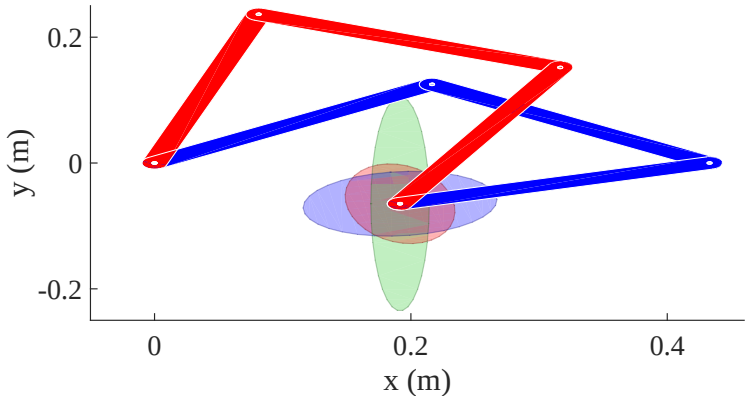

(a)

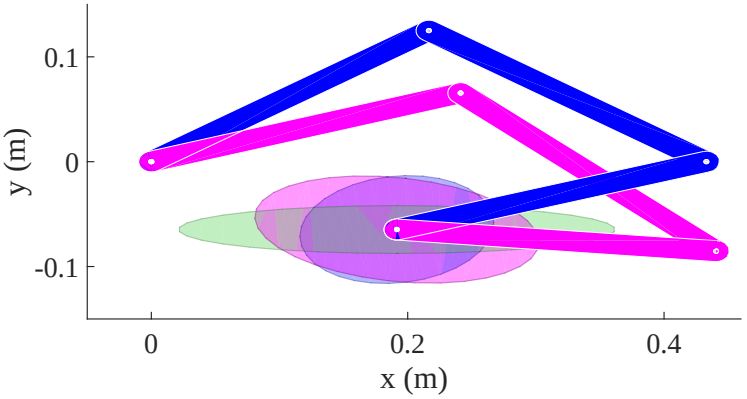

(b)

Figure 6.4: RHI's initial configuration and initial FME in blue, the desired FMEs in green, (a) RHI's optimized configuration and FME for free-space movement and soft contact in red, and (b) RHI's optimized configuration and FME for hard contact in magenta. The FMEs are scaled for better visualization.

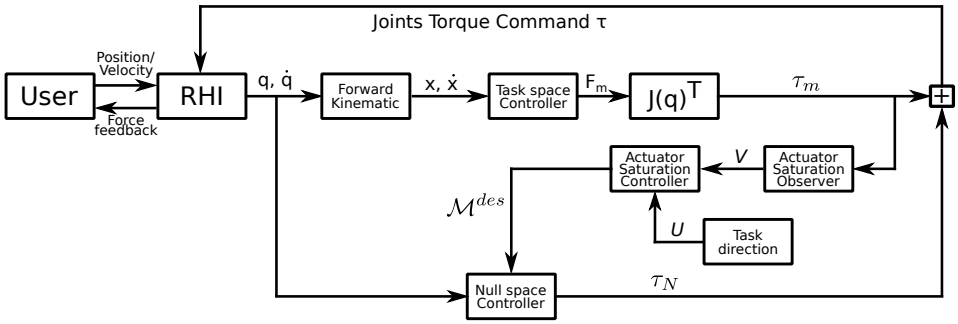

Figure 6.5: Block diagram of the control system.

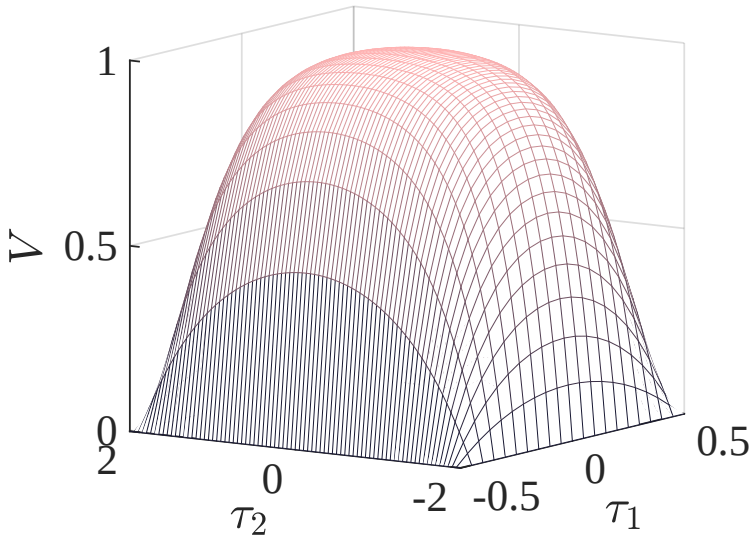

Figure 6.6: The ASO for a two-DoF robot with $s = 50$.

Here, the actuator saturation observer (ASO) is proposed to monitor the distance of the RHI's joint actuators torque from their saturation levels. Inspired by the work in [44], the ASO can be considered as the volume of a tank of actuators' unused torque output capacity. When a task demands large actuator torques, this tank is used and can become empty over time. The volume of the tank is zero when one or more of the robot's actuators are saturated; even when only one actuator is saturated, the RHI loses the ability to apply *arbitrary* force vectors at its end-effector. The ASO informs the actuator saturation controller to switch between the desired FMEs (i.e., from the desired free-space FME to the desired stiff-contact FME) to keep the actuators away from their saturation limits. The volume of the tank is defined as

$$V = \frac{1 - \exp(-S(-1)^n \prod_{i=1}^{n} \frac{(\tau_{m,i} - \mathcal{T}_{max,i})(\tau_{m,i} - \mathcal{T}_{min,i})}{(\mathcal{T}_{max,i} - \mathcal{T}_{min,i})^2})}{1 - \exp(-\frac{S}{4^n})}, \tag{6.14}$$

where n denotes the number of joints of the RHI, S is the scaling factor that determines the shape and thus the gradient of the ASO, and V is a scalar that spans the $[0, 1]$ interval. The ASO for a two-DoF robot, that has joint torques bounds $|\mathcal{T}_1| \leq 0.5$ N.m and $|\mathcal{T}_2| \leq 2$ N.m is depicted in Fig. 6.6. The ASO can be used for both redundant and non-redundant robots to determine how far the robot's actuators are from their saturation levels.

Now, the actuator saturation controller selects the desired FME for the secondary objective based on the ASO as

$$\hat{\mathcal{M}}^{des} = \begin{cases} M^{des}_{Free}, & \text{if } V \geq \epsilon \\ M^{des}_{Stiff}, & \text{if } V < \epsilon \end{cases} \tag{6.15}$$

where ϵ is a threshold that determines how far from the saturation of RHI's actuator the transition happens between the FMEs.

Let us now look at the case where the transition between the desired FMEs is required. The transition among the desired FMEs occurs when there is a change in the primary task in the Cartesian space. As highlighted in Fig. 6.2, the transition for the FME happens when one or more of the RHI's joints actuator come close to their saturation levels. To ensure continuity with respect to time for the transition from a desired FME to another one, a continuous activation parameter Ω with the value between zero and one is required [78], [82]. Here, the desired FME for (6.10) is proposed to be calculated as the composition of two FMEs as

$$\mathcal{M}^{des} = \Omega M^{des}_{Free} + (1 - \Omega) M^{des}_{Stiff}. \tag{6.16}$$

It should be noted that the RHI has dynamics. Therefore, if the change in the primary task in the Cartesian space happens very fast, the transition between the desired FMEs may not be fulfilled. In this case, the RHI's joints actuator may be saturated, and thus the primary task could not be achieved.

Two instances need to be considered; the time of transition from M^{des}_{Free} to M^{des}_{Stiff} and vice versa. For the first case, the activation parameter is defined as

$$\Omega = \begin{cases} 1, & \text{if } V \geq \epsilon_1 \\ 0.5(1 + \cos(\pi \frac{t - t_0}{t_f - t_0})), & \text{if } V < \epsilon_1 \text{ and } t < t_f \\ 0, & \text{if } t \geq t_f \end{cases} \tag{6.17}$$

and for the second case, Ω is defined as

$$\Omega = \begin{cases} 0, & \text{if } V < \epsilon_2 \\ 0.5(1 - \cos(\pi \frac{t - t_0}{t_f - t_0})), & \text{if } V \geq \epsilon_2 \text{ and } t < t_f \\ 1, & \text{if } t \geq t_f \end{cases} \tag{6.18}$$

Here, t_0 and t_f represent the start and end time of the transition, respectively. ϵ_1 and ϵ_2 are appropriately designed thresholds. If only one ϵ is defined as

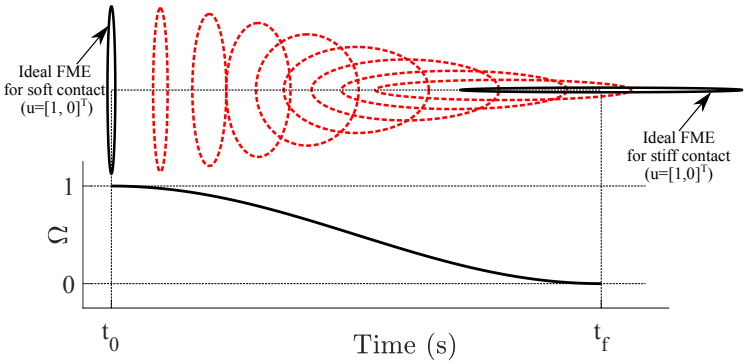

Figure 6.7: (top) Transition between two FMEs which are shown in black ellipsoids and (bottom) Activation parameter Ω.

a threshold for the transition between the FMEs, chattering can happen. In other words, slightly falling short of ϵ will cause a switch from $\mathcal{M}^{des}_{Free}$ to $\mathcal{M}^{des}_{Stiff}$ and slightly exceeding ϵ will cause a switch from $\mathcal{M}^{des}_{Stiff}$ to $\mathcal{M}^{des}_{Free}$. To avoid this, two separate thresholds (ϵ_1 and ϵ_2) are defined. The activation parameter and the transition between two FMEs are depicted in Fig. 6.7. The transition end time, t_f, defines how fast the transition is performed and it is obtained as a function of distance between the desired FMEs:

$$t_f = \rho \left\| M^{des}_{Free} - M^{des}_{Stiff} \right\|_F + t_0, \tag{6.19}$$

in which ρ is a suitable scaling factor and $\|.\|_F$ is the Frobenius norm. A block diagram of the control system is depicted in Fig. 6.5.

6.4 Experimental Evaluation

In this section, experiments are performed to evaluate the proposed null space controller using a 4-DoF planar RHI. This RHI is made by coupling two 2-DoF HIs; a 2-DOF planar upper-limb rehabilitation robot (Quanser Inc., Markham, ON, Canada) and a 2-DoF PHANToM 1.5A (3D Systems Inc., Morrisville, NC, USA). Also, a force/torque sensor (50M31A3-I25, JR3 Inc., Woodland, CA, USA) is attached to the end-effector of the RHI to measure forces that are feedback to the user. MATLAB/Simulink (MathWorks Inc., Natick, MA, USA) with Quarc real-time control software (Quanser Inc., Markham, ON, Canada) is used to interface the RHI and the force sensor with the computer.

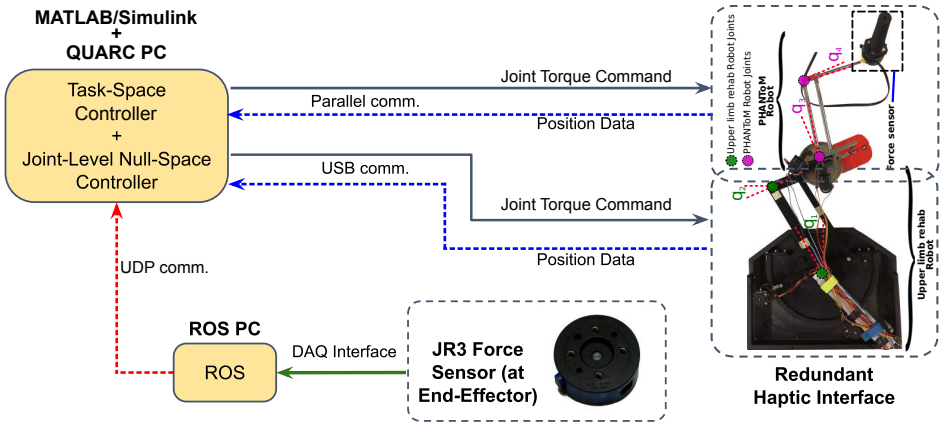

Figure 6.8: Experimental setup.

Fig. 6.8 shows the experimental setup.

For the purpose of this experiment, the RHI has joint torques limitation programmed as $\mathcal{T}_i = [3,\ 3,\ 1,\ 1]$ N.m. The Jacobian matrix of the RHI is

$$J_{_{RHI}} = \begin{bmatrix} -d_1 sq_1, & d_2 cq_2 - d_3 sq_{23} + d_4 cq_{24}, & -d_3 sq_{23}, & d_4 cq_{24} \\ d_1 cq_1, & d_2 sq_2 + d_3 cq_{23} + d_4 sq_{24}, & d_3 cq_{23}, & d_4 sq_{24} \end{bmatrix} \tag{6.20}$$

where s and c denote $sin(.)$ and $cos(.)$, respectively. $q_{ij} = q_i + q_j$ and $d_i = [0.254,\ 0.141,\ 0.21,\ 0.181]$ m, $i = 1, 2, 3, 4$, denotes the RHI's links length. Also, parameters μ, β, and K_d are selected equal to 5, 20, and 0.1, respectively. The home configuration of the RHI is defined as $q_i = [0,\ 0,\ 0,\ 0]$. Thus, $\mathcal{K}$ and ζ are calculated as 123 and 3.3, respectively.

In the experiments, a user holds the end effector of the RHI and palpates a virtual environment along the right-hand direction (i.e., $u = [0,\ 1]^T$) through it. The virtual environment is modelled as a spring with constant stiffness. In the experiments, the user palpates the virtual environment starting from a fixed point in the workspace of the RHI. The starting point is given as $X_0 = [0.5,\ 0.1]^T$ m. The Cartesian space control law used in the experiments is

$$F_m = K_e \delta X \tag{6.21}$$

where K_e is the stiffness of the virtual environment and δX is the position deviation from the starting point. The virtual environment is modelled as $K_e = 1000$ N/m to create a stiff environment.

To show the effectiveness of the proposed methods, the experiments are

carried out in two scenarios. The objective of the first scenario is to show the enhanced force feedback capability of the RHI by using the proposed null-space controller and matching the FME of the RHI with the desired FME. As stated before, a single desired FME for the secondary objective cannot be used due to the conflicting requirements of having large force feedback capability for the hard contact case and having large velocity manipulability for the free motion and soft contact case. Therefore, in the second scenario, the proposed transition method between the desired FMEs is evaluated.

Two cases are considered for the first scenario. (A) The palpation is performed on the environment through the RHI with matching the FME of the RHI with the desired FME, $\hat{\mathcal{M}}^{des}$, with $\epsilon = 0$, i.e., the desired FME is $\mathcal{M}^{des}_{Free}$. (B) The palpation is performed with FME matching with $\epsilon = 1$, i.e., the desired FME is $\mathcal{M}^{des}_{Stiff}$. In ($A$), the force feedback scaling is performed when one or more joints actuator of the RHI are saturated to preserve the direction of the force feedback, and the minor axis of the desired FME is aligned with the direction of motion (contact). For this case, the desired FME is $\hat{\mathcal{M}}^{des} = \mathcal{M}^{des}_{Free} = \text{diag}\{123,\ 3.3\}$. In ($B$), the major axis of the desired FME is always aligned with the direction of motion (contact), and it is calculated using (6.13) as $\hat{\mathcal{M}}^{des} = \mathcal{M}^{des}_{Stiff} = \text{diag}\{3.3,\ 123\}$.

Fig. 6.9 shows the experimental results for the first scenario. In this figure, the measured force using the force/torque sensor, the desired force ($K_e \times \delta X$), and the torque of the actuators are illustrated. As it can be seen in this figure, the maximum force feedback of the RHI in case (B) (Fig. 6.9(b)) is 51% more than the force feedback capability of the RHI in case (A) (Fig. 6.9(a)). As a result, the user feels the environment more stiff in case (B). This shows that the force feedback capability of the RHI is enhanced by leveraging the kinematic redundancy before the occurrence of joints' actuator saturation.

Thus far, it is shown that the force feedback capability of the RHI when its FME is matched with $\mathcal{M}^{des}_{Stiff}$ using the null-space controller is larger than that of the RHI when its FME is matched with $\mathcal{M}^{des}_{Free}$. Here, system identification experiments are performed to show that the back-drive friction and the Cartesian-space inertia of the RHI in case (A) are lower that of the RHI in

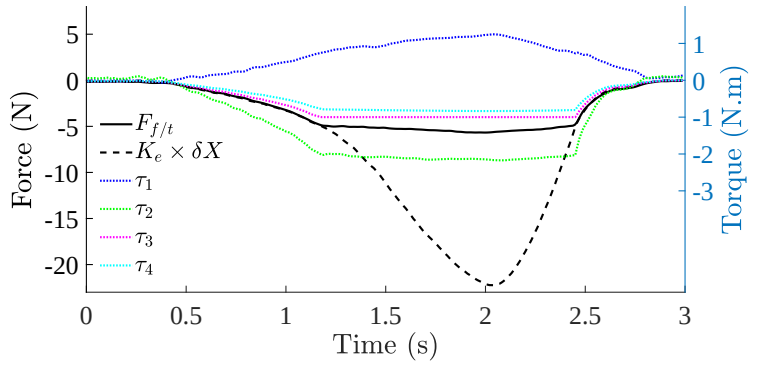

(a)

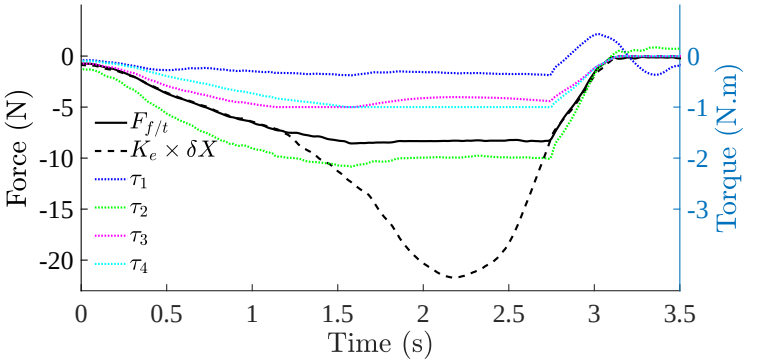

(b)

Figure 6.9: Experimental results at the optimized configuration by matching the RHI's FME to (a) $\mathcal{M}_F^{des}$ and (b) $\mathcal{M}_C^{des}$.

Table 6.1: Experimental values for inertia M_x, friction parameter Φ, and maximum force feedback capability of the planar 4-DoF RHI along $u = [0,\ 1]^T$ for the end-effector position $[0.5,\ 0.1]$ m.

Desired FME	M_x (Kg)	Φ (N.s/m)	F_{max} (N)
$\mathcal{M}^{des}_{Free}$	0.036	0.2953	-5.674
$\mathcal{M}^{des}_{Stiff}$	0.125	0.6325	-8.564

case (B). To identify the back-drive friction and the Cartesian-space inertia of the RHI, its end-effector dynamics is modelled for simplicity as

$$M_x\ddot{X} + F_f = F_{ext}, \tag{6.22}$$

where M_x is the Cartesian-space inertia, F_f is the back-drive friction force, F_{ext} is the external force applied to the end-effector of the RHI, and X is the position of the end-effector. X, M_x, F_f, and F_{ext} are scalars as the experiments are performed along one axis (i.e., along $u = [0,\ 1]^T$). Also, the back-drive friction is modelled as the viscose friction $F_f = \Phi\dot{X}$, where Φ is the friction parameter.

System identification experiments are carried out for two cases: the configuration of the RHI being determined by matching its FME with $\mathcal{M}^{des}_{Stiff}$ and with $\mathcal{M}^{des}_{Free}$. Ten trials are conducted for each case to identify M_x and Φ. In each trial, first, the end-effector of the RHI is placed at $[0.5,\ 0.05]^T$ m. Next, a constant external force in the range of $0.5-1.5$ N is applied to the end-effector of the RHI, and the position along $u = [0,\ 1]^T$, velocity, and acceleration of the end-effector are measured at $[0.5,\ 0.1]^T$ m point. The end-effector is placed 5 cm away from the point of interest to eliminate the effects of Coulomb friction in the experiments. The measured signals are filtered using a zero-phase 5^{th}-order Butterworth lowpass filter. Then, M_x and Φ are identified by applying the linear least-squares regression to (6.22). The experimental results for the Cartesian-space inertia and the back-drive friction, as well as the maximum force feedback capability, are listed in Table 6.1.

Table 6.1 shows that for the same end-effector position of RHI, the inertia, back-drive friction, and force feedback capability are lower for the configuration being determined by the desired FME for the free space $\mathcal{M}^{des}_{Free}$. Having low

inertia and back-drive friction is desirable for the free-space movement and soft contact, which leads to the smaller sensation of RHI's linkage and joint friction. However, large force feedback capability is required to recreate a stiff environment for the user. Therefore, for the stiff environment, the desired FME should be set as $\mathcal{M}^{des}_{Stiff}$ to achieve larger force feedback capability at the price of larger inertia and friction.

As the experiment for this scenario was conducted for a given starting point at the workspace, a simulational study was performed to show the force feedback enhancement across the entire workspace. The same four-DoF RHI that was used in the experiment is employed in the simulational study. For each point of the RHI's workspace, the maximum force feedback capability along $u = [0,\ 1]^T$ is calculated for two cases: Case (I) the manipulability of the RHI is matched with $\mathcal{M}^{des}_{Free} = \text{diag}\{123,\ 3.3\}$ (minimize the effect of joints friction at the end-effector), and Case (II) the manipulability of the RHI is matched with $\mathcal{M}^{des}_{Stiff} = \text{diag}\{3.3,\ 123\}$ (maximize the force feedback capability of the robot). The simulational results are shown in Fig. 6.10. As the result of the study shows, over the entire workspace, the force feedback capability of the RHI with the joints configuration being determined by matching its FME with $\mathcal{M}^{des}_{Stiff}$ is considerably larger than the force feedback capability of the RHI with its joints configuration being determined by matching its FME with $\mathcal{M}^{des}_{Free}$ at the same end-effector location.

In the second scenario, the performance of the proposed transition method between the secondary objectives in terms of preventing the discontinuity in null-space control effort is evaluated. The palpation task is performed (C) with and (C') without the proposed transition method. The parameter ϵ_1 that determines when the transition from $\mathcal{M}^{des}_{Free} = \text{diag}\{123,\ 3.3\}$ to $\mathcal{M}^{des}_{Stiff} = \text{diag}\{3.3,\ 123\}$ occurs is selected equal to 0.7 and the parameter ϵ_2 that regulate the switching from $\mathcal{M}^{des}_{Stiff}$ to $\mathcal{M}^{des}_{Free}$ is selected equal to 0.95. For the (C) case, the desired FME is calculated form (6.15) and for the (C') case, the desired FME is calculated using (6.16). Parameter ρ is selected equal to 0.003 so that the transition performed in 0.5 second.

In Figs. 6.11(a) and 6.11(b) the comparison between the behaviour of the

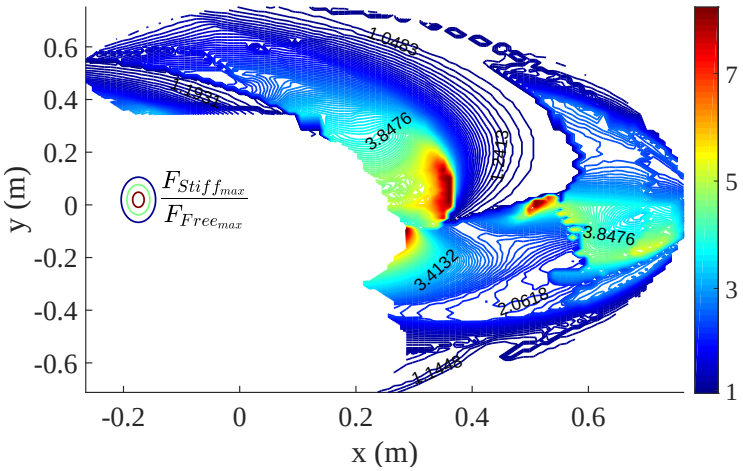

Figure 6.10: The ratio of maximum force feedback capability of the four-DoF RHI with the configuration being determined by matching its FME to $\mathcal{M}_F^{des}$ and $\mathcal{M}_C^{des}$ over the entire workspace.

RHI without and with the proposed transition method are shown, respectively. As it can be seen in Fig. 6.11(a), discontinuity in the control effort causes the interference of RHI's internal motion with the motion and force of the RHI's end-effector when the desired FME is switched suddenly from $\mathcal{M}_{Free}^{des}$ to $\mathcal{M}_{Stiff}^{des}$. However, by using the proposed method, the transition between the desired FMEs is carried out smoothly (see Fig. 6.11(b)). For the (C') case, the ASO and the activation parameter are illustrated in Fig. 6.11(c). As can be seen in this figure, the transition starts when the ASO (volume of the tank) becomes smaller than 0.7. The transition slows down the drainage of the tank, which keeps the actuators away from their saturation levels. Therefore, the RHI can provide large force feedback.

6.5 Concluding Remarks

In this chapter, we proposed a null-space controller for redundant haptic interfaces. The objective was to enable a user to experience believable interactions with an environment, be it free space, soft contact, or hard contact. The proposed null-space controller leverages the kinematic redundancy of the RHI toward secondary objectives to optimize the interaction of the user with the environment. Two secondary objectives based on the task requirements were

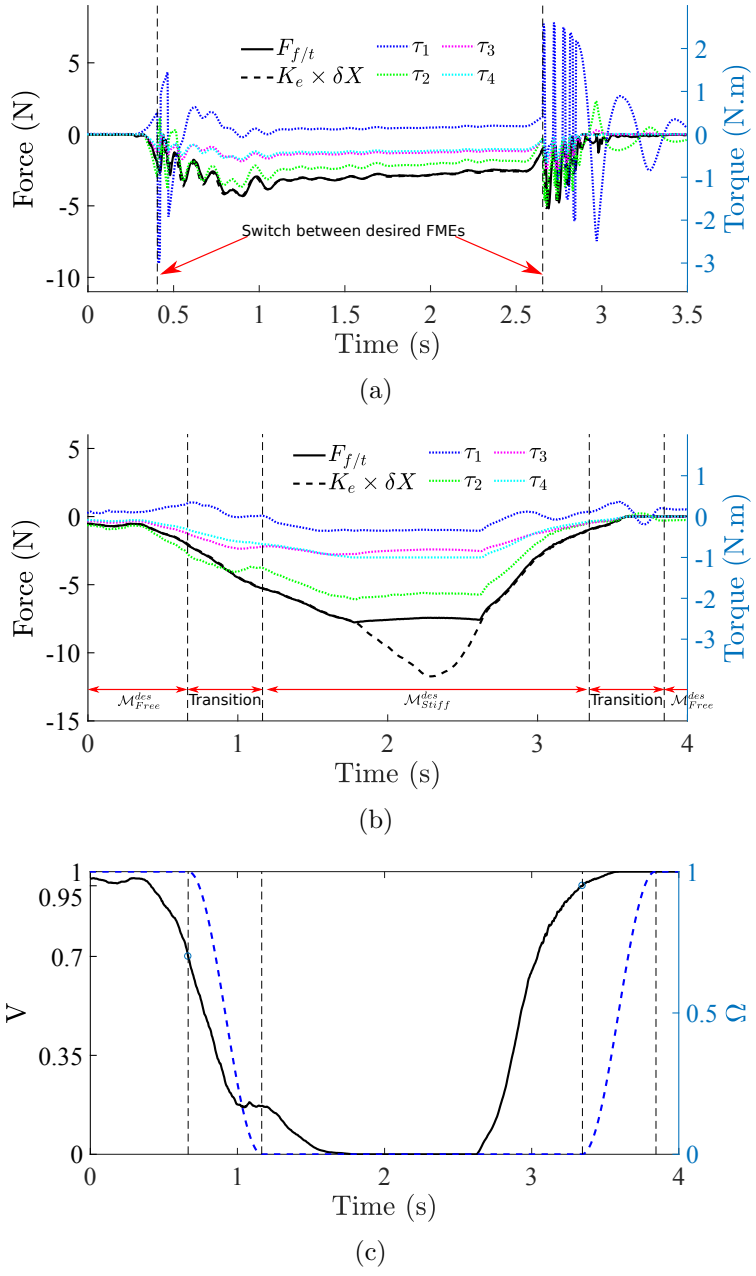

Figure 6.11: Experimental results (a) without and (b) with the proposed transition method between the desired FMEs. (c) The ASO (volume of the tank) V in solid black line and activation parameter ω in dashed blue line when the transition method is utilized.

proposed in this chapter. Also, a transition method based on the actuator saturation observer was proposed to prevent discontinuity of the control effort when switching between the secondary objectives was required. The actuator saturation observer monitors the distance between the actuators torque and their saturation levels. When the RHI's actuators are far away from their saturation levels, an appropriate secondary objective is active and manipulates the internal motion of the RHI to increase its velocity manipulability, and consequently decrease the interference of the friction forces and kinematics of the RHI with the user-environment interaction. This secondary objective is replaced with another secondary objective when the RHI's actuators become close to their saturation levels, which can happen when rendering hard contacts. It was shown that the RHI's force feedback capability is configuration dependable, and by appropriately manipulating the internal motion of the RHI, it can be enhanced. The experiments showed 51% enhancement in the force feedback capability of the RHI using the proposed methods. Also, experiments showed the practicality of the proposed transition method by preventing the discontinuity in the control effort for the RHI.

Chapter 7

Actuator Saturation Compensation of Redundant Haptic Interfaces for Improving Force Feedback Capability[1]

7.1 Introduction

In this chapter, an Actuator Saturation Compensation Method (ASCM) is proposed as a secondary objective in the null space of an RHI. This method enhances the force feedback capability of the RHI by leveraging the kinematic redundancy of the haptic interface and distributing the overloaded actuator's torque among the available unsaturated actuators. This method handles the joint torque bounds of the RHI by successively relieving the joints that exceed their limits when providing force feedback for the user (primary objective). The ASCM addresses the RHI's limitations due to its effective distribution of a desired end-effector Cartesian wrench to joints torque.

The ASCM distributes torque among the RHI's actuators as much as possible via the null-space of the RHI until the desired force feedback is not feasible for the RHI. Then, a scaling factor less than unity will be incorporated to downscale the desired force feedback. Furthermore, if after resolving

[1]A version of this chapter has been presented as Ali Torabi, Kourosh Zareinia, Garnette Sutherland, and Mahdi Tavakoli, "Redundant Haptic Interfaces for Enhanced Force Feedback Capability Despite Joint Torque Limits," IEEE/ASME International Conference on Advanced Intelligent Mechatronics, Boston, USA, 2020.

all of the actuator limits, the RHI has any redundancy left, a tertiary objective will be achieved in the null-space of the robotic system to enhance the RHI manipulability.

We discuss how appropriately manipulating an RHI's extra DoFs in joint-level control can enhance its force feedback capability and deal with saturation for small-capacity actuators that bring advantages such as low rotor inertia and friction. This is an effective way to address the trade-offs between the conflicting requirements of a haptic interface, e.g., having large force feedback capability to transparently recreate contact with stiff environments while having low apparent inertia and friction for transparently recreating the feeling of moving in free space. By employing the proposed method, a redundant haptic interface is able to generate larger force feedback with relatively smaller actuators. This feature, in addition to the potential to achieve a tertiary objective, motivates the widespread deployment and utilization of redundant haptic interfaces in the teleoperation context.

Although our proposed methods can be expanded for kinematically redundant parallel robots, here, we only considered the kinematically redundant serial robots. The main advantage of serial robots over parallel robots is their relatively larger workspace with a small footprint. However, parallel robots have relatively larger force feedback capability than serial robots. Our proposed approach tries to secure the best of both worlds (i.e., serial and parallel haptic interfaces) by appropriate control of the null-space of kinematically redundant serial haptic interfaces. This will result in having a haptic interface with a large workspace and a force feedback capability. At the same time, smaller actuators that have lower rotor inertia and friction can be utilized in the design of a haptic interface that results in the smaller reflected inertia and friction at its end-effector.

In Section 7.2, a task-space impedance control as the primary task is developed, which is to reflect force feedback to the user. As the RHI's actuators have limited capacity, for the case of hard contact, the actuators might become saturated. In this case, the secondary objective, i.e., ASCM, will be activated in order to distribute the overloaded actuators' torque among the available

unsaturated actuators. In Section 7.3, the actuator saturation compensation method in the null space of the RHI is proposed. Then, if the system has remaining redundancy after the primary task and the secondary objective are fulfilled, the manipulability of the manipulator can be enhanced along the direction of the task via the tertiary control objective, which is developed in Section 7.4. In Section 7.5, the experimental results are reported to verify the practicality of the proposed control strategy. Concluding remarks appear in Section 7.6.

Assumption: The underlying assumption in this chapter is that the RHI's joints are not at the physical range limit and thus, the end-effector of the RHI is not at the boundary of the workspace. This is because of the fact that when a joint is at its physical limit, the torque saturation level for the joint will be changed from its maximum/minimum level to $\pm\infty$.

7.2 Cartesian Space Primary Task Control: End-Effector Impedance Control

Consider a redundant haptic interface in an m-dimensional Cartesian space X with an n-dimensional vector of joint variables q whose task space dynamics can be represented as

$$M_x\ddot{X} + C_x\dot{X} + G_x + F_x = F_m + F_h \tag{7.1}$$

where $M_x = (JM_q^{-1}J^T)^{-1}$ is the $m \times m$ end-effector inertia matrix or apparent inertia, $C_x = M_x(JM_q^{-1}C_q - \dot{J})J^{\#}$ is the $m \times m$ end-effector's centrifugal and Coriolis forces/torques (wrench) matrix. G_x and F_x are $m \times 1$ vectors of gravitational and friction wrench, respectively, reflected at the end-effector. $J \in \mathbb{R}^{m\times n}$ is the Jacobian matrix and $J^{\#}$ is the generalized inverse of it, defined as $J^{\#} = M_q^{-1}J^T[JM_q^{-1}J^T]^{-1}$ [75]. $F_m = J^{\#^T}\tau_m$ is the $m\times 1$ Cartesian-space control wrench vector in which τ_m is the $n \times 1$ joint-level control wrench vector. F_h is the wrench applied by the user's hand on the haptic interface. $M_q(q) \in \mathbb{R}^{n\times n}$ and $C_q(q, \dot{q}) \in \mathbb{R}^{n\times n}$ are joint-level inertia matrix and Coriolis and centrifugal matrix, respectively.

For an RHI, the goal is to generate appropriate control signals, regardless of the operator and environment dynamics, to reflect wrench measured at the environment side (be it virtual or physical) to the operator. Given the end-effector dynamics (7.1), the Cartesian-space control law is designed as

$$F_m = -F_e - B^d\dot{X} + C_x\dot{X} + G_x + F_x \tag{7.2}$$

where F_e is the vector of the wrench, which is applied by the environment, and B^d is the desired damping matrix, which is positive definite.

The control law (7.2) imposes the dynamics of the RHI as

$$M_x\ddot{X} + B^d\dot{X} = F_h - F_e. \tag{7.3}$$

In the RHI's modified dynamics (7.3), the operator can smoothly control the desired position, velocity, and acceleration by applying the appropriate force F_h on the end-effector of the RHI. Since the acceleration and velocity are not too large in common operations, the left side of (7.3) becomes small if the values for the impedance parameters M_x and B^d are sufficiently small. Accordingly, the right side of (7.3) becomes small ($F_h - F_e \rightarrow 0$). Thus, the wrench reflection performance is achieved. If the human operator or the environment applies sudden large forces that generate large acceleration and velocity, the force tracking error at the right side of (7.3) increases. We are aware that by using slightly more complicated Cartesian space control law, the apparent inertia of the RHI can also be altered [49]. However, if the apparent inertia is reduced less than a specific threshold, the RHI becomes unstable because of losing its passivity [37]. Also, for such a control law, the applied wrench by the user F_h on the HI is also required. Therefore the apparent inertia is kept unchanged in this chapter. Also, The HIs are typically designed lightweight and cable-driven, thus, their dynamics have more significant joint friction terms compared to inertia term.

In practice, Cartesian-space control law (7.2) needs to be implemented in the joint-level. Thus, the corresponding joint-level torque control law can be calculated as

$$\tau_m = J^T F_m. \tag{7.4}$$

7.3 Joint-Level Secondary Objective: Actuator Saturation Compensation

A drawback of control law (7.4), which limits its application for the RHIs, is that joint-level torque limits are not explicitly taken into account. The underlying assumption is that the actuators' capabilities are unlimited, or the robot task has been tailored to fit within the interface's capabilities. However, during interactions between a user and an RHI, it is likely to require large instantaneous joints torque in response to an unexpected situation, e.g., contacting with a solid object. In this section, a method for resolving the torque saturation problem in the joint level is proposed.

For an RHI, the joints' torque control law (7.4) can be modified by leveraging the kinematic redundancy of the RHI through the null-space control as [74]

$$\tau = \tau_m + \underbrace{(I - J^T J^{\#^T})\tau_N}_{\text{Null-space controller}}, \tag{7.5}$$

where τ_N is a torque vector corresponding the null space controller in the joint level, and it does not create any end-effector wrench. An appropriately designed τ_N can be used to compensate for the joints' overload in τ_m.

Consider an RHI with the bounds on joint torque as $\mathcal{T}_{min,i} \leq \tau_i \leq \mathcal{T}_{max,i}$, $i = 1 \dots n$. Also, it should be noted that all the joint-level constraints (e.g., velocity and acceleration) should be converted to the joint torque bound. Now, let us consider a case in which the jth joint of the RHI is overloaded, and its corresponding value in τ_m is either larger than $\mathcal{T}_{max,j} > 0$ or smaller than $\mathcal{T}_{min,j} < 0$. The vector τ_N needs to be designed such that it brings back the torque of joint j within the torque bound by distributing the torque among other joints without overloading them. To design τ_N, first, a diagonal selection matrix $\mathcal{S}$ needs to be defined to identify the saturated joints. $\mathcal{S}$ is defined as an $n \times n$ diagonal selection matrix whose diagonal elements specify whether the joints are saturated or not, i.e., if the j element on the $\mathcal{S}$ diagonal is one, the jth joint of the RHI is saturated. Next, τ_s is introduced as the $n \times 1$ saturation torque vector which its jth non-zero element is either equal to $\mathcal{T}_{max,j}$

or $\mathcal{T}_{min,j}$ corresponding to the saturated joint j. Now, the saturated joints can be isolated with the following Jacobian matrix for the isolated system:

$$\hat{J} = J\mathcal{S}, \tag{7.6}$$

where J is the Jacobian matrix of the RHI. For the isolated system, control law (7.5) is rewritten as

$$\tau_s = \hat{J}^T F_m + (I - \hat{J}^T \hat{J}^{\#^T})\tau_N. \tag{7.7}$$

Therefore, τ_N can be calculated as

$$\tau_N = (I_n - \hat{J}^T \hat{J}^{\#^T})^{\#}(\tau_s - \hat{J}^T F_m). \tag{7.8}$$

With this choice of τ_N, the torque of joint j will be adjusted back to its saturation level and the associated torque shortage will be distributed between the other joints. However, this can overload other joints of the RHI. Thus, this method needs to be repeated iteratively until either there is no overloaded actuator left or the Cartesian space primary task is found to be infeasible. One can inspect the feasibility of control law (7.4) for the RHI by checking the rank of $J(I_n - \mathcal{S})$ matrix, i.e., how many joints are not saturated. If the rank of this matrix is smaller than the dimension of the Cartesian space m, the Cartesian space control law F_m is not feasible, and it has to be modified to become realizable for the RHI. In this case, we introduce a scaling factor $0 \leq \alpha \leq 1$ to make control law (7.2) realizable. α is equal to one unless the force feedback F_e is not feasible for the RHI. As a result, the control law (7.2) is modified as

$$\tilde{F}_m = -\alpha F_e + \mu, \tag{7.9}$$

where

$$\mu = -B^d \dot{X} + C_x \dot{X} + G_x + F_x.$$

Accordingly, the joint-level control vector τ_m needs to be modified to $\tau_m = J^T \tilde{F}_m$. The Actuator Saturation Compensation Method (ASCM) calculates the null space control law τ_N, the scaling factor α, and the joint-level control law τ. In this method, first, the most overloaded joint will be identified, and its

torque will be adjusted back to the torque saturation limits. Next, the method will look for the new most overloaded joint, if any, to adjust its torque to within the admissible torque limits. This process will be repeated until either there is no overloaded joint remaining or the rank of $J(I_n - \mathcal{S})$ is smaller than the dimension of the Cartesian space. For the latter case, the scaling factor α will be calculated to scale the force feedback and make the control law (7.5) practical. The actuator saturation compensation method Algorithm 1 shows the required steps for calculating the null space control law τ_N, the scaling factor α, and the joint-level control law τ.

Algorithm 1 Actuator Saturation Compensation Method

$\mathcal{S} = 0_{n\times n}, \quad \alpha = 1, \quad \tau_s = 0_{n\times 1}, \quad limit = 1$
while $limit = 1$ **do**
  $limit = 0$
  $\tau_N = (I_n - \mathcal{S}J^T(J^\#)^T\mathcal{S})^\#(\tau_s - (J\mathcal{S})^T\tilde{F}_m)$
  $\tau = J^T\tilde{F} + (I - J^TJ^{\#^T})\tau_N$
  if For $i = 1 \to n$, $\tau_i > \mathcal{T}_{max,i}$ or $\tau_i < \mathcal{T}_{min,i}$ **then**
    $limit = 1$
    Find the most overloaded joint, k
  end if
  $\tilde{\mathcal{S}} = \mathcal{S}$, $\tilde{\tau}_s = \tau_s$, and $S_{kk} = 1$
  if $\tau_k > \mathcal{T}_{max,k}$ **then**
    $\tau_{s,k} = \mathcal{T}_{max,k}$
  else if $\tau_k < \mathcal{T}_{min,k}$ **then**
    $\tau_{s,k} = \mathcal{T}_{min,k}$
  end if
  if rank$(J(I_n - \mathcal{S})) < m$ **then**
    $\mathcal{S} = \tilde{\mathcal{S}}$ and $\tau_s = \tilde{\tau}_s$
    $N_0 = (I_n - J^T(J^\#)^T)(I_n - SJ^T(J^\#)^TS)^\#$
    $N_1 = (-J^T + N_0(JS)^T)F_e$
    $N_2 = N_0\tau_s + (J^T - N_0(JS)^T)\mu$
    $\alpha = (\mathcal{T}_{max(min),k} - N_{2,k})/N_{1,k}$
    $\tau_N = (I_n - \mathcal{S}J^T(J^\#)^T\mathcal{S})^\#(\tau_s - (J\mathcal{S})^T\tilde{F}_m)$
    $\tau = J^T\tilde{F} + (I - J^TJ^{\#^T})\tau_N$
    Break While
  end if
end while

As stated before, one of the advantages of using an RHI over an NHI is that when some of the actuators are overloaded, ASCM saturates them

and distributes the remaining torque among the other available (unsaturated) actuators while preserving the direction of the force feedback F_e. However, if this is infeasible, the amplitude of the reflected force is adjusted by $0 \leq \alpha \leq 1$. For the NHI, however, the full capacity of each actuator will not be used and the force feedback amplitude will be much smaller than the desired value in compare to an RHI.

To investigate the continuity of the control law (7.5), let us calculate the joints torque vector at time t_0 when the j^{th} joint just became saturated:

$$\tau(t_0) = J^T F_m(t_0). \tag{7.10}$$

Now, at time t_0+T_s, where T_s is the sampling time, if the desired force feedback at the end-effector of the RHI is increased by δ (i.e., $F_m(t_0+T_s) = F_m(t_0)+\delta$), joint j will become overloaded. Therefore, The torque of joint j at time t_0+T_s needs to be brought back within its bound by distributing the torque output increment for joint j among all other joints. The joints torque vector at t_0+T_s can be calculated using (7.5) and (7.8) as

$$\tau(t_0+T_s) = J^T F_m(t_0+T_s) + N_0(\tau_s - \hat{J}^T F_m) \tag{7.11}$$

where

$$N_0 = (I - J^T J^{\#^T})(I_n - \hat{J}^T \hat{J}^{\#^T})^{\#}. \tag{7.12}$$

Without loss of generality, it is assumed that the configuration of the RHI has not been changed from t_0 to t_0+T_s. Therefore, the Jacobian matrix in time t_0 is equal to the Jacobian matrix in time t_0+T_s. Now, the joints torque vector increment from time t_0 to time t_0+T_s can be calculated as

$$\begin{aligned} &\tau(t_0+T_s) - \tau(t_0) = \\ &J^T(F_m(t_0+T_s) - F_m(t_0)) + N_0(\tau_s - \hat{J}^T F_m(t_0+T_s)) \end{aligned} \tag{7.13}$$

where τ_s can be calculated as $\hat{J}^T F_m(t_0)$. Thus, (7.13) can be rewritten as

$$\tau(t_0+T_s) - \tau(t) = (J^T - N_0\hat{J}^T)(F_m(t_0+T_s) - F_m(t_0)) \tag{7.14}$$

As $(J^T - N_0\hat{J}^T)$ is bounded, it can be concluded that

$$|F_m(t_0+T_s) - F_m(t_0)| < \delta \leftrightarrow |\tau(t_0+T_s) - \tau(t_0)| < \epsilon, \tag{7.15}$$

which proves the continuity of the joints' torque control law.

As a simulational example, consider a 3-DoF planar RHI with the links length as $L_i = [0.25,\ 0.25,\ 0.25]\ m$. The joints torque bounds are assumed to be $|\mathcal{T}_i| \leq 0.5$ Nm. The RHI is at $q_i = [\frac{\pi}{4},\ -\frac{\pi}{3},\ -\frac{\pi}{6}]$ rad configuration and supposed to provide environment force feedback to the user when he/she holds the end-effector of the RHI fixed in the task space. The environment force is $F_e = [4\sin(t\pi/2),\ 0]^T$ N, where t is time. Fig. 7.1 shows the torques of the RHI joints and the output force feedback of the RHI with and without implementing the ASCM. The results show that when a joint is saturated, the ASCM will distribute torque among other joints to provide the desired force feedback by utilizing the full capacity of the RHI's actuators (see Fig. 7.1(c)). When two joints of the 3 DoF RHI are become saturated, the rank of $J(I_n - \mathcal{S})$ matrix will be smaller than the Cartesian space dimension (2) and from this point, the scaling factor, α, scale the desired force feedback to maintain its direction. When this method is not used, not only the magnitude of desired force feedback cannot be achieved, but also the direction of force feedback is altered (Fig. 7.1(a)). It is noted that a simple scaling method can be used to maintain the direction of the force feedback (Fig. 7.1(b)), however, in this method, the maximum output force of the RHI is lower than that of the RHI when ASCM is used (12% lower for the 3-DoF RHI example).

Consider an RHI that is made by breaking the links of an NHI into half, and an actuator is added between the new smaller links. The new RHI has higher structural stiffness. As the ASCM enables the RHI to achieve a higher force feedback capability with relatively smaller actuators, the total RHI inertia is comparable with the NHI. Therefore, it can be concluded that the resonant frequency of the resulting RHI is not necessary smaller than that of the NHI. As a result, the RHI will be able to interact with high stiffness virtual or remote environments better. Additionally, smaller actuators have lower rotor inertia and friction, which lead to smaller apparent inertia and reflected friction at the end-effector. Also, they are relatively cheaper, which makes the haptic interface less costly.

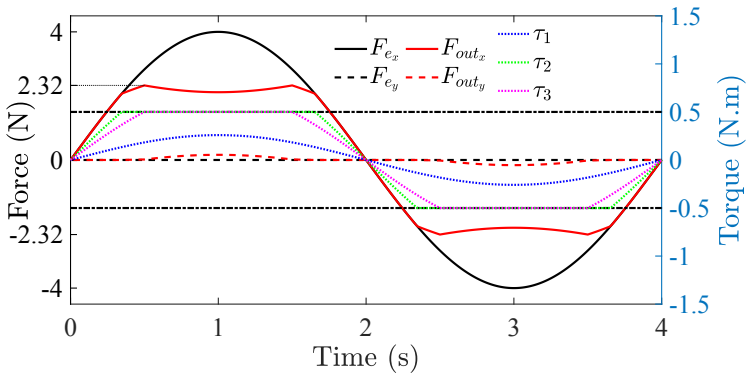

(a)

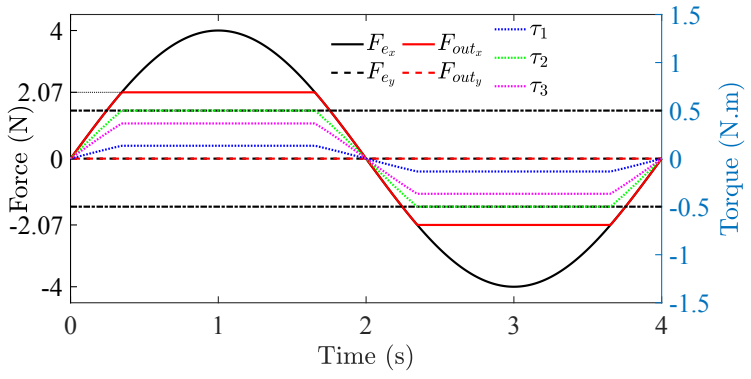

(b)

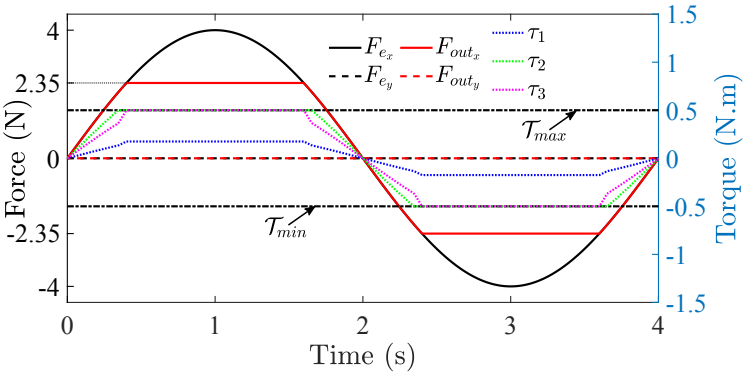

(c)

Figure 7.1: Joints torque τ_i (dotted lines), desired force feedback F_e (black solid line F_{e_x} and black dashed line F_{e_y}), and output force feedback F_{out} (red solid line F_{out_x} and red dashed line F_{out_y}) of a 3 DoF planar RHI subject to RHI joint saturation. Without any compensation method (a), with simple force feedback scaling algorithm (b), and with the actuator saturation compensation method (c).

7.4 Joint Level Tertiary Objective

After the ASCM resolves joint limits, a tertiary objective can be accommodated within the residual torque capacity generation of the RHI. The RHI still has redundant DoF if the rank of $(I_n - \mathcal{S})$ is larger than the dimension of Cartesian space m. Therefore, the RHI is capable of achieving a Tertiary objective by leveraging its redundant joints (i.e., internal motion) without affecting the position and orientation of the end-effector of the robot.

The null-space controller for tertiary objective can be utilized to work in parallel with the primary and secondary tasks controllers. The tertiary objective has a lower priority than the primary and secondary tasks. Therefore, it needs to be defined in the null-space of the primary and secondary tasks. In other words, the tertiary objective might not be achieved in favour of realizing the primary task. Also, as the torque limits of the RHI's actuators should not be violated, the ASCM is treated as a secondary task. Therefore, the tertiary objective has to be satisfied in the null space of the ASCM, which has a higher priority than it.

The joint torque command that realizes primary task, ASCM, and a tertiary objective is

$$\begin{aligned} &\tau_C = \tau + \\ &\beta(I_n - (\mathcal{S}(I_n - J^T(J^{\#})^T))^{\#})(I_n - J^T(J^{\#})^T)\tau_{to}, \end{aligned} \tag{7.16}$$

where β is the scaling factor to preserve the joint bounds that is between zero and one, τ and $\mathcal{S}$ are calculated from ASCM, and τ_{to} accounts for the tertiary objective. Algorithm 2 shows the required steps for calculating the scaling factor β. This Algorithm calculates the remaining capability of the RHI and determines the scaling factor β according to the joint bounds. If after resolving the joint limits, the RHI does not have any redundant joints left, β will be equal to zero. The flowchart and block diagram of the control system is depicted in Fig. 7.2 and Fig. 7.3, respectively.

There are different methods to implement τ_{to} [128]. Here, the gradient projection approach is used. Thus, the tertiary objective torque is calculated

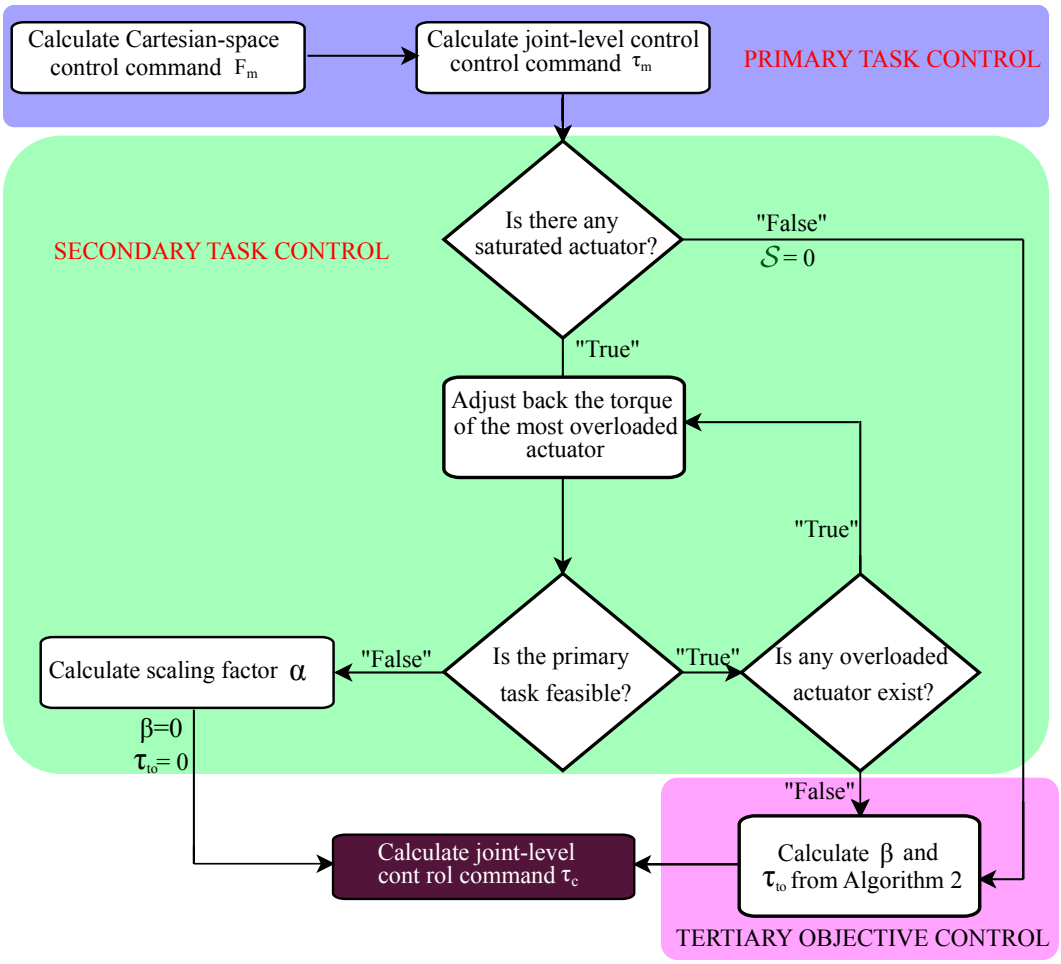

Figure 7.2: Flowchart of the control system. It shows the correlation between the primary task (end-effector impedance control), the secondary objective (actuator saturation compensation), and the tertiary objective (manipulability enhancement).

Algorithm 2 Scaling Factor β Calculation

Get $\mathcal{S}$ from ASCM
if $(I_n - \mathcal{S}) > m$ **then**
  $N_{to} = (I_n - (\mathcal{S}(I_n - J^T(J^\#)^T))^\#)(I_n - J^T(J^\#)^T)$
  $N_3 = N_{to}\tau_{to}$
  $\beta_{min,i} = (\mathcal{T}_{min,i} - \tau_i)/N_{3,i}$ For $i = 1 \rightarrow n$
  $\beta_{max,i} = (\mathcal{T}_{max,i} - \tau_i)/N_{3,i}$ For $i = 1 \rightarrow n$
  Switch $\beta_{min,i}$ and $\beta_{max,i}$ If $\beta_{min,i} > \beta_{max,i}$
  $\beta = \min(\min\{\beta_{max,i}\}, 1)$
else
  $\beta = 0$
end if

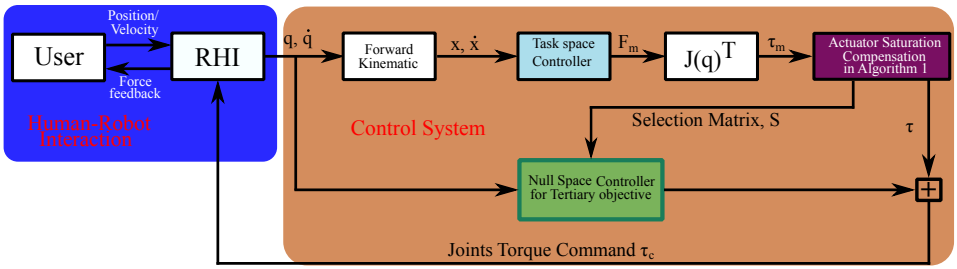

Figure 7.3: Block diagram of the control system.

as

$$\tau_{to} = -\Lambda \frac{\partial \nu(q)}{\partial q}, \tag{7.17}$$

where Λ is a suitable scalar step size and $\nu(q)$ is the cost function. With this choice of τ_{to}, the robot tries to decrease the value of $\nu(q)$ while executing a primary time-varying task. Following the approach introduced in Chapter 3, the cost function $\nu(q)$ is selected as

$$\nu = \text{logdet}(\frac{\mathcal{M} + \mathcal{M}^{des}}{2}) - \frac{1}{2}\text{logdet}(\mathcal{M}\mathcal{M}^{des}), \tag{7.18}$$

where $\mathcal{M}$ is the velocity manipulability ellipsoid of the RHI, defined as $\mathcal{M} = JJ^T$ (see Chapter 4), and $\mathcal{M}^{des}$ is the desired velocity manipulability ellipsoid. By minimizing the cost function (7.18), the manipulability of the RHI will be matched with the desired one. As shown in Chapter 3, by aligning the major axis of the velocity manipulability ellipsoid of an RHI along the desired direction of motion, the reflected joints' friction at the end-effector of the RHI will be minimized, and its manipulability will be maximized. This will consequently minimize the interference of the RHI's kinematic with the perception of the user from the rendered environment. The main limitation of this approach is that the force feedback capability of the RHI along the direction of motion will be minimized due to the fact that the force manipulability ellipsoid is inverse of the velocity manipulability ellipsoid. Therefore, the proposed ASCM is required to distribute torque among the actuators and enhance the force feedback capability of the RHI.

7.5 Experimental Evaluation

In this section, experiments are performed to evaluate the proposed ASCM and null space controller using a 4-DoF planar RHI. The experiments were performed using a 2-DOF planar upper-limb rehabilitation robot (Quanser Inc., Markham, ON, Canada) that is serially connected to a 2-DoF PHANToM 1.5A (3D Systems Inc., Morrisville, NC, USA) to make the 4-DoF planar RHI. The base joint of the 3-DoF PHANToM robot was removed to turn it into a 2-DoF planar robot. A coupler is designed and 3D-printed to connect the end-effector of the upper-limb rehabilitation robot to the base of the PHANToM robot. To measure forces at the end-effector of the RHI, a 6-DoF wrench (force/torque) sensor (50M31A3-I25, JR3 Inc., Woodland, CA, USA) is attached to it. The controllers are implemented in MATLAB/Simulink (MathWorks Inc., Natick, MA, USA) with Quarc real-time control software (Quanser Inc., Markham, ON, Canada). The wrench sensor data are sent through UDP from a Robot Operating System (ROS) PC to the MATLAB PC. The experimental setup is shown in Fig. 7.4. The joints torque limits are programmed as $\tau_{min,i} = [-3,\ -3,\ -1,\ -1]$ Nm and $\tau_{max,i} = [3,\ 3,\ 1,\ 1]$ Nm, and the links length of the RHI are $d_i = [0.254,\ 0.141,\ 0.21,\ 0.181]$ m.

Before the experiments are carried out, a simulation study was performed to validate the four-DoF RHI's force feedback capability enhancement by using the proposed method (ASCM) across the entire workspace. The inverse kinematics is solved at each point of the RHI's workspace, and the maximum force feedback capability of the RHI along $u = [0, 1]^T$ is calculated for two cases: With ASCM and without ASCM. The percent deficiency (PD) of maximum force feedback magnitude provided by the traditional method (i.e., without ASCM) as compared to the proposed method (i.e., with ASCM) is defined as

$$PD = \frac{\|F_{max(w/\ ASCM)}\| - \|F_{max(w/o\ ASCM)}\|}{\|F_{max(w/\ ASCM)}\|} \times 100, \tag{7.19}$$

and depicted in Fig. 7.5. As the results show, the maximum force feedback capacity of the RHI using the proposed ASCM is larger everywhere in the workspace than without it.

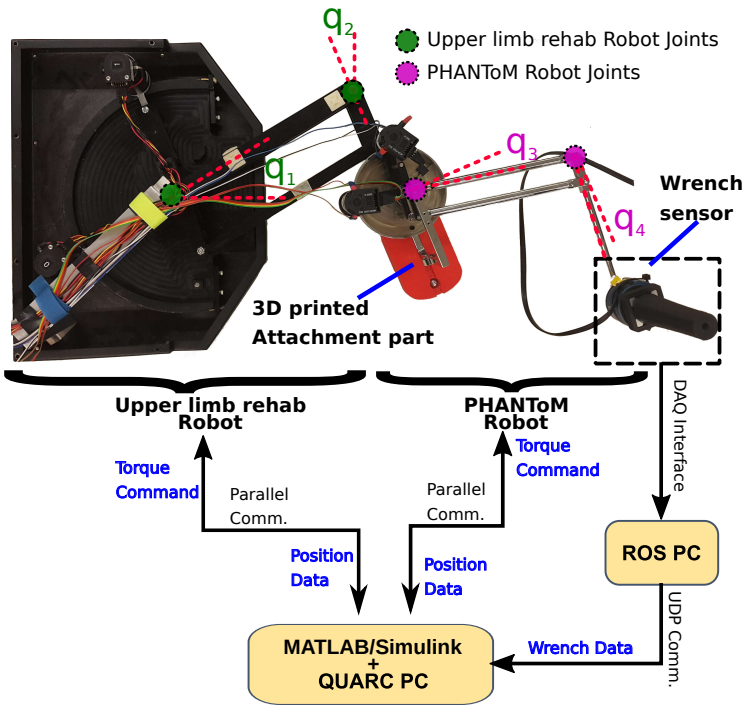

Figure 7.4: Top view of experimental setup and the diagram of the communication between devices.

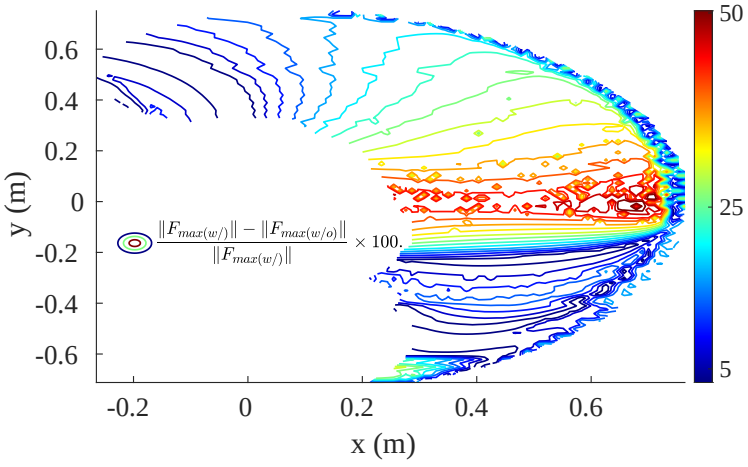

Figure 7.5: Percent deficiency of maximum force feedback provided by traditional methods as compared to the proposed method.

In the experiments, a user holds the end-effector of the RHI (where the wrench sensor is shown in Fig. 7.4) and palpates a virtual environment along the right-hand direction through it. The virtual environment is modelled as a spring with constant stiffness. In the experiments, the user palpates the virtual environment starting from a fixed point in the workspace of the RHI. The starting point is given as $X_0 = [0.45,\ 0]^T$m. The Cartesian space control law used in the experiments is

$$F_{RHI} = -F_e - B^d\dot{X} + C_x\dot{X} \tag{7.20}$$

where F_e is modeled as $K_e\delta X$ in which K_e is the stiffness of the virtual environment and δX is the position deviation from the starting point. The desired damping parameter is selected as $B^d = \text{diag}\{0.01,\ 0.01\}$Ns/m. Also, the virtual environment is modelled with $K_e = 1000$ N/m to create a stiff environment. As the end-effector movement is small in the experiment, the effect of friction is neglected, and thus, the friction compensation is not implemented. Also, the gravity compensation is not required as the RHI is planar.

The objective of the experiments is to show the enhanced force feedback capability of the RHI by using the proposed ASCM. Two cases are considered: Case (1) The palpation is performed without the ASCM, and Case (2) The palpation is performed with ASCM. In both cases, the major axis of the desired velocity manipulability ellipsoid is aligned with the direction of motion (contact) (i.e., $u = [0,\ 1]^T$), and it is designed as $\mathcal{M}^{des} = \text{diag}\{0.01,\ 170\}$. The desired velocity manipulability ellipsoid is designed using the method discussed in Chapter 3.

Fig. 7.6 shows the experimental results. In this figure, the measured force using the wrench sensor, the desired force ($K_e \times \delta X$), and the torque of the actuators are illustrated. By employing the ASCM, the maximum force feedback of the RHI is enhanced by 73% (Fig. 7.6(b)) in comparison to the case in which the palpation is performed without the implementation of ASCM (Fig. 7.6(a)). The ASCM distributes torque among the unsaturated joints when the saturation happens in one or more joints. As a result, the user feels the environment more solid in case (2).

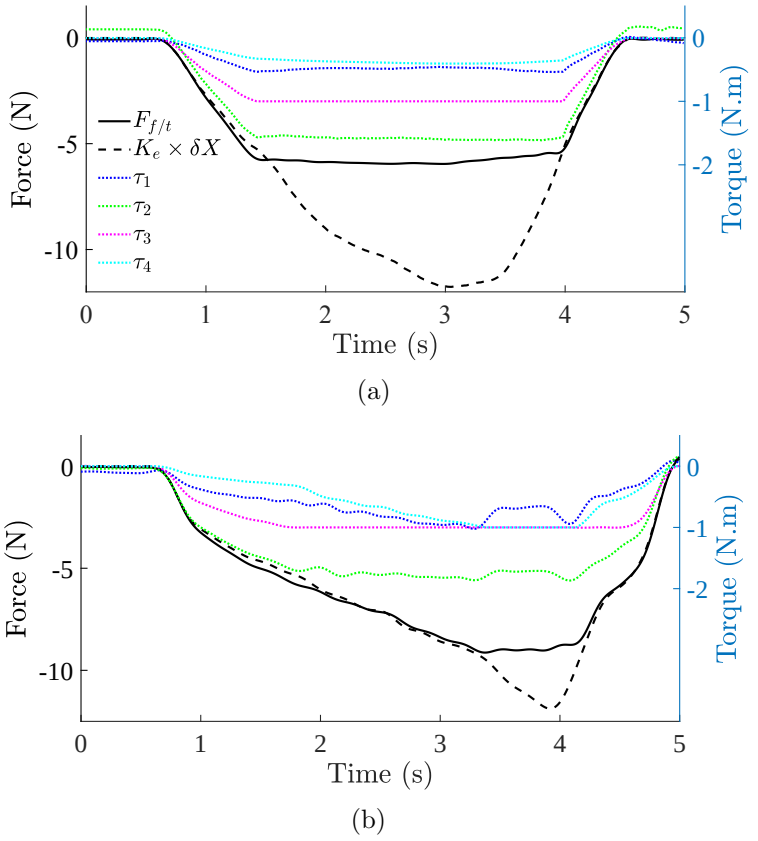

Figure 7.6: Experimental results without (a) and with (b) employing the ASCM. Joints torque τ_i, $i = 1, 2, 3, 4$, are shown with dotted lines, desired force feedback $K_e \times \delta X$ with black dashed line, and the measured force feedback $F_{f/t}$ with black solid line.

7.6 Concluding Remarks

In this chapter, we proposed an actuator saturation compensation method for redundant haptic interfaces that distributes the torque of the saturated joints among the available unsaturated joints. This method leverages the kinematic redundancy of the haptic interface to enable the haptic interface to achieve a higher force feedback capability with relatively smaller actuators. This is important as there is a trade-off between the maximum force feedback capability of the RHI versus minimum apparent inertia and back-drive friction. Indeed, a large force feedback capability requires large actuators, increasing the haptic interface's inertia. The proposed method generates torque commands in the null-space of the Jacobian matrix of the haptic interface to bring back the overloaded joints to their saturation level and distributes that excessive torque among the unsaturated joints. Also, a tertiary objective null-space controller was proposed that takes the actuator saturation compensation method (ASCM) implementation into account. If the primary task is feasible after ASCM implementation and the redundant haptic interface has available redundancy, a tertiary objective will be satisfied in the null-space of ASCM. This will guarantee that the tertiary objective will not interfere with the primary task and ASCM that those have higher priorities. The experiments with a 4-DoF planar haptic interface demonstrated 73% enhancement in the force feedback capability of the RHI using the proposed methods.

Chapter 8

Conclusions and Future Directions

8.1 Conclusions

This dissertation has delved into modeling, design, and control of haptic interfaces (HIs) to improve the quality of haptic interaction, enhance the user's control over force/velocity commands, and reduce the user's effort; all culminating in enhanced task performance outcomes. There are trade-offs between the desirable characteristics of HIs, such as maximum force feedback capability vs. minimum inertia or maximum stiffness vs. workspace size. Indeed, a large force feedback capability requires large actuators, increasing the HI's inertia. A large workspace requires long links, decreasing the HI's stiffness and increasing its inertia. Therefore, the design of the HI has to be optimized for a specific application. These design trade-offs have motivated this research to explore the advantages offered by re-configurability (via redundancy) of HIs for best addressing the design trade-offs. The specific aims in this research were (1) relax the above trade-offs by adding redundancy in the HI mechanical design, and (2) further optimize the kinematic and dynamic characteristics of redundant HIs and enhance its force feedback capability through closed-loop control.

First, we introduced the intrinsic benefits of redundant HIs in terms of better kinematic and dynamic characteristics, i.e., increased manipulability (one result of which is reduced friction) and reduced apparent impedance.

Next, a quantifiable measure of the combined HI-slave system manipulability was introduced. This measure empowers design engineers to achieve as many of the desirable HI characteristics as possible via appropriate mechanism design of HIs. Then, we discussed how by appropriately manipulating an RHI's extra DOFs in joint-level control we can further enhance its kinematic and dynamic properties as well as enhancing its force feedback capability.

The intrinsic advantages of redundant haptic interfaces over non-redundant haptic interfaces was explored in Chapter 3. It was also shown that by leveraging the redundancy of the RHI, it is possible to further optimize its kinematic and dynamic characteristics through a closed-loop null-space control. In Chapter 3, perceptual experiments were performed to compare the users' performance for a soft-tissue stiffness discrimination task using redundant and non-redundant haptic interfaces. We conducted a set of perceptual experiments to evaluate how different HIs affect the perception of virtual stiffnesses for human users. The goal was to study how a redundant haptic interface (RHI) can be used to decrease the apparent inertia and increase the manipulability of the human interface, and consequently improve the resolution of force feedback for the user. Experimental results demonstrate that the RHI leads to better sensitivity in discriminating between stiffness of two tissue samples.

The teleoperation manipulability index (TMI) for a surgical HI-slave robotic system was defined in Chapter 4. The application of the TMI in the design of HI-slave robotic systems was demonstrated. It was shown that by modifying the design of a commercially available HI using the proposed manipulability criterion, we are able to enhance the surgeon's control over force/velocity of the surgical robot by increasing the TMI, minimizing the master robot's footprint via minimizing its link length, and optimizing the surgeons control effort via minimizing the required input energy for moving the slave's end-effector.

In Chapter 5, the application of the proposed teleoperation manipulability index in Chapter 4 in designing a null-space controller for an RHI was demonstrated. We evaluated the enhanced performance of the proposed approach via a comparison with two other existing control strategies. It was shown that

by implementing our controller in a robotic HI-slave system that benefits from a redundant haptic interface, we are able to improve the overall manipulability of the system, which can improve the user's control over slave robot's end-effector force/velocities and reduce the user's control effort.

A null-space controller that leverages the kinematic redundancy of the RHI toward secondary objectives to optimize the interaction of the user with the environment was proposed in Chapter 6. Two secondary objectives based on the task requirements were proposed in this chapter. A transition method based on the actuator saturation observer was proposed to prevent discontinuity of the control effort when switching between the secondary objectives was required. The actuator saturation observer monitors the distance between the actuators torque and their saturation levels. When the RHI's actuators are far away from their saturation levels, an appropriate secondary objective is active and manipulates the internal motion of the RHI to increase its velocity manipulability, and consequently decrease the interference of the friction forces and kinematics of the RHI with the user-environment interaction. This secondary objective is replaced with another secondary objective when the RHI's actuators become close to their saturation levels, which can happen when rendering hard contacts. It was shown that the RHI's force feedback capability is configuration dependable, and by appropriately manipulating the internal motion of the RHI, it can be enhanced. The experiments showed 51% enhancement in the force feedback capability of the RHI using the proposed methods. Also, experiments showed the practicality of the proposed transition method by preventing the discontinuity in the control effort for the RHI.

In chapter 7, an actuator saturation compensation method (ASCM) for redundant haptic interfaces was proposed that distributes the torque of the saturated joints among the available unsaturated joints to enhance the force feedback capability of the RHI. The proposed method leverages the kinematic redundancy of the haptic interface to enable the haptic interface to achieve a higher force feedback capability with relatively smaller actuators. The proposed method generates torque commands in the null-space of the Jacobian matrix of the haptic interface to bring back the overloaded joints to their

saturation level and distributes that excessive torque among the unsaturated joints. Also, a tertiary objective null-space controller was proposed that takes the actuator saturation compensation method implementation into account. If the primary task is feasible after ASCM implementation and the redundant haptic interface has available redundancy, a tertiary objective will be satisfied in the null-space of ASCM. This will guarantee that the tertiary objective will not interfere with the primary task and ASCM that those have higher priorities. The experiments with a 4-DoF planar haptic interface demonstrated 73% enhancement in the force feedback capability of the RHI using the proposed methods.

8.2 Future Directions

In Chapter 3, a virtual environment was used to set up a haptic interaction system with nearly-ideal transparency and without any communication delay to show the advantages of an RHI over the NHIs in terms of stiffness discrimination. The teleoperated HI-slave system can be used to investigate the effectiveness of the proposed system in teleoperated systems. Also, throughout his research it was assumed that the direction of the movement, u, was known to the secondary objective controller. In the future works, the direction of the movement or the intention of the user can be found by using machine learning methods (e.g. Hidden Markov Model) and/or by measuring the torque/force applied by the user's hand on the haptic interface. Also, it needs to be investigated how the minimum number of added DoFs for a desired improvement in manipulability, apparent inertia, and JND can be attained.

In Chapter 4, the teleoperation manipulability index was only used to modify the design and control of haptic interfaces. The same index can be employed to modify the design of the slave robot. Also, the manipulability index can be used in motion planning of surgical tasks to find optimal trajectories that enhances manipulability and minimizes surgeon's control effort. In future, the proposed manipulability optimization method can be used on more complex teleoperation system with more DoFs. Here, we used a unilateral teleoper-

ated systems to investigate the proposed method with near-ideal transparency and without any communication delay. In the future, a bilateral teleoperated master-slave system can be considered.

The focus of this research was to show that a redundant haptic interface is able to provide larger force feedback to a user with the proposed methods discussed in Chapter 6 and Chapter 7. Therefore, the methods can be used for the design of a new haptic interface with small actuators to provide relatively large force feedback. In the future, an extensive user study needs to be performed to evaluate how using the proposed methods affects the perception of free space and stiff environments for the user.

The redundancy resolution of RHIs can be expanded to be informed by available task- and user-specific information. To have knowledge of tasks and the users' intentions and limitations, datasets of various tasks in a given application (e.g., soft-tissue surgery) need to be created by recording users' applied motions and forces. Task models and user motion/force models can be generated by applying machine learning techniques such as hidden Markov models and Gaussian mixture models on the recorded data,

The developed models can be used in task-specific and user-dependent redundancy resolution and impedance modulation of RHIs. Once a user starts to move or apply a force on the RHI, the database can be queried for the most similar pattern of motion or force to identify the specific task that this specific user intends to do. Then, the RHI can be reconfigured and adapted to yield the best task performance.

The mechanical impedance of a user's hand is regularly modified according to a task's specifications. Inspired by this, the RHI can be variable impedance controlled based on the requirements of a given task and any available information concerning the user's intentions, limitations, kinematics and dynamics. The Cartesian-level variable-impedance control of RHIs can further improve their characteristics in coordination with the joint-level secondary-objective controls developed in this thesis.

While in most haptic interaction applications it is desirable for the HI to ideally have a zero impedance itself to truthfully display the environment's

impedance to the user, there are other applications in which the HI needs to have certain impedances to enable or facilitate the user's performance of tasks. For instance, in highly precise positioning applications requiring superhuman abilities, the HI can be impedance controlled to slow down and smooth the hand motion (i.e., filter out hand tremors) for the best task performance. For such applications, Cartesian-level closed-loop impedance controls of RHIs can be developed (as adaptable virtual fixtures) to adjust the motions based on the interactions of the RHIs with users in order to best assist, guide or constrain the users.

For surgical tasks, virtual fixtures can reduce task time and errors and increase accuracy. a controller can be designed such that it would automatically generate real-time virtual fixtures to haptically assist the surgeon during the surgery. Virtual fixtures can be generated by correlating a given user's data to the experts' dataset to guide his/her motions along desired paths and regulate the movement while maintaining the user in charge. Repetitive subtasks in surgery such as cutting, ablation and suturing can also be automated to reduce surgeon's fatigue and take advantage of accuracy, dexterity, and speed of robots in surgery. By using machine learning methods, some parts of the intervention that are not critical to the procedure success can be automated.

References

[1] E. Abdi, D. Kuli, and E. Croft, "Haptics in teleoperated medical interventions: Force measurement, haptic interfaces and their influence on users performance," *IEEE Transactions on Biomedical Engineering*, 2020.

[2] G. Ahlberg, L. Enochsson, A. G. Gallagher, L. Hedman, C. Hogman, D. A. McClusky, S. Ramel, C. D. Smith, and D. Arvidsson, "Proficiency-based virtual reality training significantly reduces the error rate for residents during their first 10 laparoscopic cholecystectomies," *The American Journal of Surgery*, vol. 193, no. 6, pp. 797–804, 2007, ISSN: 0002-9610. DOI: https://doi.org/10.1016/j.amjsurg.2006.06.050. [Online]. Available: http://www.sciencedirect.com/science/article/pii/S0002961007000712.

[3] S. Ahmad, H. Zhang, and G. Liu, "Multiple working mode control of door-opening with a mobile modular and reconfigurable robot," *IEEE/ASME Transactions on Mechatronics*, vol. 18, no. 3, pp. 833–844, 2012.

[4] S. R. Ahmadzadeh, P. Kormushev, R. S. Jamisola, and D. G. Caldwell, "Learning reactive robot behavior for autonomous valve turning," in *2014 IEEE-RAS International Conference on Humanoid Robots*, IEEE, 2014, pp. 366–373.

[5] A. Ajoudani, N. G. Tsagarakis, and A. Bicchi, "Choosing poses for force and stiffness control," *IEEE Transactions on Robotics*, vol. 33, no. 6, pp. 1483–1490, Dec. 2017.

[6] V. Andaluz, F. Roberti, J. M. Toibero, and R. Carelli, "Adaptive unified motion control of mobile manipulators," *Control Engineering Practice*, vol. 20, no. 12, pp. 1337–1352, 2012.

[7] J. Angeles and F. C. Park, "Performance evaluation and design criteria," in *Springer Handbook of Robotics*. Springer Berlin Heidelberg, 2008, pp. 229–244.

[8] G. Antonelli and S. Chiaverini, "Fuzzy redundancy resolution and motion coordination for underwater vehicle-manipulator systems," *IEEE Transactions on Fuzzy Systems*, vol. 11, no. 1, pp. 109–120, 2003.

[9] S. F. Atashzar, M. Shahbazi, M. Tavakoli, and R. V. Patel, "A grasp-based passivity signature for haptics-enabled human-robot interaction: Application to design of a new safety mechanism for robotic rehabilitation," *The International Journal of Robotics Research*, vol. 36, no. 5-7, pp. 778–799, 2017. DOI: 10.1177/0278364916689139.

[10] M. Bajka, S. Tuchschmid, M. Streich, D. Fink, G. Székely, and M. Harders, "Evaluation of a new virtual-reality training simulator for hysteroscopy," *Surgical endoscopy*, vol. 23, no. 9, p. 2026, 2009.

[11] G. I. Barbash and S. Glied, "New technology and health care costs–the case of robot-assisted surgery.," *The New England journal of medicine*, vol. 363 8, pp. 701–4, 2010.

[12] A. Barrow and W. Harwin, "Design and analysis of a haptic device design for large and fast movements," *Machines*, vol. 4, no. 1, pp. 1–19, 2016, ISSN: 2075-1702.

[13] O. Baser, E. I. Konukseven, and T. Balkan, "Optimal posture control for a 7 dof haptic device based on power minimization," in *International Conference on Human Haptic Sensing and Touch Enabled Computer Applications*, Springer, 2008, pp. 555–560.

[14] Ö. BAŞER and E. I. Konukseven, "7-dof haptic device and interface design," *Turkish Journal of Electrical Engineering & Computer Sciences*, vol. 21, no. 2, pp. 493–499, 2013.

[15] B. Bayle, J.-Y. Fourquet, and M. Renaud, "Manipulability of wheeled mobile manipulators: Application to motion generation," *The International Journal of Robotics Research*, vol. 22, no. 7-8, pp. 565–581, 2003.

[16] P. J. Berkelman and R. L. Hollis, "Lorentz magnetic levitation for haptic interaction: Device design, performance, and integration with physical simulations," *The International Journal of Robotics Research*, vol. 19, no. 7, pp. 644–667, 2000.

[17] A. Bicchi, C. Melchiorri, and D. Balluchi, "On the mobility and manipulability of general multiple limb robots," *IEEE Transactions on Robotics and Automation*, vol. 11, no. 2, pp. 215–228, 1995.

[18] A. Bicchi and D. Prattichizzo, "Manipulability of cooperating robots with unactuated joints and closed-chain mechanisms," *IEEE Transactions on Robotics and Automation*, vol. 16, no. 4, pp. 336–345, 2000.

[19] C. Bolenz, A. Gupta, T. D. Hotze, R. Ho, J. A. Cadeddu, C. Roehrborn, and Y. Lotan, "Cost comparison of robotic, laparoscopic, and open radical prostatectomy for prostate cancer.," *European urology*, vol. 57 3, pp. 453–8, 2010.

[20] F. P. Brooks Jr, M. Ouh-Young, J. J. Batter, and P. Jerome Kilpatrick, "Project gropehaptic displays for scientific visualization," *ACM SIGGraph computer graphics*, vol. 24, no. 4, pp. 177–185, 1990.

[21] S. R. Buss, "Introduction to inverse kinematics with jacobian transpose, pseudoinverse and damped least squares methods," *IEEE Journal of Robotics and Automation*, vol. 17, no. 1-19, p. 16, 2004.

[22] P. Buttolo and B. Hannaford, "Advantages of actuation redundancy for the design of haptic displays," in *Proceedings ASME Fourth Annual Symposium on Haptic Interfaces for Virtual Environment and Teleoperator Systems.*.

[23] M. C. Çavuşoğlu, D. Feygin, and F. Tendick, "A critical study of the mechanical and electrical properties of the phantom haptic interface and improvements for highperformance control," *Presence*, vol. 11, no. 6, pp. 555–568, Dec. 2002, ISSN: 1054-7460.

[24] T. F. Chan and R. V. Dubey, "A weighted least-norm solution based scheme for avoiding joint limits for redundant joint manipulators," *IEEE Transactions on Robotics and Automation*, vol. 11, no. 2, pp. 286–292, 1995.

[25] F. Chen, M. Selvaggio, and D. G. Caldwell, "Dexterous grasping by manipulability selection for mobile manipulator with visual guidance," *IEEE Transactions on Industrial Informatics*, vol. 15, no. 2, pp. 1202–1210, 2018.

[26] F.-T. Cheng, T.-H. Chen, and Y.-Y. Sun, "Resolving manipulator redundancy under inequality constraints," *IEEE Transactions on Robotics and Automation*, vol. 10, no. 1, pp. 65–71, 1994.

[27] L. Cheng, M. Sharifi, and M. Tavakoli, "Towards robot-assisted anchor deployment in beating-heart mitral valve surgery," *The International Journal of Medical Robotics and Computer Assisted Surgery*, vol. 14, no. 3, e1900, 2018.

[28] A. Cherian, S. Sra, A. Banerjee, and N. Papanikolopoulos, "Efficient similarity search for covariance matrices via the jensen-bregman logdet divergence," in *2011 International Conference on Computer Vision*, Nov. 2011, pp. 2399–2406.

[29] ——, "Jensen-bregman logdet divergence with application to efficient similarity search for covariance matrices," *IEEE Transactions on Pattern Analysis and Machine Intelligence*, vol. 35, no. 9, pp. 2161–2174, Sep. 2013.

[30] P. Chiacchio, S. Chiaverini, L. Sciavicco, and B. Siciliano, "Global task space manipulability ellipsoids for multiple-arm systems," *IEEE Transactions on Robotics and Automation*, vol. 7, no. 5, pp. 678–685, 1991.

[31] P. Chiacchio, Y. Bouffard-Vercelli, and F. Pierrot, "Force polytope and force ellipsoid for redundant manipulators," *Journal of Robotic Systems*, vol. 14, no. 8, pp. 613–620, 1997.

[32] S. Chiaverini, "Singularity-robust task-priority redundancy resolution for real-time kinematic control of robot manipulators," *IEEE Transactions on Robotics and Automation*, vol. 13, no. 3, pp. 398–410, 1997.

[33] S. Chiaverini, G. Oriolo, and A. A. Maciejewski, "Redundant robots," in *Springer Handbook of Robotics*, B. Siciliano and O. Khatib, Eds., Cham: Springer International Publishing, 2016, pp. 221–242, ISBN: 978-3-319-32552-1. DOI: 10.1007/978-3-319-32552-1_10.

[34] S. L. Chiu, "Task compatibility of manipulator postures," *The International Journal of Robotics Research*, vol. 7, no. 5, pp. 13–21, 1988.

[35] T. R. Coles, D. Meglan, and N. W. John, "The role of haptics in medical training simulators: A survey of the state of the art," *IEEE Transactions on Haptics*, vol. 4, no. 1, pp. 51–66, Jan. 2011, ISSN: 2334-0134. DOI: 10.1109/TOH.2010.19.

[36] J. E. Colgate and J. M. Brown, "Factors affecting the z-width of a haptic display," in *Proceedings of the 1994 IEEE International Conference on Robotics and Automation*, May 1994, 3205–3210 vol.4.

[37] J. E. Colgate and N. Hogan, "Robust control of dynamically interacting systems," *International Journal of Control*, vol. 48, no. 1, pp. 65–88, 1988.

[38] N. Colonnese, A. F. Siu, C. M. Abbott, and A. M. Okamura, "Rendered and characterized closed-loop accuracy of impedance-type haptic displays," *IEEE Transactions on Haptics*, vol. 8, no. 4, pp. 434–446, Oct. 2015, ISSN: 1939-1412.

[39] D. Constantinescu, I. Chau, S. P. DiMaio, L. Filipozzi, S. E. Salcudean, and F. Ghassemi, "Haptic rendering of planar rigid-body motion using a redundant parallel mechanism," in *Proceedings 2000 ICRA. Millennium Conference. IEEE International Conference on Robotics and Automation. Symposia Proceedings (Cat. No.00CH37065)*, vol. 3, Apr. 2000, 2440–2445 vol.3.

[40] Y. Dai, S. Yu, Y. Yan, and X. Yu, "An ekf-based fast tube mpc scheme for moving target tracking of a redundant underwater vehicle-manipulator system," *IEEE/ASME Transactions on Mechatronics*, vol. 24, no. 6, pp. 2803–2814, 2019.

[41] A. De Luca and G. Oriolo, "The reduced gradient method for solving redundancy in robot arms," *Robotersysteme*, vol. 7, no. 2, pp. 117–122, 1991.

[42] A. De Luca, G. Oriolo, and P. R. Giordano, "Kinematic modeling and redundancy resolution for nonholonomic mobile manipulators," in *Proceedings 2006 IEEE International Conference on Robotics and Automation, 2006. ICRA 2006.*, IEEE, 2006, pp. 1867–1873.

[43] E. Dean-Leon, B. Pierce, F. Bergner, P. Mittendorfer, K. Ramirez-Amaro, W. Burger, and G. Cheng, "Tomm: Tactile omnidirectional mobile manipulator," in *2017 IEEE International Conference on Robotics and Automation (ICRA)*, IEEE, 2017, pp. 2441–2447.

[44] A. Dietrich, X. Wu, K. Bussmann, C. Ott, A. Albu-Schäffer, and S. Stramigioli, "Passive hierarchical impedance control via energy tanks," *IEEE Robotics and Automation Letters*, vol. 2, no. 2, pp. 522–529, Apr. 2017.

[45] M. D. Dyck, "Measuring the Dynamic Impedance of the Human Arm," M.Sc. Thesis, University of Alberta, 2013.

[46] R. Ellis, O. Ismaeil, and M. Lipsett, "Design and evaluation of a high-performance haptic interface," *Robotica*, vol. 14, no. 03, p. 321, 1996, ISSN: 0263-5747. DOI: 10.1017/S0263574700019639.

[47] N. Enayati, E. D. Momi, and G. Ferrigno, "Haptics in robot-assisted surgery: Challenges and benefits," *IEEE Reviews in Biomedical Engineering*, vol. 9, pp. 49–65, 2016.

[48] A. Escande, N. Mansard, and P.-B. Wieber, "Hierarchical quadratic programming: Fast online humanoid-robot motion generation," *The International Journal of Robotics Research*, vol. 33, no. 7, pp. 1006–1028, 2014.

[49] F. Ficuciello, L. Villani, and B. Siciliano, "Variable impedance control of redundant manipulators for intuitive human – robot physical interaction," *Transactions on Robotics*, vol. 31, no. 4, pp. 1–14, 2015.

[50] F. Flacco, A. De Luca, and O. Khatib, "Prioritized multi-task motion control of redundant robots under hard joint constraints," in *2012 IEEE/RSJ International Conference on Intelligent Robots and Systems*, IEEE, 2012, pp. 3970–3977.

[51] ——, "Control of redundant robots under hard joint constraints: Saturation in the null space," *IEEE Transactions on Robotics*, vol. 31, no. 3, pp. 637–654, 2015.

[52] O. Flores-Díaz, I. Juárez-Campos, and J. Carrera-Bolaños, "Procedures to determine the principal directions of kinematic performance in serial robots," *Robotica*, vol. 36, pp. 1664–1679, 2018. DOI: 10.1017/S0263574718000620.

[53] A. G. Gallagher, E. M. Ritter, H. R. Champion, G. Higgins, M. P. Fried, G. Moses, C. D. Smith, and R. M. Satava, "Virtual reality simulation for the operating room: Proficiency-based training as a paradigm shift in surgical skills training.," *Annals of surgery*, vol. 241 2, pp. 364–72, 2005.

[54] G. D. Gersem, H. V. Brussel, and F. Tendick, "Reliable and enhanced stiffness perception in soft-tissue telemanipulation," *The International Journal of Robotics Research*, vol. 24, no. 10, pp. 805–822, 2005.

[55] G. A. Gescheider, *Psychophysics: The fundamentals, 3rd ed.* Mahwah, NJ, US: Lawrence Erlbaum Associates Publishers, 1997, pp. x, 435–x, 435.

[56] M. Giftthaler, F. Farshidian, T. Sandy, L. Stadelmann, and J. Buchli, "Efficient kinematic planning for mobile manipulators with non-holonomic constraints using optimal control," in *2017 IEEE International Conference on Robotics and Automation (ICRA)*, IEEE, 2017, pp. 3411–3417.

[57] G. Golub and C. Van Loan, *Matrix Computations*, ser. Johns Hopkins Studies in the Mathematical Sciences. Johns Hopkins University Press, 1996.

[58] C. Gosselin and L.-T. Schreiber, "Redundancy in Parallel Mechanisms: A Review," *Applied Mechanics Reviews*, vol. 70, no. 1, Jan. 2018, 010802, ISSN: 0003-6900. eprint: https://asmedigitalcollection.asme.org/appliedmechanicsreviews/article-pdf/70/1/010802/5964327/amr_070_01_010802.pdf.

[59] F. Gosselin, C. Andriot, F. Bergez, and X. Merlhiot, "Widening 6-dof haptic devices workspace with an additional degree of freedom," in *Second Joint EuroHaptics Conference and Symposium on Haptic Interfaces for Virtual Environment and Teleoperator Systems (WHC'07)*, Mar. 2007, pp. 452–457.

[60] S. Grange, F. Conti, P. Rouiller, P. Helmer, and C. Baur, "The delta haptic device," *Mecatronics*, 2001.

[61] S. Grange, F. Conti, P. Rouiller, P. Helmer, and C. Baur, "Overview of the delta haptic device," in *EUROHAPTICS 2001*, 2001, pp. 164–166.

[62] A. D. Greer, P. M. Newhook, and G. R. Sutherland, "Human–machine interface for robotic surgery and stereotaxy," *IEEE/ASME Transactions on Mechatronics*, vol. 13, no. 3, pp. 355–361, 2008.

[63] B. Hannaford and A. M. Okamura, "Haptics," in *Springer Handbook of Robotics*, B. Siciliano and O. Khatib, Eds., Springer International Publishing, 2016, pp. 1063–1084, ISBN: 978-3-319-32552-1. DOI: 10.1007/978-3-319-32552-1_42.

[64] C. Hatzfeld and T. A. Kern, *Engineering Haptic Devices: A Beginner's Guide*. Springer London, 2014, ISBN: 978-1-4471-6518-7. [Online]. Available: https://doi.org/10.1007/978-1-4471-6518-7.

[65] V. Hayward, P. Gregorio, O. Astley, S. Greenish, M. Doyon, L. Lessard, J. McDougall, I. Sinclair, S. Boelen, X. Chen, J.-G. Demers, J. Poulin, I. Benguigui, N. Almey, B. Makuc, and X. Zhang, "Freedom-7: A high fidelity seven axis haptic device with application to surgical training," in *Experimental Robotics V*, A. Casals and A. T. de Almeida, Eds., Berlin, Heidelberg: Springer Berlin Heidelberg, 1998, pp. 443–456.

[66] V. Hayward and O. R. Astley, "Performance Measures for Haptic Interfaces," *International Symposium In Robotics Research*, vol. 1, pp. 195–207, 1996.

[67] P. Hsu, J. Mauser, and S. Sastry, "Dynamic control of redundant manipulators," *Journal of Robotic Systems*, vol. 6, no. 2, pp. 133–148, 1989.

[68] D.-Y. Hwang and B. Hannaford, "Teleoperation performance with a kinematically redundant slave robot," *The International Journal of Robotics Research*, vol. 17, no. 6, pp. 579–597, 1998.

[69] M. Ito, K. Kawatsu, and M. Shibata, "Kinematic control of redundant manipulators for admitting joint range of motion maximally," *IEEJ Journal of Industry Applications*, vol. 6, no. 4, pp. 278–285, 2017.

[70] Y. Jia, N. Xi, Y. Cheng, and S. Liang, "Coordinated motion control of a nonholonomic mobile manipulator for accurate motion tracking," in *2014 IEEE/RSJ International Conference on Intelligent Robots and Systems*, IEEE, 2014, pp. 1635–1640.

[71] L. Jin, Z. Xie, M. Liu, C. Ke, C. Li, and C. Yang, "Novel joint-drift-free scheme at acceleration level for robotic redundancy resolution with tracking error theoretically eliminated," *IEEE/ASME Transactions on Mechatronics*, pp. 1–1, 2020.

[72] O. Kanoun, F. Lamiraux, and P.-B. Wieber, "Kinematic control of redundant manipulators: Generalizing the task-priority framework to inequality task," *IEEE Transactions on Robotics*, vol. 27, no. 4, pp. 785–792, 2011.

[73] E. Karadogan, R. L. Williams, J. N. Howell, R. R. Conatser Jr, *et al.*, "A stiffness discrimination experiment including analysis of palpation forces and velocities," *Simulation in Healthcare*, vol. 5, no. 5, pp. 279–288, 2010.

[74] O. Khatib, "A unified approach for motion and force control of robot manipulators: The operational space formulation," *IEEE Journal on Robotics and Automation*, vol. 3, no. 1, pp. 43–53, Feb. 1987, ISSN: 0882-4967.

[75] O. Khatib, "Inertial Properties in Robotic Manipulation: An Object Level Framework," *International Journal Of Robotics Research*, vol. 13, no. 1, pp. 19–36, 1995.

[76] H. S. Kim, "Mechanism design of haptic devices," *Advances in Haptics*, pp. 283–298, 2010.

[77] ——, "Kinematically redundant parallel haptic device with large workspace," *International Journal of Advanced Robotic Systems*, vol. 9, no. 6, p. 260, 2012. DOI: 10.5772/53279.

[78] S. Kim, S. Y. Lee, K. Jang, Y. Lee, S. Park, and J. Park, "Continuous Task Transition Approach for Robot Controller based on Hierarchical Quadratic Programming," *IEEE Robotics and Automation Letters*, vol. 4, no. 2, pp. 1603–1610, 2019.

[79] R. Konietschke, T. Ortmaier, H. Weiss, G. Hirzinger, and R. Engelke, "Manipulability and accuracy measures for a medical robot in minimally invasive surgery," in *On Advances in Robot Kinematics*. Springer Netherlands, 2004, pp. 191–198.

[80] R. L'Orsa, C. J. Macnab, and M. Tavakoli, "Introduction to haptics for neurosurgeons," *Neurosurgery*, vol. 72, no. Supplement, A139–A153, 2013.

[81] P. Lambert and J. L. Herder, "A 7-dof redundantly actuated parallel haptic device combining 6-dof manipulation and 1-dof grasping," *Mechanism and Machine Theory*, vol. 134, pp. 349–364, 2019, ISSN: 0094-114X.

[82] J. Lee, N. Mansard, and J. Park, "Intermediate desired value approach for task transition of robots in kinematic control," *IEEE Transactions on Robotics*, vol. 28, no. 6, pp. 1260–1277, Dec. 2012.

[83] S. Lee, "Dual redundant arm configuration optimization with task-oriented dual arm manipulability," *IEEE Transactions on Robotics and Automation*, vol. 5, no. 1, pp. 78–97, 1989.

[84] R. Li and H. Qiao, "A survey of methods and strategies for high-precision robotic grasping and assembly tasks—some new trends," *IEEE/ASME Transactions on Mechatronics*, vol. 24, no. 6, pp. 2718–2732, 2019.

[85] W. Li, L. Ding, H. Gao, and M. Tavakoli, "Haptic tele-driving of wheeled mobile robots under nonideal wheel rolling, kinematic control and communication time delay," *IEEE Transactions on Systems, Man, and Cybernetics: Systems*, vol. 50, no. 1, pp. 336–347, Jan. 2020, ISSN: 2168-2232. DOI: 10.1109/TSMC.2017.2738670.

[86] Z. Li, D. Milutinović, and J. Rosen, "Design of a multi-arm surgical robotic system for dexterous manipulation," *ASME Journal of Mechanisms and Robotics*, vol. 8, no. 6, pp. 061 017–061 027, 2016.

[87] R. van der Linde and P. Lammertse, "Hapticmaster – a generic force controlled robot for human interaction," *Industrial Robot: the international journal of robotics research and application*, vol. 30, no. 6, pp. 515–524, 2003.

[88] A. Liu, F. Tendick, K. Cleary, and C. Kaufmann, "A survey of surgical simulation: Applications, technology, and education," *Presence: Teleoperators & Virtual Environments*, vol. 12, pp. 599–614, 2003.

[89] Y. Liu and N. Chopra, "Semi-autonomous teleoperation in task space with redundant slave robot under communication delays," in *2011 IEEE/RSJ International Conference on Intelligent Robots and Systems*, 2011, pp. 679–684.

[90] Y.-C. Liu and N. Chopra, "Control of semi-autonomous teleoperation system with time delays," *Automatica*, vol. 49, no. 6, pp. 1553–1565, 2013.

[91] K. E. MacLean, "Haptic interaction design for everyday interfaces," *Reviews of Human Factors and Ergonomics*, vol. 4, no. 1, pp. 149–194, 2008.

[92] Y. Maddahi, M. Greene, L. S. Gan, T. Hirmer, R. L'Orsa, S. Lama, G. R. Sutherland, and K. Zareinia, "Performance evaluation of a surgical telerobotic system using kinematic indices of the master hand-controller," in *International Conference on Human Haptic Sensing and Touch Enabled Computer Applications, EuroHaptics 2014*, M. Auvray and C. Duriez, Eds. Springer Berlin Heidelberg, 2014, pp. 167–175.

[93] J. Martin and J. Savall, "Mechanisms for haptic torque feedback," in *First Joint Eurohaptics Conference and Symposium on Haptic Interfaces for Virtual Environment and Teleoperator Systems. World Haptics Conference*, IEEE, 2005, pp. 611–614.

[94] T. H. Massie and J. K. Salisbury, "The phantom haptic interface: A device for probing virtual objects," in *Proceedings of the ASME Dynamic Systems and Control Division*, 1994, pp. 295–301.

[95] T. A. Mattei, A. H. Rodriguez, D. Sambhara, and E. Mendel, "Current state-of-the-art and future perspectives of robotic technology in neurosurgery," *Neurosurgical review*, vol. 37, no. 3, pp. 357–366, 2014.

[96] H. Mayer, I. Nagy, A. Knoll, E. U. Braun, R. Bauernschmitt, and R. Lange, "Haptic feedback in a telepresence system for endoscopic heart surgery," *Presence*, vol. 16, no. 5, pp. 459–470, Oct. 2007, ISSN: 1054-7460. DOI: 10.1162/pres.16.5.459.

[97] H. Mayer, I. Nagy, A. Knoll, E. U. Braun, R. Bauernschmitt, and R. Lange, "Haptic feedback in a telepresence system for endoscopic heart surgery," *Presence: Teleoperators and Virtual Environments*, vol. 16, no. 5, pp. 459–470, 2007.

[98] W. A. McNeely, K. D. Puterbaugh, and J. J. Troy, "Six degree-of-freedom haptic rendering using voxel sampling," in *ACM SIGGRAPH 2005 Courses*, 2005, 42–es.

[99] C. Melchiorri, "Multiple whole-limb manipulation: An analysis in the force domain," *Robotics and Autonomous Systems*, vol. 20, no. 1, pp. 15–38, 1997.

[100] M. Mihelj, "Human arm kinematics for robot based rehabilitation," *Robotica*, vol. 24, no. 3, pp. 377–383, 2006.

[101] M. V. Minniti, F. Farshidian, R. Grandia, and M. Hutter, "Whole-body MPC for a dynamically stable mobile manipulator," *IEEE Robotics and Automation Letters*, vol. 4, no. 4, pp. 3687–3694, 2019.

[102] K. Nagatani, T. Hirayama, A. Gofuku, and Y. Tanaka, "Motion planning for mobile manipulator with keeping manipulability," in *IEEE/RSJ International Conference on Intelligent Robots and Systems*, IEEE, vol. 2, 2002, pp. 1663–1668.

[103] Y. Nakamura and H. Hanafusa, "Inverse Kinematic Solutions With Singularity Robustness for Robot Manipulator Control," *Journal of Dynamic Systems, Measurement, and Control*, vol. 108, no. 3, pp. 163–171, 1986.

[104] J. Nakanishi, R. Cory, M. Mistry, J. Peters, and S. Schaal, "Operational space control: A theoretical and empirical comparison," *International Journal of Robotics Research*, vol. 27, no. 6, pp. 737–757, 2008, ISSN: 02783649.

[105] N. Nath, E. Tatlicioglu, and D. M. Dawson, "Teleoperation with kinematically redundant robot manipulators with sub-task objectives," *Robotica*, vol. 27, pp. 1027–1038, 2009.

[106] B. Navarro, A. Cherubini, A. Fonte, G. Poisson, and P. Fraisse, "A framework for intuitive collaboration with a mobile manipulator," in *2017 IEEE/RSJ International Conference on Intelligent Robots and Systems (IROS)*, IEEE, 2017, pp. 6293–6298.

[107] I. Nisky, M. H. Hsieh, and A. M. Okamura, "Uncontrolled manifold analysis of arm joint angle variability during robotic teleoperation and freehand movement of surgeons and novices," *IEEE Transactions on Biomedical Engineering*, vol. 61, no. 12, pp. 2869–2881, Dec. 2014, ISSN: 15582531.

[108] M. K. O'Malley and A. Gupta, "Haptic interfaces," in *HCI Beyond the GUI*, ser. Interactive Technologies, P. Kortum, Ed., San Francisco: Morgan Kaufmann, 2008, pp. 25–73, ISBN: 978-0-12-374017-5. DOI: https://doi.org/10.1016/B978-0-12-374017-5.00002-X. [Online]. Available: http://www.sciencedirect.com/science/article/pii/B978012374017500002X.

[109] A. M. Okamura, "Methods for haptic feedback in teleoperated robot-assisted surgery," *Industrial Robot: An International Journal*, vol. 31, no. 6, pp. 499–508, 2004.

[110] M. V. Ottermo, M. Øvstedal, T. Langø, Ø. Stavdahl, Y. Yavuz, T. A. Johansen, and R. Mårvik, "The role of tactile feedback in laparoscopic surgery," *Surgical Laparoscopy Endoscopy & Percutaneous Techniques*, vol. 16, no. 6, pp. 390–400, 2006.

[111] E. Papadopoulos and J. Poulakakis, "Planning and model-based control for mobile manipulators," in *Proceedings. 2000 IEEE/RSJ International Conference on Intelligent Robots and Systems (IROS 2000)(Cat. No. 00CH37113)*, IEEE, vol. 3, 2000, pp. 1810–1815.

[112] A. D. Prete, "Joint position and velocity bounds in discrete-time acceleration/torque control of robot manipulators," *IEEE Robotics and Automation Letters*, vol. 3, no. 1, pp. 281–288, 2018.

[113] J. P. Puga and L. E. Chiang, "Optimal trajectory planning for a redundant mobile manipulator with non-holonomic constraints performing push–pull tasks," *Robotica*, vol. 26, no. 3, pp. 385–394, 2008.

[114] R. Randell, N. Alvarado, S. Honey, J. Greenhalgh, P. Gardner, A. Gill, D. C. Jayne, A. Kotze, A. Pearman, and D. Dowding, "Impact of robotic surgery on decision making: Perspectives of surgical teams," *AMIA ... Annual Symposium proceedings. AMIA Symposium*, vol. 2015, pp. 1057–66, 2015.

[115] C. Richard and M. Cutkosky, "The effects of real and computer generated friction on human performance in a targeting task," in *Proceedings of the ASME Dynamic Systems and Control Division*, vol. 69, 2000, pp. 1101–1108.

[116] L. Rozo, N. Jaquier, S. Calinon, and D. G. Caldwell, "Learning manipulability ellipsoids for task compatibility in robot manipulation," in *2017 IEEE/RSJ International Conference on Intelligent Robots and Systems (IROS)*, Sep. 2017, pp. 3183–3189.

[117] S. E. Salcudean and T. D. Vlaar, "On the emulation of stiff walls and static friction with a magnetically levitated input/output device," *Journal of Dynamic Systems, Measurement, and Control*, vol. 119, no. 1, pp. 127–132, 1997.

[118] J. K. Salisbury Jr, A. J. Madhani, G. S. Guthart, G. D. Niemeyer, and E. F. Duval, *Master having redundant degrees of freedom*, Jan. 2004.

[119] J. K. Salisbury and J. J. Craig, "Articulated Hands: Force Control and Kinematic Issues," *The International Journal of Robotics Research*, vol. 1, no. 1, pp. 4–17, 1982.

[120] E. Samur, *Performance metrics for haptic interfaces*. Springer Science & Business Media, 2012.

[121] S. Schaal and N. Schweighofer, "Computational motor control in humans and robots," *Current Opinion in Neurobiology*, vol. 15, no. 6, pp. 675–682, 2005, Motor sytems / Neurobiology of behaviour, ISSN: 0959-4388.

[122] P. Schiavone, F. Chassat, T. Boudou, E. Promayon, F. Valdivia, and Y. Payan, "In vivo measurement of human brain elasticity using a light aspiration device," *Medical Image Analysis*, vol. 13, no. 4, pp. 673–678, 2009, ISSN: 1361-8415.

[123] H. Seraji, "A unified approach to motion control of mobile manipulators," *The International Journal of Robotics Research*, vol. 17, no. 2, pp. 107–118, 1998.

[124] M. Sharifi, H. Salarieh, S. Behzadipour, and M. Tavakoli, "Impedance control of non-linear multi-dof teleoperation systems with time delay: Absolute stability," *IET Control Theory Applications*, vol. 12, no. 12, pp. 1722–1729, 2018, ISSN: 1751-8644.

[125] M. Sharifi, S. Behzadipour, H. Salarieh, and M. Tavakoli, "Cooperative modalities in robotic tele-rehabilitation using nonlinear bilateral impedance control," *Control Engineering Practice*, vol. 67, pp. 52–63, 2017.

[126] M. Sharifi, H. Salarieh, S. Behzadipour, and M. Tavakoli, "Patient-robot-therapist collaboration using resistive impedance controlled telerobotic systems subjected to time delays," *Journal of Mechanisms and Robotics*, vol. 10, no. 6, pp. 061 003–17, 2018.

[127] D. H. Shin, B. S. Hamner, S. Singh, and M. Hwangbo, "Motion planning for a mobile manipulator with imprecise locomotion," in *Proceedings 2003 IEEE/RSJ International Conference on Intelligent Robots and Systems (IROS 2003)(Cat. No. 03CH37453)*, IEEE, vol. 1, 2003, pp. 847–853.

[128] B. Siciliano, "Kinematic control of redundant robot manipulators: A tutorial," *Journal of Intelligent and Robotic Systems*, vol. 3, no. 3, pp. 201–212, 1990, ISSN: 09210296.

[129] B. Siciliano, L. Sciavicco, L. Villani, and G. Oriolo, *Robotics - Modelling, Planning and Control*. Springer-Verlag London, 2009, p. 632. DOI: 10.1007/978-1-84628-642-1.

[130] M. Sitti, H. Hashimoto, and O. Kaynak, "Teleoperated nano scale object manipulation," *Recent Advances on Mechatronics*, pp. 322–335, 1999.

[131] S. Sra, "A new metric on the manifold of kernel matrices with application to matrix geometric means," in *Advances in Neural Information Processing Systems*, Curran Associates, Inc., 2012, pp. 144–152.

[132] ——, "Positive definite matrices and the s-divergence," *Proceedings of the American Mathematical Society*, vol. 144, no. 7, pp. 2787–2797, 2016.

[133] L. Stocco and S. E. Salcudean, "A Coarse-Fine approach to force-reflecting hand controller design," in *Proceedings of IEEE International Conference on Robotics and Automation*, vol. 1996, 1996, pp. 404–410, ISBN: 0-7803-2988-0. DOI: 10.1109/ROBOT.1996.503810.

[134] L. J. Stocco, S. E. Salcudean, and F. Sassani, "Optimal kinematic design of a haptic pen," *IEEE/ASME Transactions on Mechatronics*, vol. 6, no. 3, pp. 210–220, 2001, ISSN: 10834435.

[135] X. Sun, "A methodology for situated and effective design of haptic devices," PhD thesis, KTH Royal Institute of Technology, 2017.

[136] G. Sutherland, S. Lama, L. S. Gan, S. Wolfsberger, and K. Zareinia, "Merging machines with microsurgery: clinical experience with neuroArm.," *Journal of neurosurgery*, vol. 118, no. 3, pp. 521–9, 2013.

[137] H. Z. Tan, X. D. Pang, N. I. Durlach, *et al.*, "Manual resolution of length, force, and compliance," *Advances in Robotics*, vol. 42, pp. 13–18, 1992.

[138] H. Z. Tan, M. A. Srinivasan, B. Eberman, and B. Cheng, "Human factors for the design of force-reflecting haptic interfaces," *Dynamic Systems and Control*, vol. 55, no. 1, pp. 353–359, 1994.

[139] M. Tavakoli, A. Aziminejad, R. Patel, and M. Moallem, "High-fidelity bilateral teleoperation systems and the effect of multimodal haptics," *IEEE Transactions on Systems, Man and Cybernetics – Part B*, vol. 37, no. 6, pp. 1512–1528, Dec. 2007.

[140] M. Tavakoli, R. V. Patel, and M. Moallem, "A haptic interface for computer-integrated endoscopic surgery and training," *Virtual Reality*, vol. 9, no. 2-3, pp. 160–176, 2006, ISSN: 13594338.

[141] F. Tendick, M. C. Cavusoglu, N. Dhruv, and A. Sherman, "Maximizing the sensation of compliance in teleoperative surgery," in *Intl. Symp. Robotics with Applications (ISORA)*, 2000.

[142] A. Tobergte, P. Helmer, U. Hagn, P. Rouiller, S. Thielmann, S. Grange, A. Albu-Schäffer, F. Conti, and G. Hirzinger, "The sigma. 7 haptic interface for mirosurge: A new bi-manual surgical console," in *2011 IEEE/RSJ International Conference on Intelligent Robots and Systems*, IEEE, 2011, pp. 3023–3030.

[143] A. L. Trejos, R. V. Patel, and M. D. Naish, "Force sensing and its application in minimally invasive surgery and therapy: A survey," *Proceedings of the Institution of Mechanical Engineers, Part C: Journal of Mechanical Engineering Science*, vol. 224, no. 7, pp. 1435–1454, 2010.

[144] M. J. Tsai and Y. H. Chiou, "Manipulability of manipulators," *Mechanism and Machine Theory*, vol. 25, no. 5, pp. 575–585, 1990.

[145] M. Ueberle, N. Mock, and M. Buss, "VISHARD10, a novel hyper-redundant haptic interface," in *Proceedings - 12th International Symposium on Haptic Interfaces for Virtual Environment and Teleoperator Systems, HAPTICS*, 2004, pp. 58–65.

[146] F. Vigoriti, F. Ruggiero, V. Lippiello, and L. Villani, "Control of redundant robot arms with null-space compliance and singularity-free orientation representation," *Robotics and Autonomous Systems*, vol. 100, pp. 186–193, 2018.

[147] D. Wahrmann, A.-C. Hildebrandt, C. Schuetz, R. Wittmann, and D. Rixen, "An autonomous and flexible robotic framework for logistics applications," *Journal of Intelligent & Robotic Systems*, vol. 93, no. 3-4, pp. 419–431, 2019.

[148] G. D. White, R. M. Bhatt, C. P. Tang, and V. N. Krovi, "Experimental evaluation of dynamic redundancy resolution in a nonholonomic wheeled mobile manipulator," *IEEE/ASME Transactions on Mechatronics*, vol. 14, no. 3, pp. 349–357, 2009.

[149] F. A. Wichmann and N. J. Hill, "The psychometric function: I. fitting, sampling, and goodness of fit," *Perception & Psychophysics*, vol. 63, no. 8, pp. 1293–1313, Nov. 2001, ISSN: 1532-5962.

[150] P. Wisanuvej, G. Gras, K. Leibrandt, P. Giataganas, C. A. Seneci, J. Liu, and G.-z. Yang, "Master Manipulator Designed for Highly Articulated Robotic Instruments in Single Access Surgery," in *IEEE/RSJ International Conference on Intelligent Robots and Systems (IROS)*, 2017.

[151] L. Xiao, B. Liao, S. Li, Z. Zhang, L. Ding, and L. Jin, "Design and analysis of ftznn applied to the real-time solution of a nonstationary lyapunov equation and tracking control of a wheeled mobile manipulator," *IEEE Transactions on Industrial Informatics*, vol. 14, no. 1, pp. 98–105, 2017.

[152] H. Xing, K. Xia, L. Ding, H. Gao, G. Liu, and Z. Deng, "Unknown geometrical constraints estimation and trajectory planning for robotic door-opening task with visual teleoperation assists," *Assembly Automation*, vol. 39, no. 3, pp. 479–488, 2019.

[153] D. Xu, D. Zhao, J. Yi, and X. Tan, "Trajectory tracking control of omnidirectional wheeled mobile manipulators: Robust neural network-based sliding mode approach," *IEEE Transactions on Systems, Man, and Cybernetics, Part B (Cybernetics)*, vol. 39, no. 3, pp. 788–799, 2009.

[154] T. Yamamoto, N. Abolhassani, S. Jung, A. M. Okamura, and T. N. Judkins, "Augmented reality and haptic interfaces for robot-assisted surgery," *The International Journal of Medical Robotics and Computer Assisted Surgery*, vol. 8, no. 1, pp. 45–56, 2012.

[155] G.-Z. Yang *et al.*, "Medical robotics—regulatory, ethical, and legal considerations for increasing levels of autonomy," *Science Robotics*, vol. 2, no. 4, 2017. DOI: 10.1126/scirobotics.aam8638.

[156] T. Yoshikawa, "Manipulability of Robotic Mechanisms," *The International Journal of Robotics Research*, vol. 4, no. 2, pp. 3–9, 1985.

[157] ——, "Manipulability of Robotic Mechanisms," *The International Journal of Robotics Research*, vol. 4, no. 2, pp. 3–9, 1985.

[158] A. Zakerimanesh, F. Hashemzadeh, A. Torabi, and M. Tavakoli, "Controlled synchronization of nonlinear teleoperation in task-space with time-varying delays," *International Journal of Control, Automation and Systems*, vol. 0, no. 0, pp. 1–9, 2019.

[159] K. Zareinia, Y. Maddahi, C. Ng, N. Sepehri, and G. R. Sutherland, "Performance evaluation of haptic hand-controllers in a robot-assisted surgical system," *The International Journal of Medical Robotics and Computer Assisted Surgery*, vol. 11, no. 4, pp. 486–501, Dec. 2015, ISSN: 14785951. DOI: 10.1002/rcs.1637.

[160] H. Zhang, Y. Jia, and N. Xi, "Sensor-based redundancy resolution for a nonholonomic mobile manipulator," in *2012 IEEE/RSJ International Conference on Intelligent Robots and Systems*, IEEE, 2012, pp. 5327–5332.

[161] X. Zhang, M. Li, J. H. Lim, Y. Weng, Y. W. D. Tay, H. Pham, and Q.-C. Pham, "Large-scale 3d printing by a team of mobile robots," *Automation in Construction*, vol. 95, pp. 98–106, 2018, ISSN: 0926-5805.

[162] Z. Zhang and Y. Zhang, "Variable joint-velocity limits of redundant robot manipulators handled by quadratic programming," *IEEE/ASME Transactions on Mechatronics*, vol. 18, no. 2, pp. 674–686, 2012.

Appendix A

Reconfiguration of Redundant Mobile Manipulators for Enhancing Force Exertion Capability

Appendix A presents a novel method to enhance the force exertion capability of a Wheeled Mobile Manipulator (WMM). Also, to maintain precise end-effector trajectory tracking, this chapter proposes a novel coordination method between the mobile base and the manipulator via a weighting matrix. The work presented here can be extended to design and control a Wheeled Mobile Haptic Interface (WMHI). The integration of a mobile base with a haptic interface can enlarge its workspace to be unlimited and provide it with more degrees of freedoms. Therefore, this work in the present form is provided in Appendix A. A version of this chapter is published as H. Xing, A. Torabi, L. Ding, H. Gao, Z. Deng, and M. Tavakoli, "Enhancement of Force Exertion Capability of a Mobile Manipulator by Kinematic Reconfiguration," IEEE Robotics and Automation Letters, 2020. Also, selected for presentation at the IEEE/RSJ International Conference on Intelligent Robots and Systems, Las Vegas, USA, 2020. Hongjun Xing and Ali Torabi have equal contribution in this work.

A.1 Introduction

Due to their great mobility and desirable operation capability, wheeled mobile manipulators have been widely employed in many applications, including logistics, disaster rescue, and home/service applications [43], [147]. The integration of a mobile base with a standard manipulator can greatly enlarge its workspace and provide it with more degrees of freedom (DOFs). However, this combination will also bring new challenges. First, the models and operating conditions (i.e., interacting environments) for the mobile base and the manipulator are different; the base usually moves in an unstructured environment with complex dynamics and the manipulator is often in free/contact motion [160]. Second, a Wheeled Mobile Manipulator (WMM) is often a kinematically redundant robotic system due to the mix of the mobile base and the manipulator – a redundant robot has more DOFs than minimally required for performing tasks. How to use the redundancy of the WMM to execute sub-tasks (i.e., secondary goals besides the primary goal, which is typically trajectory tracking) remains an interesting research field.

Kinematic modelling and motion control for WMMs have been conducted in many studies following two fundamental approaches. Some authors add the mobile base-imposed constraints directly to the manipulator model [123], which focuses on methods to decouple the control of the two subsystems but cannot control the entire WMM system via one controller. Others explicitly formulate the admissible motions with respect to the base constraints [42], which consider the WMM as one system with a dynamic effect between the base and the manipulator taken into account. The latter approach is adopted in this work because the tasks in this chapter require that the manipulator and the base operate simultaneously.

The entire model for the WMM is usually redundant for a given task, which means there are more DOFs in the system than the task needs. Many redundancy resolution methods for standard redundant manipulators can be extended to WMMs including the reduced gradient-based method [41], the damped least-squares inverse Jacobian method [103], and the weighted inverse

Jacobian method [24]. Furthermore, the self-motion of the WMM can be used to execute sub-tasks, such as joint limit and obstacle avoidance, manipulability maximization, or singularity avoidance [15], [157], [160].

Most of the previous work views the mobile base as a new addition to the manipulator without considering the inherent differences in the dynamics and working environments between them. This approach results in considerable tracking errors for the end-effector motion due to the typically low positioning precision of the mobile base [152]. For kinematic control, Jia *et al.* [70] addressed this discrepancy between the mobile base and the manipulator and proposed a coordinated motion control method based on adaptive motion distribution for nonholonomic mobile manipulator without considering the joint limits (position, velocity, and acceleration). For dynamic control, many other dynamic control techniques can be employed including neural networks, adaptive control [6], [153].

Besides trajectory following, a WMM can be employed in payload handling tasks where it has to apply large forces to its environment. In these cases, for enhancing the force exertion capability, the redundancy of the WMM can be utilized via its null-space by defining a proper objective (i.e., the sub-task). Force manipulability ellipsoid, proposed by Yoshikawa [157], is a useful tool for visualizing the force transmission characteristics of a robot at a given configuration. Later, this measure has been extended to mobile manipulators [15]. The force manipulability ellipsoid is a measure showing the force exertion capability of a robot in all directions in the Cartesian space, and it can be enlarged using a null-space controller for the redundant robot [15]. Chiu [34] proposed the concept of task compatibility, which can optimize the velocity or force requirements in a given direction. With the consideration of joint torque differences, Ajoudani *et al.* [5] improved this concept by introducing a weighting matrix to scale the joint torques.

In the literature, the studies about improving the trajectory tracking precision have been conducted mostly in the context of dynamic control of WMMs where complicated control strategies have been used yet the system's stability is usually hard to be guaranteed [151]. In the context of kinematic control,

the coordinated control of a WMM usually ignores the difference in the motion tracking accuracies achievable by the mobile base versus the manipulator [106], and the manipulator's joint limits (position, velocity, and acceleration) are usually not considered [70]. For enhancing the manipulability, most of the recent work only considers the null-space optimization, without considering any optimization in Cartesian space for better manipulability.

The main contribution of this chapter is to propose a method to enhance the force exertion capability of a WMM in any given direction while trying the best to pursue the tracking precision of the end-effector. With this novel approach, these two goals can be achieved by first employing a weighting matrix to decompose the total desired motion for the WMM to a motion for the mobile base and another motion for the manipulator. Second, we enhance the Directional Manipulability (DM) of the manipulator in both the Cartesian space and the null-space, which is defined with consideration of joint torque differences. It should be emphasized that it is a trade-off between acquiring high tracking accuracy and achieving desirable force exertion capability.

In terms of the primary goal of trajectory tracking, the manipulator's joint limits are taken into account and, where possible, it is tried to employ only the manipulator joints due to the slippage and modelling errors of the mobile base. When the desired end-effector trajectory is beyond the workspace of the manipulator, however, the controller will transfer some of the total motion requirements to the mobile base. In terms of the secondary goal of maximizing the force exertion capability, the first step to improve the DM is by adjusting the end-effector position via Cartesian space control, and then by using the self-motion via null-space control.

The remainder of this chapter is organized as follows. In Section A.2, the kinematic model for a WMM is provided. In Section A.3, kinematic control of the WMM with consideration of DM enhancement and trajectory tracking is presented. Experiments that demonstrate the validity and performance of the proposed method are presented in Section A.4. Section A.5 concludes the manuscript.

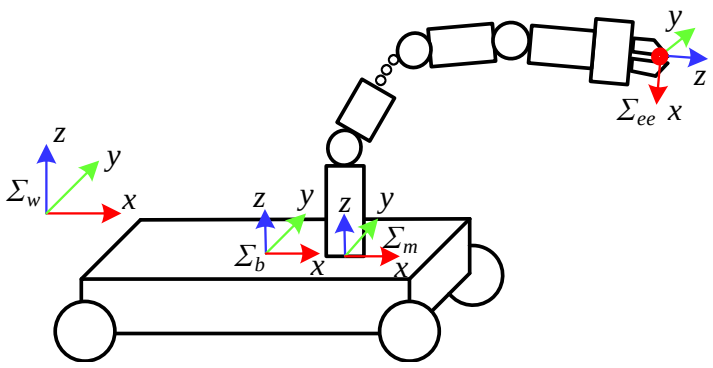

Figure A.1: Kinematic model representation of the Wheeled Mobile Manipulator

A.2 Kinematic Modeling of Wheeled Mobile Manipulators

In order to plan the motion of the end-effector of a wheeled mobile manipulator, the kinematics for the mobile manipulator should be established. The kinematic modelling contains two parts: the first is the forward kinematics, which given the joint positions calculates the robot's end-effector pose (position and orientation) and the second is the inverse kinematics that given the end-effector pose leads to the joint positions. For a redundant robot, the latter is usually an optimization process in which the redundancy of the robot is utilized in different ways to realize different sub-tasks in parallel to the main task [33].

The forward kinematics for a mobile manipulator can be derived from the kinematic models of the two subsystems, i.e., the mobile base and the manipulator. Fig. A.1 shows a standard WMM with reference coordinates defined. We denote Σ_w, Σ_b, Σ_m, and Σ_{ee} as the world reference frame, mobile base frame, manipulator reference frame, and end-effector frame, respectively. The forward kinematics of the manipulator with respect to Σ_m can be expressed as

$$x_m = h_m(q_m), \tag{A.1}$$

where $x_m \in \mathbb{R}^r$ is the pose of the end-effector in Σ_m, $h_m(q_m)$ denotes the

forward kinematics for the manipulator, and $q_m \in \mathbb{R}^m$ is the generalized manipulator coordinate. Then, the forward kinematics for the entire WMM can be expressed as

$$x(q) = x_w(q) = h(q_b, q_m) = Tq_b + T_b^w(q_b)T_m^b h_m(q_m), \tag{A.2}$$

where $x \in \mathbb{R}^r$ is the pose of the end-effector in Σ_w; $q = [q_b^{\mathrm{T}}, q_m^{\mathrm{T}}]^{\mathrm{T}} \in \mathbb{R}^n$, $q_b \in \mathbb{R}^{n_b}$ are the generalized coordinates for the WMM and the mobile base, respectively; $T \in \mathbb{R}^{r \times n_b}$ is a constant transformation matrix, which expresses the relationship between the coordinates of the mobile base and the pose of the end-effector; $T_b^w(q_b) \in \mathbb{R}^{r \times r}$ is the transformation matrix from Σ_b to Σ_w; and $T_m^b \in \mathbb{R}^{r \times r}$ is a constant matrix to express the origin of Σ_m in Σ_b.

Assuming a pure rolling contact between the wheels of the mobile base and the ground (i.e., no slippage), the mobile base kinematic model can be derived as

$$\dot{q}_b = P(q_b)v_b, \tag{A.3}$$

where $v_b \in \mathbb{R}^b$ is the velocity of the wheels, and $P(q_b) \in \mathbb{R}^{n_b \times b}$ is the constraint matrix of the base (holonomic or nonholonomic), which transfers the wheel velocities to the generalized base velocities. The model for slippery wheels can be found in other literature from our group [85] but we will not consider wheel slippage in this work. The generalized velocities for the manipulator can be expressed using the joint velocities as

$$\dot{q}_m = v_m, \tag{A.4}$$

where $v_m \in \mathbb{R}^m$ is the velocity of the manipulator joints.

The complete velocity input vector for the WMM can be expressed as $v = [v_b^{\mathrm{T}}, v_m^{\mathrm{T}}]^{\mathrm{T}} \in \mathbb{R}^{b+m}$. The end-effector velocity is actually the differential of (A.2) with respect to time. Combining (A.3) and (A.4) yields

$$\begin{aligned} \dot{x} = J_q(q)\dot{q} &= [J_b(q) \quad J_m(q)] \begin{bmatrix} \dot{q}_b \\ \dot{q}_m \end{bmatrix} \\ &= [J_b(q) \quad J_m(q)] \begin{bmatrix} P(q_b)v_b \\ v_m \end{bmatrix} \\ &= [J_b(q)P(q_b) \quad J_m(q)] \begin{bmatrix} v_b \\ v_m \end{bmatrix} = J(q)v, \end{aligned} \tag{A.5}$$

where $J_b(q) \in \mathbb{R}^{r\times n_b}$ is the Jacobian of the mobile base, $J_m(q) \in \mathbb{R}^{r\times m}$ is the Jacobian of the manipulator, $J_q(q) \in \mathbb{R}^{r\times n}$ is the Jacobian of the unconstrained WMM, and $J(q) \in \mathbb{R}^{r\times(b+m)}$ is the Jacobian of the WMM. It is worth noting that there are two Jacobians for a WMM just because the generalized velocity $\dot{q}_b$ for the mobile base is not its wheel velocity v_b.

The inverse kinematics of the WMM can be built by resorting to an optimization technique that solves the set of generalized coordinates given an end-effector desired pose. The cost function for the WMM can be written as

$$\begin{aligned} \min_{\dot{q}} \; & H(\dot{q}) = \frac{1}{2}(\dot{q}-\dot{q}_0)^{\mathrm{T}} Q (\dot{q}-\dot{q}_0), \\ \text{s.t.} \quad & \dot{x} = J_q(q)\dot{q}, \end{aligned} \tag{A.6}$$

where $Q \in \mathbb{R}^{n\times n}$ is a symmetric and positive definite weighting matrix, $\dot{q}_0 \in \mathbb{R}^n$ is the desired value for the joint velocity, and $J_q(q) \in \mathbb{R}^{r\times n}$ is the robot Jacobian as shown in (A.5). Then, we can obtain the solution to the optimization problem in (A.6) as (for brevity the dependence of the variables upon the joint variables are omitted)

$$\dot{q} = J_q^{\dagger}\dot{x} + (I_{n\times n} - J_q^{\dagger}J_q)\dot{q}_0, \tag{A.7}$$

where $J_q^{\dagger} = Q^{-1}J_q^{\mathrm{T}}(J_qQ^{-1}J_q^{\mathrm{T}})^{-1}$ is the weighted pseudoinverse of J_q, and $I_{n\times n}$ is an $n \times n$ identity matrix. The method to choose Q will be discussed in Section A.3.2.

A.3 Kinematic Control of Mobile Manipulators with Directional Manipulability Enhancement

A.3.1 Directional Manipulability

Mobile manipulation can realize mobility and manipulability simultaneously, and for a redundant robot, the redundancy can be used to execute sub-tasks via the null-space controller. As shown in (A.7), the different choice of $\dot{q}_0 = \nabla_q H(q)$ can achieve different objectives without affecting the main task $\dot{x}$, since all the motion of $\dot{q}_0$ is projected in the null-space of J_q, and $H(q)$ is the

differentiable objective function. It should be noted that the optimization in this chapter is focused on the manipulator since the mobile base is mainly used to enhance the mobility of the system.

Yoshikawa first provided velocity manipulability ellipsoid as a design quality measure [157] defined as $H_1(q_m) = \sqrt{\det[J_m J_m^{\mathrm{T}}]}$. The maximization of H_1 can simultaneously maximize the "distance" of the manipulator from singularities and let the manipulator use the least joint velocities to generate the same end-effector velocities. However, the focus of this chapter is on force exertion capability similar to the definition of force manipulability ellipsoid. It is essential to note that the force manipulability ellipsoid is the inverse of the velocity manipulability ellipsoid. This means that the direction along which the manipulator has the largest force/torque capability is perpendicular to the direction along which the manipulator uses the least joint velocities. This is a very important optimization objective, especially when the manipulator moves in contact environment. For a specific task, however, it is not necessary to pursue the maximum force manipulability for every direction. It is just a waste of optimization ability. Instead, the force manipulability should be enhanced in a needed direction for the best results. Also, the torque limit differences of the joints are not considered in force manipulability, which is a disadvantage of this measure. If a specific optimization direction for the end-effector in the world frame, say $u \in \mathbb{R}^r$, is given, with the consideration of the joint torque limits of the manipulator, the directional manipulability can be defined as [5]

$$H_2(q) = [u^{\mathrm{T}}(J_m W_\tau^{\mathrm{T}} W_\tau J_m^{\mathrm{T}})u]^{-1/2}, \tag{A.8}$$

where $W_\tau = \mathrm{diag}[\frac{1}{\tau_{\lim_1}} \ \frac{1}{\tau_{\lim_2}} \ \cdots \ \frac{1}{\tau_{\lim_m}}]$ is a scaling matrix to normalize the joint torques, and $\tau_{\lim_i}$ represents the torque limit of the i^{th} joint.

Unlike the traditional method attempting to maximize the manipulability measure only in null-space, this chapter enhances it in both Cartesian space and null-space. As shown in (A.8), if the direction u is assumed to have no relation with the generalized coordinates of the manipulator q_m, then the

partial derivative of H_2 to $q_{m,i}$ can be calculated as

$$\begin{aligned} \nabla_{q_{m,i}} H_2 &= \frac{-H_2^{-\frac{3}{2}}}{2} \frac{\partial (u^{\mathrm{T}} J_m W_\tau^{\mathrm{T}} W_\tau J_m^{\mathrm{T}} u)}{\partial q_{m,i}} \\ &= \frac{-u^{\mathrm{T}} H_2^{-\frac{3}{2}}}{2} \frac{\partial (J_m W_\tau^{\mathrm{T}} W_\tau J_m^{\mathrm{T}})}{\partial q_{m,i}} u, \end{aligned} \tag{A.9}$$

where $q_{m,i}$ is the i^{th} joint coordinate and $\nabla_{q_m} H_2 = [\nabla_{q_{m,1}} H_2 \ \cdots \ \nabla_{q_{m,m}} H_2]$.

For optimization in the Cartesian space, the partial derivative of H_2 to x_i can be expressed as

$$\nabla_{x_i} H_2 = \frac{\partial H_2}{\partial q_m} \frac{\partial q_m}{\partial x_i} = \nabla_{q_{m,i}} H_2 \ J_{m,i}^{\dagger}, \tag{A.10}$$

where x_i is the i^{th} component of the end-effector pose and $\nabla_x H_2 = [\nabla_{x_1} H_2 \ \cdots \ \nabla_{x_r} H_2]$. It should be emphasized that the optimization on the Cartesian space and the null-space cannot be conducted simultaneously to avoid instability of the robotic system.

It is worth mentioning that by enhancing DM of the manipulator in a given direction, the manipulator will only change to a configuration close to singularity (not reach singularity) to derive the optimal force exertion capability. If the manipulator is too close to singularity to make the system unstable, then, the user can avoid this by using damped least-squares methods [21] or adding another optimization objective, such as H_1, however, this operation may reduce the maximal force exertion capability of the system.

A.3.2 Weighting Matrix Adjustment

The weighting matrix in (A.7) plays an essential role in splitting the joint motion for the WMM when the desired end-effector Cartesian movement is determined. For a WMM, the properties for the mobile base and the manipulator, such as mass and inertia, are different and the working conditions for them are not the same either. Usually, the positioning precision of the mobile base is worse than that of the manipulator and, thus, it is desirable to command more joint motion to the manipulator of the WMM.

The weighting matrix Q in (A.7) is replaced by defining a new variable $W_x = Q^{-1}$ in the following sections for better expression. Also, instead of

using the unconstrained Jacobian J_q in (A.7), we choose the entire system Jacobian J in (A.5) to command motion to each actuator of the WMM. The weighted pseudoinverse of J is expressed as

$$J^{\dagger} = W_x J^{\mathrm{T}} (J W_x J^{\mathrm{T}})^{-1} \tag{A.11}$$

with the weighting matrix $W_x \in \mathbb{R}^{(b+m)\times(b+m)}$ defined as

$$W_x = \begin{bmatrix} \gamma I_{b\times b} & 0_{b\times m} \\ 0_{n_m\times b} & (1-\gamma) I_{m\times m} \end{bmatrix}, \tag{A.12}$$

where $\gamma \in [0, 1]$ is the parameter determining the motion weighting between the mobile base and the manipulator. $\gamma = 0$ means that the entire end-effector motion depends on the manipulator, $\gamma = 1$ means that the motion is realized solely by the mobile base, and $\gamma \in (0, 1)$ means that the end-effector motion is achieved via both the manipulator and the mobile base.

To further demonstrate this method, consider a simple 3-DOF serial manipulator with joint coordinate vector denoted as $q = [q_1, q_2, q_3]^{\mathrm{T}}$, if the additional joint motion requirement besides the trajectory tracking task is expressed as $q_1 = 2q_2 = 4q_3$, then, the corresponding weighting matrix for this system can be defined as $W_x = \mathrm{diag}[1, 1/2, 1/4]$, which may not achieve the desired joint motion trajectory (due to the Cartesian space trajectory), but can obtain a desirable one.

When the range or velocity requirement of the task exceeds the limit of the manipulator, the mobile base should be involved. Assuming that the WMM is controlled at the velocity level, the constraints on joint velocity are locally calculated taking into account the joint range, velocity and acceleration bounds of the manipulator. The motion limit of the manipulator's joints can be expressed at the current configuration as [51]

$$\dot{Q}_{\min}(q_m) \leqslant \dot{q}_m \leqslant \dot{Q}_{\max}(q_m), \tag{A.13}$$

where $\dot{Q}_{\min}(q_m)$ and $\dot{Q}_{\min}(q_m)$ are the upper and lower joint velocity limits of the manipulator, respectively. If the velocity command of the manipulator joints $\dot{q}_m$ exceeds the velocity limit defined in (A.13), which means that the

sole manipulator motion cannot cover the end-effector motion requirement, then γ should be increased to split more motions to the base.

The parameter γ can be adjusted as

$$\gamma = \begin{cases} 0 & \text{if } \eta \leqslant \epsilon \\ \eta & \text{if } \epsilon < \eta \leqslant 1 \\ 1 & \text{if } \eta > 1, \end{cases} \tag{A.14}$$

where ϵ is the upper limit of the motion distribution without mobile base, which will be determined by the user through trial and error, and

$$\eta = \max \left\{ \frac{\left|\dot{q}_{m,i}\right|}{\left|\dot{Q}_{\max,i}\right|}, \frac{\left|\dot{q}_{m,i}\right|}{\left|\dot{Q}_{\min,i}\right|} \right\} \tag{A.15}$$

with $i = 1, 2, \cdots, m$.

When the manipulator is within its admissible velocity limits, $\gamma = 0$ to transfer no motion to the mobile base. If the manipulator approaches its velocity limit, the manipulator cannot handle the task alone, and γ will be set equal to η to let the mobile base share part of the motion. Finally, when the manipulator command exceeds its velocity limit, γ will be set equal to one to let the mobile base solely undertake the motion requirement.

A.3.3 Kinematic Control of Mobile Manipulators

As stated before, the target of this chapter is threefold: first to complete trajectory tracking by using WMM, second to optimize DM of the manipulator to make it stay in optimal configuration for exerting large forces, and third to transfer motion requirement to the manipulator as far as possible in order to have the best motion precision (remembering that mobile bases often have inferior positioning accuracies).

According to (A.5) and (A.7), the entire kinematic controller of the WMM can be designed as

$$v = J^{\dagger}\dot{x} + (I_{(b+m)\times(b+m)} - J^{\dagger}J)v_0, \tag{A.16}$$

where $J^{\dagger}$ is the weighted pseudoinverse of J with the definition in (A.11)-(A.12), and $v_0 \in \mathbb{R}^{b+m}$ is the self-motion velocity for sub-tasks in the null-space.

For DM enhancement in Cartesian space, the null-space controller can be omitted, and controller (A.16) is rewritten as

$$v = J^{\dagger} v_c \tag{A.17}$$

with $v_{c,i}$ defined as

$$v_{c,i} = \begin{cases} k_C \left[(\nabla_x H_2)^{\mathrm{T}} \right]_i & \text{if } x_{\min,i} \leqslant x \leqslant x_{\max,i} \\ 0 & \text{else ,} \end{cases} \tag{A.18}$$

where $i = 1, 2, \cdots, r$, $v_{c,i}$ is the i^{th} component of v_c, k_C is a positive scalar gain, and $x_{\max,i}$ and $x_{\min,i}$ are the upper and lower limits of the i^{th} component of the permissible position for the end-effector, respectively.

For DM enhancement in null-space of the WMM, the controller (A.16) can be designed as

$$v = J^{\dagger}(\dot{x}_d + K_x(x_d - x)) + (I_{(b+m)\times(b+m)} - J^{\dagger} J) v_n. \tag{A.19}$$

Here, $x \in \mathbb{R}^r$ and $x_d \in \mathbb{R}^r$ are the actual and desired poses of the end-effector, respectively, $K_x \in \mathbb{R}^{r \times r}$ is a constant gain matrix, and v_n is defined as

$$v_n = k_N \begin{bmatrix} 0_{b\times 1} \\ (\nabla_{q_m} H_2)^{\mathrm{T}} \end{bmatrix}, \tag{A.20}$$

where k_N is a positive scalar gain. The desired end-effector trajectory $\dot{x}$ in (A.16) is changed to $\dot{x}_d + K_x(x_d - x)$ in (A.19) to make sure the trajectory tracking error convergences to zero. Accurate end-effector trajectory tracking is realized by adjusting the weighting matrix designed in Section A.3.2. A block diagram of the control system is shown in Fig. A.2, where the haptic interface will provide the motion command for the WMM system when needed.

A.4 Experimental Results

Several experiments have been conducted to verify the effectiveness of the proposed kinematic control method for WMMs. The experiments in this section contain two parts: (A) the verification of the weighting matrix adjustment method to improve tracking accuracy, and (B) the evaluation of the DM enhancement to increase force exertion capability.

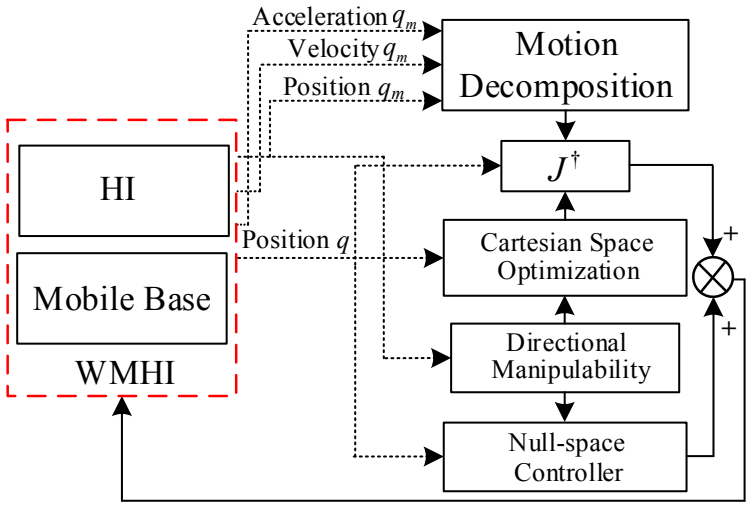

Figure A.2: Block diagram of the control system.

A.4.1 Experimental Setup

In this study, we use an omnidirectional wheeled mobile manipulator, which is composed of a custom-built four-wheel mobile base and a 7-DOF ultra-lightweight robotic arm Kinova Gen3 (Kinova Robotics, Canada), and the mobile base frame Σ_b coincides with the manipulator reference frame Σ_m. The mobile base is equipped with two pairs of Mecanum wheels so that it can realize omnidirectional motion, which shortens robot throughput times and reduces nonproductive time when searching appropriate execution pose for a given task [25].

The experimental setup is shown in Fig. A.3. It consists of a 4-wheel omnidirectional mobile manipulator as the slave robot, a Falcon haptic interface (Novint Technologies Inc., USA) as the master robot, and a motion capture system (Claron Technology Inc., Canada). The haptic interface is used to send position/velocity commands to the WMM, and the motion capture system is employed to evaluate the tracking accuracy of the end-effector and not used in the control system.

The mobile base has less motion precision compared with the manipulator due to uncertain wheel-ground contact or wheel wear [70]. It should be noted that the manipulator is installed on the mobile base, so even small motion

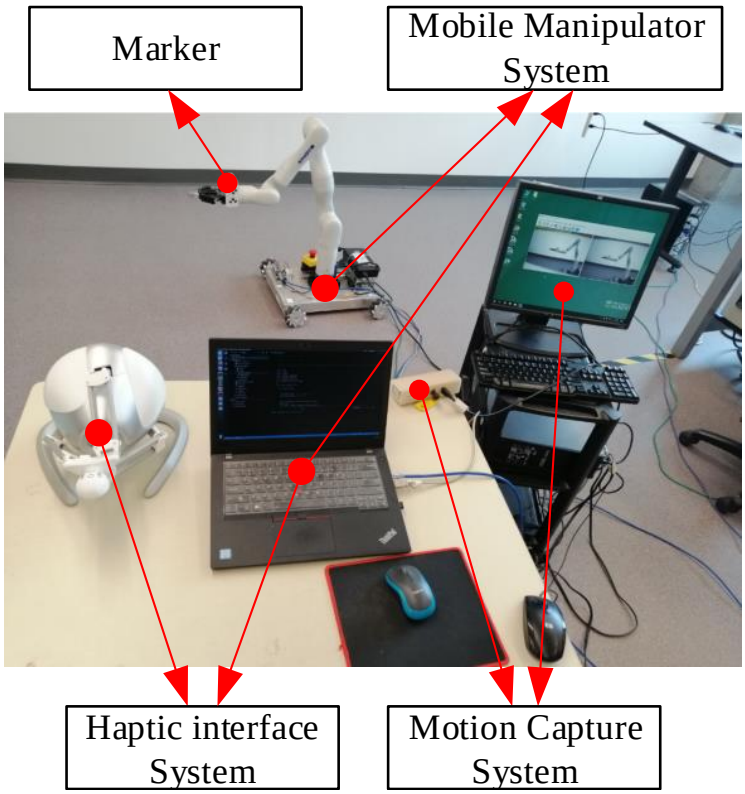

Figure A.3: Experimental setup.

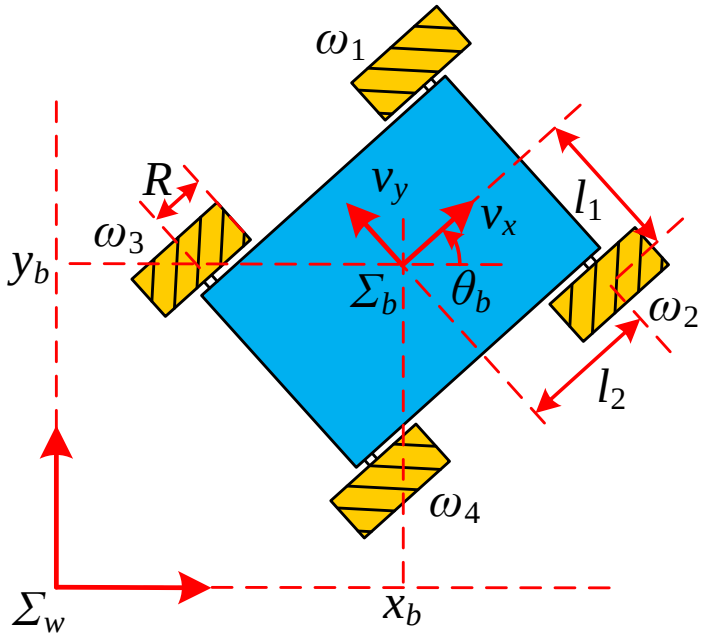

Figure A.4: Kinematics of the omnidirectional mobile base.

errors of the base, in particular the turning errors, will result in large position errors of the end-effector.

The joint velocity limit of the manipulator is expressed for motion decomposition as (A.13). The generalized coordinates for the mobile base (shown in Fig. A.4) are defined as $q_b = [x_b, y_b, \theta_b]^{\mathrm{T}} \in \mathbb{R}^3$ and the velocity command of the wheels as $v_b = [\omega_1, \omega_2, \omega_3, \omega_4]^{\mathrm{T}} \in \mathbb{R}^4$. The velocity transformation matrix $P(q_b) \in \mathbb{R}^{3\times4}$, which transfers the wheel velocities to the generalized base velocities, can be expressed as

$$P(q_b) = J_I J_V \tag{A.21}$$

with $J_I = \begin{bmatrix} \cos\theta_b & -\sin\theta_b & 0 \\ \sin\theta_b & \cos\theta_b & 0 \\ 0 & 0 & 1 \end{bmatrix}$, and $J_V = \frac{R}{4}\begin{bmatrix} 1 & 1 & 1 & 1 \\ -1 & 1 & 1 & -1 \\ \frac{-1}{l_1+l_2} & \frac{1}{l_1+l_2} & \frac{-1}{l_1+l_2} & \frac{1}{l_1+l_2} \end{bmatrix}$.
The variables θ_b, R, l_1, and l_2 are illustrated in Fig. A.4.

In this research, no constraint is imposed on the orientation of the end-effector of the WMM. Therefore, the dimension of the Cartesian space of the mobile manipulator is defined to be $r = 3$. At the initial point, the manipulator frame Σ_m is assumed to coincide with the world frame Σ_w. The starting joint position of the WMM is $q_0 = [0, 0, 0, 0, \pi/6, 0, \pi/2, 0, -\pi/6, 0]^{\mathrm{T}}$. Also, the

Table A.1: Maximum and RMS values of commanded base velocity using two kinematic control methods

	v_{xb} (cm/s)		v_{yb} (cm/s)		ω_b (°/s)	
	Max.	RMS	Max.	RMS	Max.	RMS
Proposed	2.8	1.68	1.72	0.65	0.0917	0.035
Traditional	3.91	2.58	2.38	1.42	0.882	0.504

starting position of the end-effector in Σ_w is $x_0 = [0.65, -0.0246, 0.4921]^{\mathrm{T}}$.

A.4.2 Experiment for End-effector Trajectory Tracking

To improve the tracking precision of the end-effector, the joint motion transferred to the mobile base ought to decrease if the joint limit of the manipulator is not reached. The traditional kinematic control and the proposed kinematic control (based on motion decomposition using a weighting matrix) are compared to verify the effectiveness of the latter. The traditional control method means using the pseudoinverse of the Jacobian J without adding a weighting matrix W_x defined in (A.12), expressed as $J^{\dagger} = J^{\mathrm{T}}(JJ^{\mathrm{T}})^{-1}$, to kinematically control the WMM [113]. If the desired end-effector trajectory is within the manipulator workspace, then the base will remain immobile with the proposed control approach. So, we define an end-effector trajectory beyond it, which is a circle with radius of 0.25 m, defined as $x_d(t) = x_0 + \big[-0.25(\cos(\pi/20t) - 1), -0.25\sin(\pi/20t), 0\big]^{\mathrm{T}}$. It is worth noting that the maximum radius of the circle within the manipulator workspace at this initial position is only 0.11 m. The control parameters are set as $K_x = 10I_{3\times3}$, $\epsilon = 0.2$, and the results of the experiment are shown in Figs. A.5 and A.6. It should be noted that the actual position of the end-effector is obtained via the motion capture system and the position of the mobile base is acquired by using the forward kinematics of the base. Table A.1 contains the maximum and RMS values of the commanded base velocity in the experiment, where v_{xb}, v_{yb}, ω_b represent the commanded base velocities in x_b, y_b, and θ_b, respectively.

Table A.1 shows that when the desired end-effector trajectory is beyond the manipulator workspace, the mobile base will be forced to move in both two

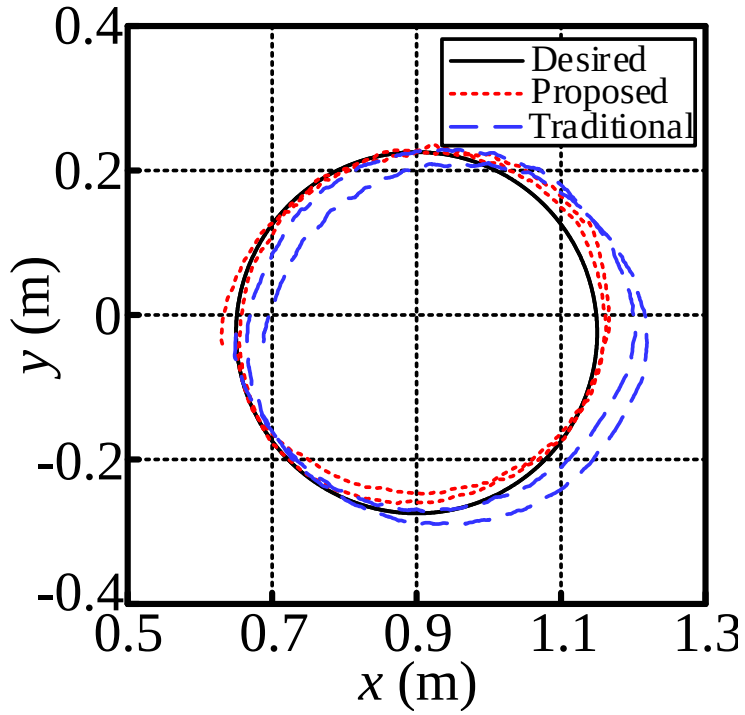

(a) End-effector trajectories

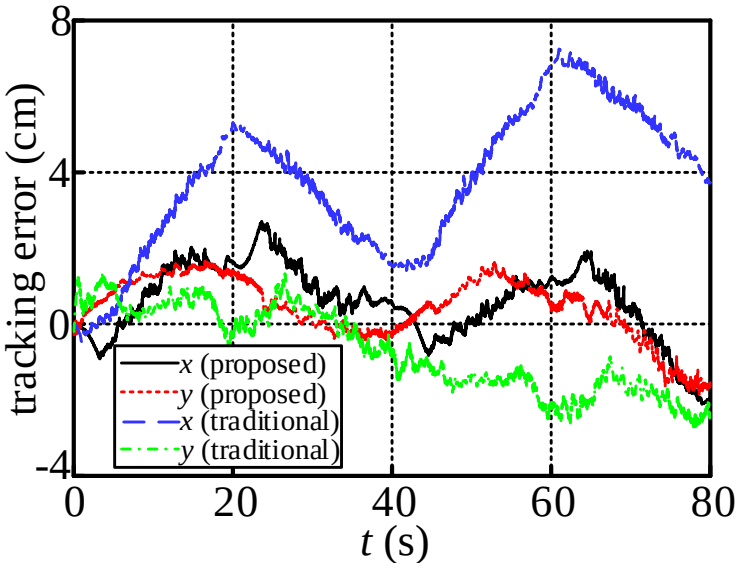

(b) Tracking errors

Figure A.5: End-effector trajectory tracking beyond manipulator workspace.

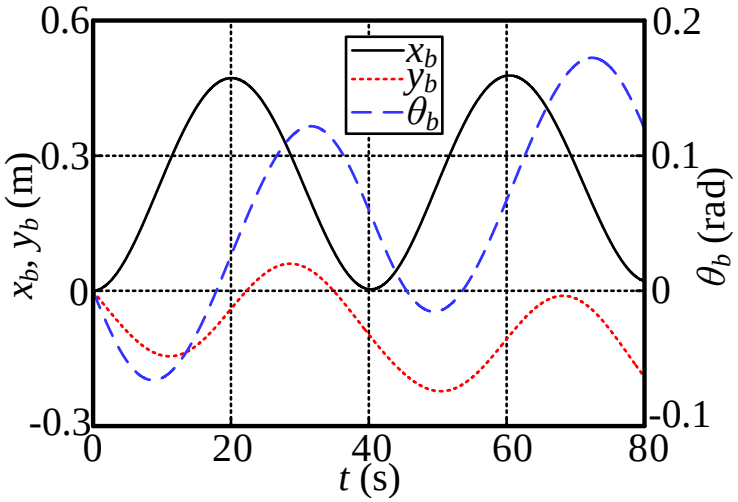

(a) Traditional control

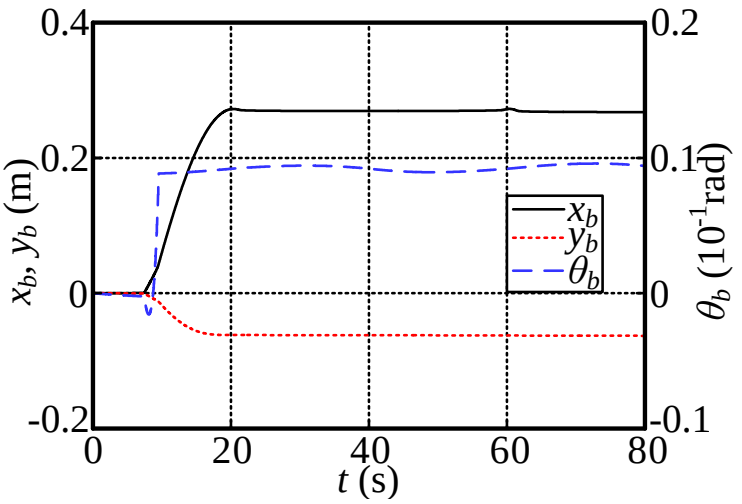

(b) Proposed control

Figure A.6: Position of the mobile base during the experiment.

scenarios. However, the velocity command to the base employing the proposed method is much smaller with the RMS value of velocity commands for x_b, y_b, and θ_b only representing 65.12%, 45.77%, and 6.94% of the commands via traditional method, respectively. Fig. A.5 contains the end-effector tracking results. As shown in Fig. A.5(b), the maximum tracking error for x is reduced from 7.25 cm to 2.71 cm, and the maximum tracking error for y is decreased from 2.71 cm to 1.88 cm with motion distribution. Fig. A.6 shows the position of the mobile base during the experiment with two different control methods. With the proposed approach, the mobile base moved only during time 7.15-20.35 s (see Fig. A.6(b)), while using the traditional approach, the mobile base was in motion ceaselessly (see Fig. A.6(a)). It is worth noting that when the base is commanded to move laterally, wheel-ground slippage and wheel-wheel interference will be more severe, and this is why the tracking accuracy in y is not improved as much as x.

A.4.3 Experiment for Force Exertion Capability Enhancement

The directional manipulability enhancement for manipulators can enhance the force exertion capability of the robotic system. The performance of the trajectory tracking method is verified in Section A.4.2. Thus, this section will focus on force exertion capability enhancement. However, motion decomposition is still adopted to improve the tracking accuracy to the greatest extent. It should be noted that it is a trade-off between acquiring high tracking accuracy and achieving maximal force exertion capability since the former demands a motionless base and the latter requires a mobile base, and the proposed method tries its best to improve the tracking accuracy when force exertion capability is enhanced. The proposed kinematic control for WMM was implemented to verify the effectiveness of the proposed method in enhancing its force exertion capability compared with the traditional method expressed in the trajectory tracking experiment (no null-space control is used) in a box pushing task. The haptic interface is used by the user to provide the desired pushing movement for the end-effector, and it should be emphasized this control methodology is

for the entire WMM system with the specific motion decomposition decided by the weighting matrix in (A.12)-(A.14) automatically. The direction of the DM is defined as $u = J_I^{-1}[1, 0, 0]^{\mathrm{T}} \in \mathbb{R}^3$ to enhance the force exertion capability only along the x axis of the world frame, and J_I is a transformation matrix, defined in (A.21), that keeps u aligned with x of the world frame when the base is rotated. The other parameters for the experiment are set as $K_x = 10I_{3\times3}$, $\epsilon = 0.2$, $W_\tau = \mathrm{diag}(1, 1, 1, 1, 2.5, 2.5, 2.5)$, $k_C = 0.01$, and $k_H = 0.2$. The DM enhancement in Cartesian space is only conducted in the z direction, which is the height of the end-effector from the world frame, with the upper and lower limits defined as 0.56 m and 0.36 m, respectively, because the mobile base can move freely in the $x - y$ plane, the optimization on these two directions has difficulty in determining the position limit. It is worth mentioning that in the experiment, u is not constant since the mobile base may rotate; thus, the practicability of the proposed method in $x - y$ plane can be verified. And for its effectiveness in z direction (load carrying enhancement) of the world frame, a simulation has been conducted.

During the simulation, all the control parameters are set the same as in the experiment with the optimization direction defined as $u = [0, 0, 1]^{\mathrm{T}} \in \mathbb{R}^3$. The simulation results show that with the proposed approach, the DM can be enhanced from 1.125 to 4.031. If a z force of 10 N is applied to the end-effector, the norm of the weighted joint torque will decrease from 8.89 Nm to 2.48 Nm, which demonstrates the validity of the suggested method in enhancing the force exertion capability in z direction.

In the box pushing experiment, the box used is approximately 26 kg, and the goal is to push it about 0.2 m forward. The experimental results are shown as follows. Fig. A.7 shows the configuration of the WMM with and without DM enhancement. Fig. A.7(b) shows that with the proposed method, the manipulator will go to a more desirable configuration to push the box. This is similar to how humans use their hands and body to push on a heavy object. However, with DM enhancement in x, the manipulator is almost fully stretched (cannot move much further in x), and most of the pushing motion will then be distributed to the base according to (A.11)-(A.14); thus, the trajectory

tracking accuracy will inevitably be reduced.

It is worth mentioning that the DM enhancement is only desirable for the case in which the WMM requires large force capability (e.g., the push task). For the movement in the free space, it is beneficial to enhance the velocity manipulability ellipsoid (i.e., maximization of H_1). This will allow the user to have an agile mobile manipulator in the free space and a mobile manipulator with large force capability for the case of contact with the environment.

Fig. A.8 shows the joint torque of the manipulator during the task. It should be noted that the joint torque is obtained via joint torque sensors, the gravity of the system has been subtracted, and the torque limits of the manipulator are 32 Nm for the first four joints and 13 Nm for the last three joints. The push task started at about 20 s, and without DM enhancement, the task could not be completed because joint four was saturated at time 23 s, as shown in Fig. A.8(a). However, as shown in Fig. A.8(b), with the proposed method, the task could be completed with the maximum joint torque no more than 20 Nm.

DM and the norm of the weighted joint torque during the experiment are shown in Fig. A.9. Fig. A.9(a) depicts the DM of the manipulator, with the proposed kinematic controller, the DM was first enhanced in Cartesian space from 3.825 to 3.905 during time 0-5 s, and the end-effector position in z was changed from 0.492 m to 0.456 m. Next, during time 5-20 s, the DM was enhanced using the null-space controller from 3.905 to 5.88, and then the push task started. Fig. A.9(b) shows the norm of the weighted joint torque during the push process. The box was pushed about 0.25 m with the proposed method, and the norm of the weighted joint torque stayed at about 30 Nm; however, without adopting it, the norm increased rapidly to almost 40 Nm and stopped the task, which indicates the effectiveness of the proposed method.

A.5 Conclusions

A method to enhance the force exertion capability for a WMM and maintain high position tracking precision is proposed in this chapter. The force exer-

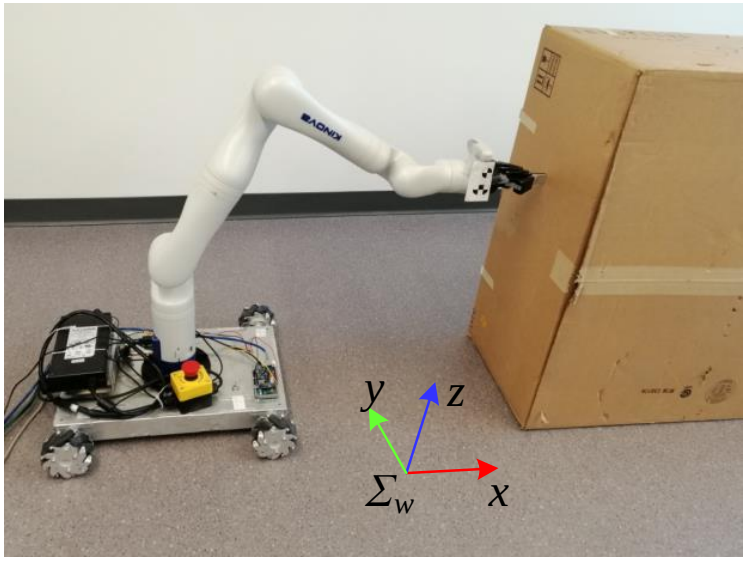

(a) Without DM enhancement

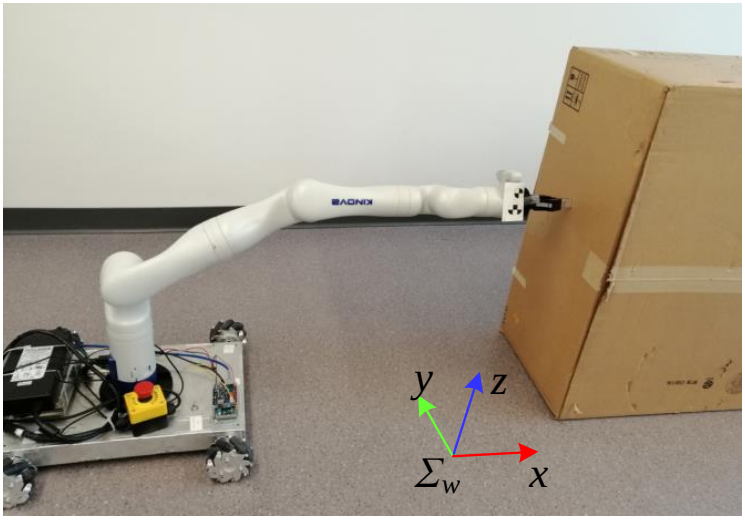

(b) With DM enhancement

Figure A.7: Final configuration of the mobile manipulator during the task.

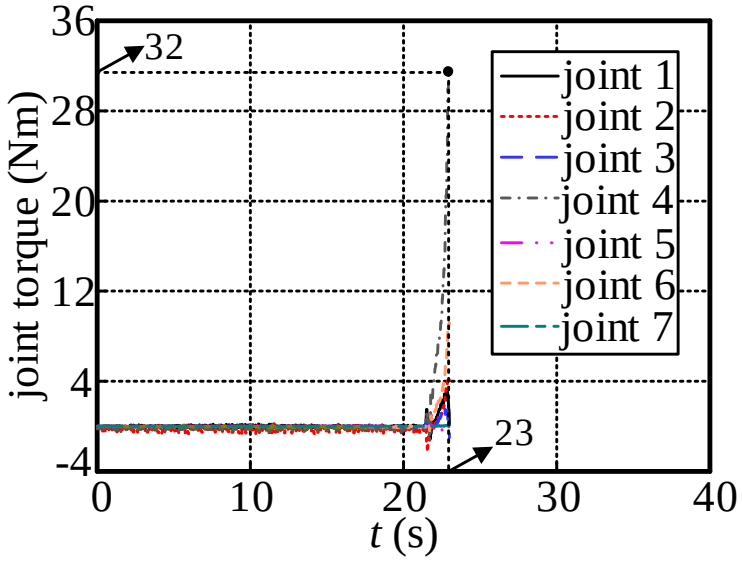

(a) Without DM enhancement

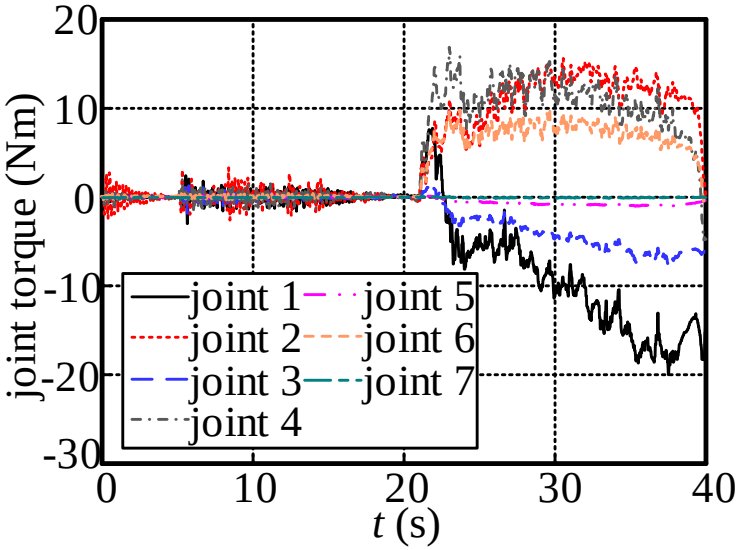

(b) With DM enhancement

Figure A.8: Joint torque output of the manipulator during the experiment

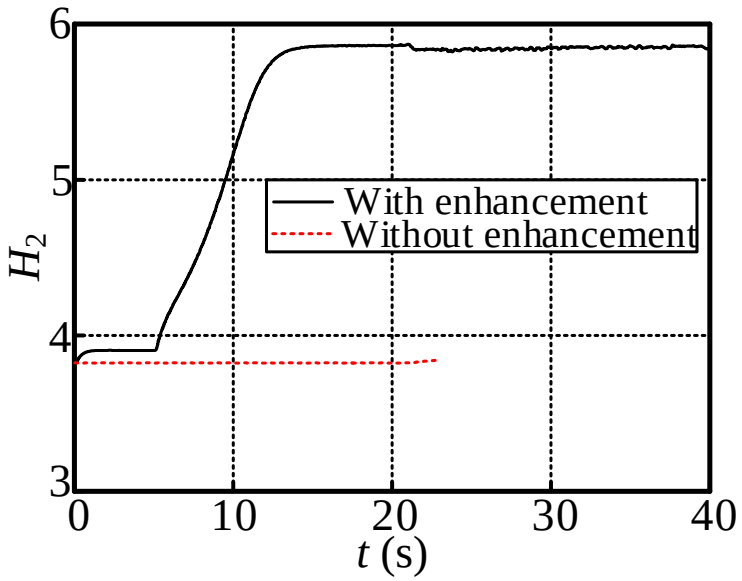

(a) Directional manipulability

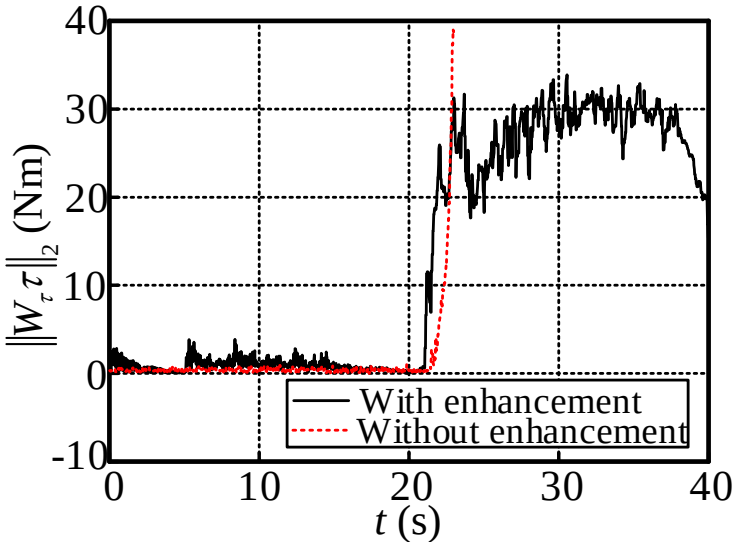

(b) Norm of weighted torque

Figure A.9: DM and norm of the weighted joint torque during the experiment.

tion capability is improved by maximizing the directional manipulability in Cartesian space and the null-space of the system successively. Also, the end-effector trajectory error is minimized by transferring less of the desired total motion to the mobile base due to its low motion accuracy. The effectiveness of the proposed method has been experimentally verified by tracking a desired end-effector trajectory and pushing on a heavy box. During the trajectory tracking experiment, the maximum tracking error of the end-effector has been improved by 62.6% and 30.6% in x and y, respectively. In the box pushing experiment, with the proposed method, the massive box can be pushed with the norm of the weighted joint torque about 30 Nm, while without using it, the task cannot be executed with the norm going rapidly up to 40 Nm. This method can enhance the force exertion capability in any desired direction. Our future work will focus on making a bilateral teleoperation system in which the WMM is haptically teleoperated from one or two user interfaces.

Appendix B

Actuator Motion Distribution of Redundant Mobile Manipulators for Accurate Motion Tracking

Appendix B presents a novel method to a novel adaptive motion distribution method as a secondary objective in the null-space of the Wheeled Mobile Manipulator (WMM) to improve the motion tracking accuracy (primary objective) of the WMM. Also, a tertiary objective to move the manipulator away from its singularity is proposed. This objective is activated if the secondary objective is feasible and the WMM still has remaining redundant degrees of freedom. As this work is not extended to haptic interfaces, it is presented in Appendix B. A version of this chapter has been submitted as H. Xing, A. Torabi, L. Ding, H. Gao, Z. Deng, and M. Tavakoli, "Accurate Motion Tracking for a Mobile Manipulator by Adaptive Motion Distribution via Null-space Control," IEEE/ASME Transactions on Mechatronics, 2020. Hongjun Xing and Ali Torabi have equal contribution in this work.

B.1 Introduction

Wheeled mobile manipulators (WMMs) fuse the advantages of the high mobility of a mobile base and the dexterous operation ability of a manipulator. WMMs have been used in executing many tasks that need high precision, in-

cluding door opening [3], [152], valve turning [4], object grasping [84], and large-scale 3D printing [161]. The addition of a mobile base to a manipulator is an efficient method of extending the reach of manipulators, which are otherwise restricted to a fixed workspace. This combination has presented new challenges to researchers. Due to the different characteristics of the base and the manipulator, such as their kinematics and dynamics, the modelling and control of the entire system (called the mobile manipulator) should take these differences into account [70]. Also, the combination of the mobile base and the manipulator often makes the WMM a kinematically redundant robotic system. A redundant robot has more degrees of freedom (DOFs) than minimally required for executing tasks. The inverse kinematics of any kinematically redundant robotic system admits an infinite number of solutions. Thus, redundancy makes it possible to have joint motions that do not affect the pose (position and orientation) of the end-effector. This inner joints motion can be used in closed-loop control to achieve a secondary objective while performing any primary objective, e.g., singularity avoidance, obstacle avoidance, manipulability enhancement, and/or force feedback capability maximization [15], [157], [160].

The mobile base is often regarded as an extension to the manipulator, and the model of the entire system is established without considering the inherent differences between these two parts. For example, the base usually moves in an environment with complex dynamics (e.g., slippage/skidding or moving on uneven ground) while the manipulator is in free or contact motion [85]. The motion accuracy of the mobile base is generally lower than that of the manipulator due to the unknown wheel-ground contact and the possibility of slippage. Thus, accurate motion control of the WMM warrants more of a given motion being given to the manipulator to execute than to the mobile base when the task permits.

Few studies have been conducted to improve the tracking accuracy of the end-effector of WMM with consideration of the motion errors of the mobile base. Shin *et al.* [127] improved the tracking precision of a WMM by discretizing the task so that the mobile base and the manipulator do not move simultaneously. Papadopoulos *et al.* [111] presented a planning and control method-

ology for nonholonomic WMMs simultaneously following desired end-effector and mobile base trajectories without violating the nonholonomic constraints with the assumption that the base has no motion control error. Nagatani *et al.* [102] presented a cooperative control method for WMM in trajectory tracking without considering the motion error of the mobile base. Jia *et al.* [70] paid attention to the differences between the mobile base and the manipulator. They proposed a coordinated motion control method based on a weighted inverse Jacobian for nonholonomic mobile manipulator without considering the joint constraints (position, velocity, and acceleration). The employment of a weighted inverse Jacobian can realize motion distribution between the two sub-systems (the base and the manipulator). Yet, the application of weighting matrix does not fully utilize the manipulator's redundancy [8] because when one of the manipulator's joint exceeds its limit, the motion requirement will simply be transferred to the base. The rest of the literature has focused on the improvement of trajectory tracking precision of WMMs in the context of dynamic control where the complex system dynamics have to be dealt with [101], [148], [153].

In this section, a novel method to improve the motion tracking accuracy of WMMs by motion distribution via a null-space control is proposed. As stated before, the motion control accuracy of the mobile base is inferior to that of the manipulator. Therefore, the redundancy of the WMM can be employed to, first, assign all of the desired motion to the manipulator to execute. Next, when the manipulator reaches its limit (being joints' range, velocity, and/or acceleration limit) and the desired motion is not feasible for it anymore, the motion distribution will be modified in the null-space of the system. Consequently, some parts of the desired motion will be transferred to the mobile base to make the desired trajectory feasible for the WMM.

The proposed method builds upon the work by Flacco *et al.* [51] for redundant manipulators and extends it to redundant WMMs. The "saturation in the null-space" (SNS) algorithm proposed by Flacco *et al.* [51] handles the joint bounds of a redundant manipulator by successively discarding the joints that would exceed their motion bounds when using the minimum norm solution.

The SNS method is excellent in addressing the redundant system's limitations due to its adequate and accurate distribution of end-effector Cartesian motion to joint motion. However, this method has never been employed to improve the trajectory tracking capabilities of WMMs. With this in mind, we present an adaptive motion distribution (AMD) method to enhance the position tracking precision of the WMM using its null-space. This method passes the desired motion as much as possible to the manipulator via the null-space of the WMM until the motion is not feasible for the manipulator. Then, the motion will be decomposed to a motion for the mobile base and a feasible motion for the manipulator. Furthermore, if after resolving all of the joint limits, the WMM has any redundancy left, a tertiary objective will be achieved in the null-space of the robotic system to avoid singularities. It is worth mentioning that the proposed method is implemented at the joint acceleration level to avoid velocity discontinuity when the mobile base is enabled/disabled.

In the proposed method, the singularity of the manipulator will first be examined. If the manipulator is close to a singular configuration, the mobile base will be activated at once. Thus, only when the manipulator is away from the singularity, the motion distribution will be executed. Meanwhile, the tertiary objective will be performed to keep the manipulator from singularity without intervening with the primary and secondary tasks.

The above-mentioned problem can also be formulated as an optimization problem with equality or inequality constraints[26], [112], [162], such as quadratic programming (QP) problem [56], [71]. The problems of the QP-based methods lie in two aspects; first is the high computational load when the number of DOFs rises, and second is the occurrence of the cases of multiple hierarchical tasks or impracticable tasks. In order to solve the problem of multiple prioritized tasks, Kanoun *et al.* [72] presented a prioritized task-regulation framework, which covered both linear equalities and inequalities. For real-time implementation, Escande *et al.* [48] proposed a generic solution to solve multiple prioritized problems of both equality and inequality constraints, which was ten times faster than the iterative-projection hierarchical solvers when only equalities considered. Nevertheless, when hard joint con-

straints of the manipulator taken into account, the QP-based approach cannot take the advantage of formulating all the inequalities in a unified framework [51], thus, the computation complexity of these algorithms is much higher than the proposed method.

The remainder of this section is organized as follows. The kinematic model and control of the WMM is provided in Section B.2. In Section B.3, our adaptive motion distribution method is presented. In Section B.4, experimental results are reported to examine the performance of the proposed control strategy. Concluding remarks appear in Section B.5.

B.2 Kinematic Modeling and Control of a Mobile Manipulator

The kinematics for a mobile manipulator can be obtained from the kinematic models of the two subsystems, i.e., the mobile base and the manipulator. As shown in Fig. B.1, Σ_w, Σ_b, Σ_m, and Σ_{ee} are considered as the world reference frame, mobile base frame, manipulator reference frame, and end-effector frame, respectively. First, let us derive the kinematic model of the mobile base. Assume the contact between the wheels of the mobile base and the ground is pure rolling (i.e., no slippage). Then, the kinematic model for it can be obtained as

$$\dot{q}_b = P(q_b)v_b, \tag{B.1}$$

where $q_b \in \mathbb{R}^{n_b}$ denotes the generalized coordinate for the mobile base expressed in Σ_w, $v_b \in \mathbb{R}^b$ denotes the velocity of the wheels, $P(q_b) \in \mathbb{R}^{n_b \times b}$ denotes the constraint matrix of the base (holonomic or nonholonomic), and n_b and b denote the dimensions of the generalized coordinate and the wheel velocity vector for the mobile base, respectively. $P(q_b)$ transfers the wheel velocities to the generalized base velocities. Also, it is worth mentioning that (B.1) is a generalized model, which can be used in both holonomic and nonholonomic mobile base.

Next, assume that the pose of the end-effector in Σ_w is defined as $x \in \mathbb{R}^r$, r is its dimension, and the generalized coordinate vector for the WMM denotes as

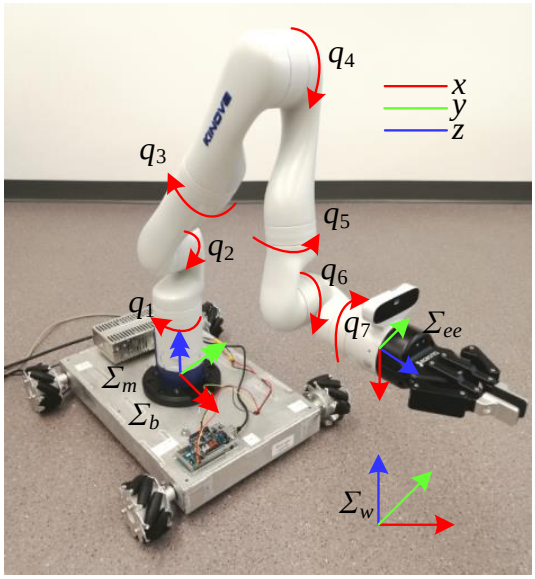

Figure B.1: Omni-directional wheeled mobile manipulator.

$q = [q_b^{\mathrm{T}}, q_m^{\mathrm{T}}]^{\mathrm{T}} \in \mathbb{R}^n$, where $q_m \in \mathbb{R}^m$ is the generalized manipulator coordinate, m is the dimension of it (the joint number), and the subscript $n = n_b + m$. It is worth mentioning that the generalized manipulator velocity is defined as the velocity of the manipulator joints. Now, the forward kinematics at velocity level for the entire WMM can be calculated as

$$\begin{aligned} \dot{x} &= J(q)\dot{q} = [J_b(q) \quad J_m(q)] \begin{bmatrix} \dot{q}_b \\ \dot{q}_m \end{bmatrix} \\ &= [J_b(q)P(q_b) \quad J_m(q)] \begin{bmatrix} v_b \\ \dot{q}_m \end{bmatrix} = J_v(q) \begin{bmatrix} v_b \\ \dot{q}_m \end{bmatrix}, \end{aligned} \tag{B.2}$$

in which $J_b \in \mathbb{R}^{r \times n_b}$ is the Jacobian of the mobile base, $J_m \in \mathbb{R}^{r \times m}$ is the Jacobian of the manipulator, $J(q) \in \mathbb{R}^{r \times n}$ is the Jacobian of the generalized WMM (i.e., no constraints for the mobile base are considered), and $J_v(q) \in \mathbb{R}^{r \times (b+m)}$ is the Jacobian of the WMM. There are two Jacobians for a WMM just because the generalized coordinate for a mobile base is not its wheel velocity. It is worth noting that when the mobile base is subjected to nonholonomic constraints, only $J_v(q)$ can be employed. For a holonomic mobile base, both $J(q)$ and $J_v(q)$ can be utilized because they are equal to one another [40].

The WMM is usually a kinematically redundant system (i.e., $r < n$). Thus,

for a given task $\dot{x}$, all solutions $\dot{q}$ can be expressed as[1]

$$\dot{q} = J^{\dagger}\dot{x} + (I - J^{\dagger}J)\dot{q}_N, \tag{B.3}$$

where $J^{\dagger} = J^{\mathrm{T}}(JJ^{\mathrm{T}})^{-1}$ is the pseudoinverse of J, I is an $n \times n$ identity matrix, $I - J^{\dagger}J$ is the null-space of J, and $\dot{q}_N \in \mathbb{R}^n$ is the null-space velocity for sub-tasks. The derivative of (B.2) with respect to time derives

$$\ddot{x} = J\ddot{q} + \dot{J}\dot{q}, \tag{B.4}$$

then, the kinematic model for the WMM with null-space control considered at the acceleration level can be expressed as

$$\ddot{q} = J^{\dagger}(\ddot{x} - \dot{J}\dot{q}) + (I - J^{\dagger}J)\ddot{q}_N. \tag{B.5}$$

B.3 Adaptive Motion Distribution Method

The mobile base of the WMM has less motion accuracy compared with the manipulator mounted on top of it due to unknown ground-wheel contact, wheel wear or wheel slippage/skidding [70]. Therefore, the AMD method is proposed here. With this method, the manipulator will solely undertake the task, and only when the range or acceleration requirements of the task exceed the limits of the manipulator, the mobile base will be involved.

B.3.1 Joint Acceleration Limits Definition

The WMM is controlled at the acceleration level. Therefore, the limits on joint acceleration need to be locally calculated, taking into account the joint position, velocity and acceleration bounds of the WMM. The acceleration limits on $\ddot{q}$ for the WMM at time $t = t_h$ can be expressed as [50]

$$\ddot{Q}_{\min}(t_h) \leqslant \ddot{q}(t_h) \leqslant \ddot{Q}_{\max}(t_h), \tag{B.6}$$

with the acceleration limits for each joint defined as

$$\ddot{Q}_{\min,i} = \begin{cases} \max\left\{\frac{2(Q_{\min,i} - q_{h,i} - \dot{q}_{h,i}T)}{T^2}, \frac{V_{\min,i} - \dot{q}_{h,i}}{T}, A_{\min,i}\right\}, & \text{if } q_{h,i} > Q_{low,i} \\ A_{\max,i}, & \text{else} \end{cases} \tag{B.7}$$

[1]For brevity, the dependence of the variables upon the joint variables are omitted.

$$\ddot{Q}_{\max,i} = \begin{cases} \max\left\{ \frac{2(Q_{\max,i} - q_{h,i} - \dot{q}_{h,i}T)}{T^2}, \frac{V_{\max,i} - \dot{q}_{h,i}}{T}, A_{\max,i} \right\}, & \text{if } q_{h,i} < Q_{up,i} \\ A_{\min,i}, & \text{else} \end{cases} \tag{B.8}$$

in which V_{max}/V_{min} and A_{max}/A_{min} are the maximum and minimum hard joint bounds for velocity and acceleration, respectively. $i = 1, \ldots, n$ denotes the i^{th} element of the corresponding vector, the sampling time is denoted as T, and $q_{h,i}$ denotes the current WMM joint position at time t_h of the i^{th} joint. $Q_{low,i}$ and $Q_{up,i}$ are defined as

$$Q_{low,i} = Q_{\min,i} - \frac{|\dot{q}_{h,i}|\,\dot{q}_{h,i}}{2A_{\max,i}},$$

$$Q_{up,i} = Q_{\max,i} + \frac{|\dot{q}_{h,i}|\,\dot{q}_{h,i}}{2A_{\min,i}}.$$

Fig. B.2 presents a sample of joint acceleration limits and their corresponding joint velocity with a given joint physical limit. In this example, the joint velocities are set as $V_{\max}/2$ and $V_{\max}$. As shown in Fig. B.2(a), with the increase of the velocity, the acceleration change happens further from the joint position bound, since it needs more displacements to cease the motion of the joint at the physical limit subjected to the limited joint acceleration. Fig. B.2(b) shows the corresponding velocity profile calculated according to the acceleration limit. It is obvious that with different velocities, the proposed acceleration limit determination method can always make the joint velocity decrease to zero when the joint is close to the position bound. It should be noted that Fig. B.2(a) shows the acceleration bounds for the joint not its current acceleration.

B.3.2 Motion Distribution Framework

As the motion precision of the mobile base is lower compared with that of the manipulator, it is desirable to distribute the motion requirement of the end-effector as much as possible to the manipulator to have high tracking accuracy. AMD method makes use of the kinematic redundancy of the WMM

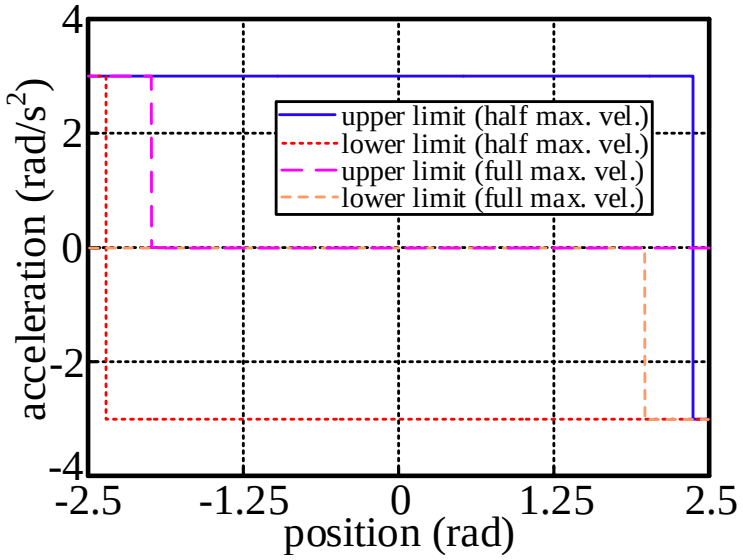

(a) Acceleration limit

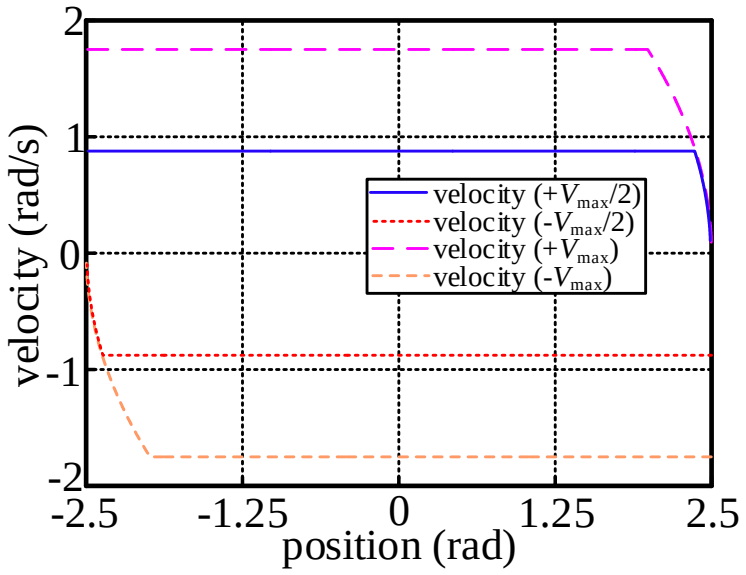

(b) Velocity profile

Figure B.2: Joint acceleration limit and its corresponding velocity. $Q_{\max} = 2.5$ rad, $Q_{\min} = -2.5$ rad, $V_{\max} = 1.75$ rad/s, $V_{\min} = -1.75$ rad/s, $A_{\max} = 3$ rad/s^2, and $A_{\min} = -3$ rad/s^2.

to break down the desired motion between the mobile base and the manipulator. This method will distribute some of the motion to the mobile base only when the manipulator cannot handle the task solely, i.e., one or more joints of the manipulator are at their limits or the manipulator is near a singular configuration.

In Appendix A, a weighting matrix was used to distribute the desired end-effector trajectory, which did not make the best use of the manipulator redundancy. Instead, in this section, we propose the AMD method to fully utilize the manipulator redundancy until it cannot execute the task. In the AMD method, first, a diagonal selection matrix $\mathcal{S}$ needs to be defined to specify the active joints. $\mathcal{S}$ is defined as an $n \times n$ diagonal selection matrix whose diagonal elements specify whether the joints are active or not, i.e., if the i element on the $\mathcal{S}$ diagonal is one, the i^{th} joint of the WMM is active. Then, by combining the selection matrix and (B.5), in the AMD method, the joint acceleration command is designed as

$$\ddot{q}_{amd} = (J\mathcal{S})^{\dagger}(\alpha\ddot{x} - \dot{J}\dot{q}) + [I - (J\mathcal{S})^{\dagger}J]\ddot{q}_N, \tag{B.9}$$

where α is a scaling factor to downscale the Cartesian task $\ddot{x}$ when it is not feasible for the WMM. It is noteworthy that $\ddot{q}_N$ in (B.9) represents the null-space acceleration vector for the joints. If the i^{th} joint is not saturated, $\ddot{q}_{N,i} = 0$, else, $\ddot{q}_{N,i}$ is defined as the corresponding joint acceleration limit expressed in (B.6)-(B.8); more details are provided below.

Initially, the selection matrix is set to be $\mathcal{S} = \begin{bmatrix} 0_{n_b \times n_b}, & 0 \\ 0, & I_{m \times m} \end{bmatrix}$, i.e., the mobile base is deactivated and no motion will be distributed to the base (the null-space acceleration $\ddot{q}_N$ vector is set to be zero). Next, the joint acceleration command is calculated using (B.9). Here, if the i^{th} joint of the manipulator is over-driven (i.e., $\ddot{q}_{amd,i} > \ddot{Q}_{\max,i}$ or $\ddot{q}_{amd,i} < \ddot{Q}_{\min,i}$), the corresponding element on the $\mathcal{S}$ diagonal is chosen to be zero to disable the joint, and the i^{th} element of the null-space acceleration $\ddot{q}_N$ is set equal to $\ddot{Q}_{\max,i}$ or $\ddot{Q}_{\min,i}$. With this choice of $\ddot{q}_N$ and $\mathcal{S}$, the acceleration of the i^{th} joint will be adjusted back to its saturation level and the associated acceleration shortage will be assigned to the other joints of the manipulator to be executed. However, this can over-

drive the other joints of the manipulator. Therefore, this method needs to be repeated iteratively until there is no over-driven joint left; otherwise, the Cartesian space acceleration $\ddot{x}$ is found to be infeasible for the WMM with the disabled mobile base.

The feasibility of the desired Cartesian acceleration can be inspected by checking the rank of $J\mathcal{S}$. If the rank of this matrix is smaller than the dimension of the Cartesian space r, the Cartesian space acceleration $\ddot{x}$ is not feasible for the manipulator. Thus, the mobile base needs to be activated by changing the corresponding elements of the selection matrix from zero to one. After activation of the mobile base, the joints' accelerations need to be adjusted again. If the desired Cartesian space acceleration is still infeasible for the WMM with the active mobile base, it has to be modified to become realizable for the WMM. In this case, we introduce a scaling factor $0 \leq \alpha \leq 1$ to make the desired Cartesian acceleration $\ddot{x}$ realizable. α is equal to one unless $\ddot{x}$ is not feasible for the WMM.

In experiments, we notice that using the above approach, the AMD method sometimes moves the manipulator to the edge of its workspace and then activates the mobile base. This causes workspace-boundary singularities as the manipulator is fully stretched out. Therefore, the proposed method should be modified to address this problem. We perform singularity avoidance in two stages. First, during each loop, the manipulator singularity will be examined. If it is determined that the current segment of the desired trajectory will make the manipulator approach its singularity, the mobile base will be activated. Second, a tertiary objective is utilised in the null-space controller that moves away the manipulator configuration from singularity when it is possible. We use the velocity manipulability ellipsoid, which is an effective measure to evaluate the distance of a robotic system from its singularity [157]. For the manipulator, it is defined as $w(q_m) = \sqrt{\det\left(J_m J_m^{\mathrm{T}}\right)}$, and instead of employing $w(q_m)$ as the optimization objective, we choose the cost function as $H(q_m) = w^2(q_m) = \det\left(J_m J_m^{\mathrm{T}}\right)$ to make the optimization more computationally efficient.

Prioritized task motion control is an effective method that ensures the

primary task gets completed. Then, if there is still redundancy remained, the sub-task (secondary task) will be executed [50]. Let us define the auxiliary null-space projection matrix in the joint space as

$$P_A = \Big[I - \big((I - \mathcal{S})P_N\big)^{\dagger}\Big]P_N, \tag{B.10}$$

with $P_N = I - J^{\dagger}J$ being the orthogonal projector in the system's Jacobian null space. Now, the joints acceleration command corresponding to the tertiary objective can be derived as

$$\ddot{q}_t = \beta P_A \ddot{q}_A, \tag{B.11}$$

where $0 \leq \beta \leq 1$ is the scaling factor to preserve the joint bounds when the remained redundancy is not enough to handle it and $\ddot{q}_A$ is the joint acceleration vector associated with the null-space projection matrix P_A. The joint velocity for the tertiary objective is defined as

$$\dot{q}_N = \gamma_1 \begin{bmatrix} 0_{n_b \times 1} \\ (\nabla_{q_m} H)^{\mathrm{T}} \end{bmatrix}, \tag{B.12}$$

and the corresponding joint acceleration can be expressed as

$$\ddot{q}_A = \begin{bmatrix} 0_{n_b \times 1} \\ \gamma_1(\nabla^2_{q_m} H)\dot{q}_m + \gamma_2[\gamma_1(\nabla_{q_m} H)^{\mathrm{T}} - \dot{q}_m] \end{bmatrix}, \tag{B.13}$$

in which γ_1 and γ_2 are two positive constants. Define the partial derivative of J_m with respect to q_m as $\partial_q J$, and specify $\Psi = JJ^{\mathrm{T}}$, the optimization velocity for the manipulator can be expressed as

$$\begin{aligned} \nabla_q H &= \nabla_q \det(\Psi) = \det(\Psi)\mathrm{tr}\big[\Psi^{-1}(\partial_q \Psi)\big] \\ &= \det(\Psi)\mathrm{tr}\big[\Psi^{-1}(\partial_q J J^{\mathrm{T}} + J\partial_q^{\mathrm{T}} J)\big]. \end{aligned} \tag{B.14}$$

Consider two arbitrary manipulator joint angles p and q, define the second order derivative of J_m first by p and second by q as $\partial_{pq} J$. First, the second order derivative of Ψ by joint position is derived as

$$\begin{aligned} \partial_{pq}\Psi &= \partial_{pq}(JJ^{\mathrm{T}}) = \partial_q[\partial_p(JJ^{\mathrm{T}})] = \partial_q[\partial_p J\, J^{\mathrm{T}} + J\partial_p^{\mathrm{T}} J] \\ &= \partial_{pq} JJ^{\mathrm{T}} + \partial_p J\partial_q^{\mathrm{T}} J + \partial_q J\partial_p^{\mathrm{T}} J + J\partial_{pq}^{\mathrm{T}} J. \end{aligned} \tag{B.15}$$

According to (B.14), the second order derivative of H with respect to joint position can be expressed as

$$\begin{aligned} &\partial_{pq} H = \partial_{pq}\det(\Psi) = \partial_q(\det(\Psi))\mathrm{tr}(\Psi^{-1}\partial_p\Psi) + \\ &\det(\Psi)\mathrm{tr}(\partial_q(\Psi^{-1}\partial_p\Psi)) = \det(\Psi)\mathrm{tr}(\Psi^{-1}\partial_q\Psi)\mathrm{tr}(\Psi^{-1}\partial_p\Psi) + \\ &\det(\Psi)\mathrm{tr}\big(\partial_q(\Psi^{-1})\partial_p\Psi\big) + \det(\Psi)\mathrm{tr}(\Psi^{-1}\partial_{pq}\Psi). \end{aligned} \tag{B.16}$$

Then, with the fact that $\partial_q(\Psi^{-1}) = -\Psi^{-1}(\partial_q\Psi)\Psi^{-1}$, we can simplify (B.16) by factoring out $\det(\Psi)$ as

$$\begin{aligned}\partial_{pq}H = \det\Psi\big[&\mathrm{tr}(\Psi^{-1}\partial_q\Psi)\mathrm{tr}(\Psi^{-1}\partial_p\Psi) - \\ &\mathrm{tr}(\Psi^{-1}\partial_q\Psi\Psi^{-1}\partial_p\Psi) + \mathrm{tr}(\Psi^{-1}\partial_{pq}\Psi)\big].\end{aligned} \tag{B.17}$$

For the general case when $p = q$ represents the manipulator joint position vector, the optimization acceleration can be obtained as

$$\begin{aligned}\nabla_q^2 H = \det\Psi\big[&\big(\mathrm{tr}(\Psi^{-1}\partial_q\Psi)\big)^2 - \\ &\mathrm{tr}(\Psi^{-1}\partial_q\Psi\Psi^{-1}\partial_q\Psi) + \mathrm{tr}(\Psi^{-1}\partial_{qq}\Psi)\big].\end{aligned} \tag{B.18}$$

The joint acceleration command that realizes the desired Cartesian space acceleration, the AMD method, and the tertiary objective is

$$\ddot{q} = \ddot{q}_{amd} + \ddot{q}_t. \tag{B.19}$$

The flowchart of the control system is shown in Fig. B.3 and the method to determine the scaling factors α and β is illustrated in Fig. B.4.

Fig. B.3 shows the method to realize motion distribution for a WMM with consideration of singularity avoidance. The primary task is to realize accurate trajectory tracking by motion distribution via AMD (secondary task). Therefore, the mobile base is kept disabled until the manipulator joint is saturated or the manipulator is close to a singularity. A criterion to distinguish the singular configuration is defined based on the minimum singular value of the manipulator Jacobian matrix J_m [32]. The minimum singular value is denoted as σ_m and the criterion for singularity is denoted as $\sigma_{m,min}$. Thus, after the singularity criterion of the manipulator becomes lower than $\sigma_{m,min}$, the mobile base will be activated to move the manipulator away from singularity. Also, when the system has remaining redundancy after the primary and secondary tasks are completed, the manipulability of the manipulator will be enhanced via the tertiary control objective provided in (B.11). When the primary task or the tertiary task cannot be fully executed, a scaling factor α or β is added to downscale the task to make it partially completed.

With the control approach executed at the acceleration level, once the mobile base is deactivated and without acceleration distributed to the base,

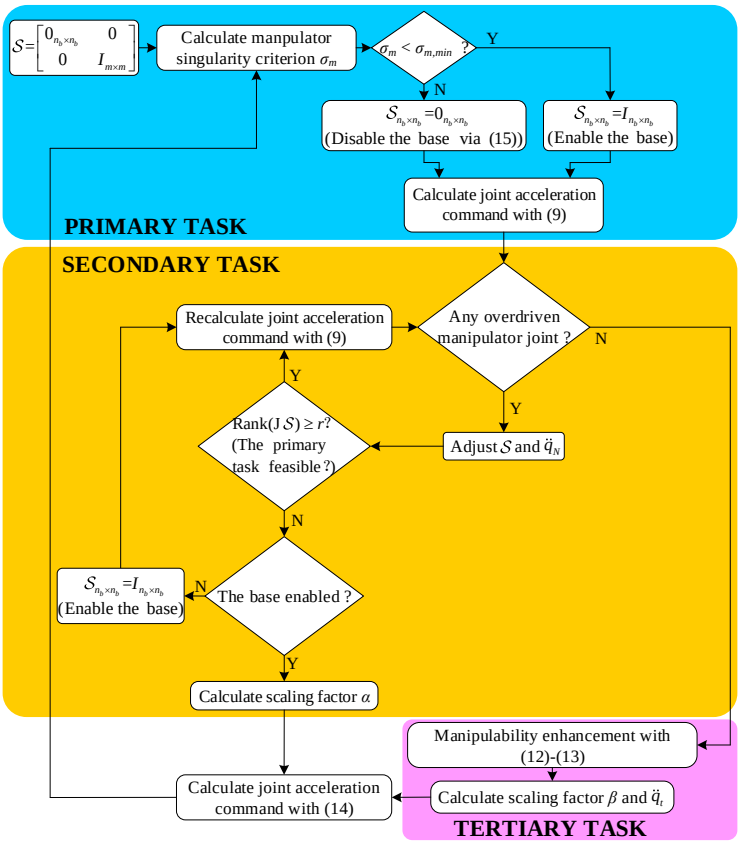

Figure B.3: Flowchart of the entire WMM control system.

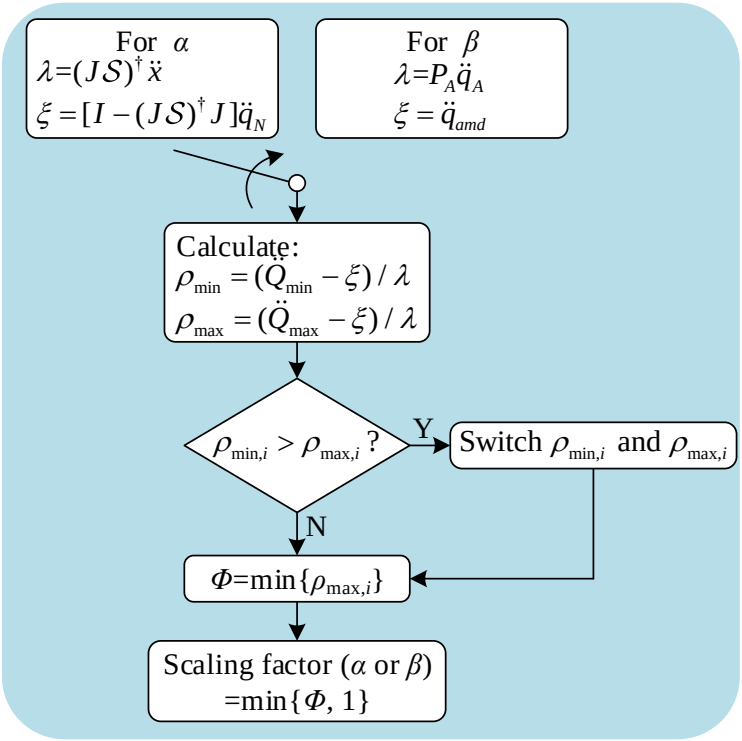

Figure B.4: Flowchart of the scaling factor determination.

the base will still move with a constant velocity. However, our goal is to stop the base smoothly to obtain a better end-effector trajectory tracking accuracy when no acceleration is distributed to it. Here, a transition function is utilized to steadily cease the mobile base

$$\ddot{q}_{b,trans}=\begin{cases}\ddot{q}_b, & \text{if } t\leqslant t_0\\ A_{\min,b}, & \text{if } sign(V_b)>0 \quad \& \quad t_0<t<t_f^+\\ A_{\max,b}, & \text{if } sign(V_b)<0 \quad \& \quad t_0<t<t_f^-\\ 0, & \text{if } sign(V_b)>0 \quad \& \quad t\geqslant t_f^+\\ 0, & \text{if } sign(V_b)<0 \quad \& \quad t\geqslant t_f^-\end{cases} \tag{B.20}$$

where $\ddot{q}_{b,trans}$ is the base acceleration during the transition process, t_0 and $t_f^+(t_f^-)$ represent the start and end time of the transition, respectively. Also, $t_f^+=|\frac{V_b}{A_{\min,b}}|+t_0$ and $t_f^-=|\frac{V_b}{A_{\max,b}}|+t_0$. For the transition process, the mobile base will be deactivated with the maximum acceleration to keep high tracking accuracy. V_b is the base velocity when the base is deactivated and $\sigma_m\geqslant\sigma_{m,min}$ is achieved, and $A_{\max,b}$ and $A_{\min,b}$ are the maximum and minimum acceleration of the base, respectively.

Fig. B.4 shows the process of determining the scaling factors according to the joint bounds (B.6)-(B.8). As shown in Fig. B.4, λ denotes the required joint acceleration for the previous task, and ξ represents the consuming joint motion capability of the manipulator for the corresponding task. Then, we will calculate the ratio of the residual joint acceleration to the required joint acceleration (denoting as $\rho_{\min}$ and $\rho_{\max}$), and get the minimum ratio of all the joints, expressed as Φ. The parameter Φ is a criterion indicating the residual capability of the manipulator to complete the task. If $\Phi \geqslant 1$, the manipulator has enough capability to accomplish the task; if $\Phi < 1$, the manipulator can not fulfill the mission. Since we should not upscale the given task, the scaling factor (α or β) is chosen as the smaller one between Φ and 1.

B.4 Experimental Results

In order to verify the effectiveness and advantages of the proposed control method, the proposed control method was applied to a wheeled mobile manipulator compared with a traditional control approach that uses the pseudoinverse of the Jacobian (we even extended the traditional approach to do manipulability enhancement). The experiments consist of two parts: (A) The verification of the importance of singularity avoidance as the tertiary objective, and (B) the evaluation of the proposed trajectory tracking method.

B.4.1 Experimental Setup

The experiments were performed using an omnidirectional wheeled mobile manipulator. The WMM is the sum of a four-wheel mobile base and a 7-DOF ultra-lightweight robotic Gen3 arm (Kinova Robotics, Canada) as shown in Fig. B.1. Kinova Gen3 is a promising robotic arm for compliant industrial application and safe human/robot collaboration. The maximum reachable distance for the manipulator is 902 mm with maximum Cartesian translation speed 40 cm/s. The mobile base is equipped with two pairs of Mecanum wheels, so it can undertake omnidirectional motion. It is noteworthy that the WMM system is controlled at the velocity level. Thus in this section,

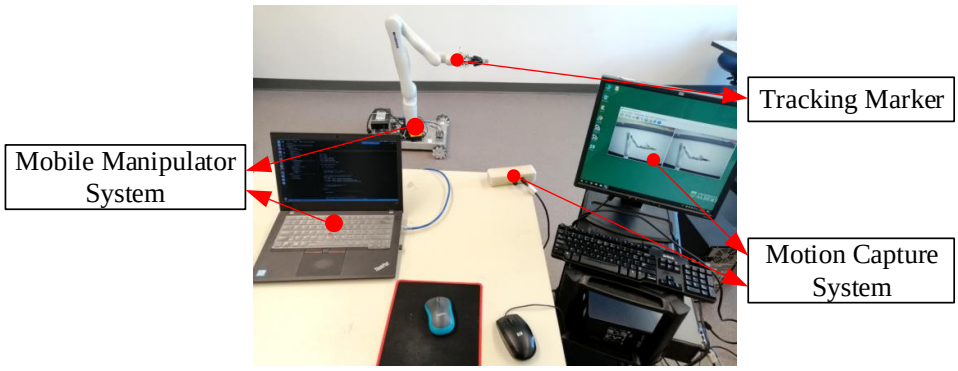

Figure B.5: Experimental setup.

the integral of the calculated joint acceleration is commanded to the robotic system.

Fig. B.5 presents the setup for the experiment, which consists of an omnidirectional wheeled mobile manipulator system (self-assembled) and a motion capture system (Claron Technology Inc., Canada), the RMS value of the calibration accuracy of the motion capture system is 0.35 mm. It should be noted that the motion capture system is only used for obtaining the actual position of the end-effector as ground truth to evaluate the tracking accuracy of the proposed method and not used in the control system.

The WMM we used in our experiment is an omnidirectional one and we chose J as the Jacobian for it as defined in (B.2). The generalized coordinate for the mobile base (shown in Fig. B.6) is defined as $q_b = [x_b, y_b, \theta_b]^{\mathrm{T}} \in \mathbb{R}^3$ and the velocity command vector of the wheels as $v_b = [\omega_{fl}, \omega_{fr}, \omega_{bl}, \omega_{br}]^{\mathrm{T}} \in \mathbb{R}^4$. The velocity transformation matrix $P(q_b) \in \mathbb{R}^{3\times4}$, which transfers the wheel velocity to the generalized base velocity, can be expressed as

$$P(q_b) = J_I J_V, \tag{B.21}$$

with

$$J_I = \begin{bmatrix} \cos\theta_b & -\sin\theta_b & 0 \\ \sin\theta_b & \cos\theta_b & 0 \\ 0 & 0 & 1 \end{bmatrix},$$

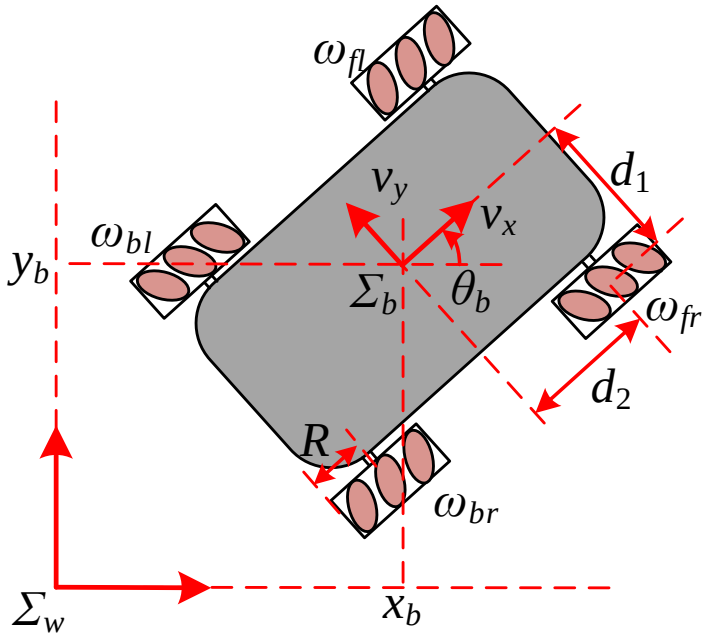

Figure B.6: Description of the omnidirectional mobile base.

and

$$J_V = \frac{R}{4}\begin{bmatrix} 1 & 1 & 1 & 1 \\ -1 & 1 & 1 & -1 \\ \frac{-1}{d_1+d_2} & \frac{1}{d_1+d_2} & \frac{-1}{d_1+d_2} & \frac{1}{d_1+d_2} \end{bmatrix}.$$

The variables θ_b, R, d_1, and d_2 are illustrated in Fig. B.6.

The joint constraints of the WMM are listed in Table B.1, where the units of angle, velocity, and acceleration for prismatic joints (the first and second joints) are m, m/s, and m/s^2; and for revolute joints (the remaining eight joints) are rad, rad/s, and rad/s^2, respectively. The dimension of the Cartesian space of the mobile manipulator is defined to be $r = 3$ as only the position of the end-effector is considered in this section. The mobile base frame Σ_b is assumed to be the same with the world frame Σ_w at the start of the experiment. The initial joint position of the WMM is $q_0 = [0, 0, 0, 0, \pi/6, 0, \pi/2, 0, -\pi/6, 0]^{\mathrm{T}}$. Also, the initial position of the end-effector in Σ_w is $x_0 = [0.65, -0.0246, 0.4921]^{\mathrm{T}}$.

Table B.1: Joint Limits of WMM. The first three joints correspond to the mobile base and the rest seven joints to the manipulator.

Joint No.	Joint type	Angle	Velocity	Acceleration
1	Prismatic	$\pm\infty$	±0.25	±0.025
2	Prismatic	$\pm\infty$	±0.25	±0.025
3	Revolute	$\pm\infty$	±1.0	±1.5
4	Revolute	$\pm\infty$	±1.75	±3.0
5	Revolute	±2.2	±1.75	±3.0
6	Revolute	$\pm\infty$	±1.75	±3.0
7	Revolute	±2.5	±1.75	±3.0
8	Revolute	$\pm\infty$	±3.14	±5.0
9	Revolute	±2	±3.14	±5.0
10	Revolute	$\pm\infty$	±3.14	±5.0

B.4.2 Experiments with and without Singularity Avoidance

The AMD method without having a tertiary objective will often put the manipulator at a singular configuration. Although the employment of singularity avoidance will somewhat decrease the accuracy of the trajectory following of WMM as it enables the mobile base, it is unavoidable. The AMD method and the modified AMD method (i.e., the AMD method with singularity avoidance) have been experimentally compared to verify the effectiveness of the latter. The end-effector acceleration $\ddot{x}$ in (B.5) is changed to $\ddot{x}_d + K_d(\dot{x}_d - \dot{x}) + K_p(x_d - x)$ to make sure the trajectory tracking error convergences to zero, where x_d is the desired end-effector trajectory, and K_d and K_p are two positive constants. During all the experiments, we define the desired trajectory as a circle with a radius of R, with the definition being $x_d(t) = x_0 + \big[-R(\cos(\pi/20t) - 1), -R\sin(\pi/20t), 0\big]^{\mathrm{T}}$. For the experiments in this section, we define the radius of the circle as $R = 0.25$ m. It should be noted that this radius is beyond the manipulator workspace (0.2 m) at its initial configuration. The close-loop control parameters for the desired trajectory K_d and K_p are the same during the two experiments to indicate the fairness of the comparison, with $K_d = 10I_{3\times3}$ and $K_p = 20I_{3\times3}$. The other control parameters are set as $\gamma_1 = 5$, $\gamma_2 = 0.5$, $\sigma_{m,min} = 0.15$. The threshold valve for singularity avoidance $\sigma_{m,min}$ is obtained by trail and error to make the system

put off the activation time of the mobile base and maintain the stability of the system simultaneously. Fig. B.7 presents the results during the experiment.

Fig. B.7(a) shows the experimental results with singularity avoidance and without it. If the AMD method is adopted, the manipulator tries to complete the task alone and ultimately puts itself at a singular configuration at about 8.35 s. This causes the system to be uncontrollable and makes the task incomplete. However, with manipulability enhancement as the tertiary objective, when the manipulator is near a singularity, the mobile base is activated and the manipulator can adjust its configuration to move away from singularity. Thus, the task can still be executed. Fig. B.7(b) shows the position tracking when no manipulability enhancement (singularity avoidance) was adopted; the desired trajectory cannot be tracked at about 8.35s and significant tracking errors start to emerge in all Cartesian directions.

B.4.3 Experiments for Trajectory Tracking

The proposed kinematic control approach can make the best use of the manipulator to execute tasks while keeping it from a singularity, and the mobile base is enabled only when the task cannot be executed by the manipulator alone or the manipulator is close to a singular configuration. With this method, the contribution of the base to the overall WMM motion is minimized, thus improving the motion tracking precision of the WMM.

The proposed kinematic control was implemented to verify the efficiency of the proposed approach compared with the traditional kinematic control by tracking a predefined end-effector trajectory. The traditional controller in the experiment means using the pseudoinverse of the Jacobian $J^{\dagger} = J^{\mathrm{T}}(JJ^{\mathrm{T}})^{-1}$ with considering manipulability enhancement for the manipulator in the null space [146]. At the acceleration level, the controller can be expressed as $\ddot{q} = J^{\dagger}(\ddot{x} - \dot{J}\dot{q}) + (I - J^{\dagger}J)\ddot{q}_A$, where $\ddot{q}_A$ is defined in (B.13). Two desired trajectories are provided, the first one is within the manipulator workspace and the second one is beyond it. The trajectory within the manipulator workspace is a circle with a radius of $R = 0.1$ m and the other one is a circle with a radius of $R = 0.25$ m. The control parameters for the experiments in this section are

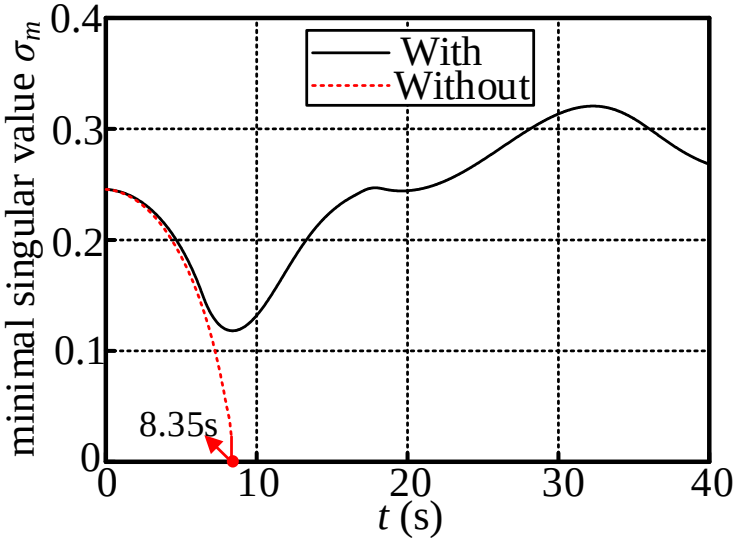

(a) Singularity criterion

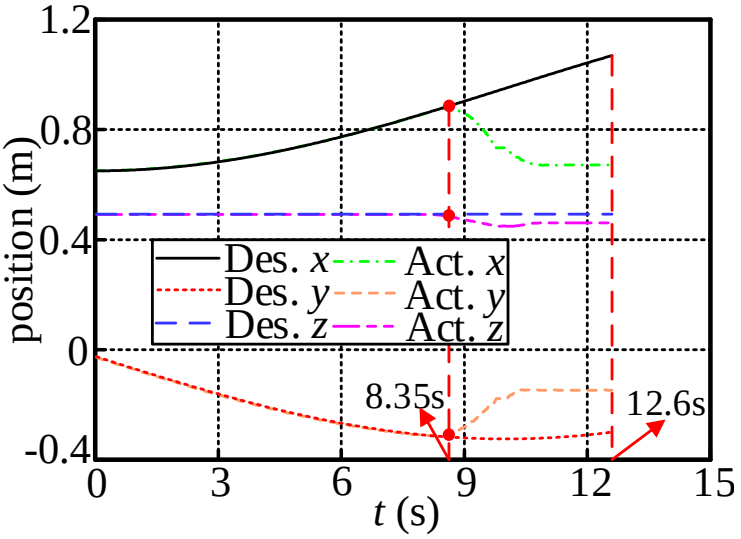

(b) Position of the end-effector

Figure B.7: Results of the manipulability enhancement experiment. The left plot presents the singularity criterion for the manipulator, and the right plot shows the end-effector position of the WMM using AMD method without singularity avoidance.

Table B.2: RMS value and commanded duration of base velocity

		Within workspace		Beyond workspace	
		Proposed	Traditional	Proposed	Traditional
x_b	RMS (cm/s)	0	1.10	1.58	2.77
	Duration (s)	0	80	12.08	80
y_b	RMS (cm/s)	0	0.75	0.24	1.86
	Duration (s)	0	80	12.08	80
θ_b	RMS (°/s)	0	0.287	0.241	0.739
	Duration (s)	0	80	12.08	80

the same as those in section B.4.2. Figs. B.8 and B.9 show the experimental results within the manipulator workspace, and Figs. B.10 and B.11 present the results beyond the manipulator workspace. It is worth mentioning that with the traditional method, the mobile base is always involved in the experiment and no joint saturation of the manipulator occurs. The actual position of the end-effector is obtained via the motion capture system to have ground-truth information. Table B.2 contains the RMS value and duration time of the commanded base velocity in these two scenarios.

Fig. B.8(a) shows that when the end-effector trajectory is within the manipulator workspace, with the proposed motion distribution method, there is only a small tracking error. This is due to the fact that no motion is assigned to the base as shown in the first column of Table B.2. With no adaptive motion distribution, some motion will be imposed on the base, as shown in the second column of Table B.2. Thus, the trajectory tracking error will be much larger compared to the motion distribution scenario due to the low motion accuracy of the base, with maximum errors in x and y being 0.91 cm and 1.89 cm, respectively. The trajectory tracking error is shown in Fig. B.8(b). Fig. B.9 shows the motion of the mobile base with the traditional method, where v_{xb}, v_{yb}, $\omega_{\theta b}$ represent the commanded base velocities in x_b, y_b, and θ_b, respectively. The motion of the mobile base with the proposed method is not presented since no motion is distributed to it.

The last two columns of Table B.2 show that if the desired end-effector trajectory is beyond the manipulator workspace, the mobile base will always be forced to move. However, the base movement is much smaller if one uses

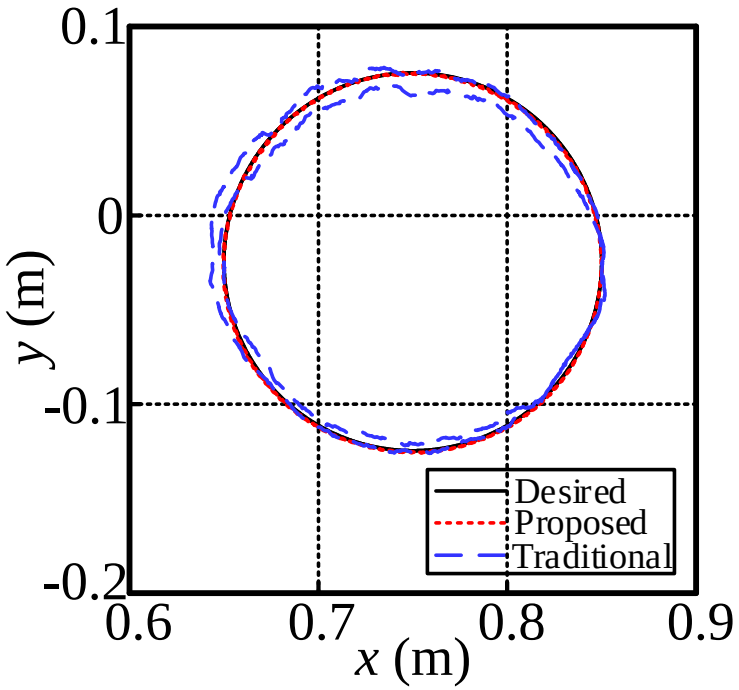

(a) End-effector trajectories

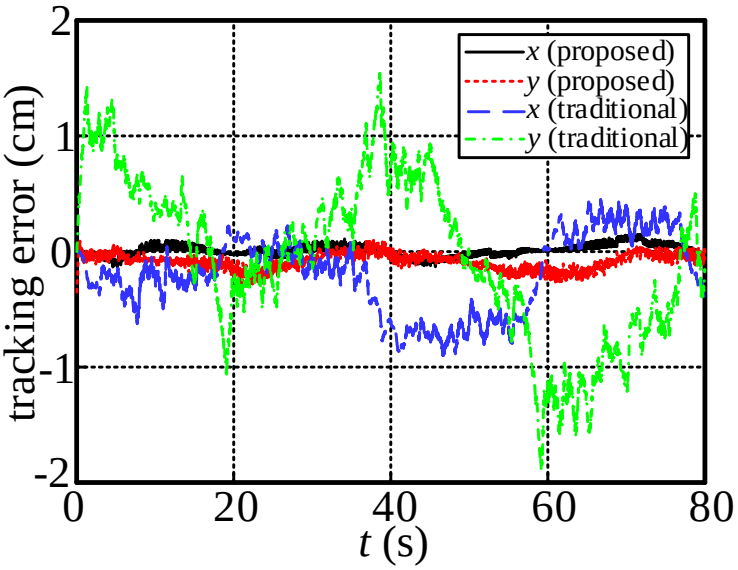

(b) Tracking errors

Figure B.8: End-effector trajectory tracking performance with traditional and proposed methods (within manipulator workspace).

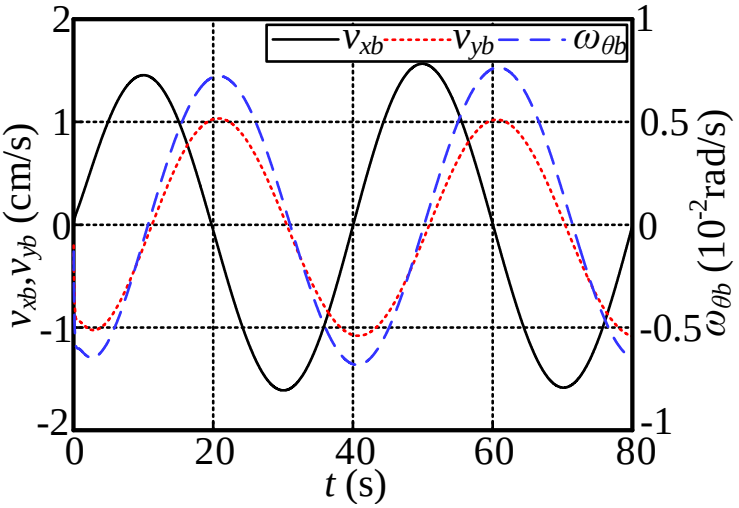

(a) Commanded velocities

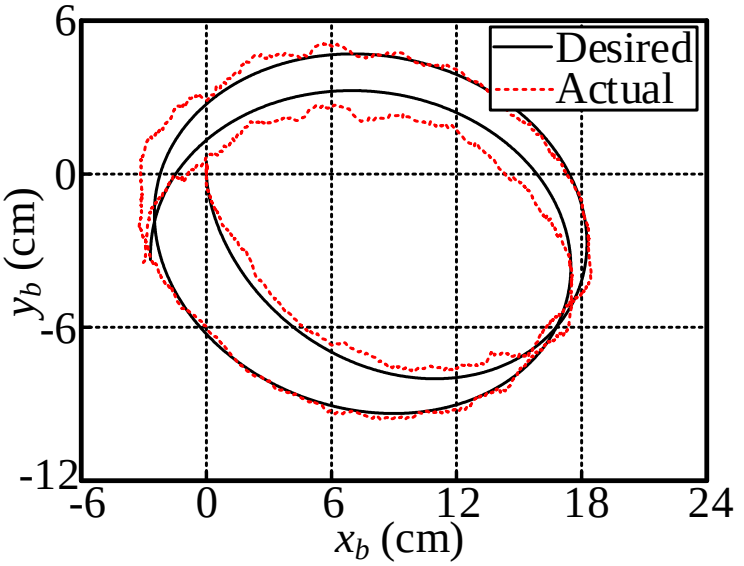

(b) Trajectories in $x - y$ plane

Figure B.9: Motion of the mobile base with traditional method (within manipulator workspace).

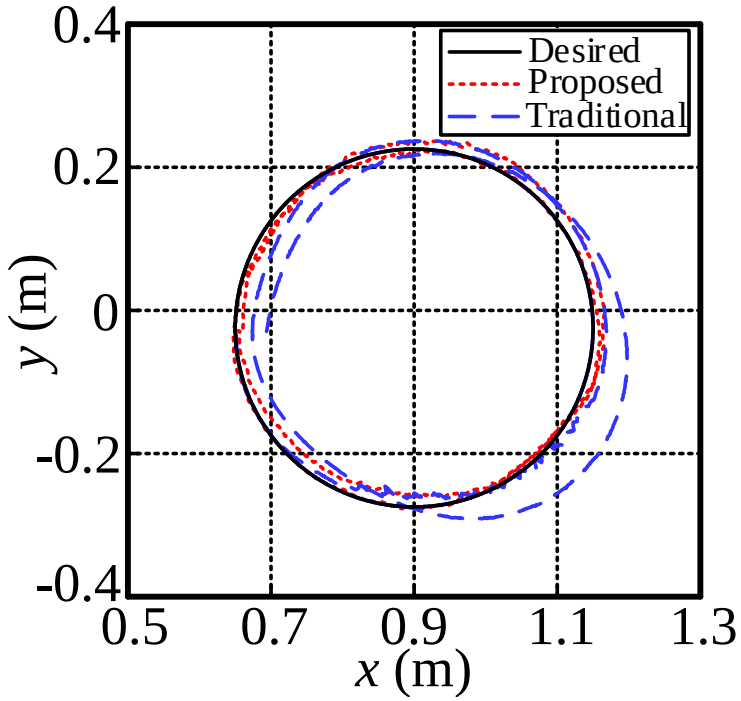

(a) End-effector trajectories

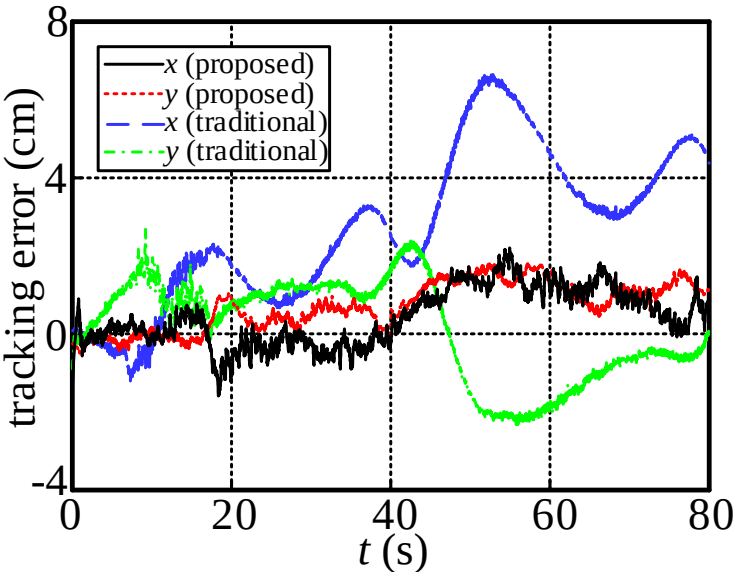

(b) Tracking errors

Figure B.10: End-effector trajectory tracking performance with traditional and proposed methods (beyond manipulator workspace).

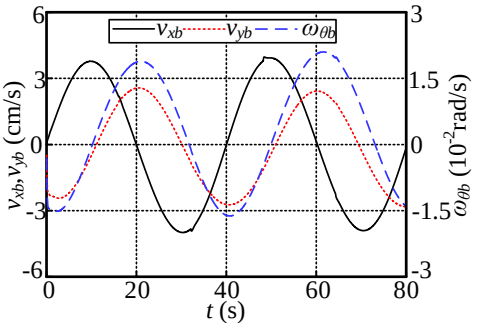

(a) Commanded velocities

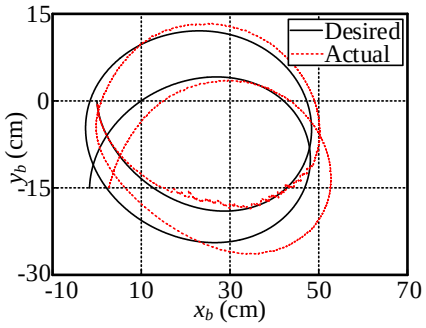

(b) Trajectories in $x - y$ plane

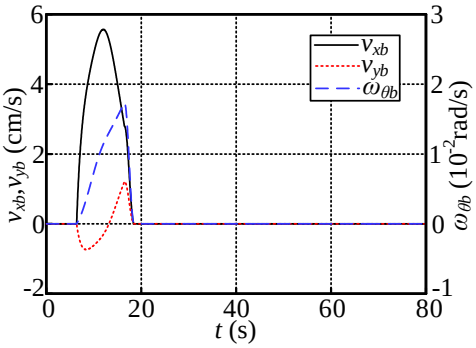

(c) Commanded velocities

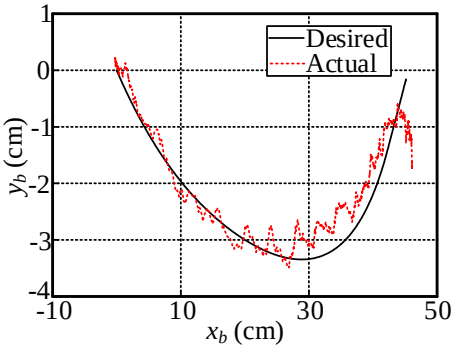

(d) Trajectories in $x - y$ plane

Figure B.11: Motion of the mobile base with traditional and proposed methods (beyond manipulator workspace).

the proposed adaptive motion distribution method. The commanded duration time and RMS values for the base velocity in x_b, y_b, and θ_b represent 15.10%, 57.04%, 12.90%, and 32.61% of the commands without distribution, respectively. Fig. B.10 contains the end-effector tracking results, and Fig. B.10(b) shows that the maximum tracking error for x is reduced from 6.65 cm to 2.44 cm and for y is reduced from 2.72 cm to 1.82 cm compared with no motion distribution.

Fig. B.11 presents the motion of the mobile base when the desired end-effector trajectory is beyond the manipulator workspace with two different control methods. Figs. B.11(a) and B.11(b) show that with the traditional method, the mobile base was consistently distributed with some motions, and thus, the trajectory tracking error was significant. The mobile base motion with the proposed method is shown in Figs. B.11(c) and B.11(d). As shown in Fig. B.11(c), the base was activated at time 6.40 s. The manipulator regained enough manipulability at about 16.48 s. However, the base was not deactivated suddenly due to the implementation of the transition function (B.20), instead, it would gradually stop. Fig. B.11(d) shows the desired and actual trajectories for the mobile base in the $x-y$ plane with proposed method. We define the integral of the tracking error for the mobile base as $\frac{\int_{T_s}^{T_f} |e_{i_b}| dt}{T_f - T_s}$, where T_s and T_f represent the start time and final time for the base motion, and e_{i_b} denotes the position tracking error for the base. With the traditional approach, the integral of the tracking errors in x_b and y_b were 2.81 cm and 1.12 cm, respectively, while these values changed to 0.81 cm and 0.37 cm with the proposed approach. It is obvious that with the proposed method, the distributed motion to the base was much less, and the tracking accuracy was improved significantly.

B.5 Conclusions

A new approach to improve the trajectory tracking capability for a wheeled mobile manipulator (WMM) is proposed considering the need for singularity avoidance. To improve the tracking accuracy of the WMM, we present an adaptive motion distribution method to transfer more motion to the manipu-

lator due to the lower motion precision of the mobile base. Using the proposed motion distribution method, the mobile base of the WMM will keep immobile until all the redundancy of the manipulator for the task has been employed or the manipulator is close to a singularity. Only when the manipulator's remaining unsaturated joints are not enough for performing the task will the controller assign some of the motion to the mobile base to execute. To avoid singularity, we adopt the task priority method to define manipulability enhancement as a tertiary task. In summary, when the primary task (trajectory tracking) and the secondary task (adaptive motion distribution) are resolved, the remaining DOFs can be used to keep the system away from the singularity (tertiary task). The proposed approach is designed at the acceleration level to avoid the discontinuity of the joint velocity due to the activation or termination of the mobile base. The effectiveness of the proposed approach has been verified compared with the traditional method through experiments by tracking several predefined end-effector trajectories. For the desired end-effector trajectory beyond the manipulator workspace, the maximum tracking error of the end-effector has been improved by 63.3% and 33.1% in x and y, respectively, and the motion time for the mobile base decreased by 84.90%. In future works, we will consider making a bilateral teleoperation system with one or two user interfaces to control the mobile base and the manipulator simultaneously to enhance the motion control of WMMs further.